

**Progress in Tests of Fundamental Physics Using a
 ^3He and ^{129}Xe Zeeman Maser**

A dissertation presented

by

Alexander Graham Glenday

to

The Department of Physics

in partial fulfillment of the requirements

for the degree of

Doctor of Philosophy

in the subject of

Physics

Harvard University

Cambridge, Massachusetts

December 2010

©2010 - Alexander Graham Glenday

All rights reserved.

Dissertation Advisor:
Professor Ronald L. Walsworth

Author:
Alexander Graham Glenday

Progress in Tests of Fundamental Physics Using a ^3He and ^{129}Xe Zeeman Maser

Abstract

We report on improved operation and understanding of the ^3He and ^{129}Xe Zeeman maser and its use in testing new theories in fundamental physics. The ^3He and ^{129}Xe Zeeman maser can make differential measurements of magnetic field versus new spin dependent forces that couple to the neutron, as ^3He and ^{129}Xe have nuclear gyromagnetic ratios that differ by a factor of ~ 2.75 , but whose spin-1/2 nuclear moments are due almost entirely to unpaired neutrons. Specifically, we evaluate the performance of the ^3He and ^{129}Xe maser in terms of searches for Lorentz and *CPT* symmetry breaking background fields to the universe described by the Standard Model Extension of Kostelecký and coworkers [1] and for placing limits on anomalous spin-spin coupling between neutrons such as those due to spin dependent forces mediated by the proposed axion particle [2]. The ^3He and ^{129}Xe maser has previously been used to place a limit on the coupling of the neutron to Lorentz and *CPT* symmetry violating fields at the level of 10^{-31} GeV (50 nHz in the ^3He Zeeman frequency). Improvements we have made to the maser system have increased our sensitivity by almost a factor of four and we believe reasonable future upgrades could lead to a further order of magnitude improvement. In this work we have also measured the nuclear Zeeman frequencies of a ^3He and ^{129}Xe maser while modulating the nuclear spin polarization of a nearby ^3He ensemble in a separate glass cell. We place limits on the coupling strength of neutron spin-spin interactions mediated by light pseudoscalar particles like the axion ($g_p g_p / (4\pi\hbar c)$) at the 3×10^{-7} level for interaction ranges longer than about 40 cm.

Contents

Abstract	iii
Table of Contents	iv
List of Figures	vi
List of Tables	viii
Acknowledgments	ix
1 Introduction to the ^3He and ^{129}Xe Zeeman Maser	1
2 Theory of the ^3He and ^{129}Xe Zeeman Maser	8
2.1 Double Bulb Maser	9
2.1.1 Pump Bulb - Spin Exchange Optical Pumping	11
2.1.2 Transfer Tube - Diffusive Transport	20
2.1.3 Maser Bulb - Maser Equations	30
2.2 Maser Equation Solutions	43
2.2.1 Steady State	44
2.2.2 Co-magnetometry and the Extended Maser	49
2.2.3 Transients	63
2.3 Polarization Relaxation Mechanisms	79
2.3.1 Polarization Lifetime T_1	80
2.3.2 Coherence Time T_2	83
2.4 Frequency Shifts	88
2.4.1 Modulation to Reduce Drifts	98
2.5 Sensitivity and Possible Improvements	99
2.5.1 Noise Sources	100
2.5.2 Scaling Laws for Sensitivity and Comparisons to Competing Technologies	104
2.5.3 Changing Detection Methods	108
3 Experimental Realization	111
3.1 Double Bulb Maser Cells	112
3.2 Magnetic Field Control	116
3.3 Maser Oven and Thermal Control	120
3.4 Optical Pumping	123
3.5 Doubly Resonant Circuit	125
3.6 Measuring Maser Frequency/Phase	131
3.7 Measuring Polarization Relaxation and Other Rates	133

4 Lorentz Symmetry Tests	145
4.1 SME Theory	146
4.2 Data Analysis Methods	149
4.2.1 Generalized Least Squares	151
4.2.2 Least Squares Periodograms and Monte Carlo Tests	152
4.3 Preliminary Results Compared to Previous Maser	158
5 Anomalous Spin-Spin Coupling Measurements	163
5.1 Limits on Anomalous Spin-Spin Couplings Between Neutrons	164
Bibliography	177

List of Figures

1.1	Simplified schematic of the maser.	3
2.1	Schematic of temperature and polarization gradients between the dual bulbs.	23
2.2	Calculated effect of choke coils on ^{129}Xe	55
2.3	Calculated effect of choke coils on ^3He	56
2.4	Maser frequency shifts due to frequency shifts of transverse polarization in the pump bulb.	61
2.5	Noise spectra of pump bulb temperature and laser power.	74
2.6	Fractional amplitude noise spectral densities of the ^3He and ^{129}Xe masers, theoretical calculations and experimental data. (Note: markers in the calculated theory curves are placed once per 100 calculated points.)	76
2.7	Frequency noise spectral densities of the masers, theoretical calculations and experimental data. (Note: markers in the calculated theory curves are placed once per 100 calculated points.)	78
2.8	Measured spectral density at the input to the amplifier of the resonant circuit.	103
3.1	Schematic of major ^3He and ^{129}Xe maser subsystems (not to scale).	113
3.2	Double bulb cell and manifold schematic.	115
3.3	Magnetic shields and solenoid schematic.	117
3.4	Maser oven schematic.	121
3.5	Cascade lock to stabilize the oven temperature.	122
3.6	Layout and equivalent circuit for the double resonant circuit.	127
3.7	Measured and calculated circuit response functions.	129
3.8	Measured and calculated noise spectra of the resonant circuit.	130
3.9	Measured spectrum of the resonant circuit frequency stability.	131
3.10	Test of phase detection system.	132
3.11	Monte Carlo fit of ^{129}Xe FID to measure T_2'	138
3.12	Measurement of ^{129}Xe T_1 and diffusive exchange rates.	140
3.13	Measurement of Rb- ^{129}Xe spin exchange for low Rb polarization.	143
3.14	Measurement of Rb- ^{129}Xe spin exchange for high Rb polarization.	143
4.1	Monte Carlo synthetic data for ^3He maser frequency spectral density with random walk correlations.	153
4.2	Monte Carlo synthetic data for ^3He maser frequency spectral density without random walk correlations.	154

4.3	Measured spectrum with different fit models.	155
4.4	Monte Carlo synthetic data that matches the measured spectra for the ^3He maser frequency.	156
4.5	Distributions of the sum of the squares of the residuals for different fit models.	157
4.6	Distributions of the sum of the squares of the residuals with fewer degrees of freedom.	157
4.7	Previous and current system maser frequency spectral densities.	159
4.8	Previous and current system maser fractional amplitude spectral densities. .	160
4.9	^3He maser spectra from the previous system grouped into small and large frequency noise sets.	162
5.1	Maser and spin source schematic.	167
5.2	Noise spectrum of the ^3He Zeeman maser frequency.	169
5.3	Distribution of frequency modulation amplitudes.	170
5.4	Exclusion region for axion interactions.	172
5.5	Wake and shockwave potential.	174
5.6	Exclusion region for wake potential.	175

List of Tables

2.1	Typical double bulb physical characteristics.	10
2.2	Rate constants for binary collision spin destruction of Rb.	15
2.3	Rate constants for binary collision spin exchange of ^3He and ^{129}Xe with Rb.	17
2.4	Longitudinal polarization loss due to wall collisions in an average cell.	25
2.5	Binary diffusion coefficient parameters.	29
2.6	Gas diffusion parameters and rates for a typical cell.	30
2.7	Noble gas gyromagnetic ratios and typical maser frequencies.	32
2.8	Doubly resonant circuit and pickup coil parameters.	37
2.9	Effective time constants for each bulb.	42
2.10	Calculated steady state maser operating parameters.	48
2.11	Coefficients for the decoherence rate due to magnetic field gradients.	86
2.12	Maser frequency shift mechanisms, magnitudes, and fluctuations.	97
3.1	Magnetic field gradient coil strengths.	118
4.1	SME limits determined by our previous version of the ^3He and ^{129}Xe maser.	148

Acknowledgments

There are many people who helped me during my graduate student career. None of this would have been possible without the help and support of my thesis advisor, Prof. Ron Walsworth, who came up with the original concept for the ^3He and ^{129}Xe maser experiment and is always looking for new fundamental physics to test using it. Much of my work builds on the efforts of previous graduate students, in particular Federico Canè, who introduced me to the experiment and designed and built many of the components that made this work possible. The knowledge and experience of the staff scientists in our group, David Phillips and Matt Rosen, were invaluable in solving the myriad technical challenges of the experiment. They were always available to listen to my ideas, help me clarify my thoughts, and teach me new physics and experimental techniques. There was also a constant exchange of ideas and camaraderie with my fellow graduate students and post-docs in the group over the years, Mason Klein, Mike Hohensee, Yanhong Xiao, Irena Novikova, Leo Tsai, Paul Stanwix, and Chih-hao Li. Outside of the lab I had the support of my family, friends and especially my wife, Justine, who made life outside of lab wonderful.

Chapter 1

Introduction to the ^3He and ^{129}Xe Zeeman Maser

Precision atomic measurements have frequently been used to test fundamental physics and search for potential modifications to our current understanding of the universe. In this work, we describe an experimental search for new forces that couple to the spin of the neutron generated either by the spins of other neutrons or background fields to the universe. We detect the presence of such new fundamental physics by measuring the differential nuclear Zeeman splittings or Larmor frequencies of co-located ^3He and ^{129}Xe noble gases held in a glass cell. These monatomic noble gases have spin-1/2 nuclei whose gyromagnetic ratios are different by a factor of ~ 2.75 , but whose nuclear magnetic moments are largely due to unpaired neutrons. Since the new physics we are searching for couples with the same strength to all neutrons we are able to separate the effects of magnetic fields from new spin dependent forces with our ^3He and ^{129}Xe comagnetometer, which is operated as a Zeeman maser for each species.

Like many atomic measurements, our experiments involve a three step process where we (i) prepare the system in a particular (useful) state; then (ii) remove the preparation interaction as its strong coupling, necessary to manipulate the populations of the states, results in an undesirable shifting in the energy separation of those states; and finally (iii)

measure the atomic system with a minimum of perturbations to search for the possible new physics of interest. Our state preparation consists of polarizing the ^3He and ^{129}Xe nuclear spins in their higher-energy Zeeman states via collisional hyperfine interactions with Rb vapor whose valence electron spins have been polarized by optical pumping with a resonant laser. This population inversion for the ^3He and ^{129}Xe spins takes place in one bulb of our double-bulb glass cell, referred to as the pump bulb, which is typically kept at a constant 120 °C to generate an appreciable Rb vapor pressure. The polarized noble gases then diffuse down a narrow tube into a much cooler bulb at 50 °C, and hence a negligible Rb vapor pressure, where the nuclear spins inductively couple to a doubly resonant circuit tuned to both the ^3He and ^{129}Xe Larmor frequencies. With a sufficient flux of polarized nuclei into the second bulb, referred to as the maser bulb, the feedback from the resonant circuit creates active Zeeman masers from both noble gases (simple and more complex schematics of the experiment are shown in Fig. 1.1 and Fig. 3.1). The advantages of running the system as a maser is that it operates in steady state, there are no large transient changes, and we can continuously monitor the Larmor frequencies. On the other hand, the feedback from the resonant circuit, necessary for masing, is clearly not a small perturbation; and hence the circuit requires very careful stabilization to avoid fluctuations in its resonant frequencies and thus the maser signals. Similarly, the nuclear Larmor frequencies must stay matched to the circuit resonances, so we provide a stable, homogeneous magnetic field by placing our double bulb cell inside a solenoid located within three nested layers of magnetic shielding; and stabilize the magnetic field generated by the solenoid with feedback generated by comparing the Larmor frequency of one maser to a frequency standard (typically a H maser) that is unaffected by the new physics we are probing.

The ^3He and ^{129}Xe maser frequencies, ω_{He} and ω_{Xe} , including the Larmor frequency and shifts generated by new spin dependent forces, ω_{SF} , are given by,

$$\omega_{He} = \gamma_{He}B_0 + \alpha_{He}\omega_{SF} \quad (1.1)$$

$$\omega_{Xe} = \gamma_{Xe}B_0 + \alpha_{Xe}\omega_{SF} \quad (1.2)$$

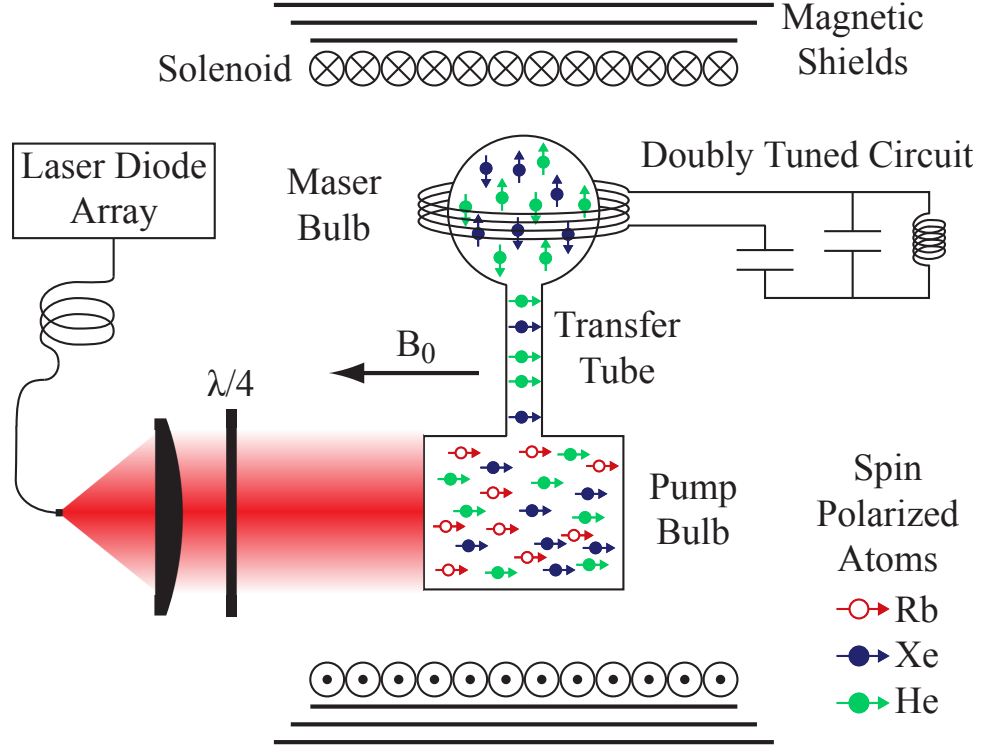


Figure 1.1: Schematic (not to scale) showing spin-exchange optical pumping of ^3He and ^{129}Xe in the pump bulb and active masing with feedback in the maser bulb.

where B_0 is the magnetic field of the solenoid, γ_{He} and γ_{Xe} are the gyromagnetic ratios, and $\alpha_{\text{Xe}} = 0.75$ [3] and $\alpha_{\text{He}} = 0.87$ [4] are the fraction of the nuclear spin due to the neutron. We can extract the new physics shift by eliminating the common mode magnetic field giving us the comagnetometry signal,

$$\omega_{\text{He}} - \frac{\gamma_{\text{He}}}{\gamma_{\text{Xe}}} \omega_{\text{Xe}} = \left(\alpha_{\text{He}} - \alpha_{\text{Xe}} \frac{\gamma_{\text{He}}}{\gamma_{\text{Xe}}} \right) \omega_{\text{SF}} \approx -1.2 \omega_{\text{SF}}. \quad (1.3)$$

It is very difficult to measure gyromagnetic ratios accurately and our maser system has a myriad of other mundane frequency shifts besides ω_{SF} , so in order for a new spin dependent force to be detectable by our ^3He and ^{129}Xe masers we have to be able to modulate the strength of the force's interaction in some manner. For detecting background fields to the universe, such as the Lorentz and CPT symmetry violating fields posited by Kostelecký

and coworkers in their Standard Model Extension [1], we orient our solenoid field and nuclear spins along the east-west direction parallel to the Earth's surface and wait for the Earth to rotate through the presumably homogeneous background field. This generates a modulation in the comagnetometry signal with the period of the sidereal day due to the changing orientation of the spins with respect to the background field and requires careful engineering of the experiment to stabilize all the mundane shifts of the masers over that timescale. In order to detect new forces between neutron spins, such as the new forces mediated by the postulated axion particle [2], we need both our ^3He and ^{129}Xe detector and a neutron spin source to apply the force. For our spin source we use a much larger cell filled with a high pressure of ^3He gas and operated at high temperature to generate a dense Rb vapor for more rapid polarization of the ^3He which ultimately leads to $\sim 2 \times 10^{21}$ polarized neutron spins located 40 cm from the maser bulb. We modulate the orientation of the spin source spins using adiabatic fast passage techniques from NMR and apply the modulation with a frequency that gives us the maximum sensitivity from the ^3He and ^{129}Xe masers.

To give a sense of scale of the experiment, the pump and maser bulbs each have volumes of order 5 cm^3 and are separated by $\sim 3 \text{ cm}$. The cell typically contains of order 50 Torr of ^{129}Xe and 1000 Torr of ^3He and the vapor pressure of Rb is more than two order of magnitude lower in the maser bulb than the pump bulb. The solenoid provides a 6 G magnetic field giving maser frequencies of 7.1 kHz for ^{129}Xe and 19.6 kHz for ^3He . The solenoid is about 1 m long and 20 cm in diameter surrounded by three layers of shields whose outer dimensions are 1.5 m in length and 40 cm in diameter. When freely precessing in the maser bulb, without feedback from the resonant circuit, the noble gas nuclear spins have coherence times on the order of 100 s to a few 100 s which corresponds to line-widths of 3 to 1 mHz. Once the masers have achieved steady state operation they deliver an output power to the resonant circuit of order 1 fW, which is limited by thermal Johnson noise in the circuit, leading to a signal-to-noise ratio (SNR) of $\sim 500 / \sqrt{\text{Hz}}$. Our ability to detect changes in the maser frequencies is the same as for measuring the center point

of any spectral line profile, the width of the line divided by the SNR of the measurement, which gives us a sensitivity of about $10 \mu\text{Hz}/\sqrt{\text{Hz}}$ for the comagnetometry measurement. However, this sensitivity scaling is only correct if the line shape has been resolved and similarly, in the case of our continuous measurement, our sensitivity is worse for timescales shorter than our non-masing line widths. For a measurement of one day in length, this level of sensitivity corresponds to an uncertainty of $\sim 30 \text{ nHz}/\sqrt{\text{day}}$, which is a level we have been able to reach for measurements of forces between spins, due to the ability to optimize the frequency of the modulation of the interaction, but not for background fields as we suffer from other frequency fluctuations when looking for modulations with the (very small) sidereal day frequency. Additionally, for a measurement of new forces between neutron spins, the size of the neutron spin source ($\sim 2 \times 10^{21}$ neutron spins in our experiment) and its proximity to the ^3He and ^{129}Xe maser (41 cm in our experiment) also determine the limits that we can place on the existence of new forces.

With previous versions of our ^3He and ^{129}Xe masers we have limited coupling to background fields to the universe at the level of $\sim 50 \text{ nHz}$ in the ^3He maser frequency [5, 6]; and with the improved version of the experiment described in this thesis we have more recently limited coupling to other neutron spins to $\sim 6 \text{ nHz}$ [7] using the spin source described above (3 nHz corresponds to approximately 1 pG or 0.1 fT or 10^{-32} GeV). However, very recent measurements of these same effects by the Romalis group at Princeton employing a different comagnetometer using ^3He and the electron spin of K – which does not have nearly as narrow line widths as our maser, but has spectacular SNR due to its optical detection method – have set limits of $\sim 0.6 \text{ nHz}$ [8] for coupling of neutrons to background fields and $\sim 0.02 \text{ nHz}$ [9] for coupling to other neutron spins over similar length scales. Additionally, the Heil group at Mainz is developing a ^3He and ^{129}Xe comagnetometer that measures the free precession of the nuclear spins with a SQUID [10]. This system has better SNR than our experiment and line widths more than two orders of magnitude narrower than ours, which could lead to even more sensitive measurements than the K- ^3He comagnetometer. With such dramatic improvements by these alternative approaches, an important question this thesis addresses

is whether we can further improve our experiment to the point that it becomes competitive with the K- ^3He or the ^3He and ^{129}Xe free precession comagnetometers. To that end we have developed a more complete theoretical model of our maser system than has previously been presented. Our model agrees well with experimental measurements of our upgraded ^3He and ^{129}Xe maser; and leads us to conclude that our experimental approach is unlikely to surpass those of the Romalis and Heil groups.

The body of this thesis is organized around increasing levels of specificity. In Ch. 2 we discuss the theory of the maser by breaking it down into the three distinct regions of the double bulb cell, using our typical experimental parameters as examples; (i) the pump bulb where there is optical pumping of the Rb and collisional interactions with the Rb and noble gases; (ii) the transfer tube between the bulbs where polarization can be lost during diffusion due to interactions with the walls and remnant Rb; and (iii) the maser bulb where the noble gases couple to the resonant circuit. We then discuss solutions to the general theory, both steady state solutions, which give us the threshold condition for achieving masing and the power output of the maser, as well as transient solutions around the steady state equilibrium, which determine our sensitivity limits for measuring the frequency due to different input fluctuations. We also discuss extensions to the basic theory to include next order effects that can lead to frequency shifts. We detail the physical mechanisms behind the relaxation and decoherence of the noble gas polarizations and enumerate the various frequency shifts that can affect the masers as well as their approximate values and the size of their fluctuations due to fluctuating experimental parameters and how we could avoid these fluctuations by modulating the experiment. Finally, we discuss the sensitivity of the maser frequency with regards to additional noise source inputs and how the sensitivity scales with experimental parameters, what aggressive, but realistic goals might be for improvement and whether they are worth pursuing in light of the other competitive experiments. In Ch. 3 we discuss the details of our specific implementation of the maser, how we stabilize crucial experimental parameters, and how we measure the parameters of our resonant circuit and the rate constants that determine the maser behavior and validate our models. In Ch. 4

we discuss using the maser to measure Lorentz symmetry and *CPT* violating background fields to the universe as parameterized by Kostelecký and coworkers in their Standard Model Extension; and the analysis tools we use to optimize the extraction of the relevant parameters from the data. In Ch. 5 we discuss the limits we set on anomalous spin-spin coupling due to new forces between neutron spins using the updated version of the ^3He and ^{129}Xe maser described in this thesis.

Chapter 2

Theory of the ^3He and ^{129}Xe

Zeeman Maser

The key characteristic of a maser is a continuous supply of atoms or molecules with a population inversion between two states whose energy difference corresponds to a frequency in the microwave regime or lower. A population inversion means that there is a net population in the excited state and this energy is used to amplify microwave (or lower frequency) electromagnetic radiation that matches the energy difference of the two states via stimulated emission, hence “microwave amplification by stimulated emission of radiation” or maser. The radiation can either come from an external source or it can come from the atoms themselves; and, with appropriate feedback, can lead to continuous generation of resonant radiation, frequently referred to as an active maser. In our experiment the two states are the Zeeman states of the spin-1/2 nuclei of the monatomic noble gases ^3He and ^{129}Xe . The population inversion is achieved via collisions of the noble gas atoms with Rb atoms whose electrons have been spin-polarized by optical pumping with a resonant laser. We generate an active maser by coupling the noble gas atoms to a resonant circuit, which provides positive feedback to the atomic ensembles.

The ^3He and ^{129}Xe maser sensitivity to new physics is limited by our ability to measure the frequency of the radiation the masers’ produce. It is also limited by our ability to keep

that frequency stable against perturbations (other than the new physics) over the timescale that the shift due to the new physics is expected to change, such as the Earth rotating through a background field. The sensitivity of a maser frequency measurement is limited by the maser's signal to noise ratio, as determined by its output power compared to noise sources, and the characteristic time that the atoms involved in the masing stay coherent with each other. In this chapter we will develop simple analytic models to capture the physics of the ^3He and ^{129}Xe maser (Sec. 2.1) and solve them to find steady state solutions and transient fluctuations around those solutions (Sec. 2.2), which will show how noise couples into each maser to distort its frequency. We will also list the effects that can lead to loss of polarization and coherence of the masers (Sec. 2.3); as well as additional effects that can perturb the maser frequency (Sec. 2.4); and their estimated size in our system. Lastly, we will discuss the ^3He and ^{129}Xe maser sensitivity to new physics in light of other noise sources; and what future directions would be most fruitful to improve its performance (Sec. 2.5). All formulas in this chapter are in SI units, but frequently values will be given in terms of units that make sense for the scale of the experiment, such as centimeters and Gauss rather than meters and Tesla; conversion is obviously necessary before using the formulas.

2.1 Double Bulb Maser

The ^3He and ^{129}Xe maser is designed to physically separate the mechanisms of noble gas Zeeman population inversion and active masing from feedback using two glass bulbs connected by a narrow tube. As shown in Fig. 1.1, population inversion occurs in the pump bulb and masing occurs in the maser bulb after the spin polarized ^3He and ^{129}Xe gases have diffused down the transfer tube. By physically separating the two bulbs we can hold them at very different temperatures, $\sim 120^\circ\text{C}$ for the pump bulb and $\sim 50^\circ\text{C}$ for the maser bulb, and hence the Rb vapor pressure is two orders of magnitude smaller in the maser bulb than the pump bulb. While a relatively high Rb density is desirable for efficient noble

Region	Description	Parameter	Value	Units
Pump bulb	temperature	T_P	120	$^{\circ}\text{C}$
	volume	V_P	6	cm^3
	radius	R_P	0.8	cm
	length	L_P	2.8	cm
Maser bulb	temperature	T_M	50	$^{\circ}\text{C}$
	volume	V_M	4	cm^3
	radius	R_M	1	cm
Transfer tube	length	L_t	3	cm
	radius	R_t	0.17	cm
	aperture area	A_t	0.1	cm^2

Table 2.1: Typical double bulb physical characteristics.

gas Zeeman population inversion, the same relatively strong interaction between the Rb electron spin and noble gas nuclear (largely neutron) spin, which leads to noble gas polarization, also generates a large frequency shift of the noble gas Zeeman frequency, limiting maser frequency stability and our ability to search for new physics. This double bulb design was used in the first ^3He Zeeman maser for the same reason, avoiding difficult-to-stabilize frequency shifts, although their method of polarization of the ^3He was different than ours [11].

A completely general theory for the ^3He and ^{129}Xe maser is not a practical goal. Hence, we will be making many approximations (and if necessary determining the next order corrections) for which we will need some approximate values for a typical maser experiment in order to take appropriate limits. The typical radius of a bulb is 1 cm (the maser bulb is a sphere and the pump bulb is a cylinder, but they have similar volumes) and the length of the transfer tube is about 3 cm. The typical gas diffusion coefficient (within about a factor of 2) is $0.5 \text{ cm}^2/\text{s}$ and hence the typical time to diffuse across a bulb is a second. The noble gas nuclear spin polarization aligned with the main applied magnetic field (B_0) is referred to as the longitudinal polarization and the characteristic time scale over which it is lost is called T_1 . The value for T_1 due to collisions with the wall and other uncontrollable interactions is tens of minutes to hours (many 100s to 10,000s of seconds), depending on the

mechanism and noble gas species. The component of the noble gas nuclear spin polarization precessing in the plane transverse to the main magnetic field is referred to as the transverse polarization and the characteristic timescale for it to lose its coherence is called T_2 , which is typically 100 to a few hundred seconds. Keeping these characteristic length and time scales in mind, we move onto the details of the theory, which is organized into three parts, one for each part of the maser: pump bulb, transfer tube, and maser bulb. In each section we will also give specific numbers for a typical double bulb cell filled at room temperature ($\sim 23^\circ\text{C}$) with 800 Torr of ^3He , 40 Torr of ^{129}Xe , and 150 Torr of N_2 ; and then operated with the pump bulb at a temperature of 120°C and the maser bulb at 50°C . See Tab. 2.1 for a listing of typical physical characteristics.

2.1.1 Pump Bulb - Spin Exchange Optical Pumping

In the pump bulb we are primarily concerned with the efficient generation of a population inversion or polarization of the spin-1/2 nuclei of ^3He and ^{129}Xe . This is achieved via spin exchange optical pumping (SEOP) with Rb (always assumed to have natural isotopic abundance), which is a two step process for transferring the angular momentum of photons from a laser to the noble gas nuclear spin. In the first step, circularly polarized laser light resonant with the Rb D_1 electronic transition (794.7 nm, $^2S_{1/2}$ to $^2P_{1/2}$) and propagating along the same axis and the main magnetic field, B_0 (see Fig. 1.1), optically pumps the spin of the Rb valence electron. In the second step, during collisions between polarized Rb atoms and unpolarized noble gas atoms, the nuclear spins of the noble gas atoms are polarized via dipolar magnetic field interactions. A detailed review of the physics of these processes can be found in [12] with further theoretical details in [13], but here we will just give an overview.

The optical pumping of Rb is complicated in general due to its different hyperfine manifolds, but it is simplified in most cases by pressure broadening of the transitions from collisions with the noble gas atoms and N_2 buffer gas to the point that the hyperfine levels are completely mixed. The broadening of the Rb D_1 line (Lorentzian FWHM) is approximately

19 GHz/amagat for either ^3He or ^{129}Xe and 18 GHz/amagat for N_2 (see [14]), so for typical pressures in our cells the line width is > 20 GHz, which is significantly larger than the ~ 7 GHz splitting of the hyperfine manifolds.¹ We prevent spontaneous emission from the excited $^2P_{1/2}$ state of Rb – since the random polarization and direction of the photon would work against optical pumping – by including enough N_2 in the cell that the non-radiative decay path to the $^2S_{1/2}$ state via Rb- N_2 collisions dominates over spontaneous emission. Lastly, the hyperfine interaction means that we are not just polarizing the valence electron, but also the Rb nuclear spin, which acts as a store of angular momentum. There is also rapid collisional exchange of spin between Rb atoms that redistributes the spin between the nucleus and electron. These effects are parameterized by the slowing down factor, S_F , for loss and gain rates of the electronic spin. S_F depends on the Rb electronic spin polarization, varying from $S_F = 5.44$ to 10.8 for fully polarized to unpolarized Rb. With these simplifications the optical pumping of the Rb can be described by a rate equation,

$$\dot{P}_{Rb} = \frac{\gamma_{opt}}{S_F}(1 - P_{Rb}) - \frac{\Gamma_{sd}}{S_F}P_{Rb} \quad (2.1)$$

where γ_{opt} is the optical pumping rate, which depends on the spectral overlap of the laser flux and the pressure broadened Rb D_1 line; and Γ_{sd} is the spin destruction/loss rate due to both spin exchange collisions with noble gases and the much larger cross section spin rotation collisions that transfer the spin angular momentum to the rotational angular momentum around the center of mass of the collision. There is also a gain term from spin exchange with polarized noble gases, but it is very small and only relevant in regions away from the optical pumping laser light.

Spin destruction collisional interactions are either binary collisions or three body collisions that produce a weakly bound van der Waals molecule that breaks upon its next binary collision. The theory for the van der Waals molecules is, in particular, rather complicated: see [15] and [16] for extensive early work including measurements and [13] for

¹1 amagat is the density of an ideal gas of 1 atm at 0 °C, $2.69 \times 10^{19} \text{ cm}^{-3}$.

a more recent formulation. Hence we will not delve into the details, but will give some general comments on spin polarization loss rates with infrequent weak interactions in order to gain insight into their scaling with gas density and temperature. In general, in the limit that a state changing interaction is weak, such that $\Omega_I\tau_I \ll 1$, where Ω_I is the effective Rabi frequency of the interaction, τ_I is the duration of the interaction, and all other state evolution during τ_I is similarly small, the fraction of the state lost per interaction event is $1 - \cos(\Omega_I\tau_I) \approx (\Omega_I\tau_I)^2/2$. Thus given a rate of interaction events of $1/T_I$ we have a loss rate of

$$\Gamma_I \approx \frac{1}{T_I} \frac{(\Omega_I\tau_I)^2}{2}. \quad (2.2)$$

For binary collisions, the interaction time is the very short duration of the collision (order of 10^{-12} s) $\tau_I = \tau_c$, which satisfies the small interaction and evolution requirements, but does not scale with any system parameter; and the rate of interactions is the rate of collisions with Rb, $1/T_I = \gamma_c$, which scales linearly with gas density. Thus the binary collision portion of the spin destruction rate is proportional to the gas density:

$$\Gamma_{sd,bc} = k_{sd,Xe}n_{Xe} + k_{sd,He}n_{He} + k_{sd,N_2}n_{N_2} + k_{sd,Rb}n_{Rb} \quad (2.3)$$

where the n are the gas densities and $k_{sd} = \langle \sigma_{sd}v \rangle$ are the velocity distribution averaged spin destruction rate constants for binary collisions. The values for k_{sd} are temperature dependent due to changes in both velocity and cross section, so the values given in Tab. 2.2 are appropriate for our typical temperatures.

For spin destruction due to van der Waals molecules, we are only interested in Rb-Xe pairs as these have been shown to have the greatest influence [15, 16]. The rate of interactions of Rb-Xe van der Waals molecules is the molecular formation rate $1/T_I \approx \gamma_{c,Xe}(\sum_i a_i\gamma_{c,i}\tau_c)$ where the term in parentheses is the probability of having a third atom collide during the Rb-Xe collision, the sum is over all gas species, and the a_i represent each species efficacy in taking away the extra energy/momentum to allow the molecule to form. To break the van der Waals molecules we need to have a binary collision that is the reverse

of the original three body collision; and since they are weakly bound compared to the kinetic thermal energy (20 meV [17]) the inverse interaction time is roughly the same as the third body collision rate $1/\tau_I \approx \sum_i a_i \gamma_{c,i}$. Hence, we find the van der Waals molecule component of the spin destruction rate to scale with the fractional composition of the gases, but not with the overall pressure,

$$\Gamma_{sd,vdW} \propto \frac{n_{Xe}}{\sum_i a_i n_i} \quad (2.4)$$

where if $a_{Xe} = 1$, then $a_{N_2} = 0.28$ and $a_{He} = 0.17$ ([18] for a_{Xe}/a_{N_2} and [19] for a_{N_2}/a_{He}) and we ignore Rb due to its low relative density in our cells. However, for Rb we have not strictly satisfied the requirement that all other state evolution is small over the course of the interaction time, as the hyperfine splitting of the Rb ground states is several GHz, so there is some suppression of the spin destruction effect for our (relatively large) typical total cell pressures (see [20]). Fortunately, careful experimental measurements of the spin destruction rate have been made for a gas composition that is close enough to ours that we could scale the rate to our gas mixture. In [20] they measured the Rb spin destruction rate for a mixture of 98% ^4He / 1% N_2 / 1% Xe, so the third body gas is dominated by He. Our typical cell has a composition of 81% ^3He / 15% N_2 / 4% Xe, which is still dominated by He, making $\Gamma_{sd,vdW} \propto n_{Xe}/n_{He}$. Using the data in Fig. 3 from [20] for our total gas density and multiplying by the slowing down factor of 10.8 and the scaling factor of 4.8 to convert to our gas mixture gives us $\Gamma_{sd,vdW} \approx 5.2 \times 10^3 \text{ s}^{-1}$.

To determine the gas densities needed to calculate the spin destruction rate in Eq. 2.3, we can use the ideal gas law along with the gas pressures the cell was filled with for ^3He , ^{129}Xe , and N_2 . For Rb density in m^{-3} , we use Killian's vapor pressure formula (see [21])

$$n_{Rb} = \frac{10^{9.55-4132/T}}{k_B T}, \quad (2.5)$$

where T is the temperature in Kelvin and k_B is Boltzmann's constant. [Note: there is disagreement in the literature among experimental groups as to the accuracy of Killian's formula, with some groups finding good agreement with independent measurements, while

Gas Species	k_{sd} (cm ³ /s)	n (cm ⁻³)	$\Gamma_{sd,bc}$ (s ⁻¹)	Ref.
^{129}Xe	9×10^{-15}	1×10^{18}	9×10^3	[20]
^3He	1×10^{-18}	2×10^{19}	2×10^1	[22]
N_2	8×10^{-18}	4×10^{18}	3×10^2	[23]
Rb	4×10^{-13}	2×10^{13}	1×10^1	[22]

Table 2.2: Rate constants for spin destruction of Rb when colliding with different atoms in binary collisions. Approximate gas densities, for typical ^3He and ^{129}Xe maser operating conditions in the pump bulb: 120 °C temperature; cell filled at room temperature with 800 Torr ^3He , 40 Torr ^{129}Xe , and 150 Torr N_2 . As can be seen, the spin destruction rate is completely dominated by ^{129}Xe . See the text for the van der Waals spin destruction contribution from Rb-Xe pairs.

others have consistent disagreement by factors of 2 or 3, and some do not even have consistency between different cells they have manufactured. We have not attempted to independently measure the Rb density, so we use Killian’s formula here with the caveat that it may be incorrect by as much as a factor of two.] We can now calculate typical gas densities for our experiment as shown in Tab. 2.2, which reveals that ^{129}Xe completely dominates the binary collision spin destruction rate with the total rate,

$$\Gamma_{sd} = \Gamma_{sd,bc} + \Gamma_{sd,vdW} \quad (2.6)$$

about 50% greater than the binary collision rate. Thus, from the steady state solution to Eq. 2.1,

$$P_{Rb} = \frac{\gamma_{opt}}{\gamma_{opt} + \Gamma_{sd}} \quad (2.7)$$

we can see that the resonant laser power necessary to highly polarize a given number of Rb atoms is effectively determined by the Xe density in the cell.

In general γ_{opt} is a function of position in the pump bulb due to the depletion of the laser as it propagates through the cell. There are also position dependent losses for Rb as collisions with the wall depolarize the Rb. We also have to take into account the overlap of the spectrum of the laser, which typically spans 500-1000 GHz for the arrays of free running diodes we use, with the Rb D₁ line. Taking these factors into account requires numerical

simulation for accurate calculation of P_{Rb} , as described in [24] and our own implementation in [25]. Under typical operating conditions we estimate the pump bulb Rb absorbs about 400 mW of the laser light and we achieve $P_{Rb} \approx 60 - 70\%$ with a transient optical pumping time of $S_F/(\gamma_{opt} + \Gamma_{sd}) \approx 0.2$ ms, which is so short that P_{Rb} can always be considered to be in steady state.

We now consider the second step of SEOP, the spin exchange collisions between Rb and the noble gases. During each collision the magnetic dipole interaction potential between the Rb electronic spin, \mathbf{S} , and the noble gas nuclear spin, \mathbf{I} , is given by,

$$V(\mathbf{R}) = A(R)\mathbf{I} \cdot \mathbf{S} + B(R)\mathbf{I} \cdot (3\mathbf{R}\mathbf{R} - 1) \cdot \mathbf{S} \quad (2.8)$$

where \mathbf{R} is the internuclear separation. The first interaction term is due to the delta function component of the dipole field (referred to as the hyperfine, contact, or Fermi contact interaction) and is typically the dominant term in spin exchange with the coefficient given by,

$$A(R) = \frac{8\pi g_s \mu_B \mu_{ng}}{3I} |\psi(0)|^2 \quad (2.9)$$

where $\psi(0)$ is the Rb valence electron wavefunction during the collision (hence the wavefunction depends on R) at the location of the noble gas nucleus. Similarly to the optical pumping of Rb, we can write the noble gas polarization rate equation as,

$$\dot{P}_{ng} = \gamma_{se,ng}(P_{Rb} - P_{ng}) - \Gamma_{ng}P_{ng} \quad (2.10)$$

where P_{ng} is the polarization of a particular noble gas, Γ_{ng} is the polarization loss rate due primarily to collisions with the walls, and $\gamma_{se,ng}$ is the spin exchange rate which, like the spin destruction rate and with the same scaling properties, consists of a binary collision term and a van der Waals molecule term with the molecule term only being important for ^{129}Xe . For ^3He , spin exchange is given by $\gamma_{se,He} = k_{se,He}n_{Rb}$ where $k_{se,He} = \langle \sigma_{se} v \rangle$ is the velocity distribution averaged binary collision rate constant and for ^{129}Xe we add a van der

Gas Species	k_{se} (cm^3/s)	n_{Rb} (cm^{-3})	γ_{se} (s^{-1})	Ref.
^{129}Xe	2.2×10^{-16}	2×10^{13}	4×10^{-3}	[28, 29]
^3He	6.8×10^{-20}	2×10^{13}	1×10^{-6}	[22, 30]

Table 2.3: Rate constants for binary collision spin exchange of ^3He and ^{129}Xe with Rb. See the text for the much larger van der Waals molecule spin exchange contribution for ^{129}Xe .

Waals molecule term (see [18]),

$$\gamma_{se,Xe} = n_{Rb} \left(k_{se,Xe} + \frac{\zeta \gamma_M}{n_{Xe} + a_{He} n_{He} + a_{N_2} n_{N_2}} \right) \quad (2.11)$$

where a_{He} and a_{N_2} are the same as in Eq. 2.4, ζ is a constant that depends on the polarization of Rb and varies between $\zeta = 0.095$ and $\zeta = 0.179$ for fully and unpolarized Rb respectively ([26] and [18]), and γ_M is a constant rate. In [18] they find $\gamma_M = 2.9 \times 10^4 \text{ s}^{-1}$ using the Killian formula for determining n_{Rb} , while in the more recent measurement in [26] they find $\gamma_M = 1.0 \times 10^5 \text{ s}^{-1}$ while measuring n_{Rb} with Faraday rotation, and hence find n_{Rb} to be consistently a factor of 2 below the Killian formula. We do not have independent measurements of n_{Rb} in our cell, so choose to use $\gamma_M = 1.0 \times 10^5 \text{ s}^{-1}$ with the assumption that the more recent measurement has greater accuracy. Unfortunately, using Eq. 2.11 to match spin exchange data in [27] (see Fig. 5.7 in that work), where they used a similar gas mixture to ours, gives a rate per Rb density 6 times larger than they observed; however, it does agree fairly well with our data (see Sec. 3.7). The binary collision components of spin exchange along with values for our typical cells are given in Tab. 2.3 and, unlike the spin destruction terms, these have been experimentally shown to have no measurable temperature dependence over our typical operating ranges. To calculate the van der Waals component of spin exchange for ^{129}Xe we use the gas density values for our typical cells in Tab. 2.2 and assume our Rb is almost fully polarized, giving $\gamma_{se,vdW,Xe} = 3.4 \times 10^{-2} \text{ s}^{-1}$, which indicates this process completely dominates over the binary collision term, giving a total rate of $\gamma_{se,Xe} = 3.8 \times 10^{-2}$.

Returning to the polarization of the noble gases, in steady state we have,

$$P_{ng} = P_{Rb} \frac{\gamma_{se,ng}}{\gamma_{se,ng} + \Gamma_{ng}} \quad (2.12)$$

where in order to maximize polarization we have to minimize Γ_{ng} , which is dominated by losses from collisions with the walls. Not surprisingly, ^{129}Xe tends to interact with the cell walls far more than ^3He , so in order to reduce Γ_{ng} for ^{129}Xe we coat the surface of the cell with a silane compound to reduce interactions with the wall. We also note from these calculations that ^{129}Xe polarizes $> 3 \times 10^4$ times faster than ^3He , so ideally we would raise the cell temperature to increase n_{Rb} via Eq. 2.5 and possibly lower n_{Xe} to reduce the laser power needed to polarize the Rb (although this is limited by the van der Waals molecule spin destruction term). However, the silane coating tends to react with Rb at higher temperatures and thus ultimately limits our ability to polarize ^3He .

In addition to providing a source of polarization for the noble gas atoms, the polarized Rb also generates a local magnetic field that shifts the Larmor frequency of the noble gas atoms. The magnetic field experienced by the noble gases from the Rb magnetization is very different for ^3He and ^{129}Xe since the average field they experience is dominated by the strong hyperfine contact interactions during collisions, the same interactions that lead to spin exchange. For a spherical volume of polarized Rb the shift on a noble gas atom is,

$$\delta\omega_{ng} = (k_{ng} - 1)\gamma_{ng}B_{Rb}, \quad B_{Rb} = \frac{2\mu_0}{3}M_{Rb}, \quad M_{Rb} = \gamma_{Rb}\frac{\hbar}{2}n_{Rb}P_{Rb}, \quad (2.13)$$

where k_{ng} is the enhancement factor over the expected shift from a bulk magnetization, and has values $k_{He} \approx 5$ and $k_{Xe} \approx 700$ (see [31] and [32] respectively for details); and $\gamma_{Rb}/(2\pi) \approx 467$ kHz/G for ^{85}Rb , the dominant isotope. A fraction of the shift for ^{129}Xe is due to contact interactions that occur when ^{129}Xe -Rb van der Waals molecules are formed, but it is relatively small, $\sim 5\%$ [32], so we will ignore it as we are interested in the gross size of the effect. For the typical density and polarization values we have been using this gives shifts of $\delta\omega_{He}/(2\pi) \approx 3$ mHz and $\delta\omega_{Xe}/(2\pi) \approx 150$ mHz. Given the extremely large

shift for ^{129}Xe and the very unstable nature of the Rb density with temperature it is clear why we can only measure the noble gas Zeeman frequencies in the cooler maser bulb with no optical pumping light.

To complete our discussion of spin exchange we consider what the Rb polarization will be in the dark away from the laser light and what effect it will have on the noble gas polarizations. Away from the laser light, both within and out of the pump bulb, non-zero Rb polarization arises from diffusive transport of polarization from the pump bulb and spin exchange collisions with polarized noble gases. Given the much stronger spin exchange and spin rotation collisional interactions between Rb and ^{129}Xe than with ^3He we only need to consider the ^{129}Xe polarization as a spin exchange source of Rb polarization. In general the steady state equation we need to solve is,

$$\dot{P}_{Rb} = 0 = D_{Rb}\nabla^2 P_{Rb} - \frac{\Gamma_{sd}}{S_F} P_{Rb} + \frac{\gamma_{se,Rb}}{S_F} P_{Xe} \quad (2.14)$$

where D_{Rb} is the Rb diffusion coefficient and $\gamma_{se,Rb} = \gamma_{se,Xe}n_{Xe}/n_{Rb}$ and P_{Xe} are positionally dependent as well. The characteristic length scale over which ^{129}Xe collisional interactions start to dominate over diffusive transport is given by,

$$l = \sqrt{\frac{S_F D_{Rb}}{\Gamma_{sd}}}, \quad (2.15)$$

where the length l is the $1/e$ length in the transition of P_{Rb} from the pump bulb down the transfer tube to equilibrium exchange with Xe. For our typical gas density values, $D_{Rb} \approx 0.6 \text{ cm}^2/\text{s}$, $\Gamma_{sd} \approx 1.5 \times 10^4 \text{ s}^{-1}$, and $S_F \approx 11$ (assuming $P_{Rb} \approx 0$), giving $l \approx 0.02 \text{ cm}$ which is much smaller than the length or radius of the transfer tube or radius of the maser or pump bulbs. Hence we can treat P_{Rb} as always being in equilibrium exchange with P_{Xe} outside the laser light and unaffected by the walls, with the local Rb polarization given by,

$$P_{Rb} = \frac{\gamma_{se,Rb}}{\Gamma_{sd}} P_{Xe}. \quad (2.16)$$

Using the same typical values as above with $\gamma_{se,Rb} \approx 3.4 \times 10^3 \text{ s}^{-1}$ and a typical high value of $P_{Xe} \approx 0.5$ we find $P_{Rb} \approx 0.12$ outside the laser light, so Rb is relatively unpolarized compared to ^{129}Xe and acts as a pure polarization sink outside of the laser light with a loss rate coefficient of $\gamma_{se,Xe}$ proportional to n_{Rb} . At typical pump bulb temperatures and outside the laser light, where Rb polarization is relatively small, the polarization loss rate for ^{129}Xe back to Rb is a nontrivial $\gamma_{se,Xe} = 7 \times 10^{-2} \text{ s}^{-1}$ (recall, ζ is larger when the Rb polarization is low); but at the maser bulb temperature of $\sim 50 \text{ }^\circ\text{C}$ we have $n_{Rb} = 1.3 \times 10^{11} \text{ cm}^{-3}$ from Eq. 2.5, so the loss rate is $\gamma_{se,Xe} = 4.4 \times 10^{-4} \text{ s}^{-1}$ which is ~ 5 times smaller than our current wall loss rate, so can be ignored in the maser bulb. We can now also calculate the hyperfine contact shift in the maser bulb. In the maser bulb the typical value of $P_{Xe} < 0.01$ gives $P_{Rb} \approx 2 \times 10^{-3}$ and hence a contact shift of $\delta\omega_{Xe} \approx 2 \text{ } \mu\text{Hz}$, which is much easier to stabilize than the 150 mHz contact shift in the pump bulb.

2.1.2 Transfer Tube - Diffusive Transport

The next step in developing the double bulb maser equations is to calculate the rate that noble gas polarization leaves one bulb and arrives in the other bulb via diffusion in the transfer tube. To calculate the diffusive transport between bulbs we start with the most general form of the diffusion equation,

$$\dot{\mathbf{M}} = \nabla \cdot (D\nabla\mathbf{M}) \quad (2.17)$$

where the diffusion coefficient, D , is a function of position, due to changes in temperature, as is the magnetization, \mathbf{M} , due to changes in the polarization and/or atomic density. In an isothermal system, such as the pump and maser bulbs, both the diffusion coefficient and the density are constant so we end up with a diffusion equation for the polarization,

$$\dot{\mathbf{P}} = D\nabla^2\mathbf{P}. \quad (2.18)$$

As discussed in the introduction to this section (Sec. 2.1), in the pump and maser bulbs the characteristic diffusion time across the bulbs, a few seconds, is always much shorter than the noble gas spin relaxation times T_1 or T_2 , several hundred seconds or longer. Thus, if we assume that the time constant associated with leaving the bulb via the transfer tube is long too, we can treat the noble gas polarization in the bulbs as being roughly homogeneous. To calculate the rate at which polarization for each species leaves the pump bulb to move down the transfer tube we start with the polarization diffusion equation and then take the volume average of both sides and apply Gauss's law,

$$\langle \dot{P}_P \rangle_V = \frac{1}{V_P} \int_{\text{bulb}} D_P \nabla^2 P_P d^3r = \frac{D_P}{V_P} \int_{\text{surface}} \nabla P_P \cdot \mathbf{n} d^2r = \frac{D_P A_t}{V_P} \frac{\partial \Pi_P}{\partial y} \Big|_{y=0} \quad (2.19)$$

where $\langle P_P \rangle_V = P_P$ is the volume average of the longitudinal polarization in the pump bulb; V_P is the volume of the pump bulb (since we have approximated it as homogeneous, the average can be ignored); D_P is the diffusion coefficient at the pump bulb temperature and gas density; A_t is the cross sectional area of the transfer tube; and Π_P is the longitudinal polarization in the transfer tube at the pump bulb end of the tube (as per the coordinates in Fig. 2.1). We can also write an analogous equation for the maser bulb with appropriate subscript changes (e.g., D_M , V_M , etc.) and a change in the overall sign.

The problem is now reduced to determining the steady-state polarization profile in the transfer tube, but given the considerable change in temperature between the pump and maser bulb (~ 70 °C) we must use the most general form of the diffusion equation (Eq. 2.17) and thus any realistic profile of the temperature between the bulbs will lead to a very complex solution. However, since we are primarily interested in the rate of polarization transfer into and out of the two bulbs, we see from Eq. 2.19 that we only need an accurate polarization profile at the entrance and exits to the transfer tube and in these regions the temperature is quite homogeneous. We will thus approximate the temperature in the transfer tube as a step function with the step occurring roughly midway between the two bulbs and the temperature and gas density on either side of the step the same as in the

nearest bulb. Changes in the temperature of the bulbs would change the height of the step, but would not change the position of the step. Continuity in the magnetization and the magnetization flux, but not the polarization, would be required across the step. A cartoon of this model is presented in Fig. 2.1.

The general equation for noble gas polarization in the transfer tube, Π , in one temperature region is,

$$\dot{\Pi} = D\nabla^2\Pi - \gamma_{se}\Pi \quad (2.20)$$

where the spin exchange loss is due to unpolarized Rb (assuming Rb polarization is immediately lost to spin rotation collisions, see Sec. 2.1.1). We are only interested in the steady state solutions, so we only have to solve,

$$0 = \nabla^2\Pi - k^2\Pi \quad (2.21)$$

where $k = \sqrt{\gamma_{se}/D}$. The boundary conditions at either end of the transfer tube are the bulb polarizations since we assumed that they were roughly homogeneous,

$$\Pi_P(y = 0) = P_P \quad \text{and} \quad \Pi_M(y = L_t) = P_z, \quad (2.22)$$

where L_t is the length of the transfer tube and the other parameters are as labeled in Fig. 2.1. At the boundary due to the step discontinuity in the temperature we require continuity in the magnetization,

$$n_P\Pi_P(y = d_t) = n_M\Pi_M(y = d_t) \quad (2.23)$$

where n_P and n_M are the gas densities for a specific noble gas species at the temperatures of the pump and maser bulbs respectively, and continuity in the magnetization flux,

$$D_P n_P \frac{d\Pi_P}{dy} \Big|_{y=d_t} = D_M n_M \frac{d\Pi_M}{dy} \Big|_{y=d_t}. \quad (2.24)$$

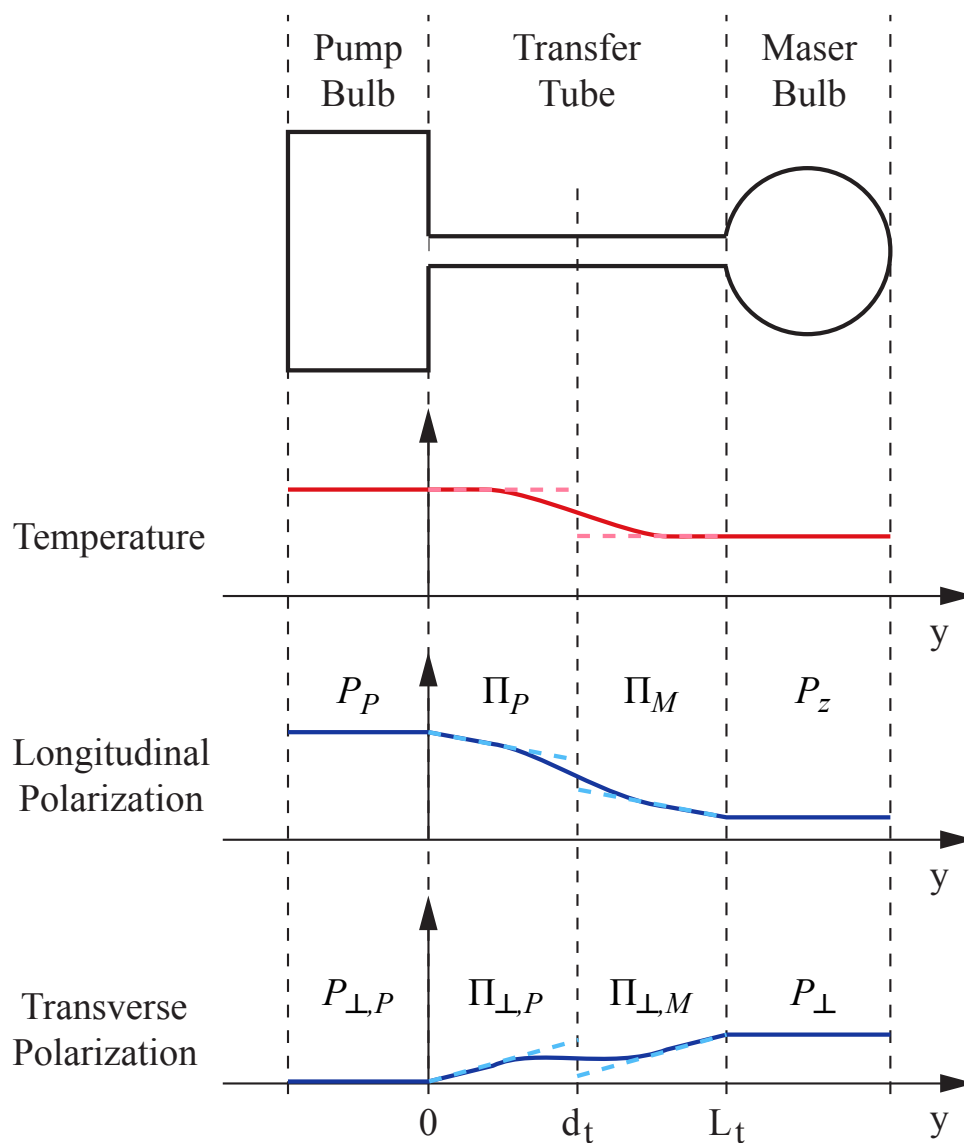


Figure 2.1: Schematic representation of the temperature as a function of position between the dual bulbs and the resulting longitudinal and transverse noble gas polarization distributions in the maser. The solid lines on the graphs are a schematic of the real distributions and the dashed lines are the step approximations used in the text.

Equivalent expressions can be written for the transverse polarizations. The only surface boundary condition remaining to be specified is the wall of the transfer tube, where there is a small loss in polarization every time an atom collides with the wall. We can express this loss in terms of the polarization flux going towards the wall, J_{in} , and away from the wall, J_{out} ,

$$J_{\text{in}} = \frac{\bar{v}}{4}n\Pi \quad (2.25)$$

$$J_{\text{out}} = (1 - \alpha)\frac{\bar{v}}{4}n\Pi \quad (2.26)$$

where α is the fractional loss in polarization per collision and $\bar{v} = \sqrt{8kT/(\pi m)}$ is the mean thermal velocity. We can relate this to diffusion via Fick's Law,

$$\mathbf{J} \cdot \mathbf{n} = J_{\text{in}} - J_{\text{out}} = \alpha\frac{\bar{v}}{4}n\Pi = -D\nabla(n\Pi) \cdot \mathbf{n}, \quad (2.27)$$

so the boundary condition on the transfer tube wall is

$$D\nabla\Pi \cdot \mathbf{n} = -\kappa\Pi, \text{ where } \kappa = \alpha\frac{\bar{v}}{4}. \quad (2.28)$$

We are now left with the question of how to estimate a value for α or κ for each noble gas species. If we consider the polarization, P , inside a sealed sphere where the characteristic diffusion time across the bulb is short compared to the wall relaxation time (i.e., our usual limit), then the full time dependent solution will be dominated by a spatially uniform polarization with an exponential decay over time (characterized by T_1), which we can link to the boundary condition for the wall and hence κ . To see this we write the time dependent equation for P in terms of both an exponential time constant and the diffusion equation

Description	Parameter	^{129}Xe	^3He	Units
Measured lifetime	T_1	400	> 6000	s
Wall loss (inferred)	κ	1	< 0.1	10^{-3} cm/s

Table 2.4: Approximate longitudinal polarization loss parameters due to collisions with the wall in a typical maser bulb.

and then apply Gauss's Law to both sides,

$$\dot{P} = -\frac{P}{T_1} = D\nabla^2 P \quad (2.29)$$

$$-\frac{\langle P \rangle_V}{T_1} = \frac{1}{V} \int_{\text{surface}} D\nabla P \cdot \mathbf{n} d^2r \quad (2.30)$$

$$\frac{\langle P \rangle_V}{T_1} = \frac{3}{R} \kappa P_{\text{surface}} \quad (2.31)$$

where R is the radius of the sphere and $\langle P \rangle_V$ is the volume averaged polarization. In the spatially homogeneous solution limit the volume average polarization is approximately equal to the surface polarization, $P_{\text{surface}} \approx \langle P \rangle_V$, so now we can directly relate κ to T_1 ,

$$\kappa = \frac{R}{3T_1}, \quad (2.32)$$

or for a more general geometry,

$$\kappa = \frac{V_T}{A_T T_1} \quad (2.33)$$

where V_T is the total volume and A_T is the total surface area. From polarization lifetime measurements of ^{129}Xe in maser bulbs with average wall coatings ($T_{1,\text{Xe}} \approx 400$ sec, $R = 1$ cm) we estimate $\kappa_{\text{Xe}} \approx 1 \times 10^{-3}$ cm/s in our system. In the case of ^3He , the measured T_1 is always at least an order of magnitude longer, so $\kappa_{\text{He}} < 1 \times 10^{-4}$ cm/s, see Tab. 2.4.

Having laid out the boundary conditions and determined characteristic values for their parameters so that we can make approximations, we can now move onto the general solution,

$$\Pi(r, y) = \sum_{n=0}^{\infty} J_0\left(\sqrt{k_n^2 - k^2} r\right) \left(A_n e^{k_n y} + B_n e^{-k_n y}\right), \quad (2.34)$$

where J_0 is a Bessel function of the first kind and k_n is defined by the wall loss boundary condition (Eq. 2.28),

$$D\sqrt{k_n^2 - k^2}J_1\left(\sqrt{k_n^2 - k^2}R_t\right) = \kappa J_0\left(\sqrt{k_n^2 - k^2}R_t\right), \quad (2.35)$$

where $R_t < 0.2$ cm is the radius of the transfer tube. Since we anticipate the polarization losses across the transfer tube radius to be very small we expand the boundary condition and solve for the lowest order term that includes the wall losses,

$$k_0^2 = k^2 + \frac{2\kappa}{R_t D} = \frac{1}{D} \left(\gamma_{se} + \frac{2\kappa}{R_t} \right), \quad (2.36)$$

which is justified as long as $(k_0 R_t)^2 \ll 1$ since J_0 and J_1 have no linear expansion terms. Even for ^{129}Xe in the presence of pump bulb level Rb densities we have $(k_0 R_t)^2 < 1 \times 10^{-2}$, so our approximation for k_0 is good and we do not need higher k_n terms as the very uniform radial profile from the k_0 term matches well with the uniform polarization in the bulbs as we discussed above. Thus we can eliminate the radial component from our solution,

$$\Pi(y) = Ae^{k_0 y} + Be^{-k_0 y} \quad (2.37)$$

and for ^3He where $k_0 L_t < 0.1$ we can ignore the the losses due to the wall and solve the linear equation,

$$\Pi(y) = A + By. \quad (2.38)$$

Using either the equation for small transfer tube losses, Eq. 2.37, or for a lossless transfer tube, Eq. 2.38, we can now calculate the gradients of the transfer tube polarization at either end and determine loss and gain terms for the pump and maser bulb due to diffusive

coupling,

$$\dot{P}_P = \frac{D_P A_t}{V_P} \frac{\partial \Pi_P}{\partial y} \Big|_{y=0} = G_{PM} P_z - G_{PP} P_P \quad (2.39)$$

$$\dot{P}_z = \frac{D_M A_t}{V_M} \frac{\partial \Pi_M}{\partial y} \Big|_{y=0} = G_{MP} P_P - G_{MM} P_z \quad (2.40)$$

where P_z is the longitudinal polarization in the maser bulb. Due to the added complexity of the lossy transfer tube equation we will just give the solution for the lossless transfer tube equation, which is applicable for ^3He , using the boundary conditions established earlier, Eq. 2.22, Eq. 2.23, and Eq. 2.24. We will also make the simplification that the transition from the pump bulb to maser bulb temperatures happens exactly in the middle of the transfer tube, so that $d_t = L_t/2$ (see Fig. 2.1), which gives,

$$\Pi_P(y) = P_P + \frac{D_A}{D_P} \left(\frac{n_M}{n_P} P_z - P_P \right) \frac{y}{L_t} \quad (2.41)$$

$$\Pi_M(y) = \frac{D_M - D_P}{D_M + D_P} P_z + \frac{D_A}{D_M} \frac{n_P}{n_M} P_P + \frac{D_A}{D_M} \left(P_z - \frac{n_P}{n_M} P_P \right) \frac{y}{L_t}, \quad (2.42)$$

where we have defined an ‘‘average’’ diffusion coefficient

$$D_A = \frac{2D_M D_P}{D_M + D_P}. \quad (2.43)$$

The rate coefficients for ^3He polarization loss from the pump and maser bulbs are given by,

$$G_{PP} = \frac{D_A A_t}{L_t V_P} \quad \text{and} \quad G_{MM} = \frac{D_A A_t}{L_t V_M} \quad (2.44)$$

and the gain rate coefficients are,

$$G_{PM} = \frac{n_M}{n_P} \frac{D_A A_t}{L_t V_P} \quad \text{and} \quad G_{MP} = \frac{n_P}{n_M} \frac{D_A A_t}{L_t V_M}. \quad (2.45)$$

This satisfies the detailed balance requirement that for a lossless transfer tube the polarization current leaving the pump bulb must equal to the polarization current arriving in the

maser bulb and vice versa,

$$V_P n_P G_{PP} P_P = n_P \frac{D_{AA} A_t}{L_t} P_P = V_M n_M G_{MP} P_P \quad (2.46)$$

$$V_M n_M G_{MM} P_z = n_M \frac{D_{AA} A_t}{L_t} P_z = V_P n_P G_{PM} P_z. \quad (2.47)$$

In the case of ^{129}Xe we need to use the equation for the lossy transfer tube, but we only need to worry about spin exchange at pump bulb Rb densities as the Rb density is two orders of magnitude lower at the maser bulb temperature (see the end of Sec. 2.1.1), so we define two k_0 parameters,

$$k_{0,P}^2 = \frac{\gamma_{se,Xe}}{D_P} + \frac{2\kappa}{R_t D_P} \quad (2.48)$$

$$k_{0,M}^2 = \frac{2\kappa}{R_t D_M} \quad (2.49)$$

where $\gamma_{se,Xe}$ is given by Eq. 2.11 with $\zeta \approx 0.18$ since the Rb is essentially unpolarized in the transfer tube. While the full expressions for the rate coefficients for ^{129}Xe are too cumbersome to report here, although they are trivially derived using Eq. 2.37 and the boundary conditions that follow, the fractional transmission of polarization down the transfer tube (the ratio of magnetization flux at the entrance to the maser bulb to the flux at the pump bulb), in the limit of small losses and $P_z \ll P_P$ due to masing, has a simple form,

$$\frac{\mathbf{J}(y = L_t)}{\mathbf{J}(y = 0)} \approx 1 - \frac{k_{0,M}^2 + \left(1 + 2\frac{D_P}{D_M}\right) k_{0,P}^2}{8} L_t^2. \quad (2.50)$$

This expression is not valid for the typical values of our maser (due to the large $\gamma_{se,Xe}$ losses), but the exact calculation using steady state masing values gives a fractional ^{129}Xe polarization transmission of approximately 50%.

In order to utilize all the formulas we have just derived it is necessary to know how the diffusion coefficients for ^3He and ^{129}Xe change with different gas mixtures and bulb temperatures. For a mixture of gases the binary collision diffusion coefficient for gas i in

Gas Species	$A_{i,j}$	$B_{i,j}$
He-He	1.62	1.71
He-N ₂	0.613	1.524
He-Xe	0.496	1.644
Xe-N ₂	0.106	1.789
Xe-Xe	0.048	1.9

Table 2.5: Binary diffusion coefficient parameters.

the mixture is given by,

$$\frac{1}{D_i} = \sum_j \frac{1}{D_{i,j}} \quad (2.51)$$

where $D_{i,j}$ is the diffusion coefficient for binary collisions between gas i and gas j (the iteration over j includes gas i). Each of the $D_{i,j}$ diffusion coefficients can be parameterized in terms of the partial pressure of the gas and the temperature using a simple extension of the hard sphere model to allow for the temperature dependence of the cross section,

$$D_{i,j} = A_{i,j} \frac{p_0}{p_j} \left(\frac{T}{T_0} \right)^{B_{i,j}} \quad (2.52)$$

where p_j is the partial pressure of gas j , T is the temperature, p_0 is one atmosphere, and $T_0 = 273.15$ K. The constants $A_{i,j}$ and $B_{i,j}$ are given in Tab. 2.5 for the gases used in the cell (note that $A_{i,j} = A_{j,i}$ and $B_{i,j} = B_{j,i}$). These constants were extracted from the more sophisticated models presented in [33, 34] by only evaluating the models around the temperature range at which we operate. Finally, we can easily determine the partial pressure of a gas given the bulb temperatures using the ideal gas law and the pressure used to fill the cell at room temperature,

$$p = p_{\text{fill}} \frac{\frac{V_M}{T_{\text{fill}}} + \frac{V_P}{T_{\text{fill}}}}{\frac{V_M}{T_M} + \frac{V_P}{T_P}} \quad (2.53)$$

where p_{fill} is the partial pressure when the cell was filled, T_{fill} was the temperature when the cell was filled and T_P and T_M are the temperatures of the pump and maser bulbs. Tab. 2.6

Region	Description	Parameter	^{129}Xe	^3He	Units
Pump bulb	density	n_P	1.2	24	10^{18} cm^{-3}
	diffusion coefficient	D_P	0.31	1.4	cm^2/s
	gain time	$1/G_{PM}$	790	140	s
	loss time	$1/G_{PP}$	450	170	s
Maser bulb	density	n_M	1.5	29	10^{18} cm^{-3}
	diffusion coefficient	D_M	0.22	1.0	cm^2/s
	gain time	$1/G_{MP}$	780	140	s
	loss time	$1/G_{MM}$	450	110	s

Table 2.6: Gas diffusion parameters for a typical cell filled at room temperature with 800/40/150 Torr of $^3\text{He}/^{129}\text{Xe}/\text{N}_2$ and bulb parameters given Tab. 2.1 and Tab. 2.4. Diffusion gain and loss times for ^{129}Xe are calculated using the lossy transfer tube equations from the text.

summarizes the gas diffusion parameters for ^3He and ^{129}Xe in both the pump and maser bulbs.

2.1.3 Maser Bulb - Maser Equations

In this section we derive the equations of motion for the ^3He and ^{129}Xe polarized nuclear spins operating as a maser. We consider each noble gas species in isolation, operating as a separate maser, and add the interactions between species in following sections, Sec. 2.2.2 and Sec. 2.2.3. Thus, in this section, when we refer to the maser, we are referring to either the ^3He or ^{129}Xe masing ensembles.

In the maser bulb, feedback is applied to the noble gas population inversions to induce active maser oscillation. This is done via inductive coupling of the noble gas magnetizations to a coil that is part of a resonant circuit tuned to the Larmor precession frequencies of the ^3He and ^{129}Xe nuclei. To determine the resulting equations of motion for the noble gas polarization vectors in this coupled system we begin with the Hamiltonian for a spin-1/2 particle in a magnetic field,

$$H = -\boldsymbol{\mu} \cdot \mathbf{B} = \gamma \frac{\hbar}{2} \boldsymbol{\sigma} \cdot (\mathbf{B}_J + \mathbf{B}_M) \quad (2.54)$$

where \mathbf{B}_J is the magnetic field generated by the currents in the pickup coil and the solenoid, \mathbf{B}_M is the magnetic field from the bulk magnetization of the polarized gas, σ is the Pauli spin matrices, and γ is the absolute value of the gyromagnetic ratio (both ^3He and ^{129}Xe have negative gyromagnetic ratios). Once the maser is operating, the pickup coil generates a field in the maser bulb along the y -axis oscillating at the maser frequency, yielding a magnetic field from all current sources of,

$$\mathbf{B}_J = \begin{pmatrix} 0 \\ B_1 \cos(\omega_M t + \phi) \\ B_0 \end{pmatrix}. \quad (2.55)$$

Here B_0 is the field from the solenoid, B_1 is the field from the pickup coil, and ω_M is the maser frequency with an arbitrary phase ϕ . The values of the ^3He and ^{129}Xe gyromagnetic ratios and typical maser frequencies with associated B_0 values are given in Tab. 2.7. The magnetic fields from the noble gas magnetization consists of a static term aligned on the z -axis with B_0 as well as a precessing magnetization that rotates in the x - y plane,

$$\mathbf{B}_M = \begin{pmatrix} -B_{M_x} \cos(\omega_M t + \psi) \\ -B_{M_y} \sin(\omega_M t + \psi) \\ B_{M_z} \end{pmatrix} \quad (2.56)$$

where B_{M_i} is the field due to the i^{th} component of the magnetization and ψ is an arbitrary phase. The relative phases between the oscillating magnetic fields can be established from Eq. 2.60 and Eq. 2.68, given below.

Assuming that the maser frequency is very close to the Larmor frequency we can simplify the Hamiltonian in the usual way by making the rotating wave approximation (RWA) for nearly resonant fields (errors due to this approximation will be dealt with in Sec. 2.4) and

Description	Parameter	^{129}Xe	^3He	Units
Gyromagnetic ratio	$\gamma/(2\pi)$	1177.673984(77)	3243.410200(91)	Hz/G
Maser frequency	$\omega_M/(2\pi)$	7107.300	19574.081	Hz
Solenoid magnetic field	B_0	6.03503184(39)	6.03503100(17)	G

Table 2.7: Noble gas gyromagnetic ratios [35, 36], typical maser frequencies, and corresponding approximate solenoid field.

transform into a frame rotating at ω_M ,

$$H \approx \frac{\hbar}{2} \begin{pmatrix} \omega_0 + \omega_z & (-i\Omega_R e^{-i\phi} - \Omega_B e^{-i\psi}) e^{-i\omega_M t} \\ (i\Omega_R e^{i\phi} - \Omega_B e^{i\psi}) e^{i\omega_M t} & -(\omega_0 + \omega_z) \end{pmatrix} \text{RWA} \quad (2.57)$$

$$H_R = \frac{\hbar}{2} \begin{pmatrix} -\Delta & -i\Omega_R e^{-i\phi} - \Omega_B e^{-i\psi} \\ i\Omega_R e^{i\phi} - \Omega_B e^{i\psi} & \Delta \end{pmatrix} \text{Frame rotating at } \omega_M \quad (2.58)$$

where $\omega_0 = \gamma B_0$ is the Larmor frequency due to the solenoid, $\omega_z = \gamma B_{M_z}$ is the Larmor frequency due to the static bulk magnetization,² $\Omega_R = \gamma B_1/2$ is the Rabi frequency due to the pickup coil, $\Omega_B = \gamma(B_{M_x} + B_{M_y})/2$ is the Rabi frequency due to the bulk magnetization,³ and $\Delta = \omega_M - (\omega_0 + \omega_z)$ is the detuning of the pickup coil magnetic field from the total Larmor frequency. In the rotating frame we now have new stationary magnetic fields,

$$H_R = \frac{\hbar}{2} \boldsymbol{\sigma} \cdot \begin{pmatrix} -\Omega_R \sin(\phi) - \Omega_B \cos(\psi) \\ \Omega_R \cos(\phi) - \Omega_B \sin(\psi) \\ -\Delta \end{pmatrix} = \frac{\hbar}{2} \boldsymbol{\sigma} \cdot \boldsymbol{\Omega} \quad (2.59)$$

and from this Hamiltonian we can use Feynman's maser analysis technique [37] to generate

²The effects of the static magnetization of the second noble gas species are considered in Sec. 2.2.2, 2.2.3, and 2.4.

³The effect of the precessing magnetization of the other noble gas maser, which is far off resonance compared to the self field we are discussing here, is considered in Sec. 2.4.

an equation for the time evolution of the ensemble polarization,

$$\dot{\mathbf{P}} = \boldsymbol{\Omega} \times \mathbf{P}. \quad (2.60)$$

To this polarization equation of motion we add terms for the phenomenological relaxation of the coherence, T_2 , and polarization, T_1 , (their origin will be discussed in Sec. 2.3 and their measurement in Sec. 3.7) as well as a source term, $P_{z,0}$, which we will shortly link back to diffusion in from the transfer tube,

$$\dot{\mathbf{P}} = \begin{pmatrix} -\Omega_R \sin(\phi) - \Omega_B \cos(\psi) \\ \Omega_R \cos(\phi) - \Omega_B \sin(\psi) \\ -\Delta \end{pmatrix} \times \mathbf{P} - \frac{P_x + P_y}{T_2} - \frac{P_z - P_{z,0}}{T_1} \quad (2.61)$$

which yields the following system of equations,

$$\dot{P}_x = (\Omega_R \cos(\phi) - \Omega_B \sin(\psi))P_z + \Delta P_y - \frac{P_x}{T_2} \quad (2.62a)$$

$$\dot{P}_y = -\Delta P_x + (\Omega_R \sin(\phi) + \Omega_B \cos(\psi))P_z - \frac{P_y}{T_2} \quad (2.62b)$$

$$\dot{P}_z = -(\Omega_R \cos(\phi) - \Omega_B \sin(\psi))P_x - (\Omega_R \sin(\phi) + \Omega_B \cos(\psi))P_y - \frac{P_z - P_{z,0}}{T_1}. \quad (2.62c)$$

This set of equations can be simplified by converting into a more useful coordinate system of transverse polarization amplitude, P_\perp , and phase, ψ ,

$$P_x = P_\perp \cos(\psi) \quad P_y = P_\perp \sin(\psi) \quad (2.63)$$

(note that the choice of phase in these definitions matches the phases in Eq. 2.56 where the minus sign comes from the negative gyromagnetic ratio) with time derivatives,

$$\dot{P}_\perp = \frac{\dot{P}_x P_x + \dot{P}_y P_y}{P_\perp} \quad \dot{\psi} = \frac{\dot{P}_y P_x - \dot{P}_x P_y}{P_\perp^2} \quad (2.64)$$

which gives,

$$\dot{P}_\perp = \Omega_R \cos(\theta) P_z - \frac{P_\perp}{T_2} \quad (2.65a)$$

$$\dot{\psi} = -\Delta + (\Omega_R \sin(\theta) + \Omega_B) \frac{P_z}{P_\perp} \quad (2.65b)$$

$$\dot{P}_z = -\Omega_R \cos(\theta) P_\perp - \frac{P_z - P_{z,0}}{T_1} \quad (2.65c)$$

where $\theta = \phi - \psi$. As one would expect, the absolute phases ϕ and ψ do not matter, only their phase difference θ , and we have chosen the relative phases of the pickup coil field in Eq. 2.55 and the polarization in Eq. 2.63 such that there is a maximum generation of coherent masing, P_\perp , when θ is zero. We also note that oscillating fields that are in phase with the precessing transverse polarization lead to frequency shifts, as evidenced by Ω_B ; and those in quadrature ($\pi/2$ phase shift) lead to transfer between the longitudinal and transverse polarizations. Avoiding generation of fields in the undesirable frequency shift phase quadrature will be a recurring theme.

The Rabi frequency Ω_R is due to the field generated by the pickup coil, so in order to determine Ω_R we need to calculate coupling of the atoms to the coil and the size of the feedback field on the atoms due to that coupling. We first return to the non-rotating frame and introduce complex fields such that their real parts are the same as their original definitions to preserve their relative phase relationship,

$$B_y = B_1 e^{i\omega_M t} e^{i\phi} \quad (2.66)$$

$$P_y = -i P_\perp e^{i\omega_M t} e^{i\psi}. \quad (2.67)$$

The voltage generated in the pickup coil, V_{pu} , from the precessing noble gas magnetization can be calculated by the reciprocity theorem [38],

$$V_{pu} = -\frac{\partial}{\partial t} \int_{\text{Bulb}} \boldsymbol{\xi} \cdot \mathbf{M} d^3 r \quad (2.68)$$

where \mathbf{M} is the magnetization of the noble gas and $\boldsymbol{\xi}$ is the magnetic field per unit current generated by the coil given by,

$$\mathbf{M} = \boldsymbol{\mu}n = -\gamma\frac{\hbar}{2}n\mathbf{P} \quad \text{and} \quad \mathbf{B}_{\text{coil}} = \boldsymbol{\xi}I, \quad (2.69)$$

where n is the gas density and I is the current flowing through the coil. The field from the coil inside the maser bulb will not be uniformly aligned with the y -axis as assumed at the beginning of this section in Eq. 2.55, nor will the dipole axis of the coil necessarily be exactly aligned with the transfer tube, which we have been using to define the y -axis. However, the field from the coil averaged over the maser bulb volume (weighted by the magnetization as in Eq. 2.68) will point in one direction in the plane transverse to the orientation of B_0 within the bulb and it is this direction that we define to be the y -axis. Thus we can simplify Eq. 2.68 to,

$$V_{pu} = \gamma\frac{\hbar}{2}n_M \int_{\text{Bulb}} \xi_y \dot{P}_y d^3r. \quad (2.70)$$

In general P_y and ξ_y are functions of position, but for long coherence times compared to the characteristic diffusion time in the cell and small transfer tube aperture through which the atoms can escape we can approximate P_y as homogeneous over the volume of the maser bulb (deviations from this approximation and their consequences will be discussed in Sec. 2.2.2) and hence it can be taken out of the integral,

$$V_{pu} = \gamma\frac{\hbar}{2}n_M \dot{P}_y \xi_0 V_M \quad \text{where} \quad \xi_0 = \frac{1}{V_M} \int_{\text{Bulb}} \xi_y d^3r \quad (2.71)$$

where ξ_0 is the volume averaged coil field per unit current and V_M is the volume of the maser bulb. To find the current and hence field produced by the voltage generated in the coil we use the effective impedance of the doubly resonant circuit near resonance,

$$Z = R_{\text{eff}} + i\omega L_{\text{eff}} - \frac{i}{\omega C_{\text{eff}}} = R_{\text{eff}} \left(1 + iQ_c \left(\frac{\omega}{\omega_c} - \frac{\omega_c}{\omega} \right) \right) \quad (2.72)$$

where $\omega_c = 1/\sqrt{L_{\text{eff}}C_{\text{eff}}}$ is the resonant frequency and $Q_c = \omega_c L_{\text{eff}}/R_{\text{eff}}$ is the fractional

FWHM of the resonance. We can remove the enigmatic R_{eff} by making one final substitution,

$$Z = \frac{\omega_c L_{pu}}{q_c} \left(1 + iQ_c \left(\frac{\omega}{\omega_c} - \frac{\omega_c}{\omega} \right) \right) = \frac{L_{pu} Q_c}{i\omega q_c} \left(-\omega^2 + i\frac{\omega_c}{Q_c}\omega + \omega_c^2 \right) \quad (2.73)$$

where L_{pu} is the inductance of the pickup coil and $q_c = \omega_c L_{pu}/R_{\text{eff}}$ determines the strength of the feedback. Note that $Q_c > q_c$ as $L_{\text{eff}} > L_{pu}$ since there is more than one inductor in the circuit. Since we have expressed Z in the Fourier domain, we convert V_{pu} in Eq. 2.71 to the Fourier domain and derive the equation for the feedback field generated by the coil,

$$B_y = \xi_0 I = \xi_0 \frac{V_{pu}}{Z} = \frac{i\omega\gamma\frac{\hbar}{2}n_M P_y \xi_0^2 V_M}{Z} \quad (2.74)$$

$$\left(-\omega^2 + i\frac{\omega_c}{Q_c}\omega + \omega_c^2 \right) B_y = -\omega^2 K P_y \quad (2.75)$$

and now convert back to the time domain,

$$\ddot{B}_y + \frac{\omega_c}{Q_c}\dot{B}_y + \omega_c^2 B_y = K\ddot{P}_y \quad (2.76)$$

with the new definitions,

$$K = \eta\mu_0 \frac{q_c}{Q_c} \gamma \frac{\hbar}{2} n_M \quad \text{where} \quad \eta = \frac{\xi_0^2 V_M}{L_{pu}\mu_0} \quad (2.77)$$

where K is a coupling constant and η is the pickup coil filling factor,

$$\eta = \frac{\xi_0^2 V_M}{L_{pu}\mu_0} = \frac{\frac{1}{2\mu_0} \int_{\text{Bulb}} B_y^2 d^3r}{\frac{1}{2} L_{pu} I^2} = \frac{\text{Field energy in bulb}}{\text{Total field energy}}. \quad (2.78)$$

We have now reduced the properties of the pickup coil and resonant circuit and their coupling to the noble gas transverse magnetization to three dimensionless constants Q_c , q_c , and η and a resonant frequency ω_c , whose typical values for our system are given in Tab. 2.8. To simplify Eq. 2.76 we take advantage of the fact that all the rates in the maser as described by Eq. 2.65, $1/T_1$, $1/T_2$, Δ , and Ω_R , are much slower than the maser frequency ω_M , so we can approximate the time derivatives of B_y and P_y by only expanding to lowest

Description	Parameter	^{129}Xe	^3He	Units
Circuit resonance	$\omega_c/(2\pi)$	7107	19562	Hz
Circuit quality factor	Q_c	76	58	
Circuit feedback strength	q_c	38	25	
Pickup coil field per current	ξ_0		440	G/A
Pickup coil inductance	L_{pu}		92	mH
Pickup coil filling factor	η		0.07	

Table 2.8: Doubly resonant circuit and pickup coil parameters.

order in the phase and fractional amplitude fluctuations. This means we only need to keep terms of order $\dot{\phi}$ and \dot{B}_1/B_1 and we can drop terms that are suppressed by $Q_c \approx 50$. Additionally, we do not have to keep any phase or amplitude derivative terms for P_y as we already have equations for \dot{P}_\perp and $\dot{\psi}$ and hence they would be second order here. Taking these approximations into account we have,

$$\left[\left(-\omega_M^2 - 2\omega_M\dot{\phi} + \omega_c^2 \right) + i \left(2\omega_M \frac{\dot{B}_1}{B_1} + \omega_M \frac{\omega_c}{Q_c} \right) \right] B_1 = i\omega_M^2 K P_\perp e^{-i\theta} \quad (2.79)$$

and equating real and imaginary parts gives,

$$\dot{B}_1 = -\frac{\omega_c}{2Q_c} B_1 + K \frac{\omega_M}{2} P_\perp \cos(\theta) \quad (2.80)$$

$$\dot{\phi} = \frac{1}{2\omega_M} (\omega_c^2 - \omega_M^2) - K \frac{\omega_M}{2} \frac{P_\perp}{B_1} \sin(\theta) \quad (2.81)$$

$$\dot{\phi} \approx \omega_c - \omega_M - K \frac{\omega_M}{2} \frac{P_\perp}{B_1} \sin(\theta) \quad (2.82)$$

where the final approximation assumes that $|\omega_M - \omega_c|/\omega_c \ll 1$, which is always the case in our system.

Now that we have calculated the Rabi frequency Ω_R we can move on to the Rabi frequency generated by the ensemble magnetization, Ω_B , and the ensemble magnetization contribution to the Larmor frequency, ω_z . To calculate the field felt by an individual spin from an ensemble we use a formalism from the derivation of the Clausius-Mossotti or

Lorentz-Lorenz relation (see Chapter 27 of [39] for a detailed explanation and derivation of this formalism). The field felt by a test or probe dipole from the entire ensemble is usually called the local field, \mathbf{B}_{loc} ; and we calculate it by removing the field generated by the test dipole (since it does not feel its own field) and dividing the problem into two regions, the near microscopic region and the far macroscopic region. The near microscopic region is a small sphere around the test dipole where we have to calculate the field from the sum of all the individual dipoles making up the ensemble in the sphere. The far macroscopic region is everything outside the sphere which we can approximate by the macroscopic field calculated from a continuum magnetization. We can express this as,

$$\mathbf{B}_{\text{loc}}(\mathbf{r}) = \mathbf{B}_{\text{micro, near}}(\mathbf{r}) + \mathbf{B}_{\text{macro, far}}(\mathbf{r}) \quad (2.83)$$

and to simplify the calculation of the far macroscopic field we just replace it with the total macroscopic field minus the macroscopic field from the small sphere assuming that the magnetization in the sphere is uniform,

$$\mathbf{B}_{\text{loc}}(\mathbf{r}) = \mathbf{B}_{\text{micro, near}}(\mathbf{r}) + \mathbf{B}_{\text{macro}}(\mathbf{r}) - \frac{2\mu_0}{3}\mathbf{M}(\mathbf{r}). \quad (2.84)$$

The radius for this sphere can be conservatively estimated as two orders of magnitude larger than that of a sphere needed for the average volume taken up by a polarized noble gas atom in the ensemble, that is,

$$r_{\text{sphere}} = 100 \left(\frac{3}{4\pi} \frac{1}{nP} \right)^{1/3} \quad (2.85)$$

which for worst case (small nP), but realistic, numbers for our experiment gives $r_{\text{sphere}} < 5 \mu\text{m}$. This sphere radius, r_{sphere} , is much smaller than the typical size of our ensembles, 1 cm, so the approximation that the sphere is uniformly magnetized is justified and we can ignore the edge effects of the ensemble where this analysis breaks down. All that is left is to calculate the value of $\mathbf{B}_{\text{micro, near}}(\mathbf{r})$ for a random distribution of dipoles oriented in one direction inside the sphere. For simplicity, and without loss of generality, we choose the

dipoles to be oriented along the z -axis and our sphere to be centered at the origin, then,

$$\mathbf{B}_{\text{micro, near}}(0) = \sum_i \frac{\mu_0}{4\pi} m \left(\frac{3\mathbf{r}_i - \mathbf{z}}{r_i^3} + \frac{8\pi}{3} \delta(\mathbf{r}_i) \mathbf{z} \right). \quad (2.86)$$

Since we are only really interested in the long time behavior of this distribution we can approximate the actual finite sum with a continuum integral,

$$\mathbf{B}_{\text{micro, near}}(0) = M \frac{\mu_0}{4\pi} \int_{r_\epsilon}^{r_{\text{sphere}}} \frac{3\mathbf{r} - \mathbf{z}}{r^3} + \frac{8\pi}{3} \delta(\mathbf{r}) \mathbf{z} d^3r, \quad (2.87)$$

where r_ϵ is the distance of closest approach of an ensemble dipole to our test dipole (see [40] for a derivation of the field distribution from a random distribution of dipoles rather than just the mean field result expressed here). The first term in the integral is zero for all values of r_ϵ by convention (see [41]) and the second term in the integral is zero as long as $r_\epsilon > 0$, i.e., there is no wavefunction overlap between the ensemble and test dipoles, which is a good approximation if both dipoles are nuclear dipoles in a noble gas atom, but very poor if one or more dipoles is from an electron in an atom as with Rb-noble gas spin exchange as described in Sec. 2.1.1. Thus, for an ensemble of noble gas atoms with polarized nuclear dipoles, the field felt by the nuclear dipole of another noble gas atom is,

$$\mathbf{B}_{\text{loc}}(\mathbf{r}) = \mathbf{B}_{\text{macro}}(\mathbf{r}) - \frac{2\mu_0}{3} \mathbf{M}(\mathbf{r}), \quad (2.88)$$

so if the macroscopic ensemble is a uniformly magnetized sphere, then a test dipole feels no field from the ensemble. In our case the magnetization is close to uniform and spherical, though somewhat distorted by the presence of the transfer tube and, to a lesser extent, manufacturing imperfections.

A simple way to include the effects of small non-sphericity is to approximate the perturbations away from a perfect uniform sphere as a uniform ellipsoid with its axes aligned to those of the magnetization. The magnetic field inside an ellipsoid with a uniform magnetization is uniform with the resulting local field (Eq. 2.88) from the magnetization component

in the i direction given by,

$$\mathbf{B}_{M_i} = \frac{2\mu_0}{3}(\beta_i - 1)M_i \quad (2.89)$$

with elliptical constant β_i given by [38],

$$\beta_i = \frac{3}{2}R_x R_y R_z \int_0^\infty \frac{ds}{(s + R_i^2)\sqrt{(s + R_x^2)(s + R_y^2)(s + R_z^2)}}. \quad (2.90)$$

In our case the transfer tube effectively extends the ellipse along the y -axis, giving a prolate spheroid ($R_y > R_x = R_z$), for which Eq. 2.90 can be solved exactly,

$$\beta_y = \frac{3}{2} \frac{1 - \varepsilon^2}{\varepsilon^3} \left[\ln \left(\frac{1 + \varepsilon}{1 - \varepsilon} \right) - 2\varepsilon \right] \quad (2.91)$$

$$\beta_x = \beta_z = \frac{3 - \beta_y}{2} \quad (2.92)$$

$$\varepsilon = \sqrt{1 - \left(\frac{R_x}{R_y} \right)^2} \quad (2.93)$$

where ε is the eccentricity. We can now write down expressions for Ω_B and ω_z in an ellipsoid,

$$\Omega_B = -\mu_0\gamma^2\hbar n_M \frac{2}{3} \left(\frac{\beta_x + \beta_y}{4} - \frac{1}{2} \right) P_\perp \approx \mu_0\gamma^2\hbar n_M \frac{\varepsilon^2}{30} P_\perp \quad (2.94)$$

$$\omega_z = -\mu_0\gamma^2\hbar n_M \frac{2}{3} \left(\frac{\beta_z}{2} - \frac{1}{2} \right) P_z \approx -\mu_0\gamma^2\hbar n_M \frac{2\varepsilon^2}{30} P_z \quad (2.95)$$

where the approximation made is applicable in the limit that $\varepsilon^2 \ll 1$. A generous estimate for the influence of the transfer tube is an aspect ratio of $R_y/R_x = 1.2$ which gives $\varepsilon^2 \approx 0.3$, which is still within the limit of applicability of our approximation. Putting this all together we finally have an expression for $\dot{\psi}$ in terms of the other parameters in the model,

$$\dot{\psi} \approx \omega_0 - \omega_M + \Omega_R \sin(\theta) \frac{P_z}{P_\perp} - \mu_0\gamma^2\hbar n_M \frac{\varepsilon^2}{30} P_z. \quad (2.96)$$

We can now combine the results from the previous two sections on the pump bulb and transfer tube to generate a complete picture of the double bulb maser. From the pump bulb

we have spin exchange with Rb as the source of longitudinal polarization, $S = \gamma_{se}P_{Rb}$, as well as wall relaxation and diffusive exchange with the maser bulb via the transfer tube,

$$\dot{P}_P = S - \gamma_{se}P_P - \frac{P_P}{T} - G_{PP}P_P + G_{PM}P_z \quad (2.97)$$

where T represents the time constant for wall relaxation in the pump bulb. In the maser bulb we have a similar situation for the longitudinal polarization, but we can ignore the interaction with Rb due to its low density (as shown in Sec. 2.1.1) and we add the effects due to feedback with the resonant circuit,

$$\dot{P}_z = G_{MP}P_P - \frac{P_z}{T_1} - G_{MM}P_z - \gamma\frac{B_1}{2}P_\perp \cos(\theta). \quad (2.98)$$

Lastly, transverse noble gas polarization in the maser bulb is only produced in the maser bulb via coupling to the pickup coil and has diffusive exchange with the pump bulb where the transverse polarization is effectively zero. Avoiding the production of transverse polarization in the pump bulb and destroying any transverse polarization that diffuses into the pump bulb is achieved by adding a small solenoid around the pump bulb that shifts the noble gas Larmor frequency far away from the maser bulb relative to the atomic line widths, as we will discuss in Sec. 2.2.2. The equation for the transverse polarization in the maser bulb thus only contains a diffusive loss rate,

$$\dot{P}_\perp = \gamma\frac{B_1}{2}P_z \cos(\theta) - \frac{P_\perp}{T_2} - G_{MM}P_\perp. \quad (2.99)$$

Using the same diffusive loss rate coefficient, G_{MM} , for the transverse polarization as we calculated for the longitudinal polarization is just an estimate. We do not know the shape of the transverse polarization profile in the transfer tube (which is necessary to calculate the rate coefficient accurately, as shown in the previous section) since coherence loss can be due to both the same wall and collisional effects as for longitudinal polarization loss, as well as additional effects such as gradients in the magnetic field (see Sec. 2.3 for details) and

Description	Parameter	^{129}Xe	^3He	Units
Pump bulb lifetime	T'	20	165	s
Maser bulb lifetime	T'_1	200	110	s
Maser bulb coherence time	T'_2	200	110	s

Table 2.9: Effective time constants for each bulb using the parameters from Tab. 2.3, Tab. 2.4, and Tab. 2.6 assuming $T_1 = T_2$, which is the best case.

we do not know the field gradients in the transfer tube. However, at least in our current implementation of the experiment, using G_{MM} in Eq. 2.99 gives reasonable agreement between our maser model and observed behavior, as discussed below.

Before putting all our equations together, a useful simplification can be achieved by combining all the loss rates for a given polarization in a given bulb into one time constant term,

$$\frac{1}{T'} = G_{PP} + \frac{1}{T} + \gamma_{se} \quad (2.100a)$$

$$\frac{1}{T'_1} = G_{MM} + \frac{1}{T_1} \quad (2.100b)$$

$$\frac{1}{T'_2} = G_{MM} + \frac{1}{T_2}, \quad (2.100c)$$

which serves to emphasize that the effective coherence time, T'_2 , critical for making sensitive measurements, can be limited/modified by the geometry of the double bulb cell and diffusion coefficients of the gases. Tab. 2.9 lists typical values for T' , T'_1 , and T'_2 for our ^3He and ^{129}Xe masers. Putting everything together gives us a final set of equations for our model of

the double bulb ^3He and ^{129}Xe maser,

$$\dot{P}_P = S - \frac{P_P}{T'} + G_{PM}P_z \quad (2.101a)$$

$$\dot{P}_z = G_{MP}P_P - \frac{P_z}{T'_1} - \gamma \frac{B_1}{2} P_\perp \cos(\theta) \quad (2.101b)$$

$$\dot{P}_\perp = \gamma \frac{B_1}{2} P_z \cos(\theta) - \frac{P_\perp}{T'_2} \quad (2.101c)$$

$$\dot{\psi} = \omega_0 - \omega_M + \gamma \frac{B_1}{2} \frac{P_z}{P_\perp} \sin(\theta) - \mu_0 \gamma^2 \hbar n_M \frac{\varepsilon^2}{30} P_z \quad (2.101d)$$

$$\dot{B}_1 = -\frac{\omega_c}{2Q_c} B_1 + K \frac{\omega_M}{2} P_\perp \cos(\theta) \quad (2.101e)$$

$$\dot{\phi} = \omega_c - \omega_M - K \frac{\omega_M}{2} \frac{P_\perp}{B_1} \sin(\theta), \quad (2.101f)$$

where there is a separate set of equations for both the ^3He and ^{129}Xe masers. We will solve these equations in the next section in various limits relevant to our maser's actual performance.

2.2 Maser Equation Solutions

In the previous section we developed a system of equations to describe the dynamics of the ^3He and ^{129}Xe nuclear Zeeman maser. Now we move forward to solving these equation in the important limits for our measurement. First, we develop the steady state solutions, which will determine for each species the minimum feedback strength and population inversion necessary to sustain a maser, the amount of signal power produced by the maser, and, critically, the equilibrium maser frequency. Next, we investigate the quality of co-magnetometry from a dual ^3He and ^{129}Xe maser and how it is limited by the actual, extended three dimensional nature of the maser; as well as changes to the steady state behavior of the maser due to its extended nature. Lastly, we determine the transient behavior of the maser and co-magnetometry signals around their steady state values, which will show how thermal noise sets the noise floor and ultimate sensitivity of the experiment and how noise in the amplitude of the maser can affect the maser frequency.

2.2.1 Steady State

In this section we will solve the maser system of equations given by Eq. 2.101 in steady state to determine the threshold necessary for masing, the output power of the maser, and the steady state maser frequency. To simplify the solutions we will introduce a few key parameters whose importance for characterizing maser performance will become evident. The first parameter is a dimensionless combination of rates,

$$\lambda = G_{PM}T'G_{MP}T'_1 \quad (2.102)$$

$$= \left(\frac{G_{PM}}{G_{PP} + \frac{1}{T} + \gamma_{se}} \right) \left(\frac{G_{MP}}{G_{MM} + \frac{1}{T_1}} \right) < 1, \quad (2.103)$$

which gives the extent that the bulb exchange rates dominate over the other rates that affect the polarization in the bulbs. The next parameter is the longitudinal polarization in the maser bulb without any feedback from the resonant circuit,

$$P_{z,0} = \frac{S\lambda}{G_{PM}(1-\lambda)}, \quad (2.104)$$

which can be found by setting $K = 0$ in Eq. 2.101. Lastly, we have the radiation damping time (approximation for $\omega_c \approx \omega_M$),

$$\frac{1}{\tau_{RD}} = \frac{\gamma K Q_c \omega_M \cos^2(\theta_{eq})}{2\omega_c} P_{z,0} \approx \frac{\gamma K Q_c}{2} P_{z,0}, \quad (2.105)$$

which is the contribution of the feedback from the coil to shortening the measured T'_2 (damping the coherence) if the longitudinal polarization has been maximized in the lower rather than the upper energy state as we do for masing. This role of τ_{RD} can be seen from our equations by reversing the sign of P_z and assuming only a small portion of the longitudinal polarization has been converted to transverse polarization,

$$\dot{P}_\perp = -\gamma \frac{B_1}{2} P_{z,0} - \frac{P_\perp}{T'_2} = -\frac{P_\perp}{\tau_{RD}} - \frac{P_\perp}{T'_2}, \quad (2.106)$$

where we have approximated B_1 by its steady state value.

We can now express the steady state maser equilibrium solutions in terms of these new parameters,

$$P_{P,eq} = \frac{ST'}{1-\lambda} \left(1 - \lambda \left(1 - \frac{\tau_{RD}}{T'_2} \right) \right) \quad (2.107a)$$

$$P_{z,eq} = \frac{\tau_{RD}}{T'_2} P_{z,0} \quad (2.107b)$$

$$P_{\perp,eq} = P_{z,0} \sqrt{(1-\lambda) \frac{\tau_{RD}}{T'_1} \left(1 - \frac{\tau_{RD}}{T'_2} \right)} \quad (2.107c)$$

$$B_{1,eq} = \frac{2}{\gamma \cos(\theta_{eq})} \sqrt{(1-\lambda) \frac{1}{T'_1 \tau_{RD}} \left(1 - \frac{\tau_{RD}}{T'_2} \right)} \quad (2.107d)$$

$$\tan(\theta_{eq}) = 2Q_c \frac{\omega_c - \omega_M}{\omega_c} \quad (2.107e)$$

$$\omega_M = \omega_0 + \frac{T_c}{T'_2 + T_c} (\omega_c - \omega_0) - \frac{4}{30} \frac{\varepsilon^2}{(T'_2 + T_c) q_c \eta \cos^2(\theta_{eq})} \quad (2.107f)$$

where $T_c = 2Q_c/\omega_c$ is the $1/e$ time constant of the resonant circuit; and from the values in Tab. 2.8 we have $T_c \approx 1$ ms and hence we can always make the approximation $T'_2 + T_c \approx T'_2$. From these solutions we can immediately see that active masing, $P_{\perp,eq} > 0$ and $P_{z,eq} < P_{z,0}$, requires that $T'_2 > \tau_{RD}$. For our typical maser parameters T'_2 is more than a factor of 10 beyond this threshold for both ^3He and ^{129}Xe (see Tab. 2.10), so we can generally make the simplifying approximation $(1 - \tau_{RD}/T'_2) \approx 1$. Ideally we would have $\omega_c = \omega_M$ so that $\theta_{eq} = 0$ and we would maximize our signal, but with careful tuning of the doubly resonant circuit (see Sec. 3.5) we can set the circuit resonant frequencies such that $|\omega_c - \omega_M|/\omega_c < 1 \times 10^{-3}$ and since $Q_c \approx 50$ we have $\theta_{eq} < 0.1$ from the steady state solutions. This small steady state phase shift between the coil field and polarization means that we can make the approximations $\sin(\theta_{eq}) \approx \theta_{eq}$ and $\cos(\theta_{eq}) \approx 1$ for equilibrium and near equilibrium situations. This simplification can be extended further by noting that the equation for B_1 has a very rapid exponential decay term with a time constant of T_c , so that on timescales relevant to all other maser equations we can treat B_1 as always being in equilibrium, $B_1 = KQ_c P_{\perp} \cos(\theta)$. If we substitute this equilibrium solution for B_1 into the

equation for θ ,

$$\dot{\theta} = \dot{\phi} - \dot{\psi} = \omega_c - \omega_0 - \frac{\omega_M}{2Q_c} \tan(\theta) - \frac{\gamma}{2} K Q_c P_z \cos(\theta) \sin(\theta) - \mu_0 \gamma^2 \hbar n_M \frac{\varepsilon^2}{30} P_z \quad (2.108)$$

we see that it too has a rapid decay with a time constant of T_c and hence we can treat it as being in equilibrium and make the general approximations $\sin(\theta) \approx \theta$ and $\cos(\theta) \approx 1$. Combining all these approximations leads to a simplified set of equations for the remaining maser parameters,

$$\dot{P}_P = S - \frac{P_P}{T'} + G_{PM} P_z \quad (2.109a)$$

$$\dot{P}_z = G_{MP} P_P - \frac{P_z}{T'_1} - \frac{P_\perp^2}{\tau} \quad (2.109b)$$

$$\dot{P}_\perp = \frac{P_z P_\perp}{\tau} - \frac{P_\perp}{T'_2} \quad (2.109c)$$

$$\dot{\psi} = \omega_0 - \omega_M + \left(\frac{2Q_c}{\tau} \frac{\omega_c - \omega_M}{\omega_M} - \mu_0 \gamma^2 \hbar n_M \frac{\varepsilon^2}{30} \right) P_z \quad (2.109d)$$

where $1/\tau = \gamma K Q_c/2$ with a simplified set of approximate steady state solutions,

$$P_{P,eq} \approx S T' \quad (2.110a)$$

$$P_{z,eq} \approx \frac{\tau}{T'_1} \quad (2.110b)$$

$$P_{\perp,eq} \approx \sqrt{S T'_1 G_{MP} \tau} \quad (2.110c)$$

$$\omega_M \approx \omega_0 + \frac{T_c}{T'_2} (\omega_c - \omega_0) - \frac{4}{30} \frac{\varepsilon^2}{T'_2 q_c \eta}. \quad (2.110d)$$

These equations emphasize a very important property of the maser: over timescales long compared to the Rabi frequency, fluctuations in spin exchange optical pumping (which is difficult to stabilize due to the sensitivity of the Rb vapor pressure on temperature, Eq. 2.5) will primarily be manifest as variations in P_\perp , as its equilibrium value scales with S , while P_z will remain constant. This suppresses fluctuations of terms in the maser phase proportional to the longitudinal polarization, and is one of the significant frequency stability benefits of

steady state maser operation.

With the steady state solution we can calculate the maser power from the RMS power dissipated in the resonant circuit,

$$\mathcal{P} = \text{Re}(Z(\omega_M))\langle I^2 \rangle \quad (2.111)$$

$$= \frac{\omega_M L_{pu}}{q_c} \frac{1}{2} \left(\frac{B_{1,eq}}{\xi_0} \right)^2 \quad (2.112)$$

$$= \frac{\hbar\omega_M}{2} V_M n_M G_{MP} S T' \left(1 - \frac{\tau_{RD}}{T'_2} \right). \quad (2.113)$$

Since the threshold condition for the maser is that $\tau_{RD} < T'_2$, the fraction of the power proportional to τ_{RD}/T'_2 is an equivalent threshold condition, the threshold power,

$$\mathcal{P}_{\text{threshold}} = \frac{(1-\lambda)}{T'_2 T'_1} \frac{2\omega_M V_M}{\mu_0 \eta q_c \gamma^2} \quad (2.114)$$

which for our typical parameters is ~ 0.5 fW for ^{129}Xe and ~ 0.05 fW for ^3He . In the limit that the maser is well above threshold, $\tau_{RD}/T'_2 \ll 1$, the power is,

$$\mathcal{P} \approx \frac{\hbar\omega_M}{2} V_M n_M G_{MP} P_{P,eq} \quad (2.115)$$

which is simply the energy delivered per polarized atom (Eq. 2.54) times the number of polarized atoms arriving per second in the maser bulb. Additionally, we note that well above threshold the maser power is independent of the strength of the coupling to the pickup coil, K , or the quality factor of the resonant circuit. We can relate the maser power to quantities that are easy to measure in the experiment,

$$\mathcal{P} = \frac{\langle V_{pu}^2 \rangle}{Z(\omega_M)} = \left(\frac{V_{\text{RMS}}}{G_{\text{amp}}} \right)^2 \frac{1}{q_c \omega_M L_{pu}} \quad (2.116)$$

where G_{amp} is the voltage gain of the amplifier connected to the resonant circuit and V_{RMS} is the measured RMS voltage at the maser frequency after the amplifier. Tab. 2.10 summarizes some typical steady state maser operating parameters calculated from the above model.

Description	Parameter	^{129}Xe	^3He	Units
Diffusive spreading	λ	0.006	>0.95	
Maser bulb coherence time	T'_2	200	110	s
Radiation damping	τ_{RD}	12	<7	s
Maser bulb non-masing polarization	$P_{z,0}$	13	>0.2	%
Pump bulb masing polarization	$P_{P,eq}$	50	0.03	%
Maser bulb masing polarization	$P_{z,eq}$	0.7	0.014	%
Maser bulb masing coherence	$P_{\perp,eq}$	3	0.012	%
Maser power	\mathcal{P}	8	0.7	fW

Table 2.10: Calculated steady state maser operating parameters based on typical system values from Tab. 2.3, Tab. 2.6, Tab. 2.7, Tab. 2.8, and Tab. 2.9.

The final result of the steady state solutions is the maser frequency, which is determined by three parameters: the Larmor frequency, the resonant circuit frequency, and interactions due to both the static longitudinal polarizations of both noble gas species and the resonant precessing transverse polarization of each species on itself. The frequency shift effect of the resonant circuit is referred to as cavity pulling (originating from masers operated in regimes where microwave cavities instead of resonant circuits are used) and is suppressed by the ratio of the circuit time constant to the polarization coherence time, which is often rewritten in terms of effective quality factors (where we have assumed $\omega_M \approx \omega_c$),

$$\delta\omega_{\text{cavity}} = \frac{T_c}{T'_2}(\omega_c - \omega_0) = \frac{Q_c}{Q_l}(\omega_c - \omega_0) \quad \text{where} \quad Q_l = \frac{\omega_M T'_2}{2}. \quad (2.117)$$

Here Q_l is referred to as the line-Q for atomic linewidth. Although this is a fairly large suppression factor of $\sim 10^{-5}$ using our typical values, we still require a high degree of fractional stabilization of ω_c since its absolute value (~ 10 kHz) is so large compared to the absolute frequency shifts we desire to measure (~ 100 nHz). The polarization frequency shifts can be estimated with our simplified model for a uniform ellipse of magnetization:

$$\delta\omega_{\text{self}} = -\frac{4}{30} \frac{\varepsilon^2}{T'_2 q_c \eta}, \quad (2.118)$$

which for our typical values and a large estimate for the eccentricity $\varepsilon^2 = 0.3$, corresponding

to a 20% elongation along the transfer tube axis, gives a shift of $< 50 \mu\text{Hz}$. This is a fairly small shift in absolute terms, requiring less stabilization of the parameters involved than $\delta\omega_{\text{cavity}}$, especially since q_c and η will be very well stabilized in order to control the cavity pulling. We will explore controlling these frequency shifts more in Sec. 2.4.

2.2.2 Co-magnetometry and the Extended Maser

We now address the quality of co-magnetometry of dual ^3He and ^{129}Xe masers in terms of the overlap of the spatial distributions of the masing ensembles as well as other corrections to the above theory that couple the maser frequency to all parts of the double bulb cell. To see the effect of spatial distribution of the masing ensemble on co-magnetometry, we return to our derivation of the pickup coil coupling to the transverse magnetization from Sec. 2.1.3,

$$V_{pu} = \gamma \frac{\hbar}{2} \int n(r) \xi_y(r) \dot{P}_y(r) d^3r. \quad (2.119)$$

In the original derivation we argued that we could remove P_y from the integral as it was roughly homogeneous across the bulb, but now we will determine the corrections that arise if we lift that approximation (we will drop the explicit dependence on position, r , for ease of reading). Following through from the previous derivation we find an equation for the current in the pickup coil,

$$\dot{I}_c = -\frac{\omega_c}{2Q_c} I_c + \frac{\omega_M}{2} K_0 \int n \xi_y P_{\perp} \cos(\theta) d^3r \quad \text{where} \quad K_0 = \frac{\gamma \hbar q_c}{2L_{pu} Q_c}, \quad (2.120)$$

where the pickup coil magnetic field can be found at any point from $B_1 = \xi_y I_c$, and an equation for the phase of the current,

$$\dot{\phi} = \omega_c - \omega_M - \frac{\omega_c}{2Q_c} \frac{\int n \xi_y P_{\perp} \sin(\theta) d^3r}{\int n \xi_y P_{\perp} \cos(\theta) d^3r}. \quad (2.121)$$

By combining this with the equations for the amplitude and phase of the transverse polarization we find in steady state a modified maser frequency equation,

$$\omega_M = \bar{\omega}_T + \frac{T_c}{T_2'}(\omega_c - \bar{\omega}_T) \quad \text{where} \quad \bar{\omega}_T = \frac{\int \omega_T n \xi_y P_\perp \cos(\theta) d^3r}{\int n \xi_y P_\perp \cos(\theta) d^3r} \quad (2.122)$$

and ω_T is the total Larmor frequency from the sum of the field from each species' longitudinal magnetization and the solenoid,

$$\omega_T = \gamma B_T = \gamma(B_0 + B_{M_z, \text{He}} + B_{M_z, \text{Xe}}). \quad (2.123)$$

Here we have excluded the self field effect of the transverse polarization as this is a resonant effect and hence affects each species differently without any need to consider spatial overlap. Note that in the derivation of the local field felt by a dipole in a magnetized gas in Sec. 2.1.3 we made no requirement that the gas was made up of one species, so the local field for either species is the same, as we have expressed above. The maser frequency can thus be thought of as the weighted average of the positionally dependent Larmor frequency. The lowest order modification to our homogeneous model is a linear gradient in the field,

$$B_T(r) = B_{T,0} + \nabla B_T \cdot \mathbf{r} \quad (2.124)$$

where $B_{T,0}$ is the uniform component of the field. This means the Larmor component of the maser frequency is determined by,

$$\omega_M = \gamma B_{T,0} + \gamma \nabla B_T \cdot \langle r \rangle_{P_\perp} \quad \text{where} \quad \langle r \rangle_{P_\perp} = \frac{\int r n \xi_y P_\perp \cos(\theta) d^3r}{\int n \xi_y P_\perp \cos(\theta) d^3r}, \quad (2.125)$$

and $\langle r \rangle_{P_\perp}$ is the weighted position of the pickup coil and magnetization coupling. The spatial aspect of co-magnetometry thus boils down to whether the two gas species have the same value of $\langle r \rangle_{P_\perp}$ and how it depends on experimental parameters. Since both species couple to one pickup coil, the coil's spatial dependence is common mode and irrelevant

for comagnetometry. Additionally, in the maser bulb the temperature and hence density is uniform, so n can be removed from the equation. This means that we are interested only in the spatial distribution of P_{\perp} , specifically the next order correction to the diffusive distribution of P_{\perp} beyond the uniform solution.

To determine the spatial distribution of P_{\perp} in the maser bulb we modify the equation for P_{\perp} given by Eq. 2.101 to explicitly include diffusion and relegate all transfer tube sources and sinks as well as wall relaxation to the boundary condition, which leaves us with,

$$\dot{P}_{\perp} = D_M \nabla^2 P_{\perp} + \Omega_R P_z. \quad (2.126)$$

Now, if we substitute in the steady state solution for P_z from Eq. 2.101, treating P_P and Ω_R as constants,⁴ we have, in steady state,

$$0 = \nabla^2 P_{\perp} + S_P - k^2 P_{\perp} \quad \text{where} \quad S_P = \frac{G_{MP} T_1' \Omega_R}{D_M} P_{P,eq} \quad \text{and} \quad k^2 = \frac{\Omega_R^2 T_1'}{D_M} \quad (2.127)$$

with the following boundary condition on the surface of the sphere including wall relaxation and flux through the entrance of the transfer tube (for convenience the transfer tube is temporarily oriented along the z -axis),

$$D_M \mathbf{n} \cdot \nabla P_{\perp} + \kappa P_{\perp} = \begin{cases} \frac{V_M}{A_t} (G_{MP} P_{\perp, P, eq} - G_{MM} P_{\perp}) = \Phi - \beta P_{\perp} & \text{for } \theta \leq \theta_0 \\ 0 & \text{for } \theta > \theta_0 \end{cases} \quad (2.128)$$

where $P_{\perp, P, eq}$ is the equilibrium transverse polarization in the pump bulb (usually considered to be near to zero) and θ_0 is the angle subtended by the transfer tube aperture in the maser bulb and is always small in our experiment, $\theta_0 < 0.2$. In this boundary condition we have assumed the previous homogeneous derivation (Sec. 2.1.2) is exact for calculating the flux through the entrance to the transfer tube and made the very minor approximation that the

⁴Treating Ω_R as a constant may seem like a contradiction since it depends on P_{\perp} , but since Ω_R depends on the integral of P_{\perp} and we expect that change to be perturbative in this new derivation our treatment is justified.

entrance of the transfer tube is also acting like a relaxing wall. The general solution is,

$$P_{\perp} = \frac{S_P}{k^2} + \sum_{l=0}^{\infty} A_l i_l(kr) P_l(\cos \theta) \quad \text{where} \quad i_l(x) = \sqrt{\frac{\pi}{2}} \frac{I_{l+1/2}(x)}{\sqrt{x}}, \quad (2.129)$$

$I_l(x)$ is a hyperbolic/modified Bessel function of the first kind, and the coefficients A_l are found by solving the boundary condition after using the orthogonality relations of the Legendre polynomials,

$$\begin{aligned} 2\kappa \frac{S_P}{k^2} \delta_{l,0} + \left[kD_M \left(l \frac{i_l(kR_M)}{kR_M} + i_{l+1}(kR_M) \right) + \kappa i_l(kR_M) \right] 2A_l = \\ \left(\Phi - \beta \frac{S_P}{k^2} \right) (P_{l-1}(\cos \theta_0) - P_{l+1}(\cos \theta_0)) \\ - \beta(2l+1) \sum_{l'=0}^{\infty} A_{l'} i_{l'}(kR_M) \int_{\cos \theta_0}^1 P_{l'}(x) P_l(x) dx \end{aligned} \quad (2.130)$$

where $\delta_{l,0}$ is the Kronecker delta function. Clearly this cannot be solved in general, but we are only interested in perturbations to the lowest order solution, so we expand everything to lowest order in $kR_M \ll 1$, we approximate $A_l \approx \pi R_M^2 \theta_0^2$ since $\theta_0 \ll 1$, expand all functions of θ_0 to lowest order, and we only keep the $l = 0$ term in the sum on the right hand side. With these approximations we find, to order $l = 1$,

$$P_{\perp} = P_{\perp,eq} \left(1 + \frac{G_{MP} P_{\perp,P,eq} - G_{MM} P_{\perp,eq}}{P_{\perp,eq}} \frac{R_M^2}{D_M} \frac{(y_M - y)}{R_M} \right) \quad (2.131)$$

where

$$P_{\perp,eq} = \frac{\Omega_R T_1' G_{MP} P_P + G_{MP} P_{\perp,P,eq}}{\frac{3\kappa}{R_M} + \Omega_R^2 T_1' + G_{MM}}, \quad (2.132)$$

which is exactly the same as $P_{\perp,eq}$ from the previous section where we approximated $P_{\perp,P,eq} = 0$ and if we identify $R_M/(3\kappa) = T_2$ as derived by different means in Sec. 2.1.2. We have also returned to our standard coordinate system such that y_M is the center of the maser bulb and the transfer tube is in the negative y direction relative to the center. This result is very intuitive, as the size of the polarization gradient relative to the size of the

bulb is the fractional flux into or out of the bulb multiplied by the characteristic time to diffuse across the cell. The average position of the transverse polarization in the cell is,

$$\langle y - y_M \rangle = \frac{\int (y - y_M) P_{\perp} d^3r}{\int P_{\perp} d^3r} = \frac{G_{MP} P_{\perp, P, eq} - G_{MM} P_{\perp, eq}}{P_{\perp, eq}} \frac{R_M^2}{D_M} \frac{R_M}{5}, \quad (2.133)$$

which can be simplified in the limit that $P_{\perp, P, eq} \ll P_{\perp, eq}$ and the transfer tube is lossless to,

$$\langle y - y_M \rangle \approx \frac{3}{10} \frac{D_P}{D_P + D_M} \frac{R_t^2}{L_t}. \quad (2.134)$$

This means the average position of the masing ensemble in the maser bulb is almost completely independent of the overall diffusion coefficient; i.e., making diffusion faster does not reduce the shift from the center, and it does not differ substantially between gas species. For our typical values we have $\langle y - y_M \rangle \approx 20 \mu\text{m}$; and if we use the diffusive loss rate coefficients that include transfer tube losses from Tab. 2.6, then we find that the difference between the average positions of ^3He and ^{129}Xe is only $\sim 2 \mu\text{m}$. However, when measuring this separation in our experiment by applying a known magnetic field gradient and measuring the differential frequency shift between species, we find the difference in average ^3He and ^{129}Xe masing ensemble positions is $\sim 20 \mu\text{m}$ along the y -axis with no significant difference along the other axes, which suggests that polarization in the transfer tube is significantly contributing to the average positions of the masers. Furthermore, when measuring the difference in average position of the masing ensembles in a cell with twice the gas pressure of our typical cell and hence half the diffusion coefficient, we found the effective maser separation increased by almost a factor of 10, further emphasizing that this model does not capture all the maser frequency shift effects of an applied magnetic field gradient. Initial experimental results showing maser frequency shifts as a function of applied field gradient with a very limited number of cells were presented in [25], but no further work has been done and the magnetic field gradient sensitivity of the maser is still not well understood.

One way of reducing the contribution from transverse polarization in the transfer tube to the masing ensemble average positions is to add a set of small closed loop coils around

the tube, which we call “choke coils”. The choke coils shield the atoms in the tube from the pickup coil by generating reactive currents that (partially) cancel out the pickup coil B_1 field in the tube (Lenz’s law). This technique has two problems: (i) at these frequencies it is difficult to make a small coil where the desired reactive part of the impedance dominates over the resistive, so the choke coils provide different B_1 shielding for ^{129}Xe vs ^3He ; and (ii) the choke coils generate quadrature fields that extend into the maser bulb, which lead to frequency shifts. The difference in efficacy of a set of choke coils in shielding the pickup coil B_1 field at the ^3He and ^{129}Xe maser frequencies, as well as the quadrature fields generated, can be seen in Fig. 2.2 and Fig. 2.3. The choke coils in this simulation consist of three layers of 24 AWG magnet wire with either 6 or 10 turns per layer, with the smaller coil near the maser bulb. The gap between coils to accommodate the spacer/cell holder between the maser and pump bulb temperature regions. Self inductances of all the choke coils and mutual inductance with the pickup coil and between all coil pairs as well as the field generated by each coil was calculated using Radia [42]. We determine the effect of generating both out of phase and quadrature fields on the maser frequency by modifying the volume averaged pickup coil magnetic field per unit current, ξ_0 , to include both real and imaginary parts,

$$\tilde{\xi}_0 = \xi_{0,r} + i\xi_{0,i}. \quad (2.135)$$

In our limit where $|\xi_{0,i}| \ll |\xi_{0,r}|$ we modify the coupling constant K ,

$$\tilde{K} = \frac{K}{\xi_0^2} (\xi_r^2 + i2\xi_r\xi_i) = K_r + iK_i \quad (2.136)$$

which leads to,

$$\dot{B}_1 = -\frac{\omega_c}{2Q_c} B_1 + \frac{\omega_M}{2} P_1 (K_r \cos(\theta) + K_i \sin(\theta)) \quad (2.137)$$

$$\dot{\phi} = \omega_c - \omega_M - \frac{\omega_M}{2} \frac{P_1}{B_1} (K_r \sin(\theta) - K_i \cos(\theta)) \quad (2.138)$$

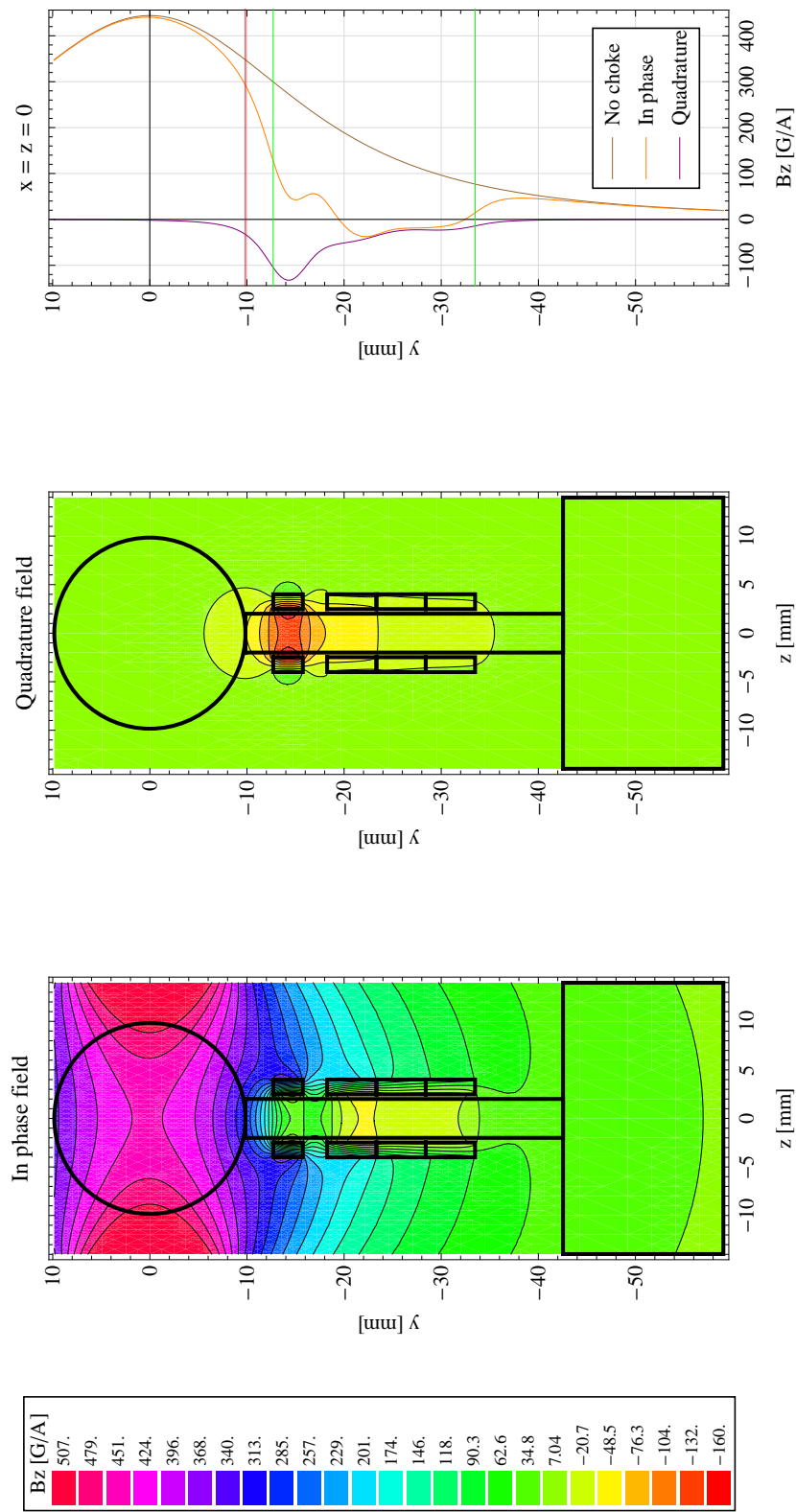


Figure 2.2: Calculated effect of choke coils on the pickup coil field per unit current at the ^{129}Xe maser frequency of 7.1 kHz.

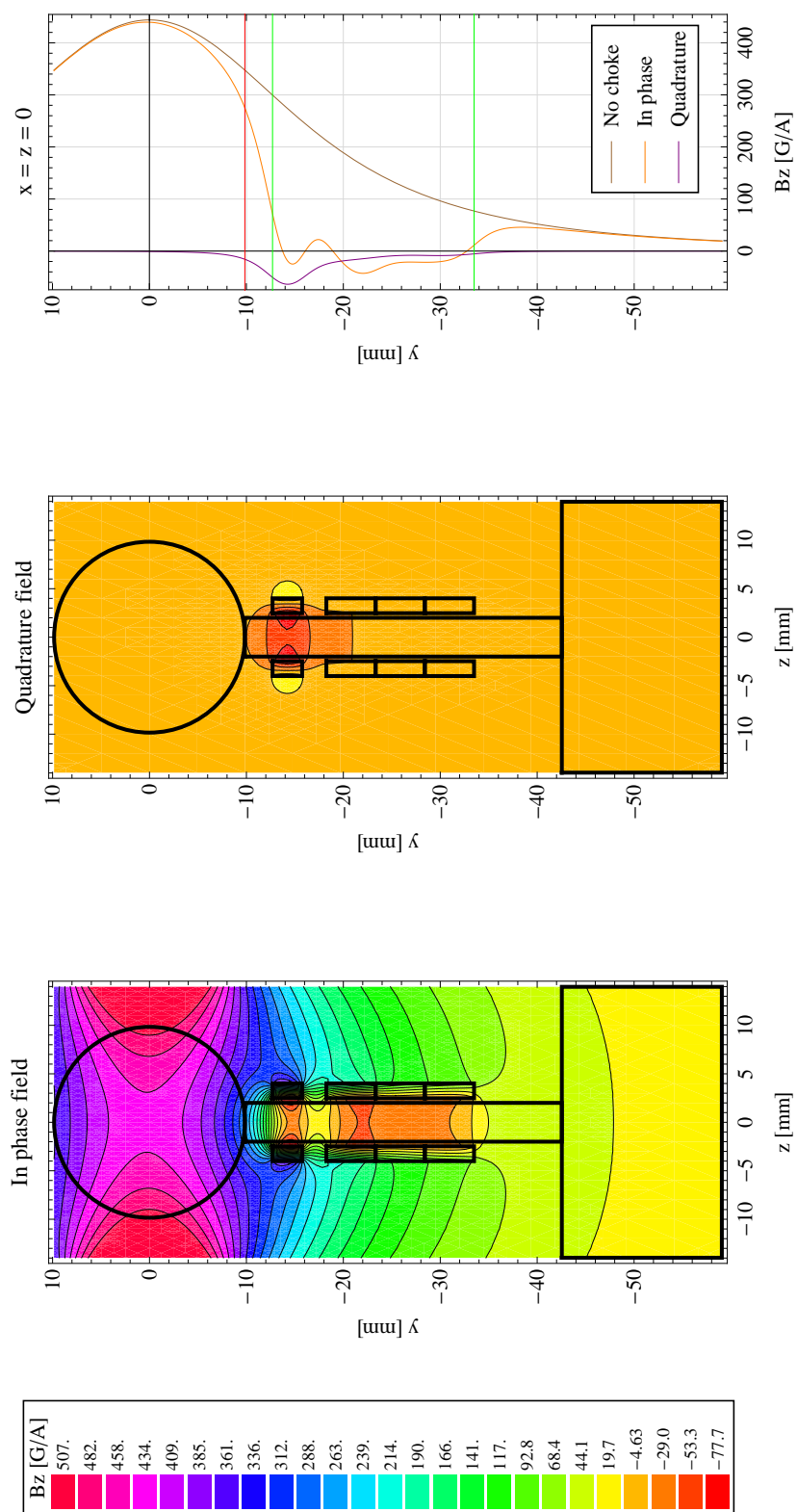


Figure 2.3: Calculated effect of choke coils on the pickup coil field per unit current at the ^3He maser frequency of 19.6 kHz.

and changes in the steady state solutions,

$$\tan(\theta_{eq}) = \frac{2Q_c}{\omega_c}(\omega_c - \omega_M) + \frac{K_i}{K_r} \quad (2.139)$$

$$\omega_M = \omega_0 + \frac{2Q_c}{\omega_c T_2'}(\omega_c - \omega_M) + \frac{K_i}{T_2' K_r} - \frac{4}{30} \frac{\varepsilon^2}{\gamma T_2' q_c \eta \cos^2(\theta_{eq})} \quad (2.140)$$

giving a new shift of,

$$\delta\omega_{\text{choke}} = \frac{2\xi_i}{T_2'\xi_r}, \quad (2.141)$$

which, for a typical system values and a ratio of $\xi_r/\xi_i < 100$ from numerical calculations using the model choke coils described above, gives a frequency shift of $< 30 \mu\text{Hz}$. While choke coils have been used in the experiment, their effects on the magnetic field gradient susceptibility of the maser frequency due to shielding of the transfer tube have not been experimentally investigated.

In addition to the concern with transverse polarization in the transfer tube coupling to the pickup coil and affecting the maser frequency, polarization in the pump bulb can also affect the maser frequency. In this case we will be interested in a discrete model with two spatially homogeneous ensembles in the pump and maser bulbs. Additionally, we will be considering large frequency differences between the two bulbs, so we cannot operate in the limit that there are only small phase shifts ($\theta \ll 1$) between parts of the maser ensemble, necessitating a return to the equations of motion expressed in terms of P_x and P_y , rather than amplitude and phase. To simplify matters we ignore self field interactions and assume that the resonant circuit exactly matches the Larmor frequency and pick the arbitrary B_1 phase, ϕ , to be zero. Thus, from Eq. 2.62 for P_x and P_y in the maser bulb and adding

diffusive coupling with the pump bulb and coupling of the coil to the pump bulb we have,

$$\dot{P}_{x,P} = \frac{\gamma}{2} B_{1,P} P_P + \Delta_P P_{y,P} - \frac{P_{x,P}}{T'_{2,P}} + G_{PM,\perp} P_x \quad (2.142a)$$

$$\dot{P}_{y,P} = -\Delta_P P_{x,P} - \frac{P_{y,P}}{T'_{2,P}} + G_{PM,\perp} P_y \quad (2.142b)$$

$$\dot{P}_P = S - \frac{P_P}{T'} + G_{PM} P_z - \frac{\gamma}{2} B_{1,P} P_{x,P} \quad (2.142c)$$

$$\dot{P}_x = \frac{\gamma}{2} B_1 P_z + \Delta P_y - \frac{P_x}{T'_2} + G_{MP,\perp} P_{x,P} \quad (2.142d)$$

$$\dot{P}_y = -\Delta P_x - \frac{P_y}{T'_2} + G_{MP,\perp} P_{y,P} \quad (2.142e)$$

$$\dot{P}_z = -\frac{\gamma}{2} B_1 P_x - \frac{P_z}{T'_1} + G_{MP} P_P \quad (2.142f)$$

$$\dot{I}_c = -\frac{\omega_c}{2Q_c} I_c + \frac{\omega_M}{2} K_0 (K_M P_x + K_P P_{x,P}) \quad (2.142g)$$

$$\dot{\phi} = \omega_c - \omega_M - \frac{\omega_c}{2Q_c} \frac{K_M P_y + K_P P_{y,P}}{K_M P_x + K_P P_{x,P}} \quad (2.142h)$$

where $P_{x,P}$ and $P_{y,P}$ are the transverse polarization terms in the pump bulb. We have also added several new parameters: bulb specific coupling constants $K_M = n_M \xi_0 V_M$ and $K_P = n_P \xi_{0,P} V_P$, the pickup coil fields in each bulb are given by $B_1 = \xi_0 I_c$ and $B_{1,P} = \xi_{0,P} I_c$, diffusive coupling rates for the transverse polarization $G_{MP,\perp}$ and $G_{PM,\perp}$, the difference between the Larmor frequency in the pump bulb, $\omega_{0,P}$, and the maser frequency, ω_M , is $\Delta_P = \omega_M - \omega_{0,P}$, and a coherence time for the transverse polarization in the pump bulb $T'_{2,P}$. Our primary concern is to determine how changes in $\omega_{0,P}$, which is a stand in for the average Larmor frequency in the pump bulb as well as any other frequency shifts that might occur in the pump bulb (such as the contact shift with polarized Rb), will affect the overall maser frequency. More specifically we can write $\Delta_P = \Delta + \delta\omega_P$ where $\delta\omega_P$ is the shift in the pump bulb and then solve our system of equations in steady state for Δ in terms of $\delta\omega_P$.

Ideally we would solve the above system of equations in general, but this is complicated to say the least, leading to a solution that gives little intuition. However, we expect the effect of transverse polarization in the pump bulb to be small, so it is sufficient to solve

the equations in a perturbative manner. First, we uncouple the transverse polarization in the pump bulb from the rest of the system by setting all of its gain terms to zero, $G_{PM,\perp} = B_{1,P} = 0$, and solve for the steady state condition which gives $P_{x,P} = P_{y,P} = 0$ and, since we assumed that $\omega_c = \omega_M$, $P_y = 0$ as well. In this situation the remaining terms have the same steady state maser solutions as in the previous section with $P_x = P_\perp$. Next, we take the equations for the terms that were zero and solve them assuming that all other terms have their steady state values,

$$\dot{P}_{x,P} = \frac{\gamma}{2}\xi_{0,P}I_{c,eq}P_{P,eq} + (\Delta + \delta\omega_P)P_{y,P} - \frac{P_{x,P}}{T'_{2,P}} + G_{PM,\perp}P_{x,eq} \quad (2.143a)$$

$$\dot{P}_{y,P} = -(\Delta + \delta\omega_P)P_{x,P} - \frac{P_{y,P}}{T'_{2,P}} + G_{PM,\perp}P_y \quad (2.143b)$$

$$\dot{P}_y = -\Delta P_{x,eq} - \frac{P_y}{T'_2} + G_{MP,\perp}P_{y,P} \quad (2.143c)$$

$$\dot{\phi} = -\frac{\omega_c}{2Q_c} \frac{K_M P_y + K_P P_{y,P}}{K_M P_{x,eq} + K_P P_{x,P}}. \quad (2.143d)$$

In the final step we simplify the remaining equation in Δ and $\delta\omega_P$ by only taking the lowest order term in Δ . This is a reasonable approximation for small values of $\delta\omega_P$ and an excellent approximation for large values. This is justified as we expect the decay of the transverse polarization in the pump bulb to be relatively rapid compared to diffusive exchange and hence very little will flow back to the maser bulb and the polarization that is in the pump bulb only couples weakly to the pickup coil and hence will only shift the maser frequency slightly from the Larmor frequency in the maser bulb.

Following this perturbative prescription we find a skew Lorentzian solution for the maser frequency,

$$\Delta = \frac{\delta\omega_P A}{\delta\omega_P^2 + B + A} \quad (2.144)$$

where,

$$A = \left(\frac{\alpha N_r}{T'_2} + G_{MP,\perp} \right) \left(G_{PM,\perp} + \frac{\alpha P_{P,eq}}{\tau_{RD} P_{z,0}} \right) \quad (2.145)$$

$$B = \frac{1}{T'_{2,P}} \left(\frac{1}{T'_{2,P}} + \alpha N_r G_{PM,\perp} \right), \quad (2.146)$$

$\alpha = \xi_{0,P}/\xi_0$ is the ratio of pickup coil field strength in the pump versus the maser bulb, and $N_r = (V_P n_P)/(V_M n_M)$ is the ratio of the number of noble gas atoms in the two bulbs which for typical values gives $N_r = 1.2$ and $\alpha = 0.055$. This result is initially surprising as even if there is no coupling of the pickup coil to the pump bulb, $\alpha = 0$, the Larmor frequency of the atoms in the pump bulb still affect the overall maser frequency and for ^3He it is this type of coupling, not coupling to the pickup coil, that is the dominant contribution. This would seem to contradict our earlier conclusion that the maser frequency was the weighted average of the Larmor frequency where the weights were proportional to the coil coupling (Eq. 2.122), but that formula was derived without diffusive coupling of the transverse polarization. The reason that diffusive coupling to other regions can lead to maser frequency shifts is that for a small difference in the Larmor frequency in the pump bulb, relative to the inverse exchange time, the polarization that travels there and back can be thought of as still being coherent, but with a phase shift; and this phase shift times the rate of exchange leads to a frequency shift in the maser frequency. For large frequency shifts in the pump bulb, the phase shift developed is no longer perturbative and rather acts as a decoherence mechanism for the pump bulb relative to the maser bulb, which leads to a reduced maser frequency shift.

Coupling the maser frequency to the frequency shifts in the pump bulb works against our original goal of separating the pump and maser bulbs to avoid the large and difficult to stabilize Rb contact shifts that always accompany effective spin exchange. Ironically, the large shift in the pump bulb for ^{129}Xe , which was a prime motivator for separating the two bulbs, actually makes ^{129}Xe less susceptible to this problem since it detunes the pump bulb frequency far from the small shift limit and well into the wings and shortens $T'_{2,P}$ such that

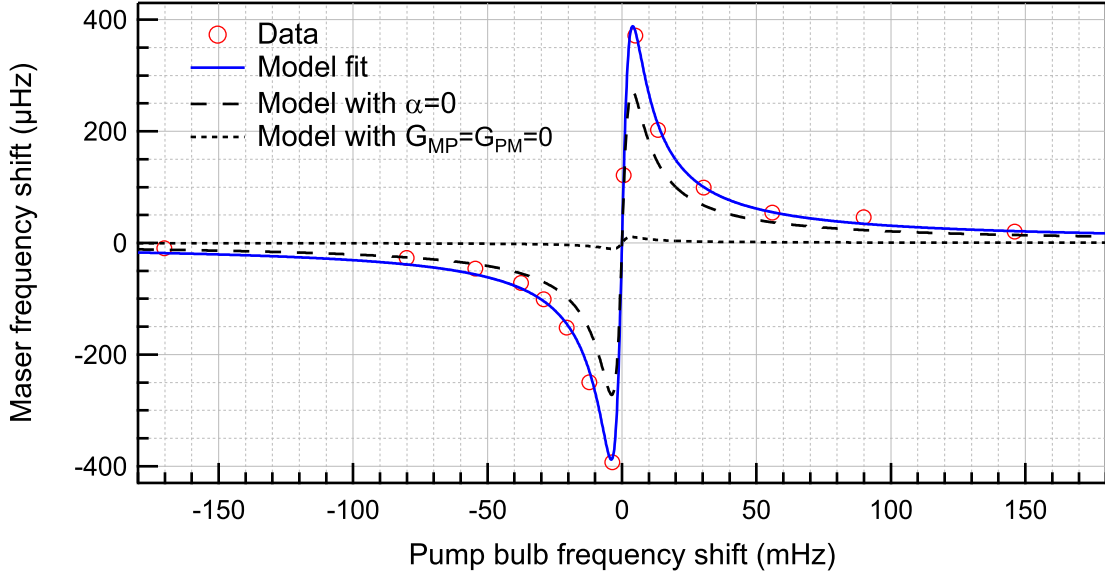


Figure 2.4: Measured and calculated ^3He maser frequency shifts due to frequency shifts of transverse ^3He polarization in the pump bulb. The isolated shifting of the pump bulb frequency was achieved with a solenoid wrapped directly around the bulb.

the total maser frequency shift is probably only a few μHz and small shifts in the pump bulb are suppressed by $\sim 10^5$. For ^3He , the Rb contact shift is not large enough to be far away from the small shift limit, so its maser frequency is very susceptible to changes in the ^3He frequency in the pump bulb from either the Rb contact shift (even though it is so much smaller for ^3He) or from magnetic field gradients that penetrate the magnetic shields. To eliminate this possibility we add a small solenoid wrapped around the pump bulb to shift the pump bulb ^3He Larmor frequency several hundred mHz away from the maser bulb. We have also used this pump bulb solenoid to measure the ^3He maser frequency shift due to frequency shifts in the pump bulb as shown in Fig. 2.4. The measured maser frequency shift data is in good agreement to a fit with the model given by Eq. 2.144 with two free parameters giving $T'_{2,P} = 45$ s and $1/G_{PM,\perp} = 1/G_{MP,\perp} = 110$ s, which is a reasonable ^3He coherence time in the pump bulb (it is ~ 70 s in the maser bulb for this cell) and close to the expected value of 90 s for the diffusive transport, and all other parameters fixed to the expected ^3He values for the cell. Additionally, we have added two other curves to

Fig. 2.4 showing the same model with either the coil coupling set to zero, $\alpha = 0$, which only reduces the size of the maser frequency shift slightly, and with the diffusive coupling of the transverse polarization set to zero, $G_{MP,\perp} = G_{PM,\perp} = 0$, which reduces the frequency shift to a negligible level, showing the dominance of the diffusive coupling effect discussed above.

Additionally, as the above model shows, the use of choke coils to reduce the coupling of transfer tube polarization to the pickup coil will not reduce the transfer tube's role in affecting the maser frequency as much as expected due to diffusive coupling. This diffusive exchange in the transfer tube is especially troubling as there is high density Rb with a polarization of several percent in the warmer parts of the transfer tube (see the end of Sec. 2.1.1), which can cause Rb contact shifts that will diffusively couple to the maser frequency. Unfortunately, modeling the transfer tube as part of the masing ensemble is complicated and would require numerical solutions. So, with the caveat that transverse polarization in the transfer tube is a somewhat unknown quantity, we can now write down a relatively complete account of the frequencies of the masers with first order corrections for all terms that would otherwise be common mode,

$$\omega_{M,Xe} = \gamma_{Xe} (\xi_s I_s + B_{ex} + B_{M_z}) + \delta\omega_{Xe} \quad (2.147)$$

$$\omega_{M,He} = \gamma_{He} (\xi_s I_s + B_{ex} + B_{M_z} + \langle \delta r \rangle \cdot \nabla (\xi_s I_s + B_{ex} + B_{M_z})) + \delta\omega_{He} \quad (2.148)$$

where $B_0 = I_s \xi_s$ with I_s and ξ_s the current and field per unit current of the solenoid, B_{M_z} is the field from the longitudinal magnetizations of the noble gases, B_{ex} is any external field that penetrates the shields or any magnetic field generated by currents inside the shields other than the solenoid, $\langle \delta r \rangle$ is the difference in average positions of the two species, and $\delta\omega$ includes all terms that are not due to macroscopic longitudinal magnetic fields and hence not common mode, such as, cavity pulling, self field interactions with transverse magnetization, contact shifts during collisions, and coupling to the pump bulb as well as additional shifts we will consider in Sec. 2.4. We stabilize the frequency of the ^{129}Xe maser by comparing it to a stable frequency reference and feeding back to the current in the solenoid. We

then compare the ^3He maser frequency against the same reference giving us the difference frequency between the two masers, which is the co-magnetometry signal,

$$\begin{aligned} \omega_{M,He} - \gamma_R \omega_{M,Xe} &= \gamma_{He} (-\alpha_r (B_{ex} + B_{Mz}) + \langle \delta r \rangle \cdot \nabla (B_{ex} + B_{Mz})) \\ &\quad + \alpha_r \gamma_R \omega_{M,Xe} + \delta\omega_{He} - (1 + \alpha_r) \gamma_R \delta\omega_{Xe} \end{aligned} \quad (2.149)$$

where $\gamma_R = \gamma_{He}/\gamma_{Xe} = 2.75408156(20)$ (see Tab. 2.7) and

$$\alpha_r = \langle \delta r \rangle \cdot \frac{\nabla \xi_s}{\xi_s}. \quad (2.150)$$

In the center of our solenoid along the y -axis we have $\nabla \xi_s / \xi_s \approx 7 \times 10^{-6} \text{ cm}^{-1}$, so with a typical cell value for the average maser separation of $\langle \delta r \rangle \approx 20 \text{ }\mu\text{m}$ we have $\alpha_r \approx 2 \times 10^{-8}$. With such a small value for α_r we can clearly make the approximation $(1 + \alpha_r) \gamma_R \delta\omega_{Xe} \approx \gamma_R \delta\omega_{Xe}$ since $\delta\omega_{Xe}$ is also small (i.e., only a few orders of magnitude larger than our sensitivity at long time scales). With our relatively high solenoid fractional field homogeneity we can also approximate $\alpha_r (B_{ex} + B_{Mz}) \approx 0$ since their fractional homogeneity will not be as good as the solenoid and hence the shift from these fields will be dominated by their own gradients. Lastly, there is the question of the term $\alpha_r \gamma_R \omega_{M,Xe}$, which is a fairly large shift of $\sim 400 \text{ }\mu\text{Hz}$, its stability will be discussed in Sec. 2.4. The reader may also notice that we have neglected to include factors of the form $1 - T_c/T_2'$ from Eq. 2.122 in the co-magnetometry signal, but these factors are so close to unity, $T_c/T_2' \approx 10^{-5}$, that they are only significant when combined with the maser frequencies themselves, at which point we revert to the cavity pulling equations embedded in $\delta\omega_{He}$ and $\delta\omega_{Xe}$.

2.2.3 Transients

In this section we will linearize the maser equations around the steady state solutions to determine how fluctuations in the system can limit our ability to measure the maser frequency at different time scales. Additionally, we will try to find a mechanism for the

behavior observed in previous thesis [43, 25] that the maser frequency was highly correlated to the maser amplitude at long time scales, which was exploited to improve the sensitivity of the maser at those time scales. We begin with a general expression for a non-linear system like the maser written in terms of a set of first order differential equations,

$$\dot{\mathbf{x}} = \mathbf{f}(\mathbf{x}, \mathbf{u}) \quad (2.151)$$

where \mathbf{x} is the state of the system undergoing dynamic evolution, in our case the ensembles polarization, field, and phase, and \mathbf{u} are the inputs to the system, such as temperature and resonant laser power. We Taylor expand the equations around the steady state solution, $\dot{\mathbf{x}}_0 = 0 = \mathbf{f}(\mathbf{x}_0, \mathbf{u}_0)$, to obtain a linearized set of equations,

$$\delta\dot{\mathbf{x}} \approx \mathbf{J}_{\mathbf{x}}[\mathbf{f}(\mathbf{x}_0, \mathbf{u}_0)]\delta\mathbf{x} + \mathbf{J}_{\mathbf{u}}[\mathbf{f}(\mathbf{x}_0, \mathbf{u}_0)]\delta\mathbf{u} = \mathbf{A}\delta\mathbf{x} + \mathbf{B}\delta\mathbf{u} \quad (2.152)$$

where $\delta\mathbf{x} = \mathbf{x} - \mathbf{x}_0$ and $\delta\mathbf{u} = \mathbf{u} - \mathbf{u}_0$ are the perturbations away from steady state and $\mathbf{J}_{\mathbf{x}}$ and $\mathbf{J}_{\mathbf{u}}$ are the Jacobian matrices taking derivatives with respect to the state and input variables respectively. Since the fluctuations that enter our system are typically random in nature, we describe them in terms of their power spectra and thus we convert our linear time model into a set of frequency transfer functions, which can transform our input noise spectra into measured noise in the amplitude and frequency of the maser. This is a standard procedure in control theory and so we will borrow their notation (see [44] for a more general discussion). In general we have,

$$\delta\dot{\mathbf{x}} = \mathbf{A}\delta\mathbf{x} + \mathbf{B}\delta\mathbf{u} \quad (2.153a)$$

$$\mathbf{y} = \mathbf{C}\delta\mathbf{x} + \mathbf{D}\delta\mathbf{u} \quad (2.153b)$$

where \mathbf{y} is the measured output of the system, in our case the frequency and amplitude of the maser. To find the transfer functions for the system we take the Laplace transform and

solve for the ratio of output to input,

$$\mathbf{H}(s) = \frac{\mathbf{Y}(s)}{\mathbf{U}(s)} = \mathbf{C}(s\mathbf{I} - \mathbf{A})^{-1}\mathbf{B} + \mathbf{D} \quad (2.154)$$

where \mathbf{I} is the identity matrix and in our system $\mathbf{D} = 0$. We define the state of our system as the familiar,

$$\delta\mathbf{x} = \begin{pmatrix} \delta P_P \\ \delta P_z \\ \delta P_\perp \\ \delta\psi \\ \delta B_1 \\ \delta\phi \end{pmatrix} \quad (2.155)$$

with the Jacobian of the full equations (Eq. 2.101) at their steady state values given by,

$$\mathbf{A} = \begin{pmatrix} -\frac{1}{T'} & G_{PM} & 0 & 0 & 0 & 0 \\ G_{MP} & -\frac{1}{T'_1} & -\frac{\gamma B_{1,eq}}{2} & 0 & -\frac{\gamma B_{1,eq}}{2KQ_c} & 0 \\ 0 & \frac{\gamma B_{1,eq}}{2} & -\frac{1}{T'_2} & 0 & \frac{1}{KQ_c T'_2} & 0 \\ 0 & \frac{\gamma KQ_c \theta_{eq}}{2} - \mu_0 \gamma^2 \hbar n_M \frac{\varepsilon^2}{30} & -\frac{KQ_c \theta_{eq}}{B_{1,eq} T'_2} & -\frac{1}{T'_2} & \frac{\theta_{eq}}{B_{1,eq} T'_2} & \frac{1}{T'_2} \\ 0 & 0 & \frac{K\omega_M}{2} & 0 & -\frac{1}{T_c} & 0 \\ 0 & 0 & -\frac{K\omega_M \theta_{eq}}{2B_{1,eq}} & \frac{1}{T_c} & \frac{\theta_{eq}}{B_{1,eq} T_c} & -\frac{1}{T_c} \end{pmatrix}. \quad (2.156)$$

In considering the different possible fluctuating input parameters to include in $\delta\mathbf{u}$, the most important is thermal Johnson noise in the resonant circuit. Johnson noise is white (constant spectral density), but we are only interested in its value near the maser frequency in a bandwidth of $\Delta\omega \approx \omega_M/Q_c$. We represent this in the time domain as a voltage made up of two quadratures oscillating at the maser frequency with relatively slowly varying,

independent random amplitudes,

$$V_n = V_{n,1} \cos(\omega_M t) + V_{n,2} \sin(\omega_M t) \quad (2.157)$$

or converted into a complex form such that the real part is the same as above,

$$\tilde{V}_n = (V_{n,1} + iV_{n,2}) e^{i\omega_M t}. \quad (2.158)$$

If we add this noise term to the voltage generated in the pickup coil we find the following modified equation for the pickup coil field,

$$\ddot{B}_y + \frac{\omega_c}{Q_c} \dot{B}_y + \omega_c^2 B_y = K \ddot{P}_y + \frac{\xi_0 q_c}{L_{pu} Q_c} \dot{\tilde{V}}_n, \quad (2.159)$$

which, to lowest order with $\dot{V}_{n,i}/V_{n,i} \ll \omega_M$ as constructed, leads to additional terms in the field amplitude and phase,

$$\dot{B}_1 = \dots + \frac{\xi_0 q_c}{2L_{pu} Q_c} V_{n,1} = \dots + \frac{1}{T_c} B_{n,1} \quad (2.160)$$

$$\dot{\phi} = \dots + \frac{\xi_0 q_c}{2B_1 L_{pu} Q_c} V_{n,2} = \dots + \frac{1}{B_1 T_c} B_{n,2}, \quad (2.161)$$

where $B_{n,i} = \xi_0 V_{n,i}/R_{\text{eff}}$.

In addition to the Johnson noise in the resonant circuit, major sources of noise are changes in the resonant laser power in the pump bulb as well as the pump bulb temperature (driven by the laser). Laser power fluctuations are incorporated by adding a fluctuation to the spin exchange parameter, $S = k_{se} n_{Rb} P_{Rb}$. Calculating the term for temperature fluctuations in the pump bulb is far more difficult as it affects many parameters and hence it will be calculated with a numerical derivative and not considered in this first analytic calculation. Combining the two Johnson noise terms with the spin exchange term we

generate our input perturbation matrix,

$$\mathbf{B} = \begin{pmatrix} 1 & 0 & 0 \\ 0 & 0 & 0 \\ 0 & 0 & 0 \\ 0 & 0 & 0 \\ 0 & \frac{1}{T_c} & 0 \\ 0 & 0 & \frac{1}{B_{1,eq}T_c} \end{pmatrix}. \quad (2.162)$$

Lastly, the measurement parameters of the maser consist of its amplitude and frequency, which are given by,

$$\mathbf{C} = \begin{pmatrix} 0 & 0 & 0 & 0 & 0 & \frac{s}{2\pi} \\ 0 & 0 & 0 & 0 & \frac{1}{B_{1,eq}} & 0 \end{pmatrix} \quad (2.163)$$

where we have the frequency in Hz in the first row and the fractional amplitude in the second. Although \mathbf{C} was supposed to consist only of constants, we get around this by adding a derivative term, $\mathbf{C}_D\delta\dot{\mathbf{x}}$, to the equation for the output \mathbf{y} in Eq. 2.153 and then solving in the same manner as before, giving the result $\mathbf{C} + s\mathbf{C}_D$ above.

We now generate the matrix of transfer functions, \mathbf{H} , where the rows correspond to the different measured outputs and each column is due to a different input. Since the fluctuations of each input are independent we determine the effect of the input fluctuations on the output by summing the product of each fluctuation's power spectrum with the magnitude squared of the appropriate transfer function,

$$S_{\text{out},i} = \sum_j |\mathbf{H}_{i,j}|^2 S_{\text{in},j} = \sum_j S_{i,j}. \quad (2.164)$$

Note that we will typically be interested in the size of each input contribution, $S_{i,j}$, to the total. If the fluctuations are not independent, then this can be expressed in \mathbf{B} by having one noise input affect multiple system parameters. Although power spectra are easily combined and compared as above, they do not have dimensions that are easily interpreted. Thus,

much like the standard deviation is typically reported instead of the variance, we will use the square root of the power spectrum instead of the power spectrum itself,

$$\sigma_{\text{out},i} = \sqrt{\sum_j (|\mathbf{H}_{i,j}| \sigma_{\text{in},j})^2} = \sqrt{\sum_j (\sigma_{i,j})^2} \quad \text{where } \sigma = \sqrt{S}, \quad (2.165)$$

and we will show the results for both the individual terms, $\sigma_{i,j}$, as well as the total output. Typically the input power spectra in our experiment are well modeled as either purely white noise, $S_{\text{in}} = S_w$, or as white noise combined with random walk behavior as in, $S_{\text{in}} = S_w(1 + (\frac{\omega_R}{\omega})^2)$, where ω_R is the crossover frequency from white noise to random walk.

To compute the input noise power spectrum of the slowly varying Johnson noise amplitudes, $V_{n,i}$, we start by noting the power spectrum of V_n is the usual $S_{V_n} = S_J = 4k_B T_M R_{\text{eff}}$ over the bandwidth $\Delta\omega = \omega_M/Q_c$ around the maser frequency. Each of the terms $V_{n,1} \cos(\omega_M t)$ and $V_{n,2} \cos(\omega_M t)$ make up one quadrature of the signal and hence contribute half of the total power for V_n . However, since the slowly varying amplitudes, $V_{n,i}$, only cover the bandwidth from $\omega = 0$ to $\omega = \Delta\omega/2$, in order for each term to provide half the total power, the amplitudes must have twice the spectral density,

$$\mathcal{P}_{V_n} = S_{V_n} \Delta\omega = \frac{1}{2} \left(S_{V_{n,1}} \frac{\Delta\omega}{2} \right) + \frac{1}{2} \left(S_{V_{n,2}} \frac{\Delta\omega}{2} \right) \implies S_{V_{n,i}} = 2S_J. \quad (2.166)$$

Hence, the noise power spectrum of the magnetic field generated by the thermal Johnson noise is,

$$S_{B_{n,i}} = \frac{8k_B T_M \xi_0^2}{R_{\text{eff}}} = B_{1,eq}^2 \frac{4k_B T_M}{\mathcal{P}}. \quad (2.167)$$

The laser power fluctuations are certainly more complicated, but we start by representing them as a flat power spectral density with a value of $S_S = (\beta S)^2$ where β is the fractional size of the fluctuation.

Before diving into the solutions for the full interaction of Johnson and spin exchange optical pumping noise with the maser frequency, we first consider a slightly simpler case. If we have perfect tuning of the resonant circuit, $\theta_{eq} = 0$, and a perfect spherical magnetization,

$\varepsilon = 0$, then the phase and amplitude components of the maser are no longer coupled, and our model reduces to just the phase components,

$$\begin{pmatrix} \delta\dot{\psi} \\ \delta\dot{\phi} \end{pmatrix} = \begin{pmatrix} -\frac{1}{T_2'} & \frac{1}{T_2'} \\ \frac{1}{T_c} & -\frac{1}{T_c} \end{pmatrix} \begin{pmatrix} \delta\psi \\ \delta\phi \end{pmatrix} \quad (2.168)$$

which are only coupled to the phase component of the Johnson noise. In the standard limit that $T_c \lll T_2'$, the spectral density of the maser frequency given by the transfer function is,

$$\sigma_{\nu, Jp} = \frac{1}{\pi T_2'} \sqrt{\frac{k_B T_M}{\mathcal{P}}} \sqrt{\frac{1 + (\omega T_2')^2}{1 + (\omega T_c)^2}}. \quad (2.169)$$

This noise spectrum has three regimes: a flat spectrum for frequencies high compared to the resonant circuit coherence time; a decreasing spectrum for frequencies between the circuit and nuclear spin coherence time, which is called the white phase noise regime; and a flat spectrum for frequencies lower than the nuclear coherence time, which is called the white frequency noise regime. Thus, the most sensitive measurements are be made in the white frequency noise regime at modulation frequencies lower than $\nu = 1/(2\pi T_2')$ (about 1 mHz for our typical maser) with the ultimate sensitivity given by,

$$\sigma_{\nu, Jp} = \frac{1}{\pi T_2'} \sqrt{\frac{k_B T_M}{\mathcal{P}}}. \quad (2.170)$$

It is this modulation frequency regime that we will be paying the most attention to when considering the influence of various input fluctuations. For our typical maser parameters in Tab. 2.9 and Tab. 2.10, the ultimate sensitivity is $\sigma_{\nu, He} = 6 \mu\text{Hz}/\sqrt{\text{Hz}}$ for ^3He and $\sigma_{\nu, Xe} = 1 \mu\text{Hz}/\sqrt{\text{Hz}}$ for ^{129}Xe . The noise for the co-magnetometry signal, $\omega_{M, He} - \gamma_R \omega_{M, Xe}$, can be calculated by propagation of error,

$$\sigma_{\nu} = \sqrt{(\sigma_{\nu, He})^2 + (\gamma_R \sigma_{\nu, Xe})^2} \quad (2.171)$$

giving $\sigma_{\nu} = 6.6 \mu\text{Hz}/\sqrt{\text{Hz}}$, which shows that our ultimate noise floor is dominated by the

^3He signal.

Returning to the transfer functions for the full set of inputs we have chosen, the solutions are complicated in general, with resonance peaks around the Rabi frequency among other features, but we will restrict the development of analytic solutions to their behavior in the white frequency noise regime. The phase component of the Johnson noise leads to the same fluctuation in the maser frequency as the ultimate sensitivity given above and leads to no fluctuation in the maser amplitude. The amplitude component of the Johnson noise leads to fluctuations in the maser frequency due to coupling through cavity shifts and self field interactions,

$$\sigma_{\nu,Ja} = \frac{1}{\pi T_2'} \sqrt{\frac{k_B T_M}{\mathcal{P}}} \left| \theta_{eq} + \frac{2\varepsilon^2}{15\eta q_c} \right| = \sigma_{\nu,Jp} \left| \theta_{eq} + \frac{2\varepsilon^2}{15\eta q_c} \right|, \quad (2.172)$$

which for our typical system values gives $\sigma_{\nu,Ja} \approx 0.13\sigma_{\nu,Jp}$, a completely irrelevant contribution once it is added in quadrature. We also generate fluctuations in the fractional maser amplitude,

$$\sigma_{A,Ja} = \frac{1}{(1 - \frac{\tau_{BD}}{T_2'})} \sqrt{\frac{k_B T_M}{\mathcal{P}}} \approx \sqrt{\frac{k_B T_M}{\mathcal{P}}}, \quad (2.173)$$

which is the inverse of the ultimate amplitude SNR and shows that the ultimate maser frequency fluctuation is just the maser coherence line width divided by the maser SNR. Unfortunately, in this frequency regime the amplitude fluctuations tend to be dominated by random walk like behavior from the laser, which makes it impossible to use as a check on the maser SNR. However, the amplitude noise in the regime between the Rabi frequency resonances and the inverse resonant circuit lifetime is also white and given by,

$$\sigma_{\nu,Ja,\text{mid}} = 2\sqrt{\frac{k_B T_M}{\mathcal{P}}} = 2\sigma_{A,Ja}. \quad (2.174)$$

This middle regime is particularly useful as all spin exchange fluctuations from the pump bulb are suppressed by slow diffusive coupling, giving us a clean check of the maser power to compare with Eq. 2.116.

The fluctuations in the spin exchange optical pumping of the noble gases lead to maser

frequency fluctuations,

$$\sigma_{\nu,S} = \frac{\omega\beta}{1 - \frac{\tau_{RD}}{T_2}} \left| \frac{\theta_{eq}}{4\pi} - \frac{\varepsilon^2}{30\pi\eta q_c} \right| \quad (2.175)$$

that are not white, but rather decrease in amplitude with decreasing frequency. Thus, a random walk in SEOP only leads to white noise in the maser frequency. This decreasing sensitivity of the maser frequency to fluctuations in S is to be expected given that the maser frequency only couples to P_z and the steady state value of P_z is independent of S (see Eq. 2.109 and Eq. 2.110). The fluctuations in fractional maser amplitude due to spin exchange are white,

$$\sigma_{A,S} = \frac{\beta}{2(1 - \frac{\tau_{RD}}{T_2})} \quad (2.176)$$

and the amplitude and frequency components can be combined,

$$\sigma_{\nu,S} = \nu\sigma_{A,S} \left| \theta_{eq} - \frac{2\varepsilon^2}{15\eta q_c} \right|, \quad (2.177)$$

so that fluctuations in the amplitude beyond the Johnson noise can be used to estimate the contribution to the frequency noise from this mechanism. For our typical maser conditions at a low modulation frequency of $\nu_0 = 11.6 \mu\text{Hz}$, a one day long modulation, the fractional amplitude noise has a random walk spectrum with a value of $\sigma_{A,S} \approx 0.5\nu_0/\nu$ fractional amplitude/ $\sqrt{\text{Hz}}$ and the quantity in the absolute value sign above is approximately 0.1, so we have a white frequency noise of $\sigma_{\nu,S} = 0.5 \mu\text{Hz}/\sqrt{\text{Hz}}$ which is clearly irrelevant in our case compared to the frequency noise generated by the phase component of the Johnson noise. Additionally, this mechanism for amplitude to frequency noise coupling is clearly not the one that causes the observed correlations between maser frequency and amplitude mentioned at the beginning of this section.

To complete our discussion of transients and fluctuations we extend our model to include a second maser and phase locking of one maser to a reference frequency by applying feedback to the current source driving B_0 . Adding a second maser requires adding a second set of

state variables and couplings between the two masers,

$$\begin{pmatrix} \delta\dot{\mathbf{x}}_{He} \\ \delta\dot{\mathbf{x}}_{Xe} \end{pmatrix} = \begin{pmatrix} \mathbf{A}_{He,He} & \mathbf{A}_{He,Xe} \\ \mathbf{A}_{Xe,He} & \mathbf{A}_{Xe,Xe} \end{pmatrix} \begin{pmatrix} \delta\mathbf{x}_{He} \\ \delta\mathbf{x}_{Xe} \end{pmatrix} + \mathbf{B}\delta\mathbf{u} \quad (2.178)$$

where the diagonal \mathbf{A} matrices are the same as before with the appropriate steady state values for each species and the off diagonal terms consist of coupling between species, limited here to local magnetic fields generated by longitudinal magnetization as described in Sec. 2.2.2. Additionally, it is important to distinguish in \mathbf{B} between common mode input fluctuations that affect (or can affect) all state parameters of both masers at the same time, such as laser power and temperature, and independent fluctuations that affect only one state parameter of one maser, such as Johnson noise, as this changes the effectiveness of co-magnetometry in reducing the fluctuations. To incorporate the phase lock of the magnetic field we switch to the Lorentz transform representation and add a feedback term, \mathbf{F} , to the input parameters,

$$\mathbf{Y} = \mathbf{H}(\mathbf{U} + \mathbf{F}) \quad \text{where} \quad \mathbf{F} = \mathbf{G}(\mathbf{R} - \mathbf{Y}) \quad (2.179)$$

where \mathbf{R} is the reference and \mathbf{G} is the open loop feedback transfer function. A detailed and thorough introduction to types of feedback control can be found in [44], but we will give a brief outline of the typical methods we use. The feedback in \mathbf{G} typically includes a sum of terms that are proportional to, the integral of, and the derivative of the difference between the output and the reference (called PID feedback),

$$\mathbf{G}_{i,j} = G \left(1 + \frac{\omega_I}{s} + \frac{s}{\omega_D} \right) \quad (2.180)$$

where G is the proportional gain, ω_I gives the frequency below which the integral term becomes important, and ω_D gives the frequency above which the differential term becomes important. The integral term provides increasing feedback gain at low frequencies, which prevents the output signal from drifting away from the reference. The derivative term provides increasing gain at higher frequencies, which is used to cancel the effects of lag

in the system to provide feedback control over a greater bandwidth (typically derivative control is implemented such that it is closer to a lead term as described in [44]). For our simulation we only include proportional and and integral control. With the addition of feedback, we now have a new total transfer function for the fluctuation inputs to the system as well as for the reference inputs,

$$\mathbf{T}_U = (\mathbf{I} + \mathbf{HG})^{-1}\mathbf{H} \quad (2.181)$$

$$\mathbf{T}_R = (\mathbf{I} + \mathbf{HG})^{-1}\mathbf{HG} \quad (2.182)$$

such that the measured output noise power spectrum is given by,

$$S_{Y,i} = \sum_j |\mathbf{T}_{U,i,j}|^2 S_{U,j} + \sum_j |\mathbf{T}_{R,i,j}|^2 S_{R,j} \quad (2.183)$$

which shows that for sufficiently high feedback gain the measured output noise is dominated by the reference noise rather than the input fluctuations. In our simulations we set the reference noise to zero as it is negligible for our typical maser.

We now have a model that includes enough of the actual system behavior to compare to typical maser data. The data comes from a cell with fill pressures of 800/45/150 Torr of $^3\text{He}/^{129}\text{Xe}/\text{N}_2$, which are very similar to the typical maser cell we have been documenting in tables in this chapter, though the measured maser powers (from Eq. 2.116) and coherence times for both species are smaller than we calculated for our typical cell, only 0.6/5 fW and 80/200 s for $^3\text{He}/^{129}\text{Xe}$. The shorter coherence times are due to a slightly smaller maser bulb volume than our typical cell model and the lower maser powers are due to a lower laser power. We adjusted these model parameters to match the measured maser power and coherence time. In the model we include input noise from the Johnson noise of the circuit as well as a white plus random walk noise model for the resonant laser power and the pump bulb temperature derived from approximate monitors of those variables in the experiment (see Fig. 2.5). We calculate numerical derivatives of the maser state with respect to the

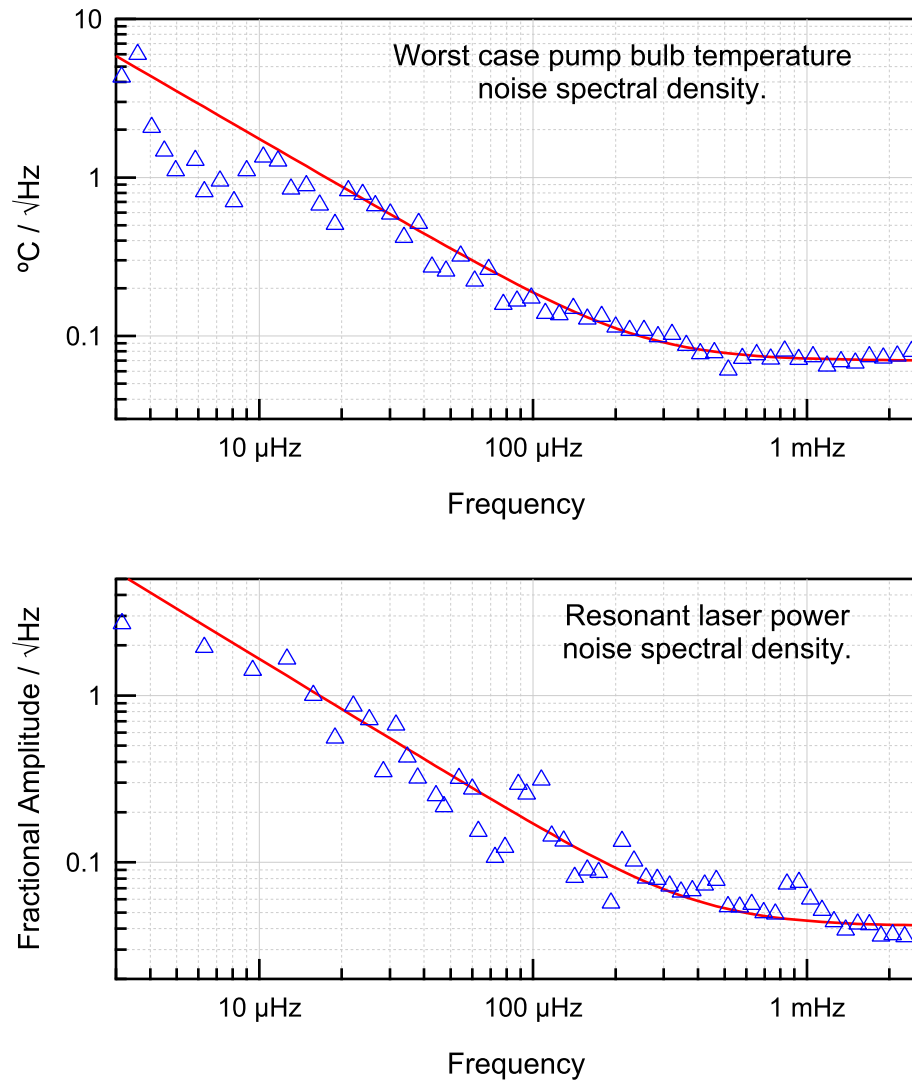


Figure 2.5: Measured noise spectral densities for pump bulb temperature and laser power fluctuations and approximate white noise plus random walk models used in the simulation.

laser power and pump bulb temperature using a one dimensional model of optical pumping as described in [25] to calculate the Rb polarization and take into account the temperature dependence of the Rb and other gas densities as well as the diffusion coefficients. We also calculate the magnetic field gradients generated in the maser bulb by the magnetizations in the pump bulb and include their effect as described at the end of Sec. 2.2.2 assuming a typical transverse polarization separation of $\langle \delta r \rangle \approx 20 \mu\text{m}$.

In Fig. 2.6 we show the resulting calculated spectra of the fractional ^3He and ^{129}Xe maser amplitude fluctuations from the largest contributors in the model as well as the maser spectra from a 26 day long data set. The figure also contains a 4 day subset of the data when the maser power was the most stable, and to which the power given by the model was matched. The points shown in the data spectra are generated by averaging power spectra over bins whose size scales logarithmically, hence there is less scatter in the high frequency points. The spectra show three distinct regions. First, for high frequency modulations above 10 mHz the fluctuations in the pump bulb do not affect the maser due to the long time necessary for diffusive coupling; hence the masers are dominated by the white Johnson noise of the resonant circuit. Second, there is resonant behavior at a few mHz where fluctuations in the pump bulb become evident. Third, for low modulation frequencies below 1 mHz, the quasi-steady state regime, the maser amplitudes follow the random walk behavior of the laser power and pump bulb temperature fluctuations. The model and data for ^{129}Xe match very well, both the thermal noise floor at high frequency and the size and location of the resonance peak. The agreement for ^3He is less good, suggesting there is some excess input noise at its Larmor frequency.⁵

We achieved reasonable agreement between our model and data for the amplitude spectra of the maser, so we now compare our model and data for the maser frequency spectra with some confidence. As shown in Fig. 2.7, we see the individual and combined effects of the noise inputs on the ^3He frequency spectrum when the ^{129}Xe frequency is phase locked,

⁵There is also a small peak in the ^3He spectrum at about 65 mHz, which is an artifact of our digitization electronics and not real. The peak also shows up in the ^3He frequency spectrum.

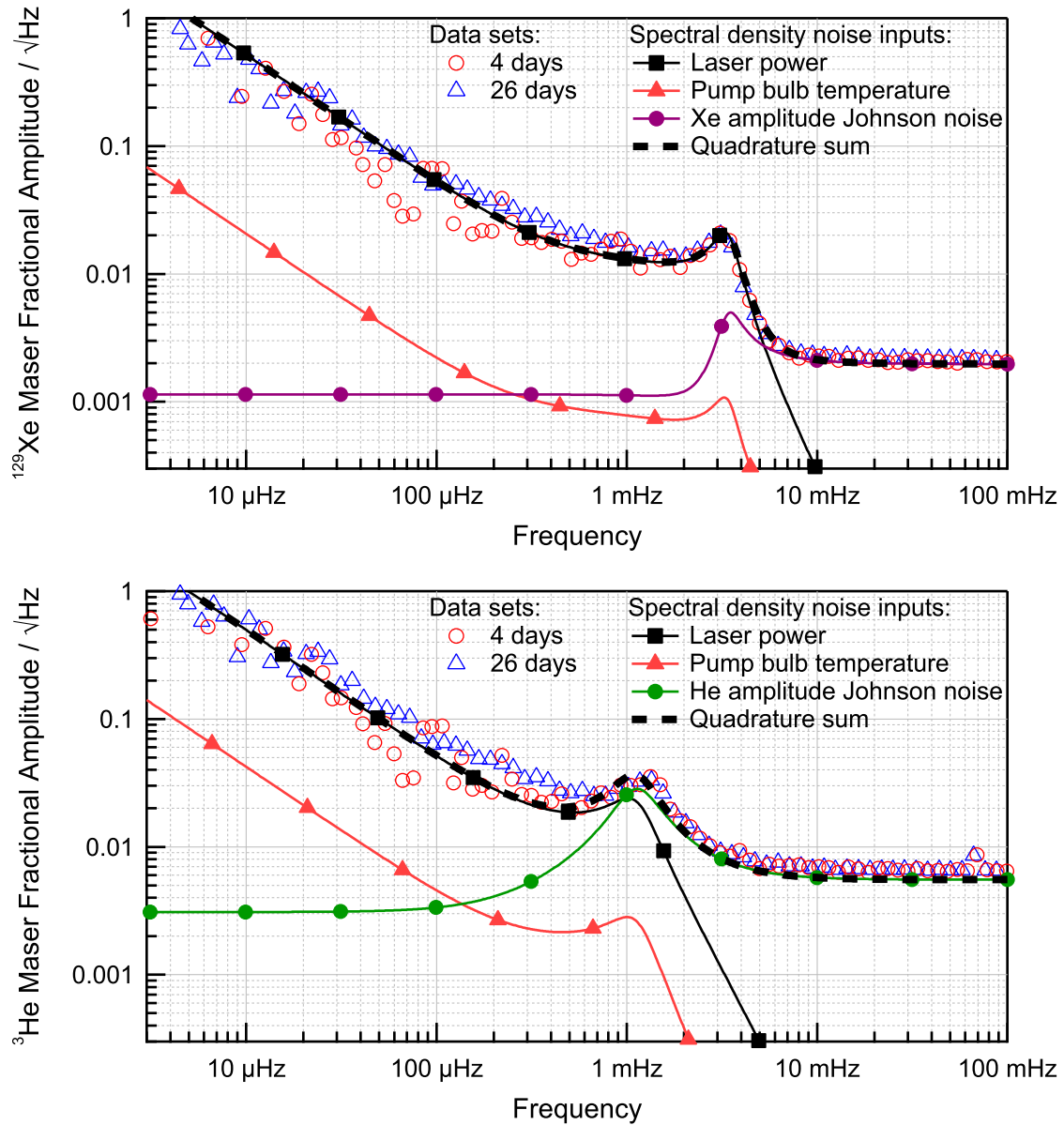


Figure 2.6: Fractional amplitude noise spectral densities of the ^3He and ^{129}Xe masers, theoretical calculations and experimental data. (Note: markers in the calculated theory curves are placed once per 100 calculated points.)

i.e., our co-magnetometry signal. We also see the reduction in frequency noise for ^{129}Xe between the anticipated unlocked noise floor and the measured locked noise floor, which is limited by our reference and measurement technique. The significant reduction between the measured and modeled ^{129}Xe frequency noise confirms that our reference and measurement noise are negligible and that all frequency noise in ^{129}Xe has been transferred to ^3He , as shown in the figure. In comparing the data and the model we divide the spectra into the same three regions as we did for the amplitude spectra. For high frequency modulations above 10 mHz we are dominated by Johnson noise and the measured noise is a little higher than the model, as we would expect from the amplitude noise in this regime. For frequencies slightly above 1 mHz we have resonant behavior in the model, which is dominated by laser induced amplitude noise in ^{129}Xe being converted to phase noise via cavity pulling. We see no sign of this resonant peak in the data and the model suggests that this is only possible with rather precise matching of the resonant circuit to within < 3 Hz of the Larmor frequency, which is close to the accuracy limit of our technique to calibrate the circuit resonance. In the calculations for Fig. 2.7 we used a detuning of -5 Hz in the model, which should just be visible in the experimental data; but it is not and hence -5 Hz is a worst case scenario for this model and data. A useful test of this aspect of the model would be to change the frequency the ^{129}Xe maser is locked to by ± 20 Hz relative to the circuit resonance, which, given the size of the amplitude noise in this data set, would result in a noise spike three times larger than the phase noise floor in the data shown here and hence could be detected in a short data set. For modulation frequencies below 1 mHz in the frequency noise we have a flat region in the model that is dominated by Johnson noise in the circuit, with the random walk amplitude fluctuations mostly being converted into white noise as we saw in the analytic results for the approximate low frequency behavior of the model (see Eq. 2.177). The emerging random walk behavior at very low frequencies due to laser power fluctuations comes from the inclusion of the field gradient generated by polarization in the pump bulb; and the random walk from the temperature fluctuations is due to both the change in the field gradient and modulation of T'_2 due to changes in

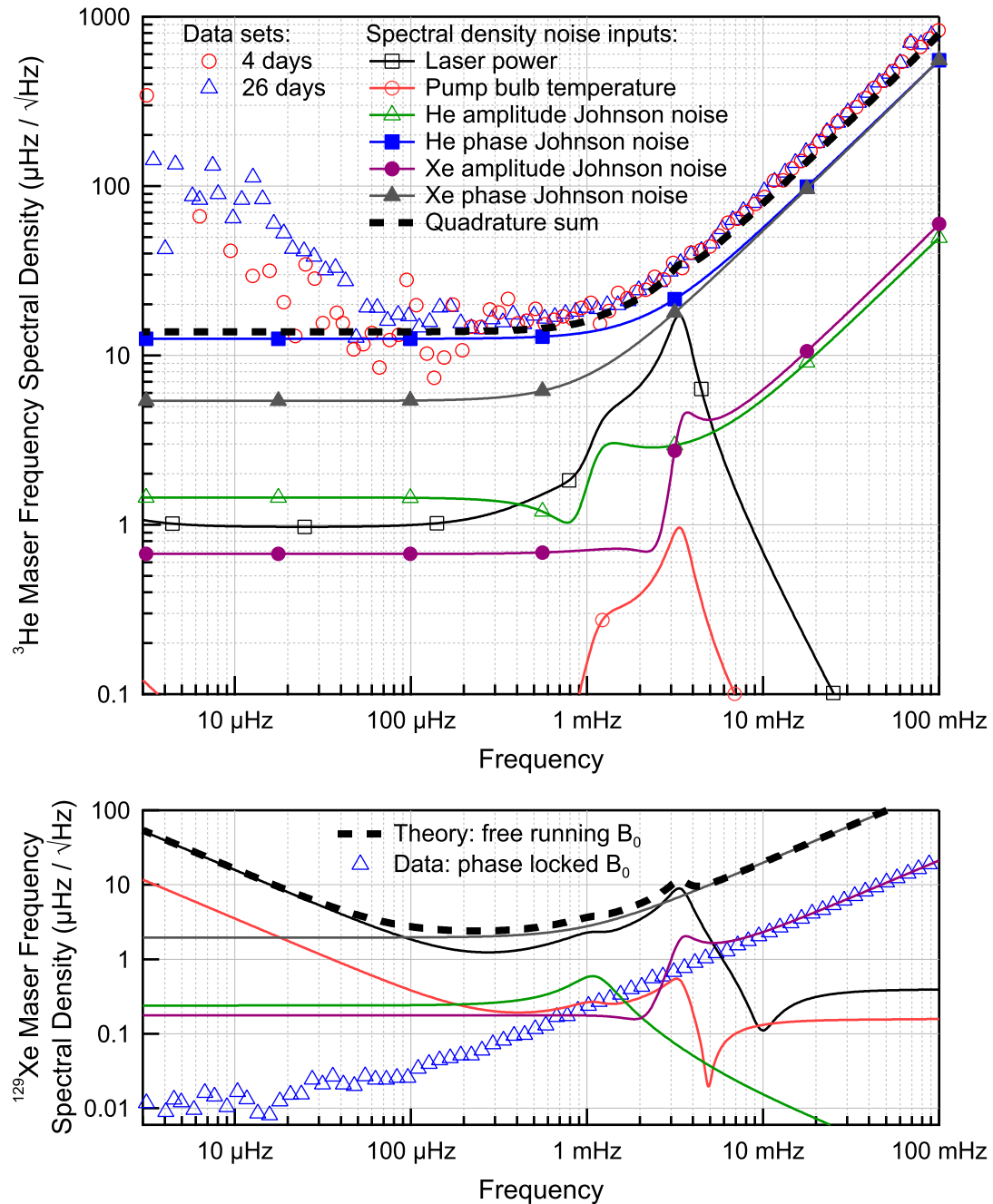


Figure 2.7: Frequency noise spectral densities of the masers, theoretical calculations and experimental data. (Note: markers in the calculated theory curves are placed once per 100 calculated points.)

the diffusion coefficients, which affects both cavity pulling and self field interactions (see Eq. 2.117 and Eq. 2.118). The disagreement between the data and the model in the white frequency noise regime between 100 μHz and 1 mHz is due to the excess noise at the ^3He maser frequency that we saw in the amplitude spectrum, as we get good agreement when taking this noise into account and using the measured coherence times.

For modulation frequencies below 100 μHz the data exhibits random walk behavior that is not accounted for in the model, and which significantly limits our sensitivity for modulations at the 11.6 μHz of the Earth's rotation. For this cell we believe the frequency drift is caused by a slow decay in the quality of the wall coating over time, which led to a reduction in the measured ^{129}Xe T_2' from 200 to 100 seconds between the beginning and end of the data set shown here; and that this wall decay coupled with a non-zero cavity pulling led to the random walk in frequency. The loss in wall coating quality is also evident in the steady 30% loss in power of the ^{129}Xe maser over this period due to decreased T_1 . However, other cells filled with similar gas pressures and having similar T_2' s have had very stable T_2' s, but have had similar input noise as well as maser amplitude and frequency noise spectra. In fact they can have higher frequency noise spectra that are only reduced to near or below the level shown here when the amplitude and frequency correlations are taken into account. Such correlations are clearly not demonstrated by the terms we have included in our model and are probably due to some of the complications discussed in Sec. 2.2.2: e.g., effects in the transfer tube that are difficult to model and are likely sensitive to changes in diffusion constants due to temperature changes. The mechanisms behind this correlated behavior are still not well understood.

2.3 Polarization Relaxation Mechanisms

In the previous section we introduced phenomenological relaxation times for the longitudinal and transverse polarization as T_1 and T_2 , respectively.⁶ In this section we will detail the

⁶Note: the T_1 and T_2 terms do not include the diffusive bulb escape rate G_{MM} that we included in the effective lifetime terms T_1' and T_2' at the end of Sec. 2.1.3.

physics underlying these relaxation processes. Relaxation of the ^3He and ^{129}Xe nuclear spin longitudinal and transverse polarization is primarily due to changes in local magnetic fields due to collisions or diffusion through macroscopic field gradients. These magnetic field changes induce fluctuations in the Larmor frequency that degrade spin coherence and fluctuations in the quantization axis that degrade spin polarization. Additionally, spin angular momentum can be lost during collisions when it is coupled to the angular momentum of the colliding pair or transferred from one species to another or to a wall. As illuminated in the previous section, minimizing spin relaxation is critical to making sensitive maser frequency measurements. Details of how we measure the noble gas spin relaxation rates are given in Sec. 3.7.

2.3.1 Polarization Lifetime T_1

There are five depolarization mechanisms that we will discuss in this section: spin exchange collisions with Rb, motion through macroscopic transverse magnetic field gradients, dipole-dipole coupling between noble gas atoms during binary collisions that couple the spin angular momentum into the angular momentum of the pair, coupling of spin angular momentum into the rotational angular momentum of transient noble gas molecules, and collisions with the wall. The first and last of these depolarization mechanisms, spin exchange with Rb and wall collisions, we have already discussed in Sec. 2.1.1 and Sec. 2.1.2 respectively, so we will only give a brief reminder of the physics here and approximate numbers in a typical cell that we use. As a guideline of the importance of each depolarization mechanism for our typical cells the total depolarization rates measured for ^3He and ^{129}Xe are $1/T_{1,\text{He}} = \gamma_{1,\text{He}} < 2 \times 10^{-4} \text{ s}^{-1}$ (with the lowest value we have measured in any cell of $\gamma_{1,\text{He}} \approx 2 \times 10^{-5} \text{ s}^{-1}$) and $1/T_{1,\text{Xe}} = \gamma_{1,\text{Xe}} \approx 2 \times 10^{-3} \text{ s}^{-1}$ respectively.

In the absence of laser light to maintain Rb polarization, spin exchange collisions with Rb act as a source of polarization loss for the noble gas polarization as discussed at the end of Sec. 2.1.1 with loss rate coefficients for ^3He and ^{129}Xe of $\gamma_{se,\text{He}}$ and $\gamma_{se,\text{Xe}}$ respectively. Using the values from Tab. 2.3 for the spin exchange coefficients and Eq. 2.5 for the vapor

pressure of Rb, we find that at the 120 °C temperature of the pump bulb the rates are $\gamma_{se,Xe} = 7 \times 10^{-2} \text{ s}^{-1}$ and $\gamma_{se,He} = 2 \times 10^{-6} \text{ s}^{-1}$, which is only significant for ^{129}Xe ; and at the maser bulb temperature of 50 °C we have $\gamma_{se,Xe} = 4 \times 10^{-4} \text{ s}^{-1}$ and $\gamma_{se,He} = 9 \times 10^{-9} \text{ s}^{-1}$, which is insignificant for both species.

Diffusion through gradients of a magnetic field perpendicular to the average solenoid field orientation generate fluctuations in the quantization axis of the noble gas nuclear spins which leads to a decrease in the ensemble polarization. In the regime that we operate in where the Larmor frequency is low enough that the phase evolution between collisions in the gas is much less than one, but high enough that there is significant phase evolution during the characteristic crossing time of the cell, the rate of depolarization is given by,

$$\gamma_{1,\nabla B_{\perp}} = D \frac{|\nabla B_x|^2 + |\nabla B_y|^2}{B_0^2} \quad (2.184)$$

where is assumed that B_0 is aligned along the z -axis. This was originally derived in [45, 46] and extended to additional regimes in [47], which also includes an intuitive introduction to this result (an intuitive explanation can also be gained by applying our discussion of repeated weak interaction events in Sec. 2.1.1). In our solenoid we do not have an independent measurement of the transverse magnetic field gradients; but assuming they are no larger than the largest B_0 gradient, then $|\nabla B_x|/B_0 \approx 3 \times 10^{-5} \text{ cm}^{-1}$ (and similarly for $|\nabla B_y|/B_0$). Taking the fastest diffusion coefficient in our typical cells from Tab. 2.6 of $D = 1.4 \text{ cm}^2/\text{s}$ for ^3He in the pump bulb we have $\gamma_{1,B} \approx 3 \times 10^{-9} \text{ s}^{-1}$, which means this mechanism is an insignificant contributor for our typical cells, even if we had field gradients 30 times larger than the ones considered here.

During binary collisions between noble gas atoms there is a dipole-dipole interaction between their nuclei that couples the angular momentum of the nuclear spin to the angular momentum of the pair around the center of mass. For ^3He - ^3He collisions this process is

calculated and measured in [48] giving a density dependent depolarization rate of,

$$\gamma_{bc,He} = 3.7 \times 10^{-7} \text{ s}^{-1} \frac{n_{He}}{1 \text{ amagat}} \quad (2.185)$$

where n_{He} is the density of ^3He in amagats (1 amagat is the density of 1 atm at 0 °C). For our typical cells $n_{He} \approx 1$ amagat, rendering this mechanism insignificant. For ^{129}Xe - ^{129}Xe collisions this process has been measured most recently in [49], giving a rate of,

$$\gamma_{bc,Xe} = 5.0 \times 10^{-5} \text{ s}^{-1} \frac{n_{Xe}}{1 \text{ amagat}} \quad (2.186)$$

which again is insignificant in our system. Additionally, there is probably a ^{129}Xe - ^3He binary collision interaction that may be significant for ^3He compared to ^3He - ^3He collisions, but still probably small compared to $\gamma_{1,He}$. However, the depolarization rate from this collisional interaction has not been measured.

In addition to binary collisions, we can also have three body collisions that form temporary molecules, particularly ^{129}Xe - ^{129}Xe molecules. During the lifetime of such molecules there is a coupling between the angular momentum of nuclear spins of the molecule and rotational angular momentum of the molecule, which leads to depolarization. For mixtures of pure ^{129}Xe this has been calculated and measured in [50] to be,

$$\gamma_{m,Xe} = 6.7 \times 10^{-5} \text{ s}^{-1}, \quad (2.187)$$

which can be reduced by the addition of other gases that act as break up agents for the ^{129}Xe molecules (the effectiveness of different gases was also measured in [50]).⁷ While there is also a three-body depolarization mechanism for ^3He , it is believed to be completely dominated by the binary collision mechanism for all densities of interest [48], and in any case is not a significant mechanism in our system.

⁷The scaling of interactions during binary collisions and temporary molecules with different gas densities is discussed in Sec. 2.1.1

Having dispensed with the above mechanisms as being only minor contributors to the observed noble gas depolarization rate, we are left with the poorly understood catch-all, wall collisions, whose detailed mechanisms are still a subject of active research: see the series of articles [51, 52, 53] for a discussion of wall relaxation mechanisms for ^3He ; and [54] for ^{129}Xe with silicone coated walls. In Sec. 2.1.2 we derived the polarization loss rate due to wall collisions for a diffusing gas in the limit that each collision had a very small probability of depolarization,

$$\gamma_{1,wall} = \alpha \frac{\bar{v} A_T}{4 V_T} \quad (2.188)$$

where α is the depolarization probability per collision, \bar{v} is the average thermal velocity, A_T is the total surface area of the cell, and V_T is the total cell volume. Crucially, the wall depolarization rate is independent of the diffusion coefficient in this limit; hence the only way to significantly reduce the rate is to reduce α (assuming the surface area to volume ratio of your cell is close to that of a sphere). The value of α depends on both the strength of the interactions with atoms on the wall and the time it resides on the wall, so not surprisingly, like all other interactions we have discussed, α is much larger for ^{129}Xe than ^3He . To try and reduce α for ^{129}Xe we coat the cell walls with a silane compound called octadecyltrichlorosilane ($\text{CH}_3\text{-(CH}_2\text{)}_{17}\text{-SiCl}_3$) or OTS, whose silane group bonds to the silicon in the glass walls of the cell leaving a long hydrocarbon chain as a buffer that reduces α for ^{129}Xe (OTS and wall losses are discussed further in Sec. 3.1).

2.3.2 Coherence Time T_2

All the effects in the previous section on depolarization contribute to the decoherence rate of the noble gas spins and, in addition, gradients in B_0 inhomogeneously broaden the Larmor frequency, i.e., lead to decoherence. The effect of gradients in B_0 is somewhat mitigated by motional averaging as each atom samples all of the cell multiple times while it diffuses. The effect of motional averaging is calculated by Cates *et al.* in [47] for linear B_0 gradients and we will now use their formalism to calculate the effects for higher order gradients in B_0 .

The formalism in [47] uses second order perturbation theory to calculate the effects of gradients in B_0 on the lifetime of the lowest order diffusion mode of the transverse polarization (the uniform mode) using the specific example of a spherical cell. They begin with a general Hamiltonian made up of a magnetic field generating a uniform Larmor frequency Ω_0 and a non-uniform Larmor frequency Ω_1 ,

$$H = H^{(0)} + H^{(1)} = \hbar\Omega_0 \cdot \mathbf{K} + \hbar\Omega_1 \cdot \mathbf{K} \quad (2.189)$$

where \mathbf{K} is the nuclear spin and the effects of $H^{(1)}$ are perturbative. Hence, they seek a perturbative solution to the general Liouville equation of motion for the density matrix,

$$\dot{\rho} = \frac{1}{i\hbar}[H, \rho] + D\nabla^2\rho \quad (2.190)$$

with the series solution,

$$\rho(\mathbf{r}, t) = \sum_i P_i f_i(\mathbf{r}) e^{-\gamma t} \quad (2.191)$$

where P_i are the eigenpolarizations of the unperturbed Hamiltonian and the index i runs over all polarizations. Cates *et al.* then find the general result for the lowest order perturbation correction to γ by assuming that the unperturbed diffusion modes are completely dominated by the lowest order uniform mode, as is the case in our cells as shown in Sec. 2.2.2. In order to proceed further they use the example of a spherical cell and a linear magnetic field gradient, but we will use a more general field gradient expansion using the solution to Laplace's equation in spherical coordinates (see [41]), which describes any magnetic field in free space using spherical harmonics,

$$\Omega_1 = \sum_{l=1}^{\infty} \sum_{m=-l}^l \Omega_{1;lm} r^l Y_{lm}(\theta, \phi). \quad (2.192)$$

Here we have eliminated terms that diverge at the origin as well as the spatially uniform

term ($l = 0$); and the spherical harmonic coefficients for a generic field can be found from,

$$\Omega_{1;lm} = \frac{l+3}{R^{l+3}} \int_0^\pi \int_0^{2\pi} \int_0^R \Omega_1 Y_{lm}^*(\theta, \phi) r^2 \sin(\theta) dr d\phi d\theta \quad (2.193)$$

where integration is only performed over the spherical cell volume with a radius of R . Using the spherical harmonic basis has two advantages, it matches the spherical harmonics that make up the higher order diffusion modes and it is the basis used to construct coils to generate magnetic field gradients to remove inhomogeneities (as we will see in Sec. 3.2). The result is that the real part of the lowest order correction to γ for the transverse polarization (the imaginary part, which generates a frequency shift, will be discussed in Sec. 2.4) from a general gradient in the magnetic field is given by (following the notation of Cates *et al.*),

$$\frac{1}{T_{2,\nabla B}} = \gamma_{2,\nabla B} = \text{Re} \left(\gamma_{0;11}^{(2)} \right) = \frac{1}{2} \gamma_{1,\nabla B_\perp} + \sum_{l=1}^{\infty} \sum_{m=-l}^l A_l |R^l \Omega_{1z;lm}|^2 \frac{R^2}{D} \quad (2.194)$$

where Ω_{1z} is due to the gradient in B_0 (assumed to be aligned with the z -axis) and $\gamma_{1,\nabla B_\perp}$ is the same as in the previous section (see Eq. 2.184, which does not need to be extended to higher order gradients as it makes a very small contribution to the decoherence rate). The coefficients in the sum above are given by,

$$A_l = \sum_{n=1}^{\infty} \frac{3l^2}{2\pi x_{ln}^4 [x_{ln}^2 - l(l+1)]} \quad (2.195)$$

and the x_{ln} are given by the boundary condition to the diffusion equation,

$$\left. \frac{dj_l(x)}{dx} \right|_{x=x_{ln}} = 0, \quad (2.196)$$

which assumes the walls are non-relaxing. The non-relaxing wall approximation is obviously not true in our cells, but the wall relaxation rate is slow enough that the uniform diffusion mode is an excellent approximation for the unperturbed Hamiltonian and has little effect on the shape of the higher order modes. Additionally, the decoherence effects of the walls

l	A_l	A_l/A_1
1	1.09×10^{-2}	1
2	2.98×10^{-3}	0.273
3	1.25×10^{-3}	0.115
4	6.45×10^{-4}	0.059
5	3.77×10^{-4}	0.035
6	2.39×10^{-4}	0.022
7	1.61×10^{-4}	0.015
8	1.14×10^{-4}	0.011

Table 2.11: Coefficients for the decoherence rate due to magnetic field gradients of order l .

can be added to the decoherence rate of the magnetic field gradients in the same way as it was added in the previous section to the depolarization rate. Although it is possible to exactly calculate the values of A_l as shown by Cates *et al.*, the sum in Eq. 2.195 is roughly made up of terms of $1/x_{ln}^6$ and the difference between successive x_{ln} is roughly π , so the sum rapidly converges and only the first few terms of the sum are necessary for a result accurate to a few percent. The results of a numerical calculation of A_l using the first 40 numerical values of x_{ln} for each l are shown in Tab. 2.11 along with the decrease in the effect on decoherence of higher order gradients relative to linear gradients.

To compare our result to Cates *et al.* we evaluate our result for a linear gradient in one direction,

$$\boldsymbol{\Omega}_1 = \frac{\partial \Omega_{1z}}{\partial z} \mathbf{z} \quad (2.197)$$

where $\partial \Omega_{1z}/\partial z$ is a constant, making the only non-zero spherical harmonic component,

$$\Omega_{1z;1,0} = 2\sqrt{\frac{\pi}{3}} \frac{\partial \Omega_{1z}}{\partial z} \quad (2.198)$$

and giving a decoherence rate of,

$$\gamma_{2,\nabla B} = 0.0457 \left(\frac{\partial \Omega_{1z}}{\partial z} \right)^2 \frac{R^4}{D}. \quad (2.199)$$

This gives us the same result as Cates *et al.*, where they find for a constant linear gradient,

$$\gamma_{2,\nabla B} = \frac{8}{175} (\nabla\Omega_{1z})^2 \frac{R^4}{D} \quad (2.200)$$

and $8/175 \approx 0.04571$. This linear term is also the dominant contributor to the non-homogeneous portion of the magnetic field generated by our solenoid with a fractional gradient of $|\nabla B_0|/B_0 \approx 3 \times 10^{-5} \text{ cm}^{-1}$ in the vicinity of the geometric center of the solenoid.

In the maser, the rate constant that determines its ultimate frequency sensitivity, Eq. 2.170, is not just the decoherence rate, but also the observation time of the spins' precession, which is limited by diffusive escape from the maser bulb. In Sec. 2.1.3 we combined the decoherence rate with the diffusive maser bulb escape rate, G_{MM} , to give an effective decoherence rate, $1/T_2'$. In terms of the mechanisms we have discussed in this section the effective decoherence rate in our cells is dominated by,

$$\frac{1}{T_2'} = G_{MM} + \gamma_{2,\nabla B} + \gamma_{1,\text{wall}}. \quad (2.201)$$

Ideally, therefore, we would reduce the magnetic field gradient contribution to $< 30\%$ of the total such that it does not significantly impact the maser's sensitivity. In our typical cell, this magnetic field gradient requirement is more stringent for ^{129}Xe than ^3He due to the smaller ^{129}Xe diffusion coefficient and bulb escape rate, which offsets its smaller gyromagnetic ratio. For our typical main field of $B_0 \approx 6 \text{ G}$ and using the fractional linear gradient given above we have $|\nabla B_0| \approx 180 \mu\text{G}/\text{cm}$; and for ^{129}Xe in the maser bulb of a typical cell $D_M = 0.22 \text{ cm}^2/\text{s}$ and $R = 1 \text{ cm}$, which gives a clearly unacceptable rate of $\gamma_{2,\nabla B} = 0.4 \text{ s}^{-1}$. To come within 30% of the measured effective decoherence rate for ^{129}Xe of $1/T_2' = 5 \times 10^{-3} \text{ s}^{-1}$ in the absence of magnetic field gradients, we must decrease the gradients to $|\nabla B_0| \approx 10 \mu\text{G}/\text{cm}$. This is achieved experimentally with a set of first and second order magnetic field gradient shim coils, which we estimate can reduce the magnetic field gradient component of the decoherence rate of ^{129}Xe to $\sim 6 \times 10^{-4} \text{ s}^{-1}$ and of ^3He to $\sim 1 \times 10^{-3} \text{ s}^{-1}$ for cells of this size and diffusion coefficients (see Sec. 3.2 for more details).

Presumably there is additional magnetic field gradient decoherence due to higher order field gradients for which shim coils could be developed, although the number of coils necessary to completely eliminate each gradient order grows rapidly. Thus, in summary, our maser's noble gas decoherence rates are not presently dominated by magnetic field gradients; and even smaller effective decoherence rates could be achieved by modifying the cell geometry.

Although it was not used in our work, higher order perturbation theory effects of magnetic field gradients on decoherence rates have also been calculated in [55]. The other common cell geometry, the cylinder, has also been evaluated through slightly different means in [56].

2.4 Frequency Shifts

In addition to constructing a ^3He and ^{129}Xe maser with excellent absolute frequency sensitivity limited by thermal Johnson noise, we must also consider mechanisms that shift the maser frequency away from the Larmor frequency and fluctuations of system parameters that determine these frequency shifts. Such frequency shifts can degrade the maser's frequency sensitivity, especially for slowly modulated signals. We have already considered several frequency shift mechanisms in Sec. 2.2 and we even considered the effects of measured fluctuations in Sec. 2.2.3. Here we reconsider all the shifts given before as well as several new shifts, giving typical fluctuation estimates (see Tab. 2.12), keeping in mind that we are ultimately interested in the comagnetometry signal, $\omega_{M,He} - \gamma_R \omega_{M,Xe}$, which can significantly suppress the effects of common mode system fluctuations. In order to put the size of these frequency shift mechanisms in the context of our typical maser performance, we recall from the end of Sec. 2.2.3 that the experimentally-realized frequency noise spectral density of the dual maser is limited only by thermal Johnson noise for modulation frequencies between 1 mHz and 100 μHz ; and hence no frequency shift mechanism is large enough to limit the maser sensitivity in this regime. However, for slower modulations, less than 100 μHz , the frequency noise has a random walk spectrum caused by some frequency shift

instability. We are particularly interested in the noise amplitude for one modulation over a day, $11.6 \mu\text{Hz}$, where the realized noise density is $\sim 100 \mu\text{Hz}/\sqrt{\text{Hz}}$. If we consider just the random walk component of the frequency noise (the white frequency and phase noise are due to thermal Johnson noise, and so are not relevant) then in the time domain this noise spectrum corresponds to an average peak to peak variation over the course of a day of about $2 \mu\text{Hz}$ in the maser frequency; and it is this level that our frequency shift mechanisms must reach to explain the data. Additionally, in order for an improved version of the ^3He and ^{129}Xe maser to only be limited by Johnson noise for a one day modulation, all frequency shifts must be smaller than $\sim 200 \text{ nHz}$ peak to peak. The scale of variation of some of the parameters that determine the frequency shifts can also be found at the end of Sec. 2.2.3, where we can read off from the random walk dominated power spectra that the transverse polarization in the maser bulb changes by about 1%, as does the longitudinal polarization in the pump bulb; and the temperature in the pump bulb varies by $0.05 \text{ }^\circ\text{C}$, which modifies the diffusive bulb escape rate and hence T'_2 by at most 1×10^{-4} of its value (as before, all variations are peak to peak values over a one day period). Measurements of the stability of T'_2 in non-masing conditions in a typical cell were limited only by measurement noise for ^3He (white noise spectrum) with a fractional limit of 1×10^{-3} , but showed a steady systematic drift for ^{129}Xe at a fractional rate of $3 \times 10^{-3}/\text{day}$ even after the cell had been in the system for ~ 2 weeks. However, once the trend was removed from the ^{129}Xe T'_2 measurements, the noise was comparable to ^3He . Higher SNR measurements of T'_2 would need to be made to determine if there is random walk noise below this current measurement limit.

We begin with the Ramsey shift [57] on a two level system due to an off resonant oscillatory field (for optical regime electric dipole transitions this is usually referred to as a light shift or AC Stark shift),

$$\delta\omega_M = \omega_M - \omega_0 = \frac{\Omega_{R,2}^2}{2(\omega_0 - \omega_2)} \quad (2.202)$$

where ω_0 is the unperturbed maser frequency, ω_2 is the frequency of the second off resonant

field, and $\Omega_{R,2}$ is the Rabi frequency generated by the second field. This is correct in the limit that $|\omega_0 - \omega_2| \gg \Omega_{R,2}$, which is always the case in our experiment. For the comagnetometry signal where each maser acts as the off resonant field for the other we have,

$$\delta(\omega_{M,He} - \gamma_R \omega_{M,Xe}) = \frac{\gamma_{He} \left(\gamma_{He} B_{1,Xe}^2 + \gamma_{Xe} B_{1,He}^2 \right)}{8(\omega_{M,He} - \omega_{M,Xe})}. \quad (2.203)$$

For the typical maser we have been describing in this chapter, the steady state B_1 values are $B_{1,He} = 0.9 \mu\text{G}$ and $B_{1,Xe} = 5 \mu\text{G}$, which means the comagnetometry Ramsey shift is dominated by the field from the ^{129}Xe nuclei and is approximately 10 nHz, which makes it irrelevant given our power fluctuations on a one day time scale are at the 1% level. In addition to the fields generated by the masers there are stray AC magnetic fields, typically 60 Hz power line harmonics, that penetrate our magnetic shields and couple to our resonant circuit. We purposefully tune our masers to avoid these stray fields, but even for relatively small detunings of 10-20 Hz the stray fields are so weak that their Ramsey shifts are only in the range of 10 pHz and hence irrelevant even if they were turned all the way off and on.

A special limit of the Ramsey shift is the Bloch Siegert shift [58] due to the counter rotating term we ignored in the rotating wave approximation made at the beginning of our derivation of the maser equations (Sec. 2.1.3). This field is effectively a rotating field at the negative of the resonant frequency, hence

$$\delta\omega_M = \frac{\Omega_R^2}{4\omega_0} \quad (2.204)$$

and for the comagnetometry signal we have,

$$\delta(\omega_{M,He} - \gamma_R \omega_{M,Xe}) = \frac{\gamma_{He} \left(B_{1,He}^2 - B_{1,Xe}^2 \right)}{16B_0}. \quad (2.205)$$

For our typical maser this has an approximate value of -3 nHz, again making it irrelevant compared to our sensitivity level and signal modulation frequencies.

As discussed in Sec. 2.3.2, diffusion through magnetic field gradients generates both

decoherence as well as a frequency shift. The frequency shift is shown in [47] to be,

$$\delta\omega_{\nabla B} \approx \frac{\gamma R^2}{10} \frac{(|\nabla B_x|^2 + |\nabla B_y|^2)}{B_0}, \quad (2.206)$$

which, for typical values of $\nabla B_x \approx 180 \mu\text{G}/\text{cm}$, $B_0 = 6 \text{ G}$, and $R = 1 \text{ cm}$ yields $\delta\omega_{\nabla B} \approx 3 \mu\text{Hz}$ for ^3He . However, when we consider the overall comagnetometry signal,

$$\delta(\omega_{M,He} - \gamma_R \omega_{M,Xe}) \approx \frac{\gamma_{He} R^2}{10} \frac{(|\nabla B_{x,He}|^2 + |\nabla B_{y,He}|^2) - (|\nabla B_{x,Xe}|^2 + |\nabla B_{y,Xe}|^2)}{B_0} \quad (2.207)$$

we see this magnetic field gradient shift is massively suppressed as both species experience nearly identical gradients and hence is completely irrelevant.

Thus far we have treated our system as existing in an inertial frame, but this is obviously not the case as the surface of the Earth is rotating. Much like in the derivation of the maser equations when we saw that moving in a rotating frame eliminated the effects of the B_0 field; being on the Earth, rotating at a frequency ω_{\oplus} , adds an effective magnetic field to B_0 of ω_{\oplus}/γ which is on the order of 10 nG. Since we are primarily interested in the magnitude of the field and not small changes in its orientation, only the component of the Earth's rotation that is aligned with B_0 has any significant effect (the other components are made irrelevant due to the quadrature sum when calculating the magnitude). Hence, we only care about the z -axis component in the lab frame,

$$\omega_{\oplus,z} = \omega_{\oplus} (\cos(\chi) \sin(\alpha) \cos(\beta) + \sin(\chi) \sin(\beta)) \quad (2.208)$$

where χ is the latitude, α is the angle north of east, and β is the angle of inclination, which gives a comagnetometry signal of,

$$\delta(\omega_{M,He} - \gamma_R \omega_{M,Xe}) = (1 - \gamma_R) \omega_{\oplus,z}. \quad (2.209)$$

In our experiment, located at a latitude of $\chi = 42.37^\circ$, B_0 is roughly aligned east-west,

$\alpha < 0.1$ rad, and horizontally, $\beta < 0.01$ rad, with fluctuations estimated at < 10 μrad over the course of a day. This leads to a total frequency shift of < 1 μHz and an insignificant fluctuation in the maser comagnetometry signal of < 0.1 nHz over a one day period.

A mismatch between the Larmor frequency and the resonant frequency of the circuit leads to a frequency shift in the maser frequency referred to as cavity pulling and derived in Sec. 2.2.1,

$$\delta\omega_{\text{cavity}} = \frac{2Q_c}{T'_2} \frac{\omega_c - \omega_0}{\omega_M}. \quad (2.210)$$

In our typical cell, ^{129}Xe is set to near zero detuning, which means a fractional detuning of $|\omega_c - \omega_0|/\omega_M \approx 2 \times 10^{-4}$ while ^3He has a fractional detuning of 1×10^{-3} giving a shift of < 300 μHz . While it is possible to use comagnetometry to try and suppress the effects of fluctuations in the cavity pulling parameters, it would only be possible for one parameter and would require a level of fine tuning that is better utilized to make the cavity pulling shifts as small as possible. Variations in T'_2 due to temperature instability in the pump bulb only cause a shift of < 30 nHz and so are not a factor. Variation in Q_c is dominated by changes in the resistive loss in the copper wire of the inductors and the thermal coefficient of the resistivity of copper has a fractional value of $3.9 \times 10^{-3}/^\circ\text{C}$, meaning the inductors temperature only needs to be stabilized to $\lesssim 0.2$ $^\circ\text{C}$, which is always exceeded by more than an order of magnitude in our experiment. The resonant frequency of the circuit, however, needs to be stabilized to a fractional value of $< 1 \times 10^{-6}$ to be equivalent to the ultimate maser sensitivity level for one day modulations. The temperature coefficients of the inductors and capacitors that make up the resonant circuit have a fractional value of $< 3 \times 10^{-5}/^\circ\text{C}$ requiring a temperature stability of < 30 m $^\circ\text{C}$ and preferably < 10 m $^\circ\text{C}$, which is challenging, but still exceeded by a factor of 3 in our experiment. However, stray and parasitic capacitances, like coupling to metal shielding and distributed capacitance between the wires of the inductors, tend to be much less stable with respect to temperature, by an order of magnitude or more, or over the course of time and so these capacitances must be minimized to ensure stability.

The static and oscillating magnetic fields generated by the nuclei can shift the maser frequency as shown in Sec. 2.2.1 giving a self field shift of,

$$\delta\omega_{\text{self}} = -\frac{4}{30} \frac{\varepsilon^2}{T'_2 q_c \eta} \quad (2.211)$$

for a uniformly magnetized ellipse with eccentricity ε . For our typical system values and a large estimate for the eccentricity $\varepsilon^2 = 0.3$, corresponding to a 20% elongation of the magnetization along the transfer tube axis, gives a shift of $< 50 \mu\text{Hz}$. There is some suppression of the overall value and fluctuation in the self field frequency shift due to comagnetometry, but it depends on the particular values of ε , T'_2 , and q_c for each species, so we will explore the worse case senario. Variation in the filling factor η is expected to be very small as it is due to geometric factors of stable materials in a temperature stabilized environment; hence it is likely to have fractional changes of $< 1 \times 10^{-6}$ and be irrelevant. We have already established that changes in q_c and T'_2 are too small to generate significant frequency fluctuations for shifts of this magnitude. Changes in the shape of the ensemble as given by the eccentricity, ε , are more diffucult to estimate, but are probably similar to T'_2 and hence are also irrelevant.

During collisions with polarized Rb atoms, noble gas nuclei experience a strong magnetic field that leads to a frequency shift in the maser. This was derived for noble gas nuclei in the maser bulb in Sec. 2.1.1 as,

$$\delta\omega_{Rbc} \approx (k_{ng} - 1) \frac{\mu_0 \hbar}{3} \gamma_{ng} \gamma_{Rb} n_{Rb} \frac{\gamma_{se,Rb}}{\Gamma_{sd}} P_{z,Xe} \quad (2.212)$$

where the enhancement factor, k_{ng} , is about two orders of magnitude larger for ^{129}Xe than ^3He , meaning that comagnetometry does little to suppress the shift on ^{129}Xe . For our typical system parameters the shift on ^{129}Xe in the maser bulb is $\sim 2 \mu\text{Hz}$ and even for large changes in the maser bulb temperature of 10 mK this only changes n_{Rb} by 0.1% and hence implies only a 2 nHz shift. Similarly, a 0.1 K change in pump bulb temperature only leads to a 0.1% fractional change in the Xe longitudinal polarization (via T'_2) and a 0.1%

change in $\gamma_{se,Rb}/\Gamma_{sd}$ due to the change in gas density, and is another irrelevant shift.

As discussed in detail in Sec. 2.2.2, a mismatch in the overlap of the ^3He and ^{129}Xe masing ensembles makes the comagnetometry signal susceptible to frequency shifts from magnetic field gradients,

$$\omega_{M,He} - \gamma_R \omega_{M,Xe} = \gamma_{He} \langle \delta r \rangle \cdot \nabla (B_{ex} + B_{Mz}) + \alpha_r \gamma_R \omega_{M,Xe} \quad (2.213)$$

where,

$$\alpha_r = \langle \delta r \rangle \cdot \frac{\nabla \xi_s}{\xi_s}. \quad (2.214)$$

In our cell the separation between ensembles, $\langle \delta r \rangle$, is along the transfer tube axis (y -axis) with a typical value, as measured by applied field gradients, of $20 \mu\text{m}$. The inhomogeneity in the center of our solenoid along the y -axis leads to a value of $\alpha_r \approx 2 \times 10^{-8}$ and a frequency shift of $\alpha_r \gamma_R \omega_{M,Xe} \approx 400 \mu\text{Hz}$. Fractional fluctuations in α_r can be caused by changes in the solenoid gradient which is estimated at 1×10^{-5} based on the linear coefficient of thermal expansion of $2 \times 10^{-5}/^\circ\text{C}$ for the solenoid (copper on an aluminum form), a temperature stability of $\sim 0.25 \text{ }^\circ\text{C}$, the scaling of the solenoid field per unit current as $1/\text{length}$, and the scaling of the strength of gradients per unit current of order l as $1/(\text{radius})^{l+1}$, which leads to a negligible frequency fluctuation of $\sim 4 \text{ nHz}$. Shifts due to external magnetic field gradients, ∇B_{ex} , include the linear gradient shim coils that oppose the gradients in B_0 contained in the α_r term, hence $\gamma_{He} \langle \delta r \rangle \cdot \nabla B_{shim} \approx -400 \mu\text{Hz}$, and that provide some common mode suppression of changes in the dimensions of the forms holding the electromagnets. However, since the gradient coils are wound on a plastic form (Nylatron) with a high coefficient of thermal expansion, this suppression is largely lost. Variation in ∇B_{ex} due to the magnetic field gradient shim coils has an estimated fractional value of 3×10^{-5} due to thermal expansion and a 1×10^{-5} component due to drifts in the power supply, which again leads to a negligible frequency fluctuation. Additional ∇B_{ex} terms could come from magnetic fields outside of the magnetic shields surrounding the maser and from magnetization of the magnetic shields themselves. We do not have serious estimates for

either of these mechanisms (though we expect them to be small), but they can be reduced if necessary by implementing a magnetic shield design with a higher shielding factor and a solenoid design that includes an electromagnetic shield to reduce the amount of magnetic flux through the shields and hence their level of magnetization. The final magnetic field gradient term, ∇B_{M_z} , is dominated by the gradient from magnetization in the pump bulb, which we approximate as a pure dipole term,

$$\nabla B_{M_z} = \frac{dB_z}{dy} = -\frac{3\mu_0 \hbar \gamma n_P V_P P_{P,eq}}{8\pi |y|^4} \quad (2.215)$$

where the separation between bulb centers, y , is approximately 5 cm. In our case this gradient is dominated by the ^{129}Xe magnetization, which generates a gradient of $0.05 \mu\text{G}/\text{cm}$ leading to a shift of 300 nHz in the comagnetometry signal and a negligible frequency fluctuation of 3 nHz due to magnetization fluctuations. Lastly, we need to consider fluctuations in $\langle \delta r \rangle$, but to do so we need to determine the size of the residual linear magnetic field gradient after the linear gradient shim coils have been used to maximize T'_2 in order to calculate the size of the frequency shift due to all field gradients, $\delta\omega = \gamma_{He} \langle \delta r \rangle \cdot \nabla B$. We estimate the size of residual linear gradients based on the size of the error, $\Delta T'_2$, when maximizing T'_2 ,

$$|\nabla B_0| \approx \frac{1}{\gamma T_2 R^2} \sqrt{\frac{175 D \Delta T_2}{8}}. \quad (2.216)$$

In a typical cell $\Delta T'_2 \approx 3$ s per gradient axis for a 200 s T'_2 for ^{129}Xe , giving $|\nabla B_0| \approx 3 \mu\text{G}/\text{cm}$ per gradient axis and a shift of $20 \mu\text{Hz}$. The fluctuations in $\langle \delta r \rangle$ are probably similar in size to those of T'_2 leading to frequency fluctuations of 2 nHz.

As discussed in Sec. 2.2.2, we wind a set of choke coils around the transfer tube to reduce the coupling of noble gas atoms in the tube to the pick up coil B_1 field, but this introduces a frequency shift in the maser due to the phase shift in the reactive current in the choke coils from their finite resistance. As was calculated in Sec. 2.2.2, we expect the maser frequency shift from the choke coils to be $< 30 \mu\text{Hz}$ and its stability will primarily be limited by the temperature stability of its resistance. The fractional stability of the resistivity of copper

in the coil's temperature environment is $\sim 1 \times 10^{-4}$, which leads to a negligible frequency fluctuation of ~ 3 nHz.

Collisions of polarized ^3He and ^{129}Xe with other atoms and the walls generate chemical shifts in their Larmor frequencies due to perturbations of the electronic structure of the atoms, which changes the diamagnetic and paramagnetic shielding of the nuclear magnetic moment by the electrons (see [59]). For ^3He the fractional diamagnetic shielding is only around 60 ppm (parts per million, 1×10^{-6}), but for ^{129}Xe it is around 7000 ppm [60], so we will only consider chemical shifts involving ^{129}Xe . Collisions between ^{129}Xe and Xe and collisions between ^{129}Xe and N_2 at the 50°C temperature of the maser bulb produce changes in shielding of -0.514 ppm/amagat of Xe and -0.213 ppm/amagat of N_2 ([61] and [62] respectively); while we expect ^{129}Xe and ^3He collisions to have a negligible effect based on theoretical work in [63] comparing the interaction of ^{129}Xe with other noble gases. For the gas densities in the maser bulb of our typical cells we have 0.06 amagats of ^{129}Xe and 0.2 amagats of N_2 , which gives a total change in shielding of -0.07 ppm corresponding to a 1.5 mHz shift in the comagnetometer signal. Fluctuations in the pump bulb temperature will change the fractional gas densities in the maser bulb by $< 1 \times 10^{-4}$ leading to maser frequency fluctuations of < 150 nHz. There is also a change in the shielding due to temperature changes in the gas, but this is very small at our temperatures with a coefficient of 2×10^{-5} ppm/ $^\circ\text{C}$, which is 100 nHz/ $^\circ\text{C}$ for the maser frequency. Collisions with the wall also introduce a chemical shift when the atom is adsorbed onto the wall with a change in shielding of around 300 ppm [64], but each atom only spends a small fraction of its time stuck to the wall, about 1×10^{-6} [54] (for a coated cell with a similar surface area to volume ratio to ours), so the maser frequency shift is < 10 μHz . In the limit that only a small fraction of the atoms are adsorbed onto the wall, the wall shift should be insensitive to gas density since the collision rate onto the wall increases the same amount as the number of atoms in the bulk, so the fraction on the wall stays constant. The wall shift is sensitive to temperature changes; and using the sensitivity to temperature of the absorbed fraction given in [54] gives < 0.5 $\mu\text{Hz}/^\circ\text{C}$ and hence a negligible fluctuation of < 5 nHz for our maximum temperature

Shift Mechanism	Mag. (μHz)	Fluctuation Mech.	Mag. (nHz)
Ramsey	0.01	Laser power & T_P	0.1
Bloch Siegert	0.003	Laser power & T_P	0.03
Inertial Earth Rotation	< 1	Room temperature	0.1
Cavity Pulling	300	Circuit temperature	20
		T_P (T'_2)	30
Self Field	50	T_P (T'_2)	5
Rb Contact Shift	2	T_M & T_P	2
Ensemble Overlap:			
Solenoid Gradient	400	Room temperature	4
Shim Coil Gradient	400	Room temperature	12
^{129}Xe P_P Gradient	0.3	Laser power & T_P	3
Residual Gradient	20	T_P (T'_2)	2
Choke Coil Field	30	T_M	3
^{129}Xe Wall Chemical Shift	10	T_M	5
^{129}Xe -Xe- N_2 Chemical Shift	1500	T_P (n_M)	150
		T_M	0.3

Table 2.12: Maser frequency shift mechanisms and their approximate magnitudes as well as the system parameters that cause the largest frequency fluctuations and their approximate peak to peak magnitudes at a one day modulation. The order is the same as presented in the text.

fluctuation of 10 m°C in the maser bulb.

None of the frequency shifts discussed above and summarized in Tab. 2.12 come close to generating the frequency fluctuations observed in the experiment for modulation periods of a day. In fact, all but one of the shifts are estimated to be at least an order of magnitude lower than the masers ultimate frequency sensitivity and two orders of magnitude lower than the observed fluctuations. Only chemical shifts from collisions of ^{129}Xe with Xe and N_2 are of the same order of magnitude as the maser's ultimate frequency sensitivity. We can check to see if we have accounted for all the frequency shifts by using the values in Tab. 2.7 for the ^3He and ^{129}Xe gyromagnetic ratios and maser frequencies, which gives $(\omega_{M,\text{He}} - \gamma_R \omega_{M,\text{Xe}})/(2\pi) = -2.85 \pm 0.51$ mHz which is slightly higher than our estimate of -1.8 mHz from the ^{129}Xe chemical shift (this raises the ^{129}Xe frequency and hence drops the comagnetometer frequency) and cavity pulling (^3He cavity resonance is below the Larmor frequency), so there could be another mechanism on the order of 1 mHz. Additionally, one

of our inputs could be much less stable than we have estimated, in particular other groups [27] have observed that there is a significant temperature difference (based on measurements of Rb density) when their pumping lasers are on versus off even though there is no observed change in the temperature of the oven surrounding the cell (although we believe we have a reasonable estimate and monitor of the size of the laser heating as explained in Sec. 3.3). Such a mechanism could be the cause of our frequency instability as it would drive maser shifts from the ^{129}Xe chemical shifts, which are far larger than all others. In the case of the cell we used as an example in Sec. 2.2.3, we believe the frequency fluctuations were also influenced by the observed degradation of T'_2 of ^{129}Xe between the start and end of the data set and the associated change in the cavity pulling shift. Since there was no significant change in the T'_2 of ^3He we believe the change in ^{129}Xe was due to slow degradation of the anti-relaxation OTS wall coating. Other possible frequency shift mechanisms for which we do not have good estimates include changes in diffusion coefficients, which affect diffusive coupling of the maser bulb to less stable frequency environments as explained in Sec. 2.2.2.

2.4.1 Modulation to Reduce Drifts

For symmetry tests using the ^3He and ^{129}Xe maser, reducing the effect of drifts and random walks in frequency shifts is possible by modulation of the ^3He and ^{129}Xe spin quantization axis orientation. This can be achieved by either physically rotating the experiment or reversing the B_0 field in place. Modulation of B_0 is advantageous for measuring new physics due to background fields to the universe as it shortens the time scale of interaction with the background field compared to waiting for the Earth to rotate over a sidereal day; but for anomalous spin-spin interactions the spin source orientation can be modulated more easily than the maser as shown in Ch. 5. Modulating the spins' quantization axis works for all frequency shifts that are constant regardless of the direction of B_0 , cavity pulling, self field, collisional, Ramsey, etc.; but not for shifts due magnetic field gradients external to the experiment or the rotating reference frame of the Earth, as these both change sign in the same way as background fields due to new physics when the spins' quantization axis is

modulated.

In practice, changing the orientation of B_0 in place can only be performed infrequently as it introduces large transients in the maser signal, thus it is only really an option for modulation on time scales longer than a day. This means that we are not affected by the Earth's rotation shift; however, modulations on time scales longer than a day only reduce the component of the frequency drift that is coherent with the sidereal day, it has no effect on random drifts, which are our primary concern.

The simplest way to modulate the spins' quantization axis by physically rotating the experiment is flipping the experiment back and forth between two positions, one with B_0 pointing east and the other with B_0 pointing west. It is impractical to try and orient the experiment in an absolute direction to zero out the shift due to Earth's rotation, even determining the actual direction B_0 is pointing would be challenging let alone aligning it relative to the Earth's axis at the level of $100 \mu\text{rad}$. Thus, flipping the spins' quantization axis back and forth will generate a frequency shift due to Earth's rotation at that modulation frequency making it impossible to look for new physics background fields at that modulation frequency. However, since Earth is also rotating through the background field it will produce sidebands separated from the modulation frequency by the sidereal day frequency. In order to make a sensitive measurement at these sideband frequencies we only need a stable and repeatable alignment of the spins' quantization axis in its east and west positions: the positions do not have to be accurate or even exactly 180° opposite each other, they just need to be consistent under repeated reversal. It should be reiterated though, that noise generated by magnetic field gradients external to the experiment is not reduced by this technique and will show up around the frequency that the experiment is modulated.

2.5 Sensitivity and Possible Improvements

As we established in Sec. 2.2.3, the fundamental limit to the frequency shift sensitivity of the ^3He and ^{129}Xe maser operated as a comagnetometer, $\omega_{M,He} - \gamma_R \omega_{M,Xe}$, is due to thermal

Johnson noise in the resonant circuit; and the spectral density of the comagnetometer signal is given by,

$$\sigma_\nu = \frac{\sqrt{k_B T_M}}{\pi} \sqrt{\frac{1}{(T'_{2,He})^2 \mathcal{P}_{He}} + \frac{\gamma_R^2}{(T'_{2,Xe})^2 \mathcal{P}_{Xe}}}. \quad (2.217)$$

In this section we will discuss other noise terms, both technical and fundamental, that can limit frequency sensitivity, as well as simple scaling laws of how to improve the maser's frequency sensitivity, and detection methods other than inductive pickup coils that could improve sensitivity.

2.5.1 Noise Sources

In addition to thermal Johnson noise in the circuit there are other sources of broadband noise that can reduce the maser frequency sensitivity in certain operating regimes: thermal currents in the aluminum form of the solenoid generate fluctuating magnetic fields that contribute to both B_0 and couple directly to the pickup coil; thermal fluctuations in the magnetization of the magnetic shields generate $1/f$ noise in B_0 ; rotational vibrations of the pickup coil generate noise as the coils axis is modulated relative to B_0 ; input noise of the amplifier connected to the resonant circuit; and shot noise. To put these noise sources in perspective, we recall that for our typical maser the measured white frequency noise spectral density of the comagnetometry signal is $\sigma_\nu \approx 15 \mu\text{Hz}/\sqrt{\text{Hz}}$.

Thermal Johnson noise currents generated in the aluminum form of the solenoid (and in the magnetic shields, but the aluminum form is closer to the maser) generate magnetic fields that add white noise to B_0 with a spectral density of [65],

$$\delta B_{z,curr} = \sqrt{\frac{3}{16}} \frac{\mu_0 \sqrt{k_B T} \sigma t}{a} \quad (2.218)$$

for the case of an infinite cylinder⁸ where a is the radius of the form (11.8 cm), σ is the conductivity ($2.7 \times 10^7 \text{ Ohm}^{-1}\text{m}^{-1}$), and t is the thickness (1.5 mm), generating a field of

⁸The infinite cylinder is a good approximation for our solenoid form with a length to radius ratio of 10.

0.6 nG/ $\sqrt{\text{Hz}}$. If our maser had perfect comagnetometry, then it would be unaffected by $\delta B_{z,curr}$, but for small displacements between field measurement points the field fluctuations are still correlated and so the field noise is suppressed by roughly, $\langle \delta r \rangle / a \approx 2 \times 10^{-4}$ leading to a frequency noise of 0.3 nHz/ $\sqrt{\text{Hz}}$, which is clearly irrelevant compared to our typical maser performance. It is not necessary to actually calculate the coupling of the thermal magnetic field noise from the aluminum form to the pickup coil to know that it does not significantly contribute to our existing thermal Johnson noise floor, as we know that there is the same noise power in the form as the circuit, so at worst they exchange the same amount of power back and forth (assuming both are at the same temperature) and some of the maser power is dissipated in the form. However, it is still instructive to estimate the noise level of the thermally generated magnetic field in the transverse direction to evaluate the limits of methods other than a room temperature pickup coil. To calculate the magnetic field generated in the aluminum form that couples to the pickup coil we approximate the transverse orientation of the cylinder as an infinite plane. In this approximation with the pickup coil a distance d above the plane, it is shown in [65] that the dominate magnetic field contribution comes from current flowing in a washer in the plane centered on the pickup coil with an average radius of d and a width of d ,

$$\delta B_{y,curr}(\omega) = \frac{\mu_0}{4\sqrt{2}d} \frac{\sqrt{4k_B T R(\omega)}}{\sqrt{R^2(\omega) + (\omega L)^2}} \quad (2.219)$$

where $R(\omega)$ is the frequency dependent resistance of the washer, and L is the washer inductance given by,

$$R = \frac{2\pi}{\sigma t(\omega)} \quad \text{and} \quad L \approx 1.6\mu_0 d. \quad (2.220)$$

Here σ is the washer conductivity and $t(\omega)$ is the frequency dependent washer thickness,

$$t(\omega) = \begin{cases} t_0 & \text{for } \omega \ll \omega_{skin} \\ \sqrt{\frac{2}{\mu_0 \sigma \omega}} & \text{for } \omega \gg \omega_{skin} \end{cases} \quad \text{where } \omega_{skin} = \frac{2}{\mu_0 \sigma t_0^2} \quad (2.221)$$

where t_0 is the washer thickness at $\omega = 0$ and $\omega_{skin}/(2\pi) \approx 4$ kHz is the frequency at which the skin depth becomes influential. For our system parameters we have $\delta B_{y,curr}(\omega_{M,Xe}) \approx 5$ pG/ $\sqrt{\text{Hz}}$ and $\delta B_{y,curr}(\omega_{M,He}) \approx 2$ pG/ $\sqrt{\text{Hz}}$, which are much smaller than the corresponding Johnson noise in the circuit, which generates fields of 8 and 4 nG/ $\sqrt{\text{Hz}}$ at the ^{129}Xe and ^3He maser frequencies.

In addition to thermal current fluctuations generating magnetic field noise, there are thermal magnetization fluctuations in the high permeability magnetic shields [66, 65], which generate $1/f$ magnetic field noise with a spectral density of,

$$\delta B_{z,magn} = \frac{0.26\mu_0}{r\sqrt{t}} \sqrt{\frac{4k_B T \mu''}{\omega \mu'^2}} \quad (2.222)$$

where r is the radius of the shields (19.1 cm), t is the thickness of the shields (1.5 mm), and μ' and μ'' are the real and imaginary parts of the shields' permeability, respectively. Assuming the material properties of our shields are similar to those in [66] we have $\mu'/\mu_0 \approx 3 \times 10^4$ and $\mu''/\mu' \approx 3 \times 10^{-2}$; and with a comagnetometry suppression of $\langle \delta r \rangle / r \approx 1 \times 10^{-4}$ we find $\delta B_{z,magn} \approx 2/\sqrt{\nu}$ pG/ $\sqrt{\text{Hz}}$, which limits the sensitivity of any measurement over one modulation period to ~ 6 nHz. The $\delta B_{z,magn}$ noise is primarily an issue for day long modulations, which have a sensitivity limit of ~ 50 nHz with our typical maser, meaning this is not currently a limitation, but it is a potential issue for the future.

The heated compressed air that we pass through the oven holding the maser cell to heat it and stabilize its temperature also introduces mechanical vibration of the pickup coil, which leads to a time varying magnetic flux and additional noise in the resonant circuit. In particular, rotation of the pickup coil relative to B_0 leads to a voltage of,

$$V = A_{pu} N_{pu} B_0 \frac{d\theta_{pu}}{dt} \quad (2.223)$$

where A_{pu} is the loop area of the pickup coil, N_{pu} is the number of turns in the pickup coil (with $A_{pu} N_{pu} \approx 2$ m²), and $\pi/2 - \theta_{pu}$ is the angle between the pickup coil and B_0 . As seen in Fig. 2.8 the vibration noise is limited to frequencies below the maser operation. To give

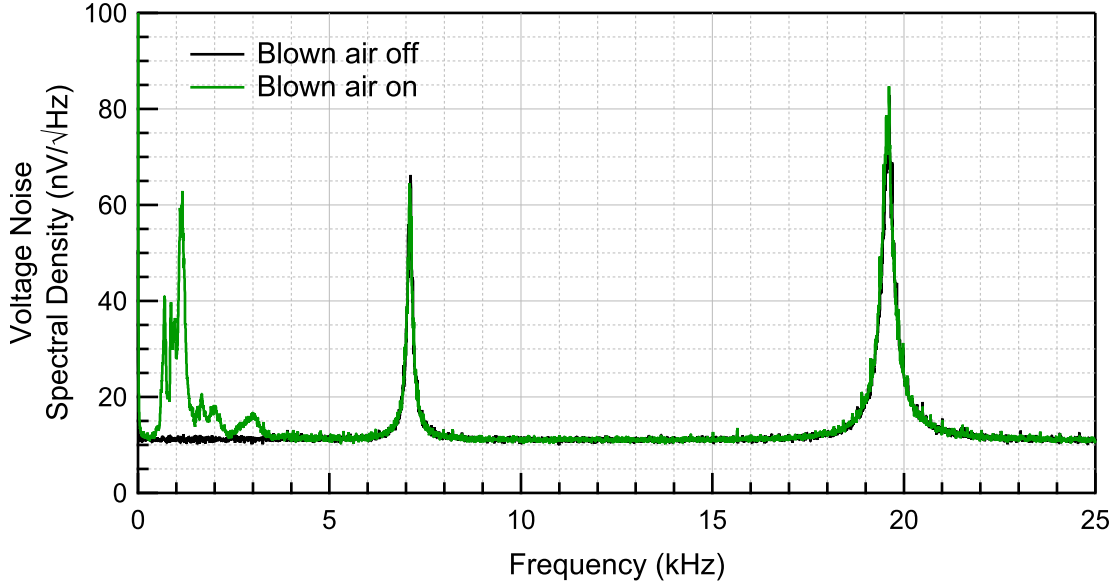


Figure 2.8: Measured spectral density at the input to the amplifier of the resonant circuit with and without the blown air (the masers are not active and 60 Hz harmonic spikes have been removed). The circuit double resonances for ^3He and ^{129}Xe are clearly seen, as well as air flow induced noise.

an idea of the size of the vibrations, we convert the voltage spectrum to angle and then integrate giving a standard deviation of θ_{pu} of order 100 nrad, which, given the radius of the coil ~ 2 cm, means we are detecting vibrations on the order of 1 nm coil displacement.

The amplifier connected to the resonant circuit adds noise in the form of independent voltage and current noise, which must be combined with the thermal Johnson noise to find the total voltage noise floor. At each of the circuit resonances the total voltage noise power spectral density is,

$$S_T = 4k_B T R_{\text{eff}} + \frac{S_V}{q_c^2} + (q_c R_{\text{eff}})^2 S_I \quad (2.224)$$

where S_V and S_I are the amplifier voltage and current input noise power spectral densities respectively. The amplifier we use is an instrumentation amplifier, an INA110, with rated input noise spectral densities of $\sqrt{S_V} = 10$ nV/ $\sqrt{\text{Hz}}$ and $\sqrt{S_I} = 1.8$ fA/ $\sqrt{\text{Hz}}$, which leads to an increase of no more than 2% of $\sqrt{S_T}$ over the pure thermal Johnson noise value.

A more fundamental limit to the maser sensitivity than thermal noise is the shot noise

of the magnetic field generated by the maser. This limits the frequency sensitivity to,

$$\sigma_{\nu,shot} \approx \frac{1}{\pi T'_2} \sqrt{\frac{\hbar\omega_M}{\mathcal{P}}}, \quad (2.225)$$

which for our typical maser gives $\sigma_{\nu,shot} \approx 1 \text{ nHz}/\sqrt{\text{Hz}}$, which is 2×10^4 times smaller than the sensitivity limit from Johnson noise in the resonant circuit. The shot noise SNR is also about 10 times smaller than the SNR limit set by $\delta B_{y,curr}$, so such thermal current generated magnetic fields could be the limiting factor in the case that a shot noise limited detector was used.

2.5.2 Scaling Laws for Sensitivity and Comparisons to Competing Technologies

By only scaling the current system there are two ways to improve the maser frequency sensitivity, increase maser power, \mathcal{P} , and increase coherence times, T'_2 , as per the now familiar frequency spectral density,

$$\sigma_{\nu} = \frac{1}{\pi T'_2} \sqrt{\frac{k_B T_M}{\mathcal{P}}} \quad (2.226)$$

where increasing coherence times has the greatest payoff. In addition to frequency sensitivity we must also consider the scaling of frequency shifts and as we noted in Sec. 2.4, the most sensitive frequency shift is the cavity pulling shift, which already requires a thermal stability of the resonant circuit to $< 10 \text{ mK}$ to avoid limiting the detection of day long modulations. Reaching a thermal stability of the resonant circuit of $< 1 \text{ mK}$ is possible, but beginning to push the technical limit, which means that there will be little practical benefit in increasing the maser power by more than a factor of 100. On the other hand, increasing T'_2 decreases the sensitivity of the maser to cavity pulling in the same way as it increases the maser sensitivity meaning no additional stabilization is required. However, if the system is modulated via rotation as described in Sec. 2.4.1 then increasing T'_2 would require increased time between rotations in order to reach the white frequency noise floor and see any sensitivity improvement and requires stabilization of frequency shifts over longer

time scales whereas increasing the maser power increases sensitivity at all time scales.

To determine the scaling of the maser power, recall from Sec. 2.2.1 that the power is just the energy per polarized nucleus times the arrival rate of polarized nuclei in the maser bulb,

$$\mathcal{P} \approx \frac{\hbar\omega_M}{2} V_M n_M G_{MP} P_{P,eq}. \quad (2.227)$$

In the usual case where the maser is well into saturation, $\tau_{RD} \ll T'_2$, then $P_{P,eq} \approx ST'$ and invoking detailed balance from Sec. 2.1.2 for a lossless transfer tube and expanding T' and S gives,

$$\mathcal{P} = \frac{\hbar\omega_M}{2} V_P n_P \gamma_{se} P_{Rb} \frac{G_{PP}}{\gamma_{se} + G_{PP} + \frac{1}{T}}. \quad (2.228)$$

In the case of ^3He , the diffusive escape rate from the pump bulb is much more rapid than either the spin exchange or depolarization rates, $G_{PP,He} \gg \gamma_{se,He}, 1/T_{He}$, so the power is determined by,

$$\mathcal{P} \approx \frac{\hbar\omega_{M,He}}{2} n_{P,He} P_{Rb} n_{Rb} k_{se,He} V_P. \quad (2.229)$$

To increase the ^3He power we can increase the temperature of the pump bulb to increase the Rb density or increase the size of the pump bulb (with the requisite increase in resonant laser power to keep P_{Rb} close to unity) or increase the density of ^3He atoms by increasing the ^3He fill pressure or increase B_0 to increase ω_M . Increasing temperature is not currently an option as the Rb in the cell tends to react with and ruin the anti-relaxation coating (OTS) we use to increase ^{129}Xe lifetimes once the cell temperature is over ~ 140 °C for a few days and we are already running at ~ 120 °C (see Sec. 3.1 for a further discussion of cell coatings). Increasing the ^3He density by a significant amount is not recommended as it makes the system more susceptible to magnetic field gradients that cause both frequency shifts (see Sec. 2.2.2, although this is not really well understood), and decoherence (see Sec. 2.3.2). Increasing B_0 means that we need higher fractional magnetic field homogeneity to reach the same absolute field homogeneity necessary for long T'_2 times which will probably require higher order magnetic field gradient trim coils. Increasing the volume of the pump bulb

leads to an increase in the size of the system which makes thermal stabilization more difficult as it is easier for thermal gradients to develop across the system, but this is probably not a significant concern for at least a doubling of the pump bulb's linear dimensions. However, the requisite increase in laser power necessary to polarize the greater number of Rb atoms in a larger pump bulb will require a better stabilized laser so that the absorbed laser power thermal load on the cell does not lead to instability.

In the case of ^{129}Xe , the spin exchange rate is faster than the other rates by an order of magnitude. In this limit, $\gamma_{se,Xe} \gg G_{PP,Xe}, 1/T_{Xe}$, the maser power is given by (for a lossless transfer tube),

$$\mathcal{P} \approx \frac{\hbar\omega_{M,Xe}}{2} n_{P,Xe} P_{Rb} D_A \frac{A_t}{L_t}. \quad (2.230)$$

If ^{129}Xe was the only gas in the system, then the ^{129}Xe maser power would not depend on its gas density as $D_A \propto 1/n_{Xe}$ and would only be a function of the geometry of the transfer tube and ω_M (as long as we stay in our usual regime that the diffusive bulb escape time is much longer than the time to cross the bulb). However, since D_A includes contributions from all gases, increasing the gas density of other gases over ^{129}Xe leads to a reduction in ^{129}Xe maser power. In our typical cells the ^{129}Xe diffusion coefficient is dominated by the contribution from ^3He , so for modest increases in the ^{129}Xe density there would be a linear increase in ^{129}Xe maser power. Increasing the ^{129}Xe maser power by increasing the diffusive transfer rate between bulbs by modifying the transfer tube geometry, A_t and L_t , would lead to a decrease in T'_2 due to the faster diffusive bulb escape rate and hence a likely decrease in maser frequency sensitivity. Increasing the density of ^{129}Xe requires an increase in laser power as ^{129}Xe is the dominant contributor to the Rb spin destruction rate (see Sec. 2.1.1). Increasing B_0 to increase ω_M has the same caveats as in the case of ^3He and also makes the chemical shifts of ^{129}Xe larger in absolute terms.

Increasing the length of T'_2 requires reducing each of the three dominant underlying

effective decoherence mechanisms,

$$\begin{aligned} \frac{1}{T_2'} &= G_{MM} + \gamma_{1,wall} + \gamma_{2,\nabla B} \\ &= \frac{3A_t}{4\pi L_t} \frac{D_A}{R_M^3} + \alpha \frac{3\bar{v}}{4} \frac{1}{R_M} + \sum_{l=1}^{\infty} \sum_{m=-l}^l A_l |R_M^l \Omega_{1z;lm}|^2 \frac{R_M^2}{D_M} \end{aligned} \quad (2.231)$$

which have conflicting scaling with respect to R_M and D_M . The greatest unknown is the size of higher order magnetic field gradients generated by the solenoid as their effects grow very rapidly with cell radius, R_M , constraining the advantages gained by increasing the cell radius to reduce the size of G_{MM} and $\gamma_{1,wall}$. Keeping this in mind, an achievable scaling goal would be to increase the bulb volumes by a factor of 4 and hence increase all linear dimensions, except the transfer tube radius, by 1.6. In such a cell we would be able to realize a T_2' of ~ 500 s for each species assuming we could reduce the linear gradients to $< 2 \mu\text{G}/\text{cm}$ and similarly constrain the size of the Larmor frequency change due to higher order gradients across the cell, i.e. $R^l \Omega_{1z;lm}$. The ^{129}Xe T_2' could be increased even further if cells could be reliably made with walls with small α . With these changes ^{129}Xe becomes the limiting factor in the sensitivity, so an increase in the ^{129}Xe density by a factor of two would improve the overall sensitivity without increasing the diffusion coefficients. This system would require 3 W of resonant laser power to polarize the Rb and give maser powers of $\mathcal{P}_{He} \approx 4$ fW and $\mathcal{P}_{Xe} \approx 10$ fW. This leads to a white frequency noise level of $< 1.5 \mu\text{Hz}/\sqrt{\text{Hz}}$ which gives a sensitivity of ~ 5 nHz for modulations with a one day period which is the same size as the $1/f$ thermal magnetization noise floor of Sec. 2.5.1 (here we are assuming that the magnetic field gradient susceptibility of the maser will remain the same, as its origin and scaling are unclear). In order to utilize this lower noise floor it will be necessary to rotate the experiment as described in Sec. 2.4.1 to avoid drifts in frequency shifts and the $1/f$ thermal magnetization noise. The rotation period of the experiment would have to be $> 3 \times 10^3$ s in order to reach the white frequency noise limit, which requires a reduction in the current random walk frequency noise by a factor 2 to 3 to ensure the thermal white frequency noise floor is reached.

How would such a maser compare to the competition? A white frequency noise floor of $1.5 \mu\text{Hz}/\sqrt{\text{Hz}}$ translates into a sensitivity of $5 \text{ nHz}/\sqrt{\text{day}}$ for a sidereal modulation measurement or any other modulation frequency in the white frequency noise regime averaged over a day. The Romalis group's K- ^3He SERF comagnetometer used in [8] had a typical sensitivity of $6 \text{ nHz}/\sqrt{\text{day}}$ in their sidereal modulation measurement, but their ultimate noise floor is actually $0.2 \text{ nHz}/\sqrt{\text{day}}$ which they utilized in their anomalous spin-spin coupling experiment [9]. The Heil group's ^3He and ^{129}Xe free precession comagnetometer detected by a SQUID in [10] does not have a white frequency noise regime, but Monte Carlo simulations show that an optimal measurement can be obtained by measuring for $2 T_2$ and then refreshing the cell (although the decrease in sensitivity changes slowly so that $5 T_2$ is only $\sqrt{2}$ times worse and $10 T_2$ is 2 times worse) which gives a sensitivity of approximately,

$$\frac{1}{2^{3/2} T_2 \text{SNR} \sqrt{T_d}} \quad (2.232)$$

per $\sqrt{\text{day}}$ where SNR is their signal to noise ratio per $\sqrt{\text{Hz}}$ when the FID starts and T_d is the length of the day. The Heil group's system [10] has $\text{SNR} \approx 1000$ and $T_2 \approx 1.5 \times 10^4 \text{ s}$ for ^{129}Xe with much better numbers for ^3He , so we have to scale the above sensitivity by γ_R , which gives a sensitivity of $0.2 \text{ nHz}/\sqrt{\text{day}}$ (very similar to the Romalis group's K- ^3He system). Competing against systems whose promise is ~ 25 times better than the promise of a substantial reworking of our ^3He and ^{129}Xe maser is probably not a wise investment.

2.5.3 Changing Detection Methods

An even more radical step for possible improved performance would be changing detection methods of the maser frequency from a room temperature inductive coil to a cryogenic system or a third, lower noise AC magnetometer. A cryogenic system would involve cooling the resonant circuit to lower its thermal noise floor, with a 4 K temperature giving a factor of 9 improvement in maser SNR. The resonant circuit does not have to have high Q, in fact, a Q similar to the current system would be ideal to avoid excessive cavity pulling. The

cryogenic coils would also have to be shielded from inductive coupling to metal surfaces at room temperature as this would increase the noise in the circuit.

Adding a more sensitive AC magnetometer to the system with a separate feedback coil is more difficult to quantify as it depends on proximity of the magnetometer to the cell. However, we can look at some of the scaling properties of introducing such a detector, which is typically characterized by its detection noise floor for AC magnetic fields over a frequency range: e.g. the SQUID used in [10], which has a white noise floor of ~ 2 fT/rtHz for modulations between 20 and 100 Hz. First, we determine the noise floor of our pickup coil by calculating the RMS magnetic field that generates an SNR of 1 per $\sqrt{\text{Hz}}$ as given by the ratio of the RMS voltage generated in the pickup coil to the Johnson noise voltage,

$$\delta B_c = \frac{\sqrt{4k_B T_M R_{\text{eff}}}}{A_{pu} N_{pu} \omega_M} = \xi_0 \sqrt{\frac{4k_B T_M}{\omega_M L_{pu} q_c}}, \quad (2.233)$$

which gives 10-15 fT/ $\sqrt{\text{Hz}}$ at our maser frequencies. We can now write our standard ultimate thermal frequency noise floor in terms of the coil AC magnetic field detection noise floor or more generally the noise floor of any detector,

$$\sigma_\nu = \frac{1}{\pi T_2'} \sqrt{\frac{q_c \omega_M \frac{1}{2\mu_0} \delta B^2 V_M}{\mathcal{P}}}, \quad (2.234)$$

where the filling factor, η , in this case includes both the field overlap of the feedback coil with the cell and the field overlap of the magnetometer with the cell and q_c is a measure of the gain necessary to bring the maser well above threshold. The disappointing aspect is that, all other parameters being the same, the SQUID only brings a factor of 7-5 improvement in the noise floor, less than just a cryogenic pickup coil. However, the frequency noise floor is now independent of the maser frequency ($\mathcal{P} \propto \omega_M$) as we would expect when treating the magnetic field detection limit as a constant since the magnetic field generated by the maser does not change with ω_M . This means that much lower B_0 fields can be used making it much easier to minimized field gradients for long T_2' s and reducing the chemical shifts of

^{129}Xe . Basically, in the quest for ultimate sensitivity, all the scaling possibilities point in the direction already taken by [10] where they have gotten around our bottleneck of bulb escape limiting T_2' by having a single sealed bulb. Thus, our double bulb approach is unlikely to be competitive with their ultimate sensitivity.

Chapter 3

Experimental Realization

In Chapter 2 we discussed all the required elements for a dual noble gas maser as well as many of the particulars of our implementation including dimensions, temperatures, and gas pressures of the double bulb glass cell that holds the noble gases, properties of the doubly resonant feedback circuit, as well as the magnetic fields in the system. In this chapter we will discuss the manufacture and/or characterization of the primary components of our system. The experimental apparatus used for the work described in this thesis is only moderately changed from the system described in the previous thesis regarding this experiment [25], so we only give summaries of those areas previously described in detail and concentrate on improvements to and improved understanding of the apparatus.

The experiment is made up of six main subsystems: a sealed glass double bulb cell containing ^3He , ^{129}Xe , and N_2 gases and Rb metal, an oven to hold the cell and heat the pump bulb while keeping the maser bulb cool and all temperatures stable, a laser system to optically pump the Rb vapor, a stable doubly resonant circuit tuned to both maser frequencies, a stable and homogeneous magnetic field environment, and a detection system to measure and record the maser frequencies. A schematic representation of all of these subsystems is given in Fig. 3.1, which shows two components that we have not discussed yet, the stabilization of the total laser power and the monitoring of the Rb magnetization, which we will discuss in Sec. 3.4. In Fig. 3.1, LCVR is a liquid crystal variable retarder,

PBC is a polarizing beam splitter cube, and ESR is electron spin resonance.

3.1 Double Bulb Maser Cells

Our double bulb maser cells are made by a scientific glass blower¹ out of borosilicate glass (e.g., Pyrex) attached to a glass manifold that allows us to clean the cells, apply the OTS wall coating (the effects of which are discussed in Sec. 2.3.1), evacuate them, introduce Rb metal, add noble gases and nitrogen, and then seal the cells. The cells and manifold are shown in Fig. 3.2 where the two small open tubes opposite the cells allow access to the cells with a long pipette to introduce and remove liquids, the vertical sidearm of the manifold holds the Rb metal ampule, and the opening at the left is for attaching the manifold to the vacuum and gas handling system. In brief, the cells are cleaned with an acid solution, rinsed, dried, coated with a solution containing OTS, rinsed to wash off the excess OTS, and then baked in an oven to drive off any excess solvent. At each stage, the liquids have to be pipetted into and out of the cells due to the narrow pinch off just above the cell (which aids in sealing the cell) and the narrow transfer tube. Next, an open ampoule of Rb metal is added to the sidearm and all the access tubes are sealed except for the left hand one which is attached to the vacuum and gas handling system via an ultra-Torr seal. The manifold is then pumped on by the vacuum system which has a base pressure of $\sim 1 \times 10^{-9}$ Torr. A temperature sensor is placed on the bottom of one of the maser bulbs (this is expected to be the hottest point) and a makeshift oven is constructed around the manifold out of thick aluminum foil which is then wrapped with heater tape, more aluminum foil, and fiberglass insulation. The sidearm containing the Rb is not placed inside the oven and is kept cool with a small fan to avoid evaporating the Rb. The oven temperature is then raised to ~ 150 °C and left for several days while the pressure of the vacuum system is monitored. Once the vacuum system pressure has stopped going down, typically in the low 10^{-8} Torr, the oven is removed and a macroscopic quantity of Rb (~ 100 mm³) is chased into the cells using a

¹Most recently, Yankee Glassblower, Concord MA.

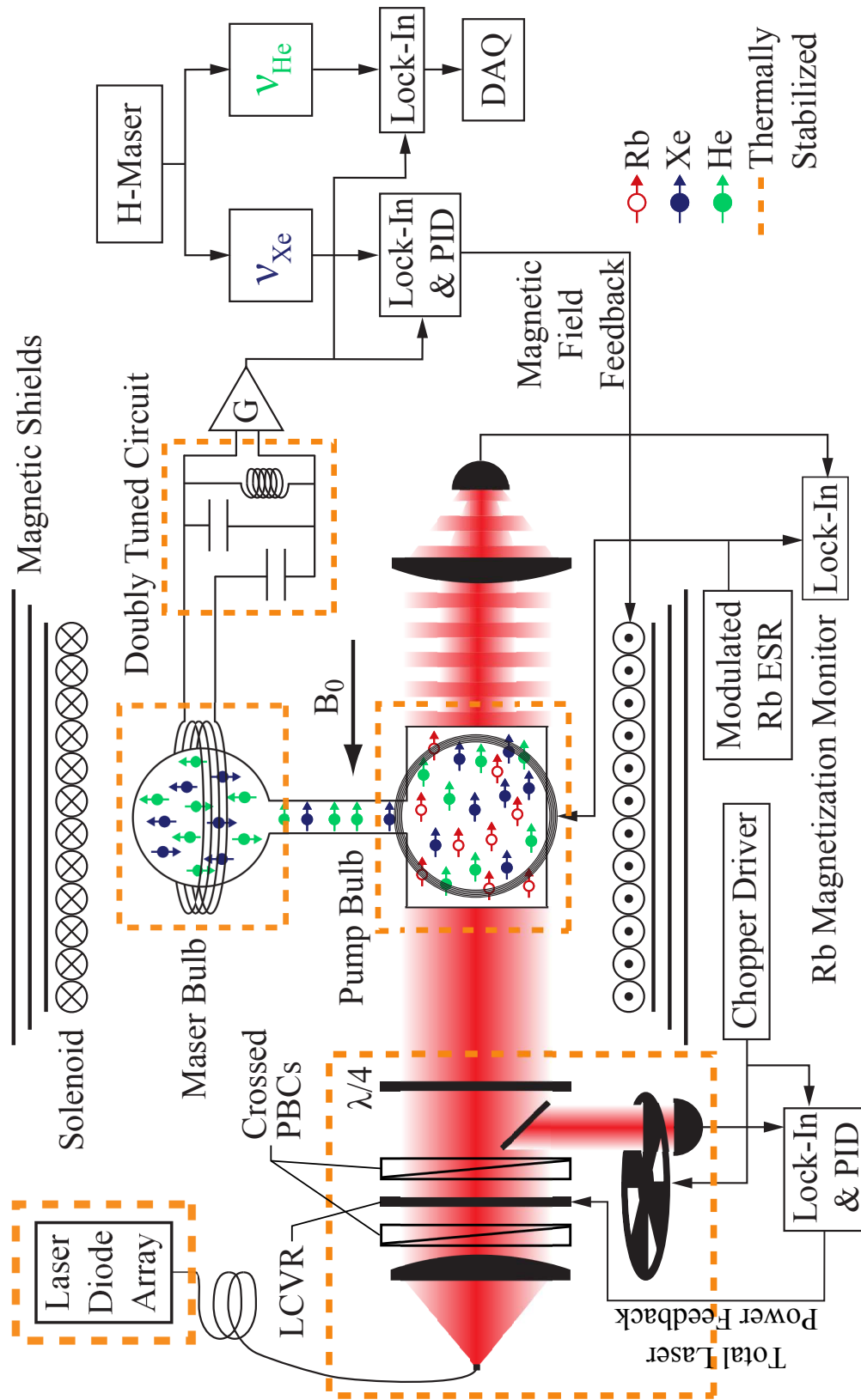


Figure 3.1: Schematic of major ^3He and ^{129}Xe maser subsystems (not to scale).

heat gun by sequential evaporation and condensation on the manifold walls. Sufficient Rb is chased into the tubes above the cells such that it will roll down the tube into the cell, so that when the cell is operated as a maser the Rb is not quickly depleted, as Rb vapor is effectively chased out of the pump bulb due to the large temperature gradient between it and the maser bulb. After Rb has been introduced into the cells the pinched region near the Rb sidearm is sealed with a torch and the sidearm is removed to avoid any contaminants that might move from the sidearm (which was not baked out) into the maser cells once the manifold is gated off from the vacuum system and gases are introduced. The cell manifold is calibrated with respect to the gas handling system as described in [25] and filled with ^{129}Xe , ^3He , and N_2 ; and then sealed at the pinched region above the pump bulb and pulled off the manifold.²

Our cells have several potential longevity problems: loss of Rb from the pump bulb due to condensation in the cooler regions of the cell; diffusion of ^3He out of the cell through the glass (especially when the pump bulb is heated); and damage to the OTS coating due to reactions with Rb. The loss of Rb has been solved by simply adding enough Rb to the pump bulb that the supply cannot be exhausted over any reasonable time span (this is enough Rb that it can be rolled around the cell, on the order of 100 mm^3). Helium will diffuse through borosilicate glass, and much more rapidly at higher temperatures, such that we observe a decrease in ^3He maser power by about half after the cells have been kept at $120\text{ }^\circ\text{C}$ for 6 months (see older work on He diffusion with multiple glasses in [67] and more recent numbers in [51]). This could be solved by use of aluminosilicate glasses (e.g., GE180), which are more dense and have much lower effective ^3He diffusion coefficients, especially at raised temperatures. Thicker walls in the pump bulb region is another possibility, but the escape rate only decreases linearly with thickness.

In all recently manufactured cells in our lab the wall coating has been damaged when

²The one deviation from the procedure described in [25] is that the ^3He should be added after the ^{129}Xe and the filling region in the gas handling system only needs to be filled with ^3He at the pressure needed just before the cells are pulled off. This takes several rounds of moving gas through the valve system of the gas handling system, but maximizes the use of ^3He , which is fantastically expensive (currently \$1,000 per liter atmosphere).

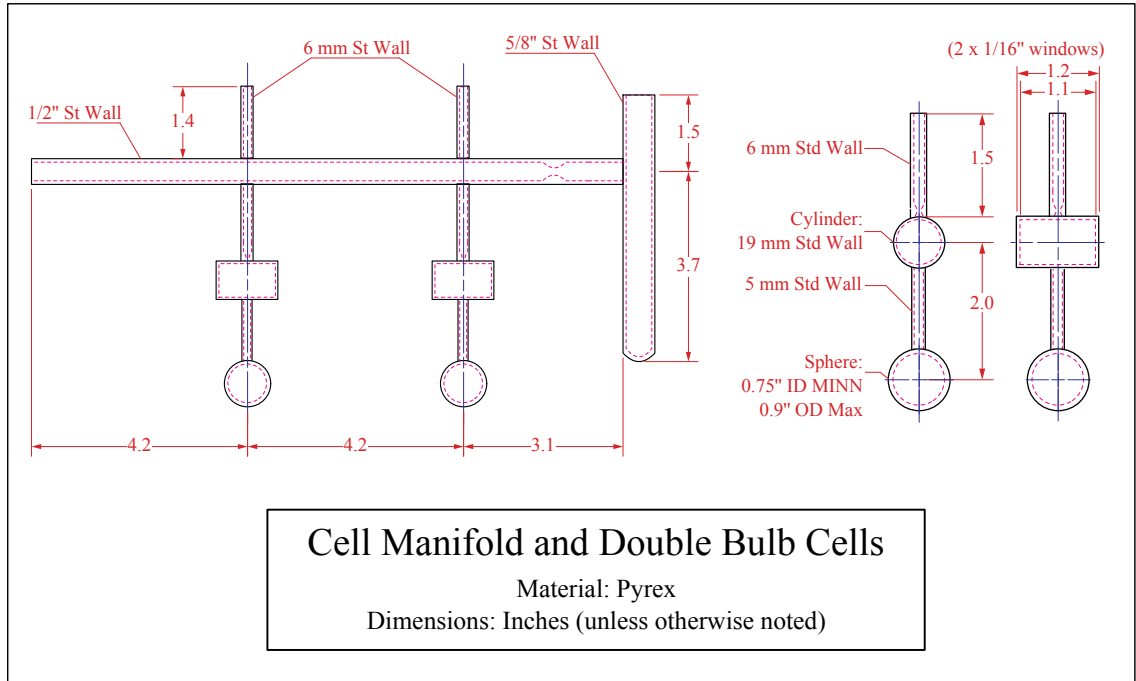


Figure 3.2: Double bulb cell and manifold schematic.

operated in the maser, as observed by a slow decrease in the ^{129}Xe T_2' , T_1' , and maser power, while ^3He parameters have remained unaffected. This wall coating degradation has occurred over the time scale of days to a few weeks after the cell has been placed into the oven and brought to temperature. The cause for this decay is unknown, but the Heil group, in [10], have produced bare (uncoated) glass cells out of GE180 that exhibit ^{129}Xe polarization relaxation per wall collision 30 times smaller than one of our typical successfully coated cells, so moving to such an aluminosilicate glass could solve both the ^{129}Xe wall relaxation and ^3He leak problems. Our inability to coat cells successfully that will operate at 120°C with Rb, and even those which are successfully coated fail after a day at temperatures above $\sim 140^\circ\text{C}$, is confusing as the Romalis group, in [68], has coated Pyrex cells with OTS that exhibited no problems up to 160°C in the presence of Rb using a procedure adapted from ours [69]. In [69] they also showed that our procedure did not lead to a monolayer of OTS on the silicon wafers they used, but rather was twice as thick as a single layer coating, and that coatings produced with our procedure changed over time and with temperature more

than the monolayer coatings they produced, but were also more effective in suppressing relaxation (at least of the electronic spins in K they were testing).

Resolving the coating degradation issue is critical to moving forward with the maser. Almost a year was spent making cells after completely replacing all the chemicals involved in the coating and cleaning process, increasing the temperature and/or time that the cell manifold is baked out on the vacuum system to remove contaminants, and testing all the input gases and monitoring for any unusual contaminants during the manifold bake out with a mass spectrometer that was attached to the vacuum system. Ultimately all these attempts were unsuccessful and the impending advancements in tests of new spin physics made by the Romalis group, [9] and [8], made the immediate resolution of our cell coating problem moot.

3.2 Magnetic Field Control

There are three main elements to controlling the magnetic fields experienced by the maser, the high permeability magnetic shields, the solenoid which generates B_0 , and the first and second order magnetic field gradient coils to improve the field homogeneity. The magnetic shields and solenoid dimensions are shown in Fig. 3.3. The magnetic shields were measured to have a longitudinal shielding of ~ 300 and a transverse shielding of 2×10^4 , with the low longitudinal shielding attributed to the large access holes at either end of the shield [25]. However, the maser is only sensitive to field gradients, and we did not characterize the efficacy of the magnetic shields in reducing external field gradients. The solenoid (constructed from 5 mm copper wound on an aluminum cylindrical form) produces a field of a few gauss (typically 6 G for the maser results described here) when driven by a homemade current supply that delivers ~ 50 V and ~ 0.25 A to the solenoid, with a fractional stability of $< 1 \times 10^{-5}$ for typical room thermal stability of 0.2 °C. The three first order magnetic field gradient coils are single turn coils wound along machined groves in a cylindrical Nylatron form that slides inside the solenoid form. The five second order coils are single turn coils

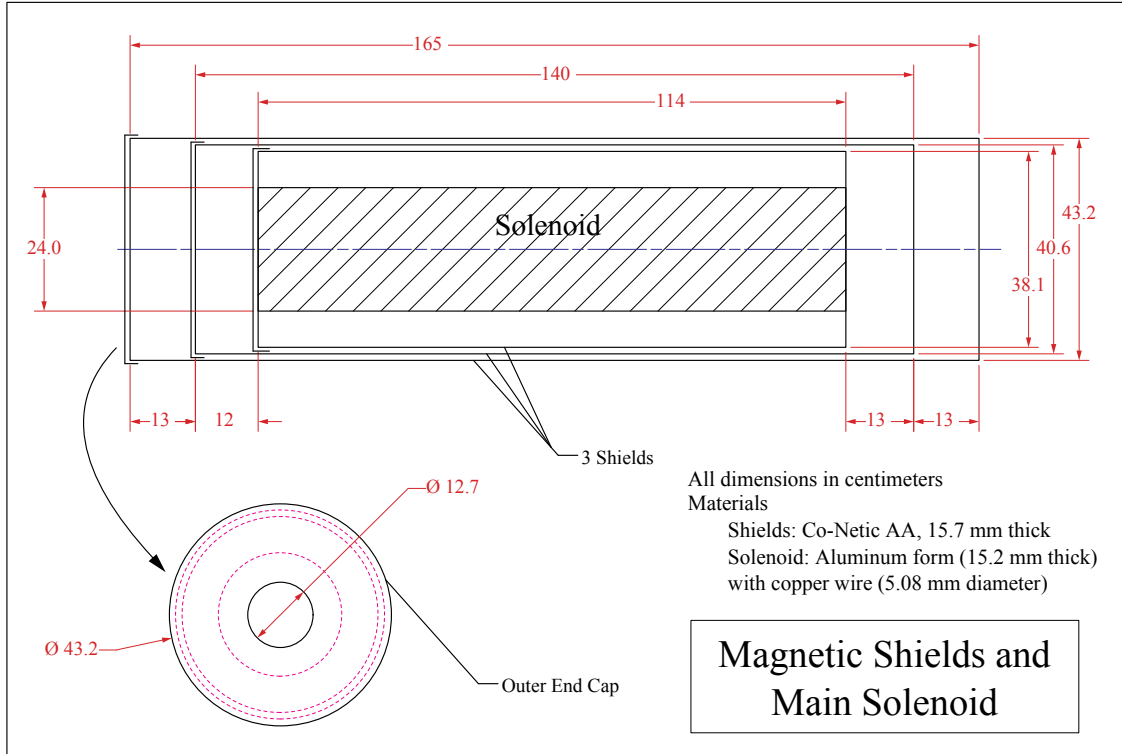


Figure 3.3: Magnetic shields and solenoid schematic.

epoxied directly onto the solenoid. All the gradient coils are driven by home made current supplies with currents in the range of 10 mA and a fractional stability of $< 1 \times 10^{-5}$ in our room. The designs for both the first order and second order coils can be found in [70]. The strength of the gradients generated by the coils can be expressed in several ways, but here we have chosen the spherical harmonic basis set, $Y_{l,m}$, (assuming each coil's geometry exactly conforms to its design specification) in order to match the theory for the decoherence rate due to field gradients from Sec. 2.3.2.³ The usual spherical harmonics are complex functions, but we can only have real fields, so we generate a new basis of functions, $T_{l,m}$, in

³The basis used to describe the gradient coils is not the same basis as used in [25], so there is a difference in reported gradient strength, but the linear gradient coils are exactly the same.

$T_{l,m}(l, m)$	Cartesian Coordinates	Gradient Strength	Units
(1, 0)	$\frac{1}{2}\sqrt{\frac{3}{\pi}} z$	12	$\mu\text{G}/\text{cm}/\text{mA}$
(1, ± 1)	$\frac{1}{2}\sqrt{\frac{3}{\pi}} x, \frac{1}{2}\sqrt{\frac{3}{\pi}} y$	14	$\mu\text{G}/\text{cm}/\text{mA}$
(2, 0)	$\frac{1}{2}\sqrt{\frac{5}{\pi}} \left(z^2 - \frac{(x^2+y^2)}{2} \right)$	1.8	$\mu\text{G}/\text{cm}^2/\text{mA}$
(2, ± 1)	$\frac{1}{2}\sqrt{\frac{15}{\pi}} zx, \frac{1}{2}\sqrt{\frac{15}{\pi}} zy$	0.59	$\mu\text{G}/\text{cm}^2/\text{mA}$
(2, ± 2)	$\frac{1}{2}\sqrt{\frac{15}{\pi}} xy, \frac{1}{4}\sqrt{\frac{15}{\pi}} (x^2 - y^2)$	1.0	$\mu\text{G}/\text{cm}^2/\text{mA}$

Table 3.1: Magnetic field gradient coil strengths.

the following way,

$$T_{l,m} = \begin{cases} \frac{-1^m(Y_{l,m}+Y_{l,m}^*)}{\sqrt{2}} & \text{for } m > 0 \\ Y_{l,m} & \text{for } m = 0 \\ \frac{i(Y_{l,m}-Y_{l,m}^*)}{\sqrt{2}} & \text{for } m < 0 \end{cases} \quad (3.1)$$

which gives an orthonormal basis of real functions that has the same A_l coefficients given in Eq. 2.194 for calculating the decoherence rate due to field gradients. The strength of our gradients coils in terms of the $T_{l,m}$ functions is given in Tab. 3.1. We optimize the field homogeneity by disengaging the pickup coil from the rest of the resonant circuit and then applying short, resonant rf pulses to the ^3He and ^{129}Xe and measuring their T_2' decay time, typically referred to as a free induction decay or FID (this is discussed in more detail in Sec. 3.5 and Sec. 3.7). We then systematically change the current going through each gradient coil until we have maximized T_2' . Unfortunately, the first and second order gradients do not overlap perfectly, so the second order gradients produce some first order component and the first order gradients must be re-optimized after the second order gradients. The measured FID decoherence rate ($1/T_2'$) follows the expected quadratic behavior with respect to the magnetic field gradient magnitude for both the first and second order gradients, but we find that for both ^3He and ^{129}Xe the coefficients are consistently twice as large as we would expect from Eq. 2.194 for the first order gradients and ten times as large for the

second order gradients. Some of the error for the second order gradients is probably due to the fact that they have a linear component as well, but these discrepancies have not been characterized in detail.

In practice, for our typical cells there is an increase of $\sim 25\%$ in T'_2 when trimming the fields with the second order gradients in addition to the first order gradients leading to T'_2 times of ~ 90 s for ^3He and ~ 200 s for ^{129}Xe for the experimental parameters in Tab. 2.1 and Tab. 2.6. The repeatability of T'_2 when replacing the cell in the oven or otherwise disassembling and reassembling the experiment is also improved when the second order gradients have been optimized. We were able to better observe improvements in T'_2 using the second order gradients by making a cell that was the same as our typical cells, but had a much narrower transfer tube and hence a much slower diffusive bulb escape rate (this cell was produced during the period we were trying to diagnose our cell coating degradation problems, see Sec. 3.1, so it did not have a long ^{129}Xe T'_2 and its maser performance could not be tested). In this cell we achieved ^3He T'_2 times of ~ 170 s with just the first order gradients and ~ 280 s with both first and second order gradients, which was not bulb escape limited as the diffusive escape time for the ^3He longitudinal polarization, $1/G_{MM}$, was measured to be ~ 430 s (see Sec. 3.7 for the details of how this is measured). This suggests that for our typical cells and gas pressures, the magnetic field gradient component of the effective decoherence rate, $1/T'_2$, due to gradients above second order is $\sim 6 \times 10^{-4}$ s $^{-1}$ for ^{129}Xe and $\sim 1 \times 10^{-3}$ s $^{-1}$ for ^3He .

The final level of magnetic field control is a small solenoid that we wind directly on the pump bulb. It is used to generate a field of ~ 100 μG to shift the ^3He Larmor frequency in the pump bulb far away from the maser frequency relative to $1/T'_2$ to avoid the frequency shifting effects described in Sec. 2.2.2. The pump bulb solenoid is driven by the same type of current supply as the gradient coils. The pump bulb solenoid generates a small field gradient at the maser bulb, so it is energized before any careful field trimming is attempted.

3.3 Maser Oven and Thermal Control

There are three regions that require high temperature stability: the pump bulb, the maser bulb, and the doubly resonant circuit. The double bulb cell with its pump and maser bulbs is housed inside an oven, shown schematically in Fig. 3.4, which is placed inside the gradient coil form and solenoid such that the maser bulb is centered vertically and the pump bulb can be accessed optically through the hole in the magnetic shields. The oven is made out of Ultem, a plastic that can be continuously operated at up to 170 °C, with each bulb surrounded by a boron nitride ceramic block whose large thermal mass and conductivity provide a stable and uniform temperature. The boron nitride blocks are heated by blown air flowing through manifolds in the oven surrounding each block. The pickup coil was wet wound with epoxy (Stycast 1266) and placed around the ceramic block surrounding the maser bulb⁴; and a set of quasi-Helmholtz coils, referred to as the Rb drive coil, were wound in grooves on the block surrounding the pump bulb to enable detection of the Rb magnetization as well and the ³He and ¹²⁹Xe polarizations (see Sec. 3.4 and Sec. 3.7 respectively).

The feedback scheme to stabilize the temperature of each boron nitride block is shown in Fig. 3.5. The temperature of the air in the manifolds surrounding the boron nitride blocks as well as the blocks themselves are measured with platinum RTDs (Omega series PT100KN) connected by twisted three wire cables to resistive Wheatstone bridges that are driven and sensed with lock-in amplifiers. The temperature of each block is stabilized using analog PID controllers in a cascade lock configuration where the feedback from the block is used to offset the error signal from the air temperature, which then determines the feedback to the heater. Thus, at short time scales the air temperature is stabilized to the bridge set point combined with the effectively fixed offset from the block feedback and over long time scales the air temperature set point is shifted to stabilize the block temperature. With this

⁴The initial attempt to directly wind the pickup coil on the ceramic block form broke off the thinner side of the form, so the coil had to be wet wound on a separate form and then placed on the ceramic block form which was then epoxied back together.

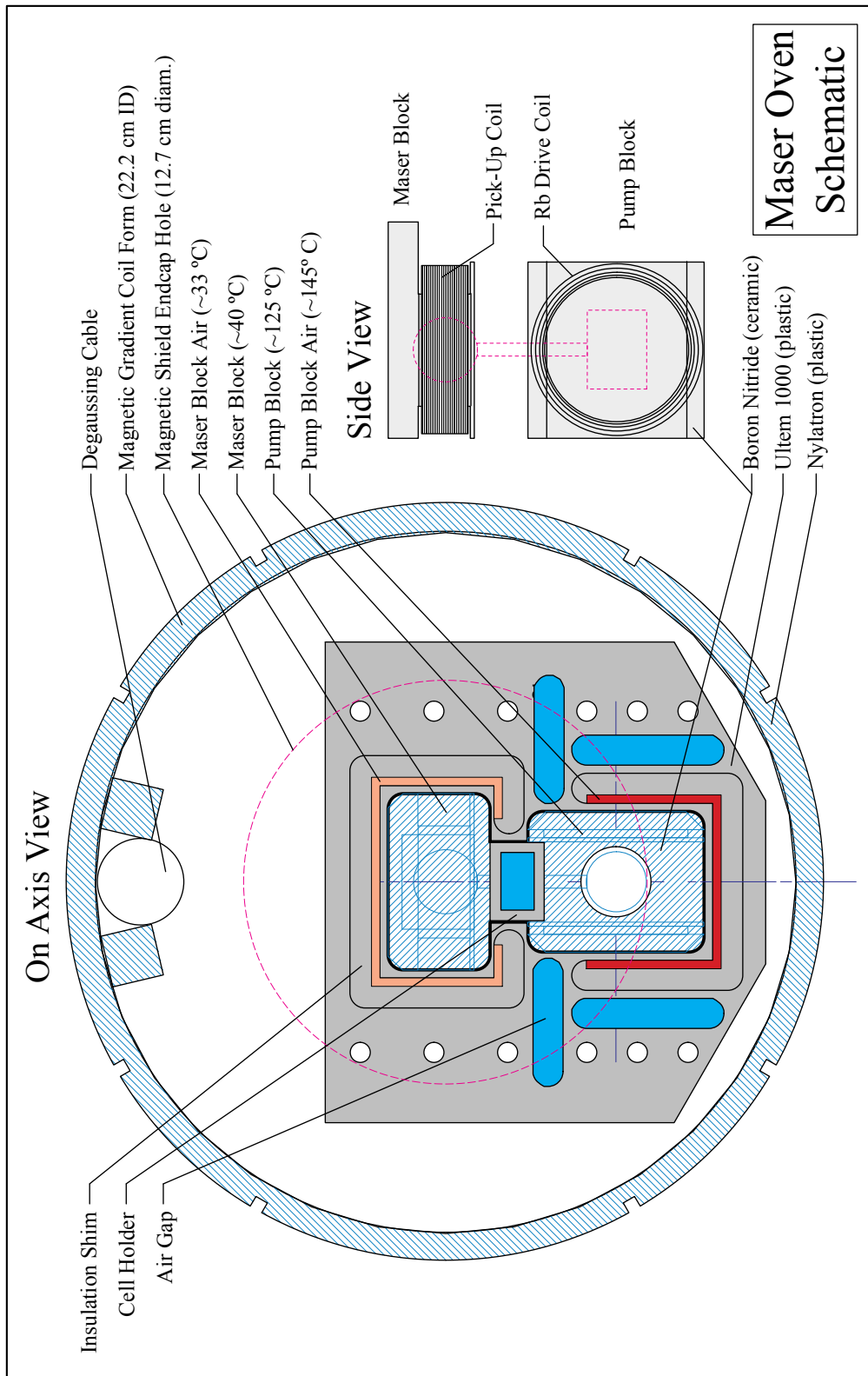


Figure 3.4: Maser oven schematic.

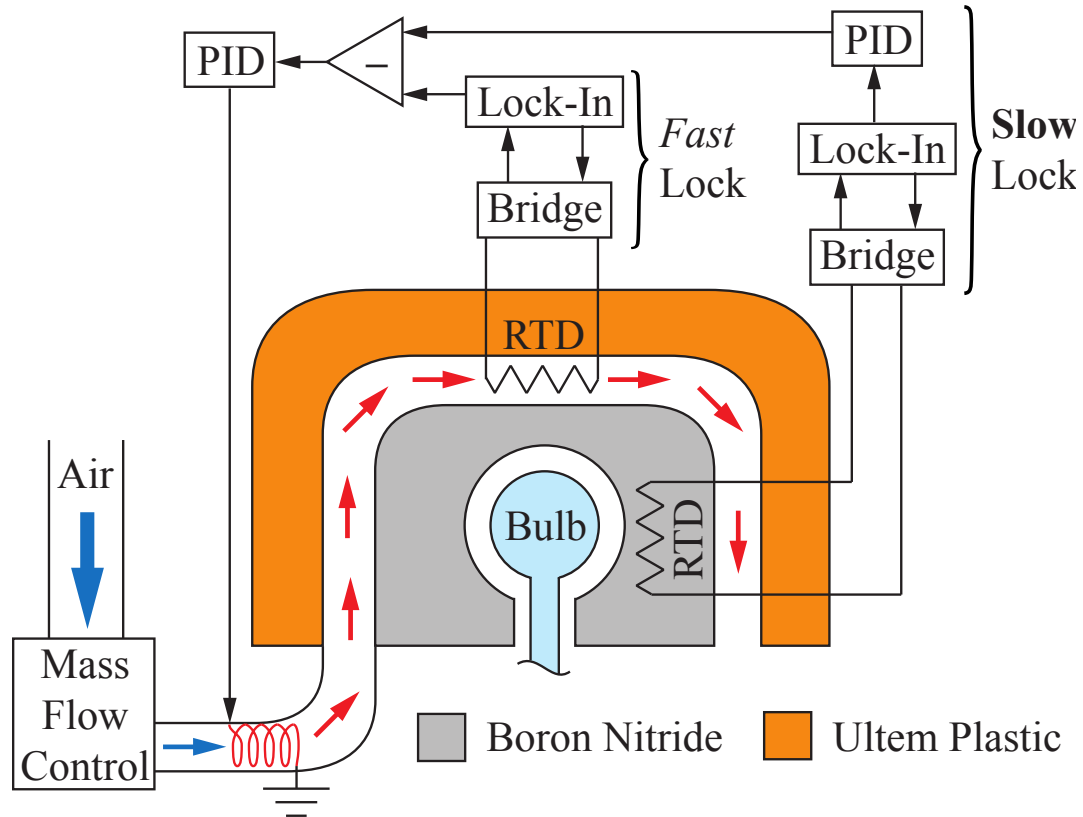


Figure 3.5: Feedback system to stabilize the oven temperature using a cascade locking scheme.

locking scheme we are able to achieve temperature stabilities of ~ 1 mK over the course of a day inside the pump and maser bulbs based on a dummy cell fitted with temperature sensors. However, with the optical pumping laser on we believe this stability is significantly reduced, due to the instability in the laser spectrum, which changes the amount of absorbed resonant laser power, and the small thermal conductivity between the pump bulb and its block due to the air gap, which leads to a significant temperature gradient. This instability can be observed on the temperature of the air in the manifold around the pump bulb block as there is a similar temperature gradient between the air and the block as between the block and the bulb, so the change in temperature of the bulb is similar to the change in temperature of the air (assuming the ambient temperature outside of the oven remains relatively stable). This is easiest to observe when the laser is first turned on and the air

temperature reduces by ~ 5 °C to compensate and keep the block stable. By turning the laser on and off when the pump bulb is a relatively cold 80 °C and the Rb density is low and hence absorbs little laser power, compared to when it is at the full operating temperature, we find that about a third of the heating is due to resonant light while the rest is due to light being scattered by the cell. In particular, it is difficult to fill the cell with light and not impinge somewhat on the pump bulb solenoid. Using data from the air manifold RTD indicates the pump bulb is only stable to ~ 50 mK over the course of a typical day.

The resonant circuit, other than the pickup coil, is suspended in the center of a sealed PVC cylinder surrounded by fiberglass insulation and bolted to a Nylatron cylindrical shell which fits inside a second, smaller, set of 3 nested cylindrical magnetic shields.⁵ Blown air passes through the PVC cylinder impinging directly on the circuit with an RTD placed in the air flow behind the inductor and connected to a similar type of temperature control setup as the maser oven: a Wheatstone bridge driven by a lock-in with PID feedback to a heater, but without the cascade lock. We have verified, using a four wire thermistor driven by a homemade precision current source and placed ~ 10 cm away from the RTD, that the air temperature in the PVC cylinder is stable to ~ 1 mK over the course of a day.

3.4 Optical Pumping

Our optical pumping laser is a Coherent Fiber Array Integrated Package (FAP-I) which consists of an array of fiber coupled free running laser diodes that are temperature stabilized and driven by a stable current source. The laser has an output of ~ 30 W of unpolarized light covering a bandwidth of ~ 2 nm centered roughly on the the Rb D1 line at 795 nm. To both stabilize the total power and polarize the light we use two polarizing beam splitter cubes (PBC) in series, with their transmission polarization axes orthogonal to each other, together with a liquid crystal variable retarder (LCVR) placed in between them as shown

⁵Magnetic shields are not particularly necessary to shield the rest of the resonant circuit as we are primarily concerned with reducing coupling to external noise sources at the maser frequencies, but the low magnetic field inside the shields does avoid noise generated by vibration of the inductor, see Sec. 2.5.1.

in Fig. 3.1. The LCVR is a voltage controlled variable birefringence plate set to nearly $\lambda/2$ to rotate the polarization, so that almost all the light is transmitted through the second PBC with some leeway to either decrease or increase the total transmitted power. (Only half the total laser light makes it through the first PBC due to the unpolarized output of the laser.) We measure the total transmitted laser power by picking off a few percent with a microscope slide and passing it through a diffuser plate, to ensure we are detecting the average power of the full beam profile; and then through an optical chopper wheel and finally a lens focused onto a temperature stabilized amplified photo detector, which is connected to a lock-in and PID feedback as shown in Fig. 3.1. After the laser light passes through the total power stabilization optics it goes through a zero-order $\lambda/4$ waveplate to generate circularly polarized light to optical pump the Rb atoms in the pump bulb. All of these optics are contained inside a two inch thick Styrofoam box, which filters out the rapid temperature oscillations of the room's on-off temperature control, leaving only the < 0.2 °C long term drift of the room (assuming no dramatic changes in the local weather, as adjacent rooms do not have as stable temperature control).

In addition to stabilizing the total laser power, we also monitor the Rb magnetization by applying an amplitude modulated weak rf field resonant with the ^{85}Rb Zeeman splitting (or electron spin resonance, ESR) through the Rb drive coils around the pump bulb. The application of the weak ESR rf field mixes the spin states of the Rb and hence adds an additional spin destruction mechanism, which increases the amount of light absorbed. Thus, the amplitude modulation of the ESR rf leads to an amplitude modulation of the transmitted laser power whose modulation amplitude is roughly proportional to the strength of the ESR field, the density of Rb, and the fractional amount of resonant light (assuming the total power is stabilized) and hence the Rb magnetization. This Rb magnetization monitor setup is shown in Fig. 3.1 with exaggerated modulation of the laser amplitude indicated by apparent changes in the transmitted laser beam diameter. We have not determined a good way to stabilize the resonant power from the laser diode array. The best solution is to use a laser diode array or broad area laser diode that incorporates a diffraction grating to both

narrow and stabilize the laser spectrum, so there is less off resonant light to scatter and heat the oven. Increased resonant laser power would also allow the Rb to be driven close to saturation, so that changes in resonant power lead to smaller changes in absorbed power. An attempt over more than six months to use a different type of laser system with a low power grating stabilized diode laser (~ 50 mW) amplified by a tapered amplifier diode (output of ~ 500 mW) was ultimately unsuccessful as the tapered amplifiers steadily decreased in gain such that after ~ 1000 hours of operation the total output power was halved and a subsequent attempt with a second tapered amplifier showed the same behavior. However, the narrow band light did dramatically improve the thermal stability of the pump bulb which was evident in the improved stability of the fractional maser amplitudes.

3.5 Doubly Resonant Circuit

Critical to the effective operation of the maser is the careful tuning of the doubly resonant circuit to match the ratio of the maser frequencies, to avoid large cavity pulling shifts, and measurement of the circuit's Q_c and q_c values, to be able to predict the size of the cavity pulling shift and measure the maser's power (see Eq. 2.116). To aid us in this task we have made an accurate model of the circuit accounting for all significant inductances, capacitances, and resistances, which we use to verify that the response curves measured by the amplifier are equivalent to those seen by the atoms to within the level of tuning we are able to achieve in practice. We also use our circuit model to verify that the broadband noise measured by our amplifier agrees with the expected Johnson noise and there are no other noise components degrading our SNR.

In its ideal form, the doubly resonant circuit consists of an inductor and capacitor in series connected to a second inductor and capacitor in parallel, as shown in Fig. 3.1. In reality, the layers of adjacent wires in the inductor coil act as a capacitor and the wire is resistive and the resistance at the maser frequencies is much higher than the coil's DC resistance and scales with the square of the frequency. This AC resistance is due to eddy

current losses in the wires from magnetic fields generated by adjacent wires, frequently referred to as the proximity effect.⁶ We incorporate these effects into a lumped element model of the inductor coil, which consists of an ideal inductor in series with a frequency dependent resistor that are both in parallel with a capacitor. There are also hidden capacitances in the semi-rigid coaxial cable that connects the pickup coil to the rest of the resonant circuit via a junction box containing the output amplifier. The semi-rigid cable has a capacitance per unit length of 95 pF/m, giving a total capacitance of ~ 150 pF; and the amplifier has a differential input capacitance of 6 pF, which is small enough to ignore. All of these elements are shown in Fig. 3.6 with the approximate values for each component as well as the equivalent circuit we use to calculate the voltage measured by the amplifier for a voltage source generated from inductive coupling to the pickup coil. The amplifier consists of two stages, an instrumentation amplifier (INA110) whose voltage gain is set to 100 and a low noise op-amp (OPA227) configured as a non-inverting amplifier with a voltage gain of 11, giving an overall voltage gain of 1100 with a bandwidth of 470 kHz and input voltage and current noises of $10 \text{ nV}/\sqrt{\text{Hz}}$ and $1.8 \text{ fA}/\sqrt{\text{Hz}}$. In addition, Fig. 3.6 shows the switch, S_1 , and output connector, S_2 , which allow us to disengage the pickup coil from the resonant circuit and inductively couple the remaining pickup coil circuit to a function generator so that we can pulse the atoms and measure their FIDs in order to optimize T_2' (as discussed in Sec. 3.2) and measure T_1' and G_{MM} (as we will see in Sec. 3.7). The values of the lumped elements that make up the inductor coils, L_{pu} , C_{pu} , and $R_{pu}(\omega)$ for the pickup coil, are determined by measuring the resonance frequency, ω_c , and Q_c of each coil connected to a set of fixed capacitors, C_f , whose values are checked with an impedance meter. We can then determine the coil parameters from the standard results of LRC circuits $\omega_c^2 = 1/[L_{pu}(C_r + C_f)]$ and $R_r(\omega_c) = \omega_c L_{pu}/Q_c$.

To measure the full circuit's resonance frequencies, q_c , and Q_c values, we use a small coil affixed to the top of the maser oven and aligned with the pickup coil to inductively

⁶Details of the proximity effect and how it and the coil's capacitance scales can be found in [71] and references therein, in particular [72].

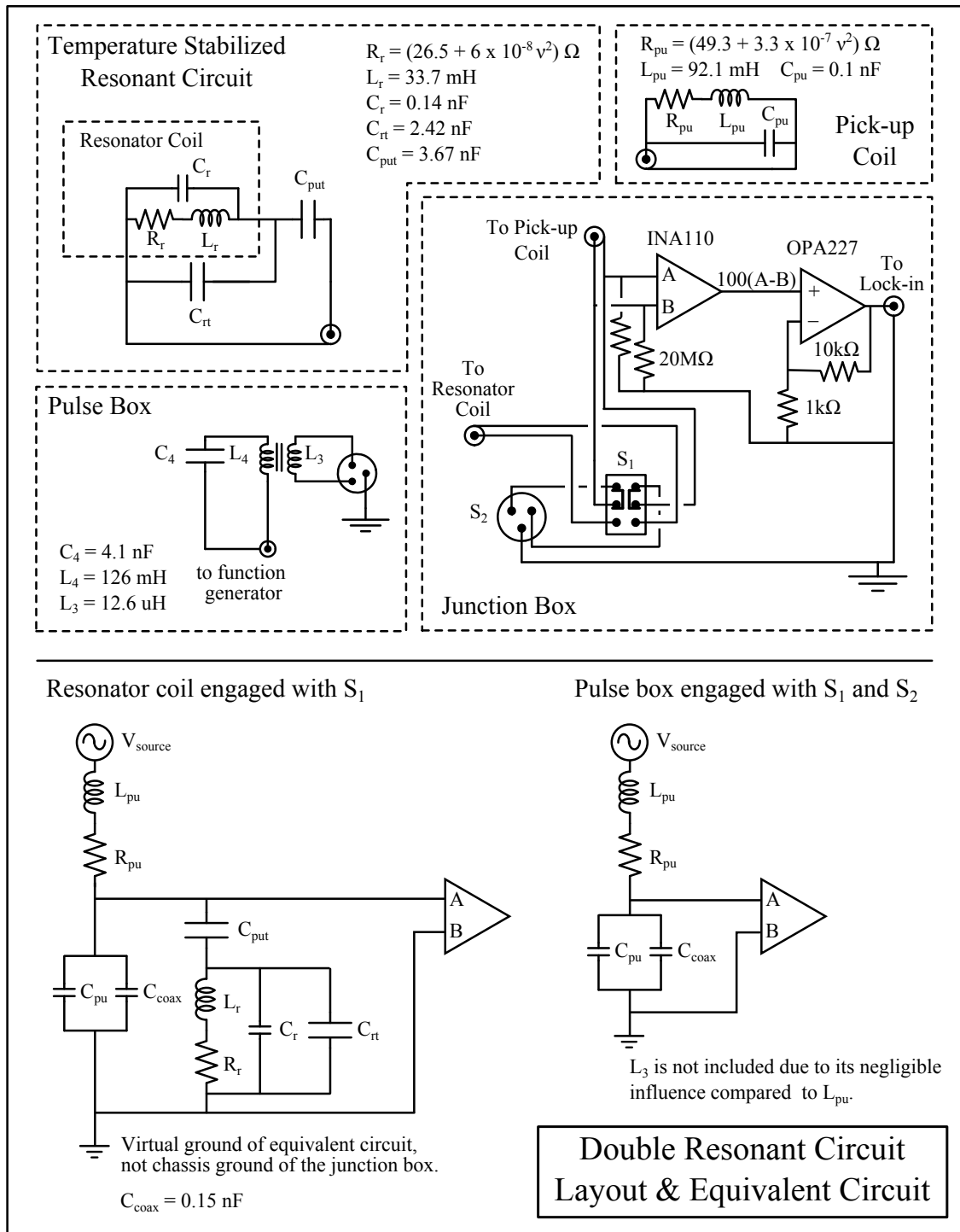


Figure 3.6: Layout and equivalent circuit for the double resonant circuit.

generate the V_{source} term in Fig. 3.6. We drive this small coil with a function generator with a $10\text{ k}\Omega$ resistor in series to generate a constant drive current across our frequency range, which ensures V_{source} is directly proportional to the drive frequency. We short the $10\text{ k}\Omega$ resistor in the second stage of our amplifier in Fig. 3.6 to increase the measurements' dynamic range and detect the amplitude of the amplifier voltage with a lock-in detector phase-locked to the function generator driving the small coil. To convert the lock-in data into the response measured by the amplifier, that is $q_{c,\text{amp}}(\omega) = |Z_{AB}(\omega)/Z_T(\omega)|$ where Z_{AB} is the impedance across the amplifier inputs and Z_T is the total impedance seen by V_{source} , we scale the voltage measured by the lock-in by its inverse drive frequency to account for the frequency dependence of V_{source} and then normalize the result to its low frequency values, 100-200 Hz, where $q_{c,\text{amp}} = 1$. The amplifier response $q_{c,\text{amp}}$ is clearly not the same in general as the atoms response $q_{c,\text{atoms}}(\omega) = |\omega L_{pu}/Z_T(\omega)|$, which gives the usual value for q_c on resonance when $\omega = \omega_c$; but it is almost exactly correct on resonance where the reactive components of $Z_{AB}(\omega)$ cancel the ωL_{pu} component of the pickup coil reactance in order to generate the resonance condition. We can see this agreement on and near to the circuit resonances in Fig. 3.7, which shows the calculated curves for both $q_{c,\text{atoms}}$ and $q_{c,\text{amp}}$ from our model as well as the measured values of $q_{c,\text{amp}}$. We can also use the amplifier response curve to determine Q_c and the resonance frequencies by taking the square of the response curve and then fitting each resonance peak over a domain twice its FWHM with a skew Lorentzian curve whose peak position and inverse fractional width give the resonance frequency and Q_c . Using our model we have checked that this fitting procedure matches the true resonance frequency $\text{Im}(Z_T(\omega)) = 0$, which corresponds to zero cavity pulling, to within a fractional value of 1×10^{-4} ; and that this is no better than finding the stationary points of $|Z_T(\omega)|$ by measuring the current in the circuit, since the parallel LC pair in the circuit introduces a difference of about $1/Q_c^2$ between the zero phase points and the stationary points of the magnitude (this is always true for a parallel LC circuit).

Using our model we can analytically determine the tuning capacitor values needed for C_{put} and C_{rt} by solving $Z_T(\omega) = 0$ with $R_r = R_{pu} = 0$, an approximation that has

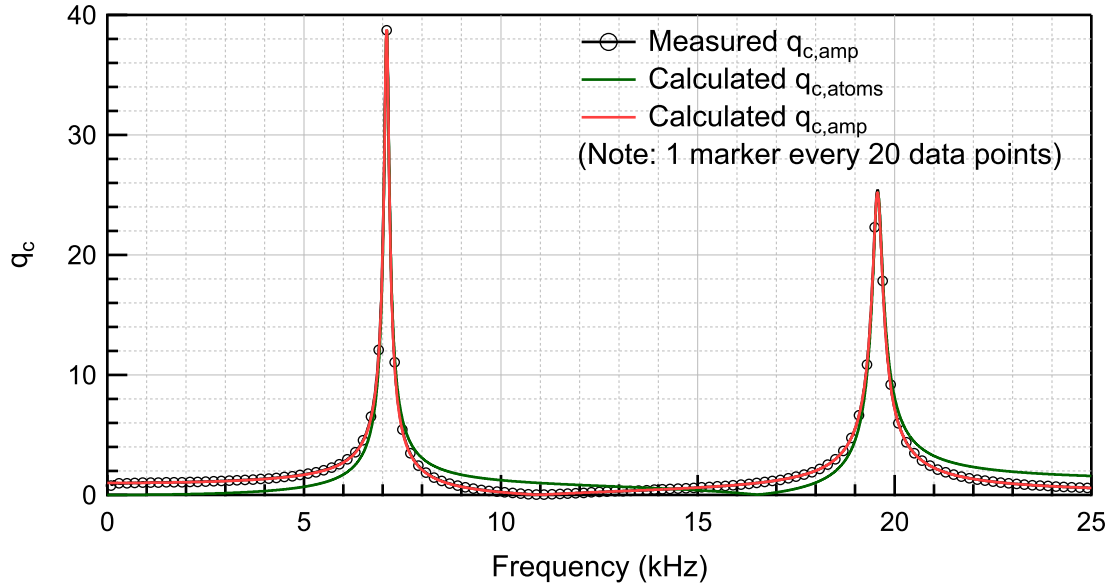


Figure 3.7: Measured q_c with circuit models for the response seen by the atoms and the amplifier. The measured values lie directly underneath the calculated values for the amplifier q_c .

much smaller errors than our knowledge of any of the parameters involved (see [25] for equations). After adding these initial capacitors we measure the resonant frequencies using the method described above and then series expand the analytic forms of the resonance frequencies around the current capacitor values of C_{put} and C_{rt} and invert the expansion to find the change in capacitance necessary to fine tune the resonant frequencies to avoid 60 Hz harmonics and match their ratio to $\gamma_R \approx 2.7541$. This process is then repeated (usually only once, at most) until the fractional difference in the resonant frequency ratio and γ_R is less than 1×10^{-3} . When tuning, it is important to have all the circuit components at their operating temperatures before measuring their resonant frequencies to ensure an accurate measurement.

Our circuit model also allows us to confirm that the broadband noise at the input to the amplifier is consistent with the thermal Johnson noise of the circuit and the input voltage and current noise of the amplifier coupled to the circuit. As we see in Fig. 3.8, on resonance the noise is dominated by thermal noise, but off resonance the noise is dominated by the

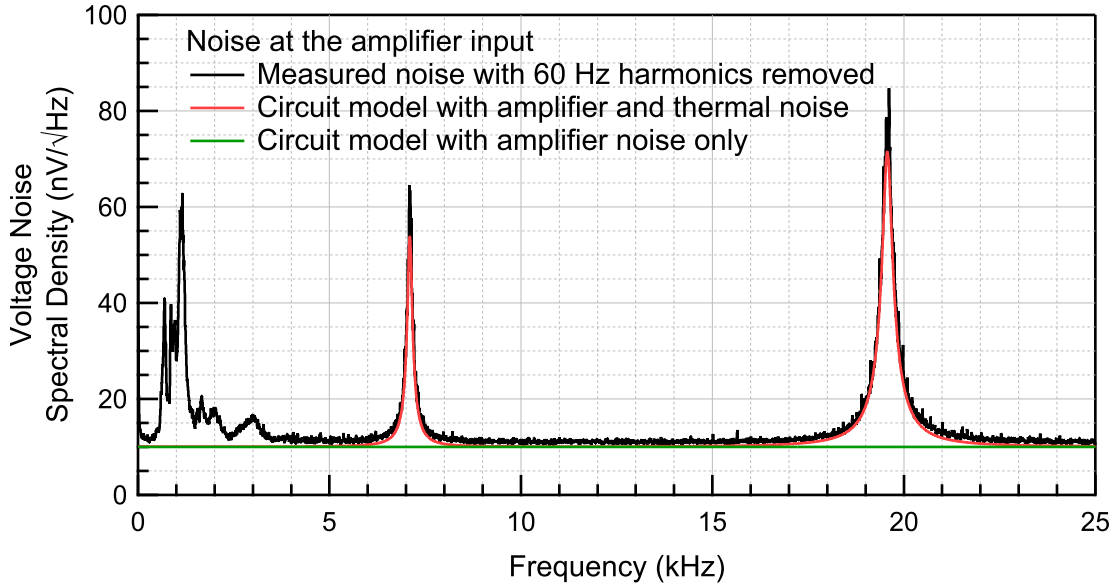


Figure 3.8: Measured noise spectral density of the double resonant circuit at the input to the amplifier; and circuit noise models showing the dominance of thermal noise at the maser resonant frequencies. Low frequency noise is due to vibration of the pickup coil in B_0 (see Sec. 2.5.1).

amplifier input voltage noise and at low frequencies there is additional noise due to vibration of the pickup coil in B_0 as discussed in Sec. 2.5.1.

Lastly, we discuss the measured stability of both resonant frequencies and their anticipated cavity pulling. One point of concern for stability is that there is a relatively significant fraction of the total capacitance in the coaxial cables, which are not temperature stabilized beyond the room temperature stability. Measurements of the double resonant frequencies with local changes in the coax temperature lead to an anticipated cavity pulling of ~ 250 nHz/ $^{\circ}$ C of change in the room temperature, so we expect a typical influence of 50 nHz in peak to peak fluctuation of the maser frequency, which is smaller than the 200 nHz thermal noise limit. To conclusively show that the circuit stability is acceptable, we simultaneously swept both resonances for three days and calculated their cavity pulling effects on the co-magnetometer frequency. We found that the ^3He resonance exhibited a steady linear drift with a slight curvature over the three days, but the drift was linear enough that removing

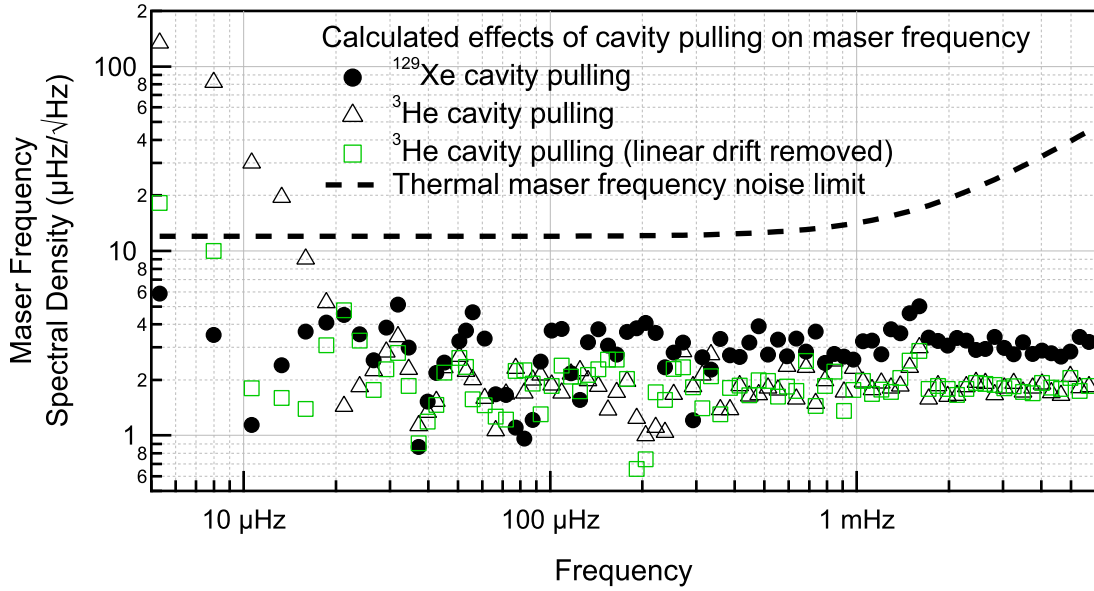


Figure 3.9: Spectral density of the measured maser resonant circuit frequencies converted into their component effects on the cavity pulling of the maser comagnetometry signal. The white noise floor of the cavity pulling is solely due to measurement noise, not actual fluctuations of the resonant frequencies.

only the linear component (linear drift removal is part of our standard analysis, see Sec. 4.2) leads to a cavity pulling frequency shift spectral density that is below the maser’s thermal noise limit for modulation frequencies as low as a day, as shown in Fig. 3.9. Thus, we conclude that our resonant circuit is presently stable enough not to limit our current maser sensitivity level for detecting sidereal modulations.

3.6 Measuring Maser Frequency/Phase

Our ^3He and ^{129}Xe maser phase and frequency measurements require a frequency reference stable enough to avoid cavity pulling shifts when phase locking the magnetic field,⁷ which means a fractional stability of at least 1×10^{-7} . Additionally, the frequency reference cannot

⁷Since cavity pulling is the difference between the circuit resonance and the Larmor frequency, a change in B_0 due to a change in the reference frequency used to phase lock the field is just as detrimental as a change in the circuit resonance.

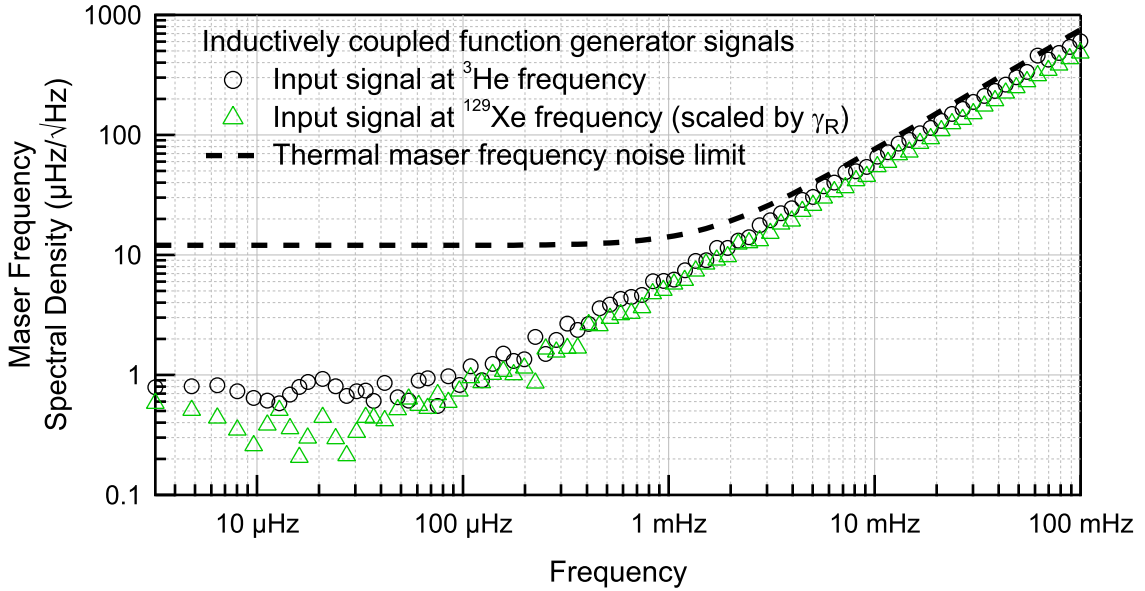


Figure 3.10: Test of maser signal phase detection system by inductively coupling signals from function generators to the pickup coil to generate signal amplitudes of the same level as the masers. Each spectrum is the component due to the respective species to the overall maser comagnetometry signal (see Sec. 2.2.3). In the actual maser the ^3He and ^{129}Xe signals would be combined in quadrature, which would match the white phase noise section of the maser thermal noise limit.

have first order sensitivity to magnetic fields, so that it does not couple to the new spin physics we are trying to detect. These conditions are met by all typical frequency standards, but we use a hydrogen maser, which operates on a magnetic field insensitive transition ($\Delta m_z = 0$) and has a fractional frequency stability of 1×10^{-14} over the course of a day. The phases of the ^3He and ^{129}Xe masers relative to the hydrogen maser are calculated by Stanford Research Systems (SRS) SR830 and SR850 digital lock-in detectors phase locked to SRS DS345 function generators, which are in turn phase locked to the hydrogen maser signal. The analog output of the SR830 lock-in measuring the ^{129}Xe maser phase is connected to an analog PID controller whose output modifies the set point of our homemade current supply that drives the B_0 solenoid. The ^{129}Xe maser function generator signal frequency is set to match the ^{129}Xe circuit resonance; and the signal generator frequency for the ^3He maser is set to be ~ 60 mHz below the ^3He maser frequency. The SR830 lock-in used to phase lock B_0

is set to have a relatively large bandwidth filter of 5–10 Hz to enable a high bandwidth lock to stabilize B_0 . Two SR850s then measure both quadratures of the mixed down and low pass filtered maser signals and store them in the lock-ins' internal circular buffers. In order to ensure that the measurements are stored at regular intervals, the lock-ins are triggered at 1 Hz by another signal derived from the hydrogen maser and the SR850 filters are set such that their equivalent noise bandwidth is less than or equal to the Nyquist frequency of the sampling (i.e. ≤ 0.5 Hz). The latest data in the SR850 internal memory circular buffers are periodically downloaded onto a computer such that there is an overlap of at least 20 data points with the previously downloaded data to unambiguously identify the new data and avoid any data loss. To test this system we drove the small coil used to measure the double resonant circuit (see Sec. 3.5) at both maser frequencies (this requires another function generator to enable the offset measurement of the ^3He frequency) with their amplitudes matched to the typical maser signals. The results of a four day measurement are shown in Fig. 3.10 which shows that we are not limited by our detection system.

3.7 Measuring Polarization Relaxation and Other Rates

There are several transient experiments we run, with the system configured such that it is below maser oscillation threshold, in order to measure the rate constants essential to predicting maser behavior, T'_2 , T'_1 , G_{MM} , τ_{RD} , and γ_{se} . In almost all cases we use the system with the resonant circuit disengaged, so that the amplifier only measures across the pickup coil, and we send in short pulses, < 0.1 s, resonant with the maser frequencies from a function generator connected to the pulse box as shown in Fig. 3.6. The resulting FID signals are recorded by lock-ins sampled at 2 Hz with filter bandwidths to match. We then either measure the transient behavior of the transverse polarization in the maser bulb or, after turning off the optical pumping laser, we apply repeated pulses to probe the transient behavior of the longitudinal polarization. In either case, we have to solve the general equations for polarization in a double bulb system with no source terms other than

the initial conditions,

$$\dot{P}_p = -\frac{P_p}{T'_p} + G_{pm}P_m \quad (3.2a)$$

$$\dot{P}_m = G_{mp}P_p - \frac{P_m}{T'_m} \quad (3.2b)$$

where p and m denote the pump and maser bulbs respectively and the effective lifetimes T' include diffusive and Rb spin exchange losses as usual (see Eq. 2.100). We should note that in this model we are neglecting the transient diffusion modes, the homogeneous solutions, but these are very short lived with time constants for the first order mode of $\tau_M \approx R_M^2/(20D)$ for the maser bulb and $\tau_t \approx L_t^2/(10D)$ for the transfer tube which are < 1 s for ^3He and < 5 s for ^{129}Xe in our typical cell and hence can be ignored. The solution for our general system of equations give us two exponentials for each noble gas species with rates of,

$$\Gamma_{\pm} = -\frac{1}{2} \left[\frac{1}{T'_m} + \frac{1}{T'_p} \pm \sqrt{\left(\frac{1}{T'_p} - \frac{1}{T'_m} \right)^2 + 4G_{mp}G_{pm}} \right], \quad (3.3)$$

which have two particular limits of interest. First, for the ^3He depolarization rates, $\Gamma_{\pm,1,He}$, there is a clear hierarchy of rates with the diffusive exchange rates much faster than the underlying relaxation rate (which is dominated by wall relaxation, see Sec. 2.3.1), which is faster than Rb spin exchange, $G_{MM}, G_{PP} \gg 1/T_{He}, 1/T_1 \gg \gamma_{se}$. Additionally, the transfer tube is roughly lossless so $G_{MP}G_{PM} \approx G_{MM}G_{PP}$, which gives us,

$$\Gamma_{+,1,He} \approx -(G_{MM} + G_{PP}) \quad (3.4a)$$

$$\Gamma_{-,1,He} \approx -\frac{1}{2} \left(\frac{1}{T_1} + \frac{1}{T} \right), \quad (3.4b)$$

so we have both a very short, less than a minute, and a very long, several hours, time constant. This hierarchy of timescales allows a clear measurement of the average wall relaxation rate for ^3He ; also initial conditions are irrelevant for measuring this rate as diffusion rapidly mixes the two bulbs. The second limit is relevant for ^{129}Xe depolarization

rates as well as decoherence rates for either ^3He or ^{129}Xe where the effective decay rate in the pump bulb, $1/T'_p$, is faster than any of the other rates, either due to Rb spin exchange in the case of ^{129}Xe depolarization or from magnetic field gradients in the case of decoherence of either species. In this limit, we have characteristic rates of,

$$\Gamma_+ \approx - \left(\frac{1}{T'_p} + G_{mp}G_{pm}T'_p \right) \quad (3.5a)$$

$$\Gamma_- \approx - \left(\frac{1}{T'_m} - G_{mp}G_{pm}T'_p \right) \quad (3.5b)$$

which consists of a relatively fast initial equalization between the bulbs as the pump bulb rapidly reaches equilibrium at rate, Γ_+ , with a slower decay rate in the maser bulb, Γ_- , where the time constant is biased to slightly longer times since the polarization is not instantly destroyed in the pump bulb. Measuring the decoherence versus depolarization rates each have their own complications, so we will begin with the method to measure decoherence and then move on to depolarization and the other rates.

When measuring decoherence from the FID lifetime we assume that there is no transverse polarization in the double bulb before we pulse the atoms and that we only generate coherence in the maser bulb, so the fractional amplitudes associated with each exponential rate are,

$$A_+ \approx G_{MP,\perp}G_{PM,\perp}T'^2_{2,P} \quad (3.6a)$$

$$A_- \approx 1 - A_+. \quad (3.6b)$$

For ^3He we have $1/T'_2 \approx G_{MP,\perp} \approx G_{PM,\perp}$ when the gradients are minimized and so, even for a relatively long pump bulb coherence time of $T'_{2,P} \approx 0.3T'_2$, there is little evidence of it in the FID, since $A_-/A_+ \approx 0.1$, but it does have a relatively large effect on the measured decoherence time $1/\Gamma_- \approx 1.5T'_2$. This effect is highly suppressed by the pump bulb solenoid and would not be seen in ^{129}Xe due to its strong interactions with Rb in the pump bulb, but there is the question of whether our measured coherence times could be biased to be

longer than the coherence time that matters for calculating the thermal noise floor, normally assumed to be T'_2 . We can calculate the new thermal noise floor by extending the model used in Sec. 2.2.3 by adding a coherence term in the pump bulb to our maser model,

$$\dot{P}_{\perp,P} = G_{PM,\perp} P_{\perp} - \frac{P_{\perp,P}}{T'_{2,P}} \quad (3.7a)$$

$$\dot{P}_{\perp} = \gamma \frac{B_1}{2} P_z - \frac{P_{\perp}}{T'_2} + G_{MP,\perp} P_{\perp,P}. \quad (3.7b)$$

Then, for transient phase fluctuations around the equilibrium phase value we have, from Sec. 2.2.3,

$$\delta\dot{\psi} = \dots + \gamma \frac{B_{1,eq}}{2} \frac{P_{z,eq}}{P_{\perp,eq}} (\delta\phi - \delta\psi), \quad (3.8)$$

where the coefficient in front of the phase terms is the relevant one for the thermal noise limit (see Sec. 2.2.3) and is given by the steady state solution to Eq. 3.7,

$$\gamma \frac{B_{1,eq}}{2} \frac{P_{z,eq}}{P_{\perp,eq}} = \frac{1}{T'_2} - G_{MP,\perp} G_{PM,\perp} T'_{2,P}. \quad (3.9)$$

Thus, the measured value of the decoherence rate in the limit of rapid decoherence in the pump bulb, Γ_- in Eq. 3.5, is the relevant value for the thermal noise limit, not just $1/T'_2$.

In addition to concerns about transverse polarization in the pump bulb when measuring FID decay rates, we also have to be concerned about feedback from the pickup coil, even though it is off resonance. We can calculate the effect of the pickup coil by repeating our analysis from Sec. 2.1.3 for coupling between the atoms and the circuit. The circuit impedance for the off resonant pickup coil is given by,

$$Z(\omega) \approx \frac{\omega_c L_{pu}}{i\omega Q_c} (i\omega + \omega_c Q_c) \quad \text{for} \quad \left(\frac{\omega}{\omega_c}\right)^2 \ll 1 \quad (3.10)$$

which leads to equations for the pickup coil field and phase

$$\dot{B}_1 = -Q_c \omega_c B_1 + Q_c K_0 P_\perp \sin(\theta) \quad (3.11)$$

$$\dot{\phi} = -\omega_M + Q_c K_0 \frac{\omega_M^2}{\omega_c} \frac{P_\perp}{B_1} \cos(\theta) \quad (3.12)$$

where $K_0 = \mu_0 \eta \gamma n \hbar / 2$, and which, similarly to the standard maser equations, can be approximated as always being in steady state relative to the polarizations (see Sec. 2.2),

$$B_{1,eq} = \left(\frac{\omega_M}{\omega_c} \right) K_0 P_\perp \sin(\theta) \quad \text{and} \quad \tan(\theta_{eq}) \approx \frac{\omega_c}{\omega_M} Q_c \gg 1. \quad (3.13)$$

Thus, we can make the approximations $\sin(\theta) \approx 1$ and $\cos(\theta) \approx \omega_M / (\omega_c Q_c)$, giving us an equation for the transverse polarization of,

$$\dot{P}_\perp = \frac{\gamma}{2} B_1 \cos(\theta) P_z - \frac{P_\perp}{T_2'} = -P_\perp \left(\frac{1}{T_2'} - \frac{\gamma}{2} \left(\frac{\omega_M}{\omega_c} \right)^3 \frac{K_0}{Q_c} P_z \right). \quad (3.14)$$

For our off resonant pickup coil we have $Q_c \approx 40$ and $\omega_c / (2\pi) \approx 40$ kHz. For ^3He in a fully polarized, typical cell, where only a small fraction of the longitudinal polarization is transferred into the transverse plane for the FID so that $P_z \approx P_{z,0}$, we find that the decoherence rate is reduced by $\sim 1 \times 10^{-3} \text{ s}^{-1}$. This is negligible for our typical cells with $T_2' < 100$ s for ^3He , but was quite noticeable in the cell with a narrow transfer tube (see Sec. 3.2), which we used to test the second order magnetic field gradient coils, where the FID lifetime was 280 s for the cell at low polarization, but 400 s once the cell was fully polarized.

The final complication in measuring the decoherence rate in the maser bulb is bias in estimation of the decoherence rate using least squares fits of low SNR signals. Due to drifts in the power supply it is difficult to fit directly to the mixed down signal from the lock-in since it is both decaying in time and changing oscillation frequency. Instead, we combine both quadratures of the lock-in output, X and Y , to generate an R trace of the FID where $R = \sqrt{X^2 + Y^2}$, which gives just the amplitude without the beat note.

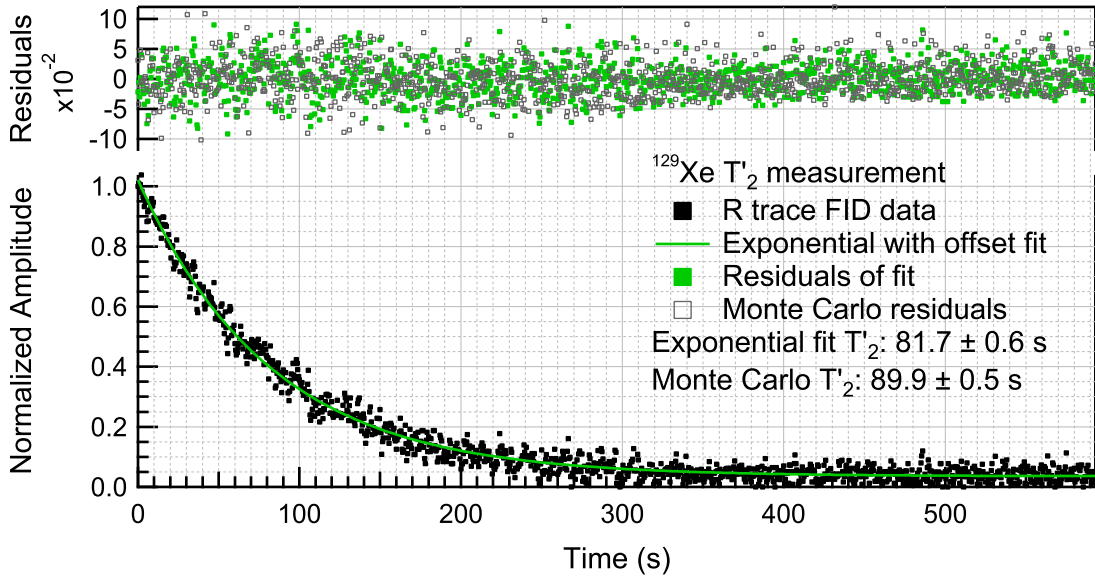


Figure 3.11: Fit of a low SNR ^{129}Xe FID to extract T_2' with both a least squares exponential and a Monte Carlo procedure. Note the change in the distribution of residuals as the exponential approaches zero around 300 s, which leads to bias in the measurement of the exponential time constant if the Monte Carlo procedure is not followed.

Unfortunately, this means the residuals are no longer normally distributed, especially as the signal approaches zero, so a Monte Carlo procedure is required to obtain accurate results for low SNR measurements as shown in Fig. 3.11, where we see there is a 10% bias error in the least squares exponential fit. The Monte Carlo procedure consists of generating X and Y decaying oscillations with normally distributed errors based on the residuals of the measured R trace and then adjusting the input time constant for the generated X and Y traces until a least squares fit of the generated R trace to an exponential gives the same time constant as the data. This process is repeated 20 times giving an average and standard deviation for the real time constant that are reported in Fig. 3.11 along with the residuals of the exponential fit to the Monte Carlo R trace. The fitting bias in the time constant becomes negligible, $< 1\%$, once the SNR increases by a factor of ~ 5 from the data shown here. In our measurements we have not seen the double exponential behavior that would suggest significant transverse polarization in the pump bulb, but this is not surprising as

even a small frequency difference between the pump and maser bulbs will suppress any coherence between them as we saw in Sec. 2.2.2. Double exponential behavior is far easier to observe in depolarization measurements, as we will see shortly.

To measure depolarization rates we wait for longitudinal polarization to build up either to equilibrium, in the case of ^{129}Xe , since that only takes about half an hour, or to a level that gives acceptable SNR, in the case of ^3He . Then we turn off the optical pumping laser and periodically pulse the noble gas spins in the maser bulb and record the change in the amplitude of their FIDs over time. The first complication of this scheme is that every time we pulse the noble gas atoms we reduce their longitudinal polarization by a factor of $1 - \cos(\theta_{\text{tip}})$, where the tip angle is the pulse length times the Rabi frequency, $\theta_{\text{tip}} = \Omega_R \tau_{\text{pulse}}$. In the limit that the tip angle is small, $\theta_{\text{tip}}^2 \ll 1$, and there are many tips over the characteristic depolarization time, the losses due to tipping the spins can be approximated as a continuum relaxation with a rate of,

$$\Gamma_{\text{tip}} \approx \frac{\theta_{\text{tip}}^2}{2T_{\text{rep}}} \quad (3.15)$$

where T_{rep} is the time between pulses.⁸ We would like to have $\Gamma_{\text{tip}} \ll 1/T_1', 1/T_1$, as appropriate, which means that for six FIDs per depolarization time our tip angle should be no larger than 10° in order to limit the increase in the depolarization rate to $< 10\%$. There is also a problem in measuring depolarization rates for ^{129}Xe as $T_2' \approx T_1'$, so we cannot generate multiple FIDs over the course of T_1' without them interfering with each other. To avoid this problem, we temporarily ramp up one of our magnetic field gradient coils to decohere the spins before initiating the next FID: a technique referred to as a crusher gradient, which is useful for measuring any rate comparable to T_2' .⁹ Analysis of the results of a depolarization measurement are straightforward for ^3He due to its well separated time scales, as shown in Eq. 3.4 at the beginning of this section; but for ^{129}Xe we have to use

⁸Note that Γ_{tip} is exactly the same as the rate we derived in Sec. 2.1.1 for collisional interactions.

⁹The use of rapid small tip angle pulses with a crusher gradient inbetween them is one way to calibrate θ_{tip} by making Γ_{tip} larger than all other rates.

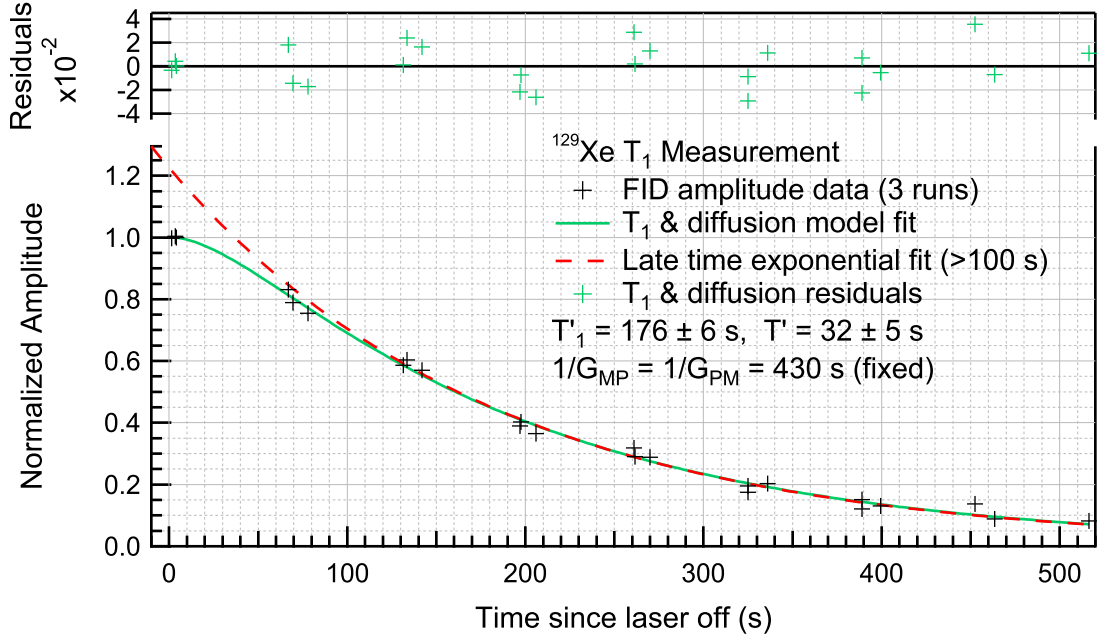


Figure 3.12: Fit of ^{129}Xe FID amplitude data using the T_1 and diffusion model described in the text.

the mixed rates of Eq. 3.5, where the relative amplitudes of the associated exponentials for a system begun in equilibrium are,

$$A_{+,1,Xe} \approx -\frac{T'}{T_1} \left(1 + \frac{T'}{T_1} \right) + G_{MP}G_{PM}T'^2 \approx -\frac{T'}{T_1} \quad (3.16a)$$

$$A_{-,1,Xe} \approx 1 - A_{+,1,Xe}. \quad (3.16b)$$

Fig. 3.12 shows an example measurement of the ^{129}Xe depolarization rate in a typical cell filled with 600/30/80 Torr of $^3\text{He}/^{129}\text{Xe}/\text{N}_2$, using all the techniques described above. Double exponential behavior at early times is clearly seen, which fulfills our expectation of a system starting in equilibrium with an initial time derivative of zero. The fit estimate of $T' = 32 \pm 5$ s is close to the expected value of ~ 20 s given that the rate is dominated by γ_{se} , there could be up to a factor of 2 uncertainty in the pump bulb Rb density, and there is significant disagreement over the strength of van der Waals interactions (see Sec. 2.1.1). Combining

the fit estimate of $T_1' = 176 \pm 6$ s with an estimated bulb escape time of $1/G_{MM} \approx 260$ s from our diffusion model (see Sec. 2.1.2), we find that the wall relaxation time is $T_1 \approx 540$ s.

There are two other key rates we can measure, the radiation damping rate, $1/\tau_{RD}$, and the diffusive maser bulb escape rate, G_{MM} . To measure the radiation damping rate, we reverse the circularity of the optical pumping laser so that the spins are pumped into the low energy state and wait until the noble gas polarization has reached equilibrium, $P_z = P_{z,0}$. Then we apply a small tip angle pulse so that the longitudinal polarization is barely depleted and engage the resonant circuit (see Sec. 3.5). This leads to an FID with a significantly shortened time constant,

$$\dot{P}_\perp = -\gamma \frac{B_1}{2} P_{z,0} - \frac{P_\perp}{T_2'} = -P_\perp \left(\frac{1}{\tau_{RD}} + \frac{1}{T_2'} \right), \quad (3.17)$$

where we can extract τ_{RD} from the measured FID since we have already measured T_2' . While measuring τ_{RD} for each species is an important check to ensure that the masers operate well above threshold, it can be a very lengthy measurement given the long ^3He T_1 ; and so we typically combine a τ_{RD} measurement with a measurement of the ^3He longitudinal polarization while the spins are being polarized, since the time constant is the same as for depolarization, T_1 . Our measured values for τ_{RD} are consistent with those given in Tab. 2.10.

To measure G_{MM} for ^3He , wall relaxation is too rapid to make the measurement conclusive for ^{129}Xe , we turn off the optical pumping laser and apply $\sim 90^\circ$ tip angle pulses to the pump bulb every 10 s using the Rb drive coils (see Fig. 3.4) to keep the pump bulb longitudinal polarization near zero and then probe the maser bulb longitudinal polarization in the usual way using crusher gradients between FIDs. In order to avoid the large tip angle pulses in the pump bulb tipping any ^3He polarization in the maser bulb, we use the pump bulb solenoid to detune the ^3He Larmor frequency in the pump bulb by 12 Hz and use pulses with a \cos^4 envelope and a pulse length of 0.25 s, so that the first zero of its

Fourier transform lines up with the maser bulb ^3He Larmor frequency and the smooth pulse envelope leads to less power around the zero than with a square pulse. The relatively large magnetic field generated by the pump bulb solenoid also generates large enough magnetic field gradients that the pump bulb decoherence rate is much faster than the time between pulses, so there is no possibility of returning any transverse ^3He polarization to longitudinal polarization with subsequent pulses. In order to accurately tune the pump bulb solenoid, we measure FIDs in the pump bulb by making the Rb drive coil resonant at the ^3He Larmor frequency ($Q \approx 23$), connecting a function generator to the circuit through a 1 M Ω resistor to keep it isolated, and measure the result with a lock-in after a low noise amplifier. We measured bulb escape rates for cells with our typical transfer tube; and for a cell with a narrow transfer tube and in each case the rates for G_{MM} were within 20% of the theoretical values calculated from Sec. 2.1.2, which is within the manufacturer's tolerance for the tubing's inner diameter.

Using the Rb drive coil we can also measure the Rb spin exchange rate with ^{129}Xe in the pump bulb, since it is so rapid compared to all other rates that $1/T' \approx \gamma_{se}$. The setup for the Rb drive coil is the same as when measuring ^3He in the pump bulb except that the coil is tuned to the ^{129}Xe Larmor frequency ($Q \approx 8$) and the pump bulb solenoid is not turned on. We calibrate the tip angle for ^{129}Xe by measuring the change in FID amplitude as we increase the pulse length, which is easy for ^{129}Xe as the recovery time is very rapid and the results can be applied to ^3He with the appropriate scaling. We used a cell with more ^{129}Xe than usual, 1000/200/150 Torr of $^3\text{He}/^{129}\text{Xe}/\text{N}_2$, which gave higher SNR, but should have a comparable spin exchange rate to our usual cells based on Sec. 2.1.1. We used a tip angle of $\sim 13^\circ$ followed by a crusher gradient with a time between tips of 11 s, giving $1/\Gamma_{\text{tip}} \approx 430$ s, which has a negligible influence on the results. We measured the spin exchange rate both after the laser was turned off, as shown in Fig. 3.13, and after the laser was turned back on, as shown in Fig. 3.14, which have different spin exchange rates due to the different Rb polarization levels in each case as parameterized by ζ in Eq. 2.11. The ratio of the low versus high Rb polarization spin exchange rates is ~ 1.4 , which compared to the

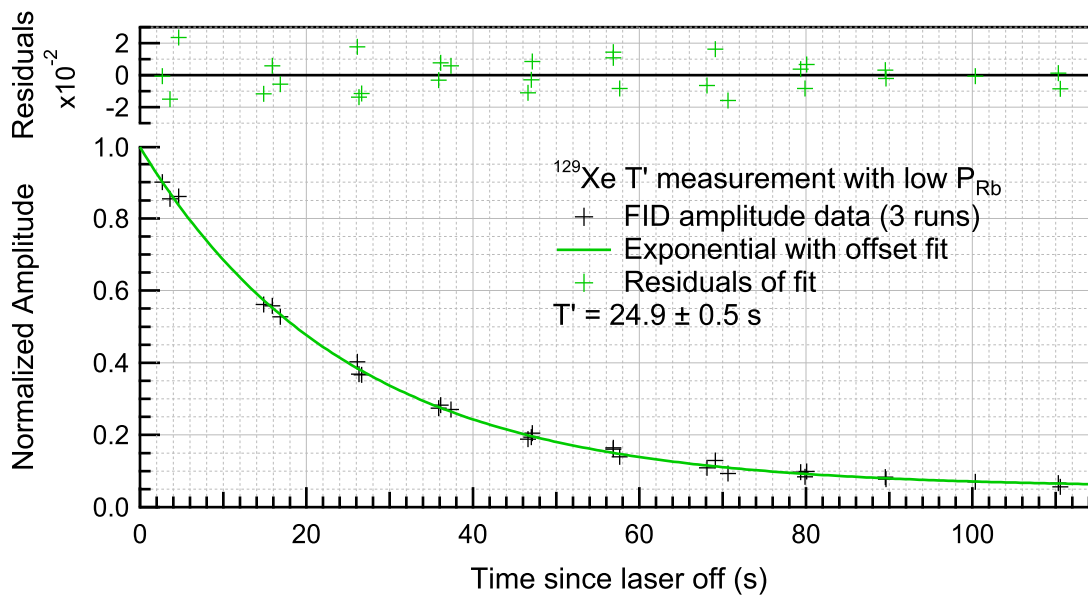


Figure 3.13: Fit of measured ^{129}Xe FID amplitude in the pump bulb, showing the effect of spin exchange with low Rb polarization.

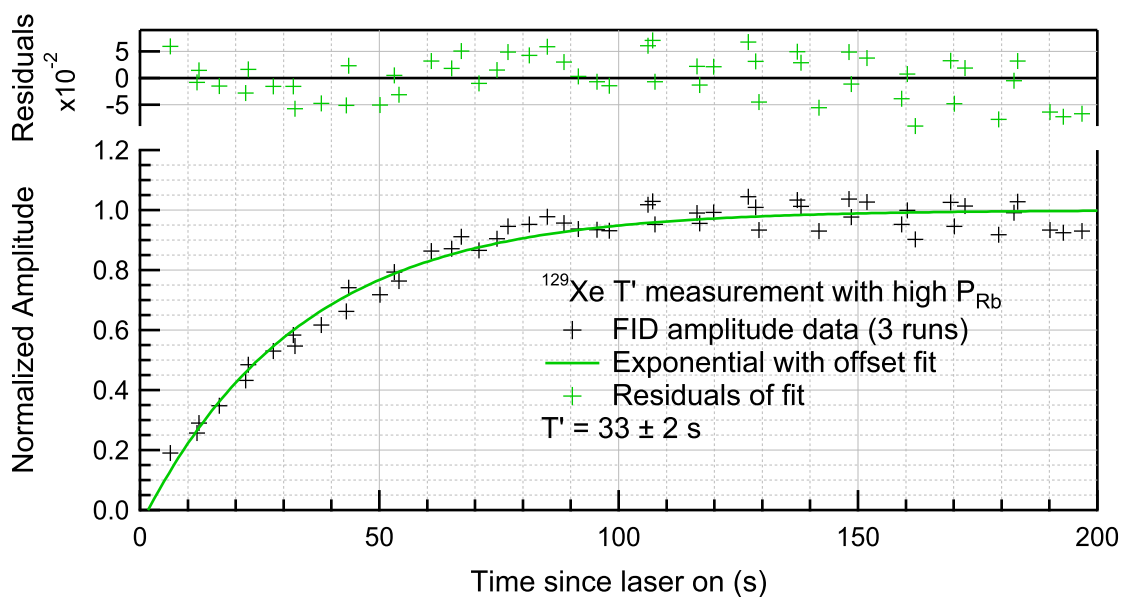


Figure 3.14: Fit of measured ^{129}Xe FID amplitude in the pump bulb, showing the effect of spin exchange with high Rb polarization.

expected ratio of ~ 1.9 for completely unpolarized versus fully polarized Rb suggests that we have a Rb polarization $\approx 50\%$. Rb polarization of this level is roughly what we expect from the model described in Sec. 2.1.1 and from the magnitude of the ^{129}Xe pump bulb FIDs, since the ^{129}Xe polarization level in the pump bulb is similar to Rb. The measured spin exchange time constants are also in good agreement with the expected value ≈ 30 s. Note that in order to obtain accurate time constants the exponential fit must include an offset, as the FIDs are so short that we measured their amplitude by taking the maximum value of the first few points in the FID, which naturally leads to a baseline offset due to the additive noise from the amplifier.

Chapter 4

Lorentz Symmetry Tests

In this chapter we discuss the techniques we use to analyze the ^3He and ^{129}Xe maser frequencies to place limits on the coupling of neutron spins to Lorentz and *CPT* violating background fields to the universe, which can be interpreted using the Standard Model Extension (SME) developed by Kostelecký and coworkers. We give a brief overview of the SME as it pertains to our experiment as well as the limits set on SME parameters by the previous version of the ^3He and ^{129}Xe maser (a more extensive discussion can be found in [1]). Of particular interest is how to determine if our data has been corrupted by systematic effects and no longer can be well described by our model, especially since the observed fluctuations in the maser frequency do not have a flat power spectrum. Monte Carlo simulations will be shown, which largely verify our data analysis procedures, but also indicate some remaining shortcomings. Finally, we present preliminary results of our tests of Lorentz and *CPT* symmetry using the upgraded ^3He and ^{129}Xe maser; and compare these results to the previous version of the experiment. We find that the current system provides more than a factor of four better sensitivity per root sidereal day, through practical technical limitations limited the current Lorentz symmetry test to 19 days.

4.1 SME Theory

The Standard Model Extension (SME) posits a minimal set of background fields to the universe that lead to Lorentz violation, as particles coupled to these fields would experience energy shifts as they change inertial frames. Such effects are referred to as violations of particle Lorentz invariance; but all the fields transform normally under local Lorentz transformations, so observers in different inertial frames will agree on the effects on a particle, or, in the language of the SME, the fields are observer Lorentz invariant.

It is particle Lorentz violation we take advantage of, since our laboratory on the surface of the Earth is in a non-inertial frame that is both rotating and boosted, leading to time varying modulations of the masers' frequencies due (primarily) to coupling of the ^3He and ^{129}Xe neutron spins with the SME fields. The set of Lorentz-violating fields which we are ultimately trying to observe or limit is given by the minimal SME Lagrangian for neutrons and other spin-1/2 fermions [1]:

$$\mathcal{L} = \frac{1}{2} i \bar{\psi} \Gamma_\nu \overleftrightarrow{\partial}^\nu \psi - \bar{\psi} M \psi, \quad (4.1)$$

where

$$M = m + a_\mu \gamma^\mu + b_\mu \gamma_5 \gamma^\mu + \frac{1}{2} H_{\mu\nu} \sigma^{\mu\nu} \quad (4.2)$$

and

$$\Gamma_\nu = \gamma_\nu + c_{\mu\nu} \gamma^\mu + d_{\mu\nu} \gamma_5 \gamma^\mu + e_\nu + i f_\nu \gamma_5 + \frac{1}{2} g_{\lambda\mu\nu} \sigma^{\lambda\mu} \quad (4.3)$$

and the terms containing a_μ , b_μ , e_μ , f_μ , and $g_{\lambda\mu\nu}$ are odd under CPT . This Lagrangian formulation is then converted to a perturbative Hamiltonian and transformed from an inertial Sun centered frame to the rotating and boosted laboratory frame of the noble gas atoms, generating a modulated shift in the comagnetometry frequency [6],

$$\delta\nu_{M,He} - \gamma_R \delta\nu_{M,Xe} = \delta\nu_X \sin(\omega_\oplus T) + \delta\nu_Y \cos(\omega_\oplus T) \quad (4.4)$$

where $\omega_{\oplus}/(2\pi) \approx 11.606 \mu\text{Hz}$ is the sidereal rotation frequency of the Earth. The amplitudes of the two quadratures of the modulated shift are given by,

$$\delta\nu_X = k[\lambda_s + \beta_{\oplus}(\Lambda_{ss} \sin(\Omega_{\oplus}T) + \Lambda_{sc} \cos(\Omega_{\oplus}T))] \quad (4.5)$$

$$\delta\nu_Y = k[\lambda_c + \beta_{\oplus}(\Lambda_{cs} \sin(\Omega_{\oplus}T) + \Lambda_{cc} \cos(\Omega_{\oplus}T))] \quad (4.6)$$

where Ω_{\oplus} is the frequency of Earth's orbit around the Sun, $\beta_{\oplus} \approx 9.9 \times 10^{-5}$ is the speed of the Earth in its orbit as a fraction of the speed of light, and k is the difference in the coupling of ^3He and ^{129}Xe to magnetic fields versus SME fields,

$$k = \frac{2\left(\alpha_{He} - \alpha_{Xe} \frac{\gamma_{He}}{\gamma_{Xe}}\right)}{2\pi\hbar} = -5.77 \times 10^{32} \text{ nHz/GeV} \quad (4.7)$$

where $\alpha_{Xe} \approx 0.75$ [3] and $\alpha_{He} \approx 0.87$ [4] are the fraction of the noble gases' nuclear spin due to the neutron.¹ The SME λ coefficients determine the amplitude of the spatial components of possible Lorentz violation and the Λ coefficients determine the boost components [6],

$$\lambda_c = \tilde{b}_Y - 0.0034\tilde{d}_Y + 0.0034\tilde{g}_{DY} \quad (4.8a)$$

$$\lambda_s = -\tilde{b}_X + 0.0034\tilde{d}_X - 0.0034\tilde{g}_{DX} \quad (4.8b)$$

$$\begin{aligned} \Lambda_{cc} = & -\cos(\eta)\left[\left(\frac{1}{2}\tilde{b}_T + \frac{1}{2}\tilde{d}_- - \tilde{g}_c - \frac{1}{2}\tilde{g}_T\right) + (\tilde{g}_T - 2\tilde{d}_+ + \frac{1}{2}\tilde{d}_Q)\right] \\ & + \sin(\eta)(\tilde{d}_{YZ} - \tilde{H}_{XT}) \end{aligned} \quad (4.8c)$$

$$\Lambda_{cs} = -\tilde{H}_{ZT} \quad (4.8d)$$

$$\Lambda_{ss} = \left(\frac{1}{2}\tilde{b}_T + \frac{1}{2}\tilde{d}_- - \tilde{g}_c - \frac{1}{2}\tilde{g}_T\right) - (\tilde{g}_T - 2\tilde{d}_+ + \frac{1}{2}\tilde{d}_Q) \quad (4.8e)$$

$$\Lambda_{sc} = \cos(\eta)(\tilde{H}_{ZT} - \tilde{d}_{XY}) - \sin(\eta)\tilde{H}_{YT} \quad (4.8f)$$

where $\eta = 23.4^\circ$ is the tilt of the Earth's axis relative to its orbital plane around the Sun. The limits for the λ and Λ parameters using the previous version of the ^3He and ^{129}Xe maser

¹In previous papers with bounds for SME parameters using the ^3He and ^{129}Xe masers, [5] and [6], it was assumed that $\alpha_{Xe} = \alpha_{He} = 1$, so $k = -8.46 \times 10^{32} \text{ nHz/GeV}$.

SME coefficients	Fit result (GeV)
λ_c	$(1.2 \pm 1.4) \times 10^{-31}$
λ_s	$(0.3 \pm 1.2) \times 10^{-31}$
Λ_{cc}	$(-1.6 \pm 1.5) \times 10^{-27}$
Λ_{cs}	$(0.3 \pm 2.6) \times 10^{-27}$
Λ_{ss}	$(-2.6 \pm 2.8) \times 10^{-27}$
Λ_{sc}	$(-1.6 \pm 1.2) \times 10^{-27}$

Table 4.1: Limits on SME parameters as determined by the previous version of the ^3He and ^{129}Xe maser in [6] and corrected for the lower k value reported here in Eq. 4.7.

are given in Tab. 4.1 where the boost parameters sensitivity is reduced by approximately β_{\oplus} compared to the spacial parameters, as expected. Note that the tilde accented SME parameters above are made up of linear combinations of the fundamental SME fields [73],

$$\tilde{b}_J = b_J - \frac{1}{2}\epsilon_{JKL}H_{KL} - m(d_{JT} - \frac{1}{2}\epsilon_{JKL}g_{KLT}) \quad (4.9a)$$

$$\tilde{b}_T = b_T + mg_{XYZ} \quad (4.9b)$$

$$\tilde{g}_T = b_T - m(g_{XYZ} - g_{YZX} - g_{ZXY}) \quad (4.9c)$$

$$\tilde{g}_{DJ} = -b_J + m\epsilon_{JKL}(g_{KTL} + \frac{1}{2}g_{KLT}) \quad (4.9d)$$

$$\tilde{g}_c = m(g_{XYZ} - g_{ZXY}) \quad (4.9e)$$

$$\tilde{d}_J = m(d_{TJ} + \frac{1}{2}d_{JT}) - \frac{1}{4}\epsilon_{JKL}H_{KL} \quad (4.9f)$$

$$\tilde{d}_{\pm} = m(d_{XX} \pm d_{YY}) \quad (4.9g)$$

$$\tilde{d}_Q = m(d_{XX} + d_{YY} - 2d_{ZZ} - g_{YZX} - g_{ZXY} + 2g_{XYZ}) \quad (4.9h)$$

$$\tilde{d}_{YZ} = m(d_{YZ} + d_{ZY} - g_{XYX} + g_{XZZ}) \quad (4.9i)$$

$$\tilde{d}_{XY} = m(d_{XY} + d_{YX} - g_{ZXX} + g_{ZYX}) \quad (4.9j)$$

$$\tilde{H}_{XT} = H_{XT} + m(d_{ZY} - g_{XTT} - g_{XYX}) \quad (4.9k)$$

$$\tilde{H}_{YT} = H_{YT} + m(d_{XZ} - g_{YTT} - g_{YZZ}) \quad (4.9l)$$

$$\tilde{H}_{ZT} = H_{ZT} + m(d_{YX} - g_{ZTT} - g_{ZXX}). \quad (4.9m)$$

While all these transformations are critical to determine what fraction of the SME param-

eter space we have covered, the bottom line for experimentally detecting any background Lorentz-violating field coupling to the neutron spin is described through the sidereal modulation of the comagnetometry signal,

$$\delta\nu_{M,He} - \gamma_R \delta\nu_{M,Xe} = \delta\nu_X \sin(\omega_{\oplus}T) + \delta\nu_Y \cos(\omega_{\oplus}T) \quad (4.10)$$

and the ability of our upgraded ^3He and ^{129}Xe maser to bound the standard deviation of the quadrature amplitudes $\delta\nu_X$ and $\delta\nu_Y$. In the following sections we will try and optimize the extraction of a set of $\delta\nu_X$ and $\delta\nu_Y$ values from maser data by introducing additional terms to the model to account for non-SME related frequency shifts in the maser and reject any instances where our corrections do not work.

4.2 Data Analysis Methods

We have three basic criteria for the analysis methodology used to determine sidereal modulations in our data: (i) our methods must be able to differentiate between data segments with frequency shifts that can be explained by our model and those that do not; (ii) since we will be rejecting segments of our data our methods must be robust with respect to the parameters used in the rejection criteria; and, (iii) since each data point takes a full day to collect, we need to use the data as efficiently as possible. We begin with a linear fit model whose basis set consists of both quadratures of sidereal modulation, the amplitudes of the masers (which are correlated to changes in the pump bulb and hence most of the frequency shift mechanisms), a linear frequency drift, and a constant frequency offset. In order to differentiate between data whose fluctuations can and cannot be accounted for by the model, we need the sum of the squares of our residuals to follow a χ^2 probability distribution, which is a problem as the maser frequency does not have a white noise spectrum for frequencies above $1/(2\pi T_2')$ (the white phase noise part of the spectrum, see Sec. 2.2.3), and hence our residuals are serially correlated and the sum of their squares will

not follow a χ^2 distribution.² One solution to this is to low pass filter the frequency data to remove the white phase noise portion of the spectrum, but to do this effectively leaves us with relatively few degrees of freedom, which is not always desirable and would become increasingly problematic if we moved to a system with longer T_2' . Instead, we correct for the serial correlation by calculating the full covariance matrix for the residuals to weight the least squares optimization correctly, as described in Sec. 4.2.1. Additionally, we apply our least squares basis set, properly corrected, to the phase evolution of the maser, rather than the frequency, which is how the maser signal is measured by the lock-in. Note, however, that the techniques described in Sec. 4.2.1 could also be applied to the frequency data.

Using the corrected χ^2 distribution to differentiate good data from bad data in terms of explainable frequency shifts, we fit the data in segments of one sidereal day to help ensure linearity of the maser amplitude and frequency correlations and that other drifts will be primarily linear in nature. We stagger the start of each segment we fit over by ~ 1 hour and then run a 5 point moving average over the resulting χ^2 values for each fit and reject all start times that have a probability of less than 5% based on the χ^2 distribution. This ensures that only data which robustly matches the model is used, while also trying to use as much of the data as possible by finding good segments that might last for only a day and avoiding measurement disruptions that could be very short. Once we have collected sufficient data, we calculate the standard deviation of the full set of sidereal modulation terms and compare it to the standard deviation of the same terms in a simplified fit model, which does not include the linear drift or maser amplitude terms, to gauge the efficacy of our drift removal. We generalize this further by performing a set of fits over each data segment with the full and simplified models where the sidereal frequency is replaced each time with a higher frequency, up to the Nyquist frequency. The set of standard deviations of the sinusoidal terms scaled by the inverse square root of the bandwidth of each frequency bin, $1/\sqrt{\nu_{\text{sidereal}}}$ for a one sidereal day data segment, generate, what we call, a least squares periodogram

²We could use Monte Carlo methods to generate the probability distribution in this case, but that is very computationally intensive.

(LSP), which is an estimation of the noise spectral density of the maser frequency with (and without) frequency shift corrections. In Sec. 4.2.2, we use LSPs with Monte Carlo tests to evaluate the efficacy of our analysis methodology.

4.2.1 Generalized Least Squares

In order that the sum of the squares of the residuals of our least squares fit model follow a χ^2 distribution we use the generalized least squares transformation of the fit model (see [74]),

$$\mathbf{Ax} = \mathbf{b} \implies \mathbf{V}^{-1/2} \mathbf{Ax} = \mathbf{V}^{-1/2} \mathbf{b} \quad (4.11)$$

where \mathbf{A} is the set of basis functions, \mathbf{x} are the basis function coefficients, \mathbf{b} are the measured values, and \mathbf{V} is the covariance matrix whose inverse square root can be calculated by eigen decomposition of \mathbf{V} and taking the inverse square root of the diagonal matrix. In order to calculate the covariance matrix for the ^3He maser phase we begin with a Johnson noise limited phase power spectral density,

$$\sigma_{\phi, Jp}^2 = \left(\frac{2}{T_2'} \right)^2 \frac{k_B T_M}{\mathcal{P}} \left(T_2'^2 + \frac{1}{\omega^2} \right) = \sigma_{\phi, w}^2 + \left(\frac{2\pi\sigma_{\nu, w}}{\omega} \right)^2 \quad (4.12)$$

where $\sigma_{\nu, w}$ and $\sigma_{\phi, w}$ are the white frequency and phase noise spectral densities, respectively, which we determine via the power spectrum of the data. The phase noise spectrum consists of a white noise and random walk noise component, which can be represented in the time domain with a discretely sampled set of phase measurements, ϕ_n , each taken at time $t_n = n\Delta t$ as,

$$\phi_n = \Delta\phi_n + 2\pi \sum_{i=0}^{n-1} \Delta\nu_i \Delta t \quad (4.13)$$

where $\Delta\phi_n$ and $\Delta\nu_n$ are independent random variables with expectation values $E(\Delta\phi_i) = E(\Delta\nu_i) = E(\Delta\phi_i \Delta\nu_j) = 0$ and variances,

$$\text{Var}(\Delta\phi_i) = \frac{\sigma_{\phi}^2}{2\Delta t} \quad \text{and} \quad \text{Var}(\Delta\nu_i) = \frac{\sigma_{\nu}^2}{2\Delta t}. \quad (4.14)$$

The variance and covariance of ϕ_n , which represent the diagonal and off diagonal terms of the covariance matrix, can now be calculated:

$$\text{Var}(\phi_n) = \frac{\sigma_\phi^2}{2\Delta t} + \frac{(2\pi\sigma_\nu)^2}{2}t_n \quad \text{and} \quad \text{Cov}(\phi_n, \phi_m) = \frac{(2\pi\sigma_\nu)^2}{2}t_n \quad \text{where} \quad n < m. \quad (4.15)$$

For our typical raw data set, sampled once per second over one sidereal day, $\sim 9 \times 10^4$ data points, the covariance matrix is too large for practical work; so instead we average together phase measurements in blocks of $2k + 1$ data points,

$$\bar{\phi}_n = \frac{1}{2k + 1} \sum_{i=n-k}^{n+k} \phi_i \quad (4.16)$$

which means the spacing between measurements is now $\Delta T = (2k + 1)\Delta t$. The new phase data points, $\bar{\phi}_n$, have the same covariance $\text{Cov}(\bar{\phi}_n, \bar{\phi}_m) = \text{Cov}(\phi_n, \phi_m)$, but a slightly different variance,

$$\text{Var}(\bar{\phi}_n) = \frac{\sigma_\phi^2}{2\Delta T} + \frac{(2\pi\sigma_\nu)^2}{2}\Delta t \left(n - \frac{2k(k+1)}{3(2k+1)} \right) \quad (4.17)$$

and we typically reduce the size of a sidereal data set to ~ 300 data points, which gives a more reasonably sized covariance matrix. The maser amplitudes used in the fit model are averaged in the same manner. In Sec. 4.2.2 we will validate these calculations using Monte Carlo tests.

4.2.2 Least Squares Periodograms and Monte Carlo Tests

We use least squares periodograms (LSP, see Sec. 4.2) and discrete Fourier transforms (DFT) of Monte Carlo generated data sets that match the measured maser power spectrum to test the efficacy of our data analysis methods. The DFT and the simple model LSP, which does not contain the correlation and drift terms, should have the same values since each quadrature contains only half the power, which implies a factor of $1/\sqrt{2}$ reduction. However, we are measuring the amplitude, not the RMS value, so the resultant increase by $\sqrt{2}$ cancels the quadrature effect and we should have identical values for DFT and LSP.

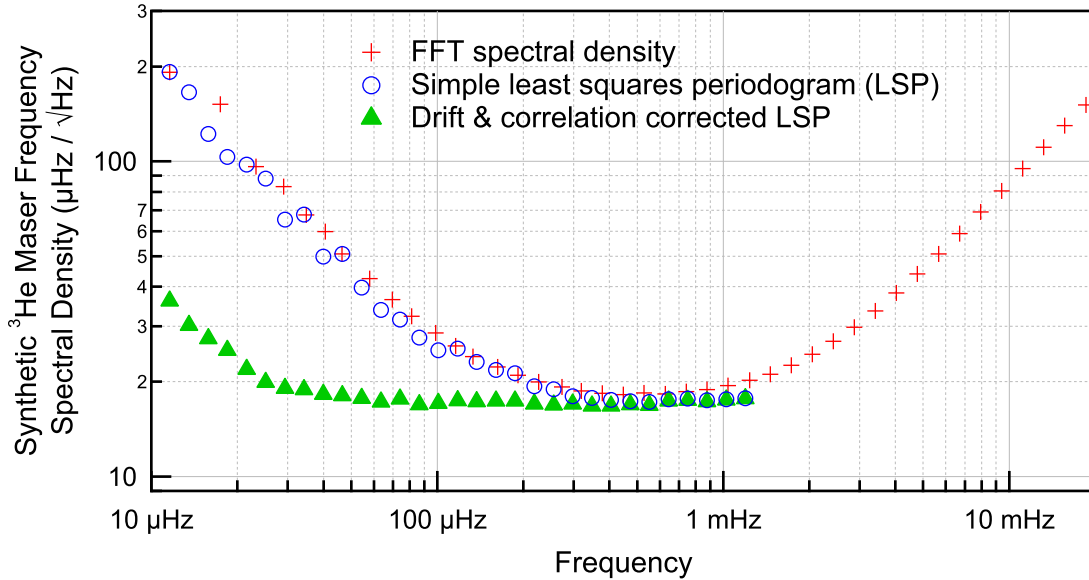


Figure 4.1: Monte Carlo synthetic data for ^3He maser frequency spectral density with random walk correlations.

In our first test we generate Monte Carlo data that has the same power spectrum as the data shown in Sec. 2.2.3. We use two random walk variables to generate the low frequency noise and then included them in our full model LSP; but we do not include a specific linear frequency drift in the Monte Carlo data. As expected, the simple fit model LSP and the DFT spectral density follow very closely, as shown in Fig. 4.1, but we find that the full model LSP does not maintain the expected white noise floor all the way down to the sidereal modulation frequency; and at the critical sidereal modulation frequency is a full factor of two above the expected white noise floor. This is due to a loss of independence between elements in the basis set of the model between the sinusoids, the linear term, and the random walk terms once the frequency of the sinusoids becomes low enough that there is only one full period in the data set. From the spectrum we see that we need to use data sets with approximately three full periods in order to restore full independence; however, we still obtain a reduced $\chi^2 = 1$ for the full fit model regardless of the frequency, confirming the correctness of our covariance matrix. To confirm the loss of independence between basis

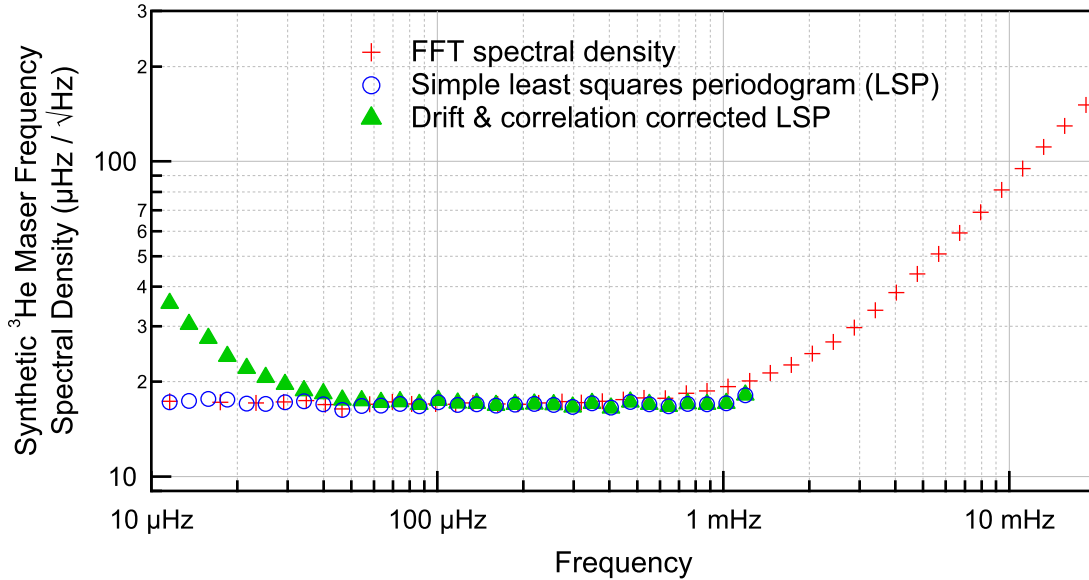


Figure 4.2: Monte Carlo synthetic data for ${}^3\text{He}$ maser frequency spectral density without random walk correlations.

sets we generate Monte Carlo data with no correlated random walk frequency noise and employ the full fit model, yielding the same power spectrum, although it still has a reduced $\chi^2 = 1$, as shown in Fig. 4.2. By trying all combinations of correlation and linear drift terms on this Monte Carlo data set we determined that each of these terms, linear or correlation, adds $\sim 30\%$ above the noise floor and extends the number of periods that must be included to ensure independence between the terms.

To determine the impact of these limitations on our analysis methodology of using data segments of one sidereal day in length, we run our full analysis procedure on the four weeks of data used in Sec. 2.2.3, which yielded 21 sidereal day data segments that passed our fit criteria. The spectrum for this data is shown in Fig. 4.3, where we see that our frequency shift corrections have reduced the frequency random walk by a factor of two, but this is still a factor of two greater than the limiting sensitivity found from our Monte Carlo tests. We can also confirm that the remaining fluctuations at the sidereal frequency are incoherent noise as the average values of $\delta\nu_X$ and $\delta\nu_Y$ are consistent with their standard errors. There

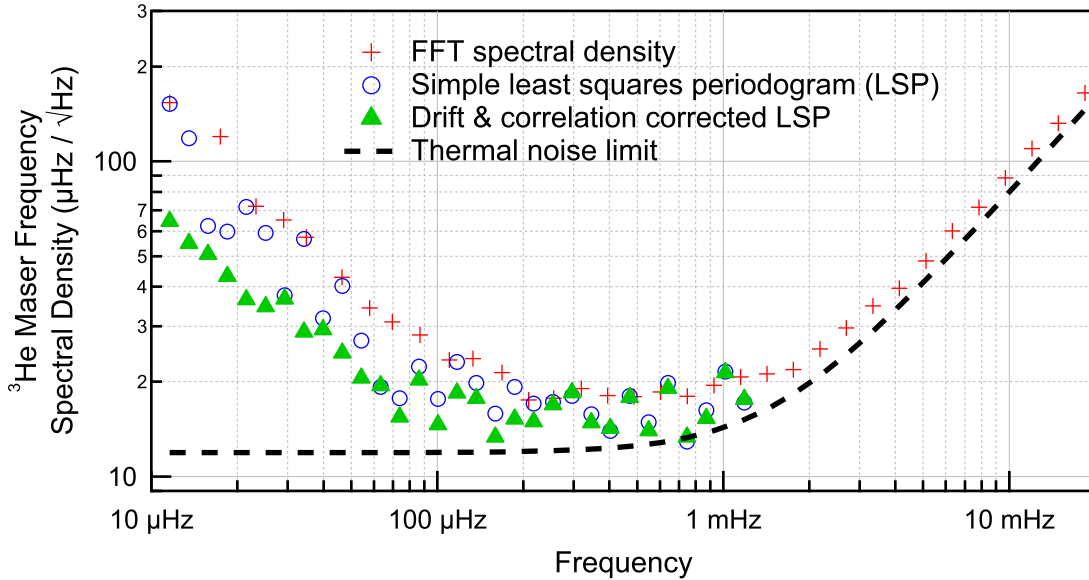


Figure 4.3: Measured spectrum with different fit models.

also appears to be greater disagreement between the simple LSP and DFT spectral densities than in the Monte Carlo data of Fig. 4.1. Note, however, that the periodic dips in the simple LSP compared to the DFT in the random walk regime are due to the combination of the effective rectangular window of the fit; the linear drift in the actual data, which is not present in the simulation used for Fig. 4.1; and the sampling of frequencies beyond the resolution of the data in the simple LSP, which are not present in the DFT spectra.

Despite the incomplete correction of frequency random walk in our data, all 21 sidereal data segments passed our χ^2 distribution cutoff. So to determine how likely that is, we generated a Monte Carlo data set that included correlated and uncorrelated frequency random walk components, but no linear drift term. We generated the usual spectral densities as well as a LSP without the correlation terms, but with a linear frequency drift term, as shown in Fig. 4.4, which matches the trends of the data spectrum in Fig. 4.3. From a plot of the probability distributions of the sum of the squares of the residuals of each fit model, with the sinusoidal frequency equal to the sidereal frequency shown in Fig. 4.5, we see that even though we only had a partial frequency correlation, the full fit model agrees very well with

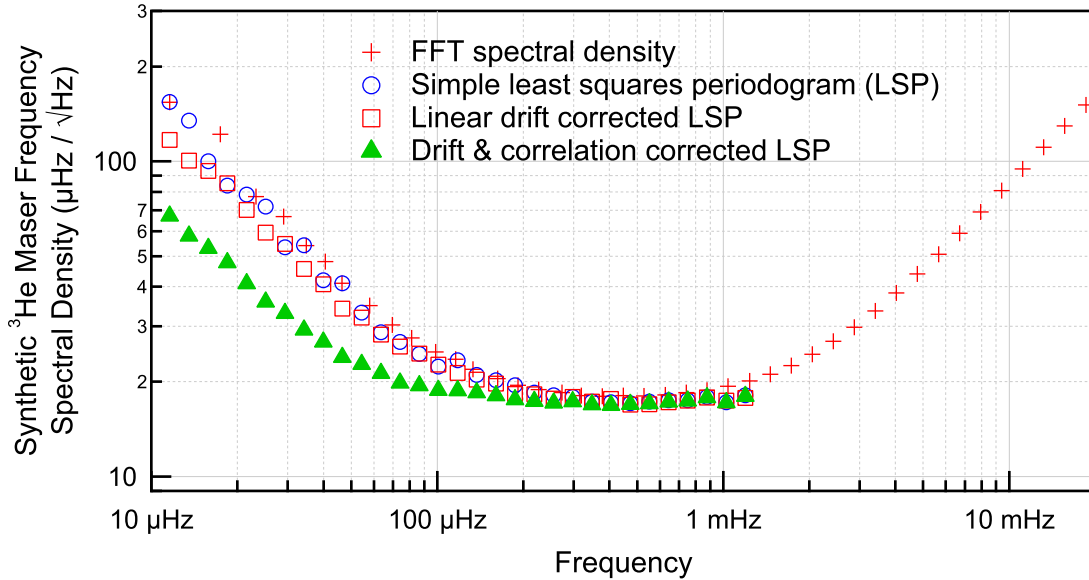


Figure 4.4: Monte Carlo synthetic data that matches the measured spectra for the ^3He maser frequency.

the theoretical χ^2 distribution and even the linear drift corrected model and uncorrected models have significant overlap. Additionally, the spectral densities of the portions of the simple and linear fit models that cross the 95% χ^2 line at the sidereal modulation frequency in Fig. 4.5 are only $\sim 15\%$ less than the values shown in Fig. 4.4, so there could be significant corruption of the real data due to the extensive overlap of the distributions.

Although the agreement between the sum of squares of residuals and the χ^2 distribution is initially surprising as we are a factor of four or more from the noise floor, recall that the sum of squares is the integral of the power spectrum and our random walk frequency noise, while very detrimental to our sensitivity, only occurs over a relatively small fraction of the spectrum. There are several ways to reduce the possibility of contamination of the data by segments that are uncorrelated with the model. Decreasing the χ^2 cutoff point shown in Fig. 4.5 would eliminate more of the uncorrelated data sets, but at the cost of correlated data sets, which ultimately does not improve our sensitivity. Averaging the data down to fewer points before fitting decreases the overall bandwidth and increases the fraction of the

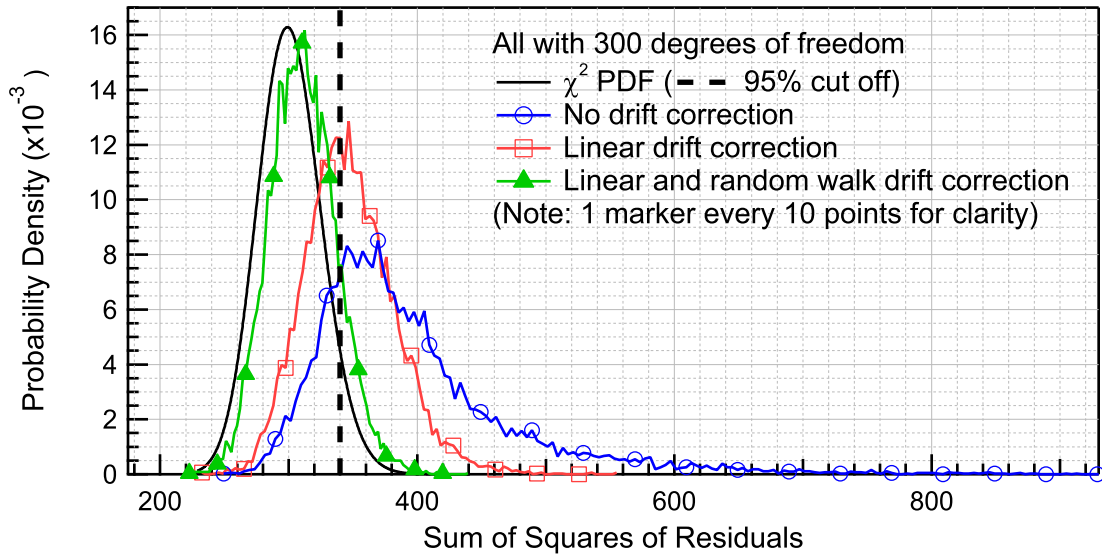


Figure 4.5: Distributions of the sum of the squares of the residuals for different ${}^3\text{He}$ maser phase fit models of the matched Monte Carlo synthetic data looking for one sidereal day modulations. For 300 degrees of freedom, the bandwidth of the fit goes up to a Nyquist frequency of 1.8 mHz and thus the residuals are dominated by white frequency noise and not the low frequency random walk μ component that starts around 150 μHz , see Fig. 4.4.

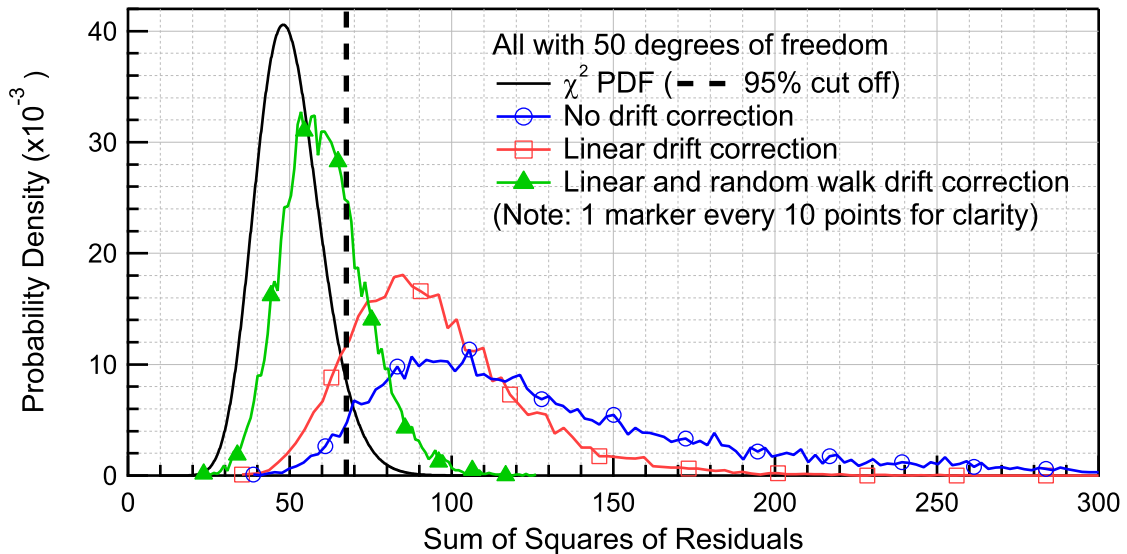


Figure 4.6: Fit model residual distributions for the same data set as above, reduced to 50 degrees of freedom. The bandwidth of the fit goes up to a Nyquist frequency of 330 μHz and thus the residuals contain a considerable amount of the low frequency random walk μ component that starts around 150 μHz leading to less overlap between χ^2 and the linear and uncorrected distributions.

total noise power due to the random walk, which improves rejection of uncorrelated data sets as shown in Fig. 4.6; but this has diminishing returns for our data once the Nyquist frequency reaches the corner frequency of the random walk. Fitting longer data segments would also increase the fraction of the total noise power due to the frequency random walk and improve our rejection of data which does not fit our model; but while it does lead to a data set with a smaller standard deviation, we have to throw out so much data, since we are unable to use short data segments, that there is no improvement in the standard error and hence no real improvement in our sensitivity. Reducing the bandwidth by increasing the averaging does help improve sensitivity (see the improvement in Fig. 4.7), but the only real improvements would be to fix the source of the random walk drifts (which we believe to be due to the optical pumping laser, see Sec. 3.4) or to rotate the experiment at a frequency higher than the corner of the random walk noise (without inducing other systematic technical problems) as discussed in Sec. 2.4.1.

4.3 Preliminary Results Compared to Previous Maser

In this section we show the improvements to the maser frequency spectral density compared to the previous maser system used in [43]. Our current maser data set is the same as in Sec. 4.2.2, but we use a reduced bandwidth to improve sensitivity when determining good matches to our fit model, as described in Sec. 4.2.2, and a wider bandwidth to calculate the LSPs for the chosen data segments. From four weeks of data from the current system we choose 19 one sidereal day segments using our methodology, compared to ~ 90 days of data using the previous system. Note, we where we have used the data segments they picked and calculated the spectra from those segments as shown in Fig. 4.7.

The primary realized differences between the previous and current systems, based on the spectra shown in 4.7, are the improved SNR of the current system, the reduced coupling of maser amplitude fluctuations into frequency of the current system, and the closer approach of the current system to the theoretical thermal noise limit. This overall improvement in

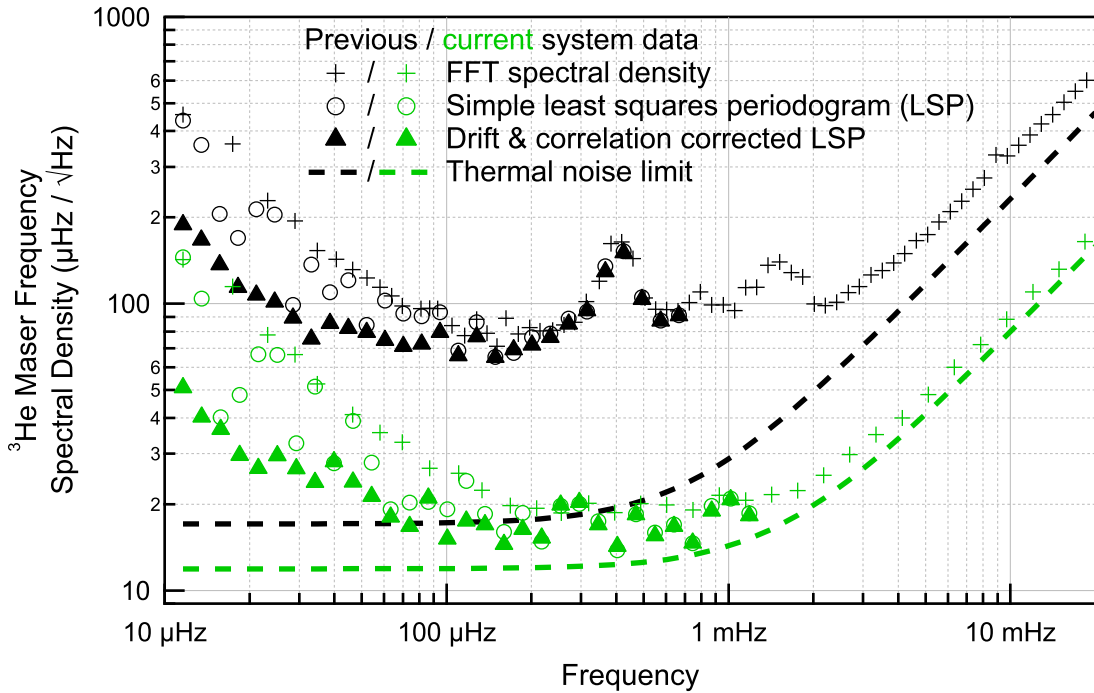


Figure 4.7: Previous and current system spectral densities for the ^3He maser.

the thermal noise limit of the current system is due entirely to the increased maser power, and hence SNR, of the current system as can be seen by the factor of >3 improvement in the measured white phase noise of the current system (the improvement in the measured white frequency noise is more complicated, as we will discuss shortly). Most of the increase in maser power for both ^3He and ^{129}Xe is due to an increase of B_0 by a factor of four. The remainder of the increase in the ^3He maser power due to a slightly higher pump bulb temperature and hence n_{Rb} , with the increase in the pump bulb volume mostly offset by the decrease in ^3He gas density and the remainder of the increase in the ^{129}Xe maser power due to an increase in the transfer tube diameter and shortening of the transfer tube length, which is partially offset by the decrease in the fraction of ^{129}Xe that makes up the total gas pressure (see Sec. 2.5.2 for the scaling of maser power with system parameters). There is significant coupling of the maser amplitude fluctuations into the maser frequency in the previous system from both ^3He at $400\ \mu\text{Hz}$ and ^{129}Xe at 1.5 mHz , which is due to both the much larger

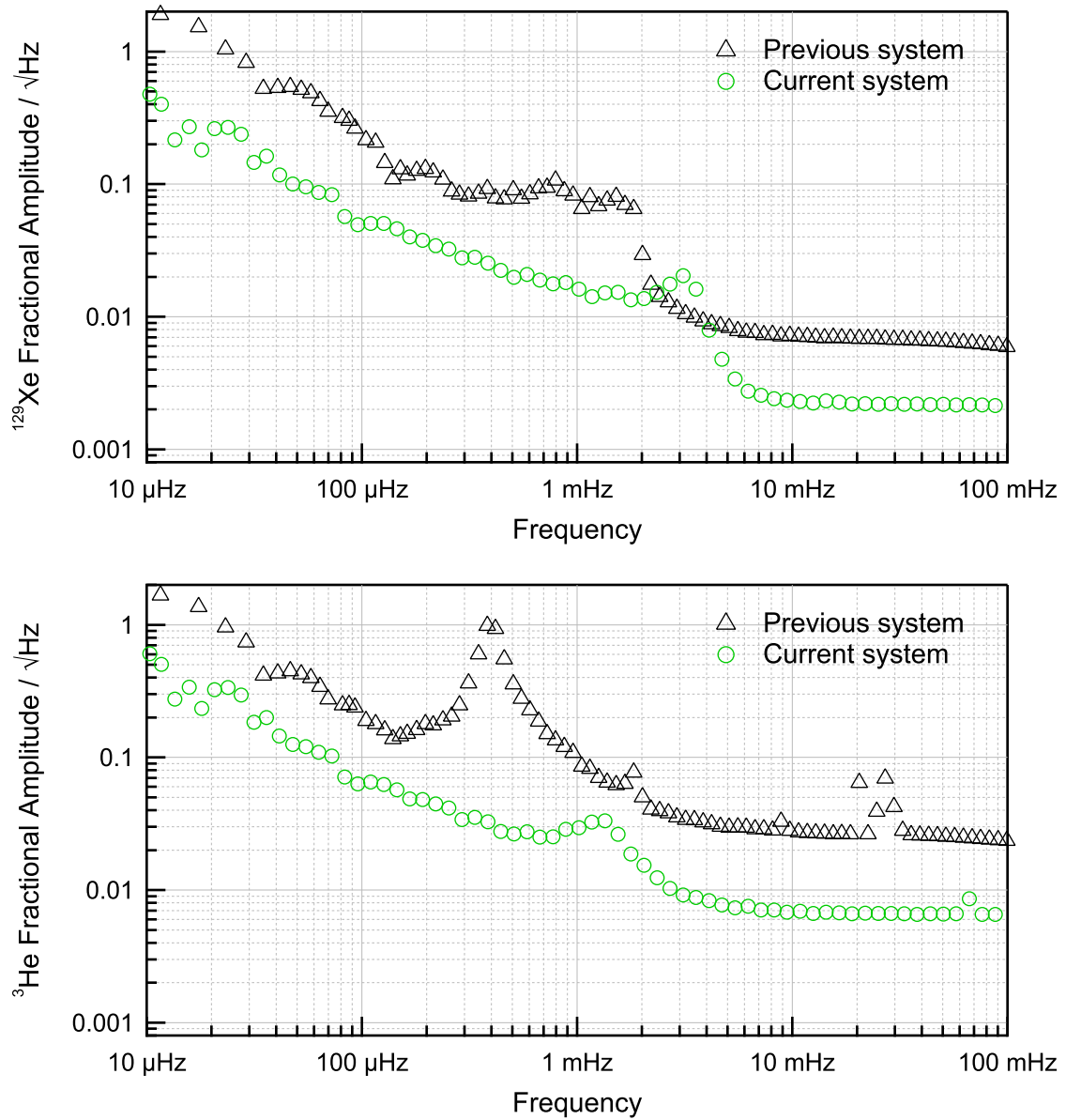


Figure 4.8: Previous and current system maser fractional amplitude spectral densities.

fractional fluctuations in the maser amplitudes compared to the current system, as can be seen in Fig. 4.8, as well as larger amplitude to frequency coupling coefficients in the previous system, since the maser bulb was not a sphere and hence had larger self field interactions (see Sec. 2.1.3 and Sec. 2.2.3 for self field and transient interactions). Additionally, the larger low frequency fractional fluctuations in the previous system point to a more unstable pump bulb environment, which drives many of the frequency shift mechanisms listed in Sec. 2.4, leading to the larger random walk noise observed in the previous system compared to the current one in Fig. 4.7.

The current system is much closer to its thermal noise limit than the previous system, especially for the white frequency noise regime where the previous system is a factor of >3 above the thermal limit. To calculate the thermal noise limit for the previous system we used the longest T'_2 times reported in [43], 330 s for ^{129}Xe and 170 s for ^3He , for all the data sets and calculated the power for each data set based on the maser amplitude and the values for ω_M , L_{pu} , q_c , and G_{amp} reported in [43]. However, it is possible that there was a bias in the measured ^3He T'_2 making them appear longer than they actually were due to feedback from the pickup coil as described in Sec. 3.7, as the procedure for trimming the magnetic field gradients to optimize T'_2 in the previous system called for waiting for the noble gases to fully polarize and reach steady state. The increased white phase noise of the previous system compared to its theoretical limit, on the other hand, is due to vibrations of the pickup coil in the magnetic field (as discussed for the current system in Sec. 2.5.1), which generated noise above the thermal limit in the resonant circuit and affected both white phase and frequency noise. The increase in white phase noise shown in Fig. 4.7 agrees well with the $\sim 40\%$ increase measured for the previous system in [43]; and this 40% should also be taken into account with the white frequency noise limit.

In addition to the explanations mentioned above, the previous system's increased frequency noise was caused by amplitude to frequency noise coupling. If we divide the data into two groups based on the frequency noise in the flat region around $150 \mu\text{Hz}$ into a large and small amplitude frequency noise (31 data sets are large and 61 are small), as shown in

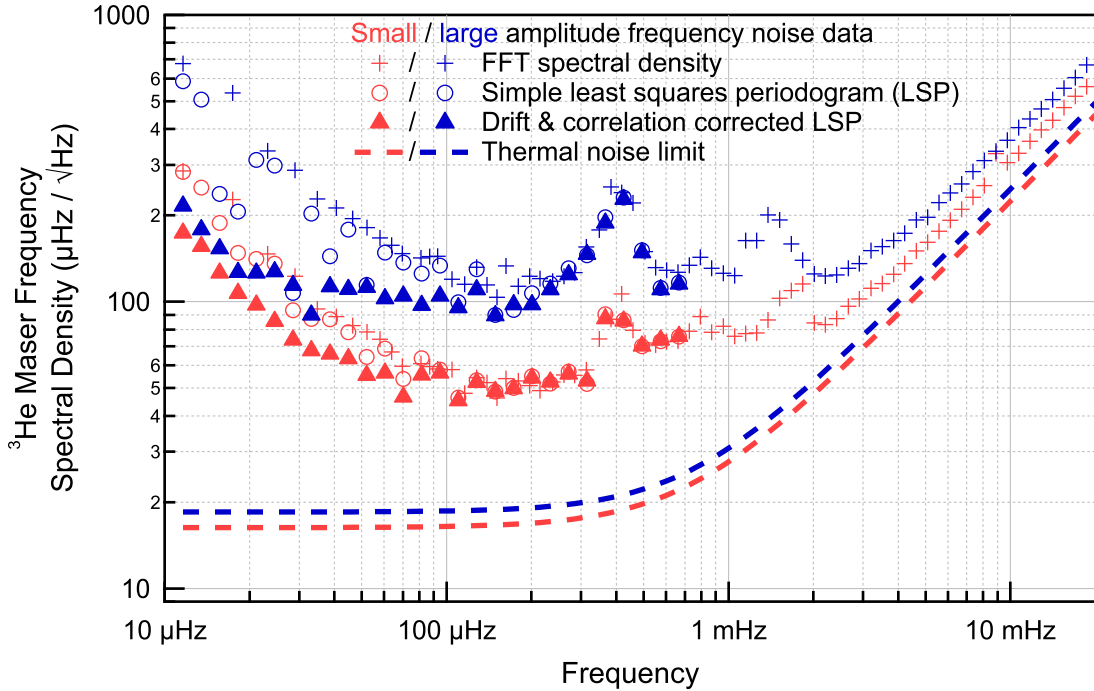


Figure 4.9: ^3He maser spectra from the previous system grouped into small and large frequency noise sets.

Fig. 4.9, we find that the small amplitude noise group shows significantly reduced resonance peaks from the amplitude noise in addition to having a lower flat noise region. Additionally, the large amplitude noise group shows excellent reduction of its low frequency noise when the full fit model is used, to the point that it matches the small amplitude limit, again emphasizing the amplitude to frequency coupling. The current system has reduced all of these shortcomings by using a spherical maser bulb, which reduces amplitude to frequency couplings; and a lower ^{129}Xe pressure, which reduces the amount of light absorbed to polarize the same amount of Rb as in the previous system and hence reduces the thermal load and fluctuations the laser places on the pump bulb and the frequency shifts caused by those fluctuations.

Chapter 5

Anomalous Spin-Spin Coupling Measurements

Searches for new spin-spin forces can be interpreted using a variety of theoretical frameworks and different spin-spin coupling potentials within those frameworks, not all of which can even be tested simultaneously. However, they all require the same basic experimental ingredients: a sensitive detector with spin, in our case the ^3He and ^{129}Xe masers; and a source of spins, for which we use a large glass cell filled with high pressure, high polarization ^3He , which should be located as close to the detector as possible. In order for a complete search for new spin-spin forces we also have to consider the particles carrying the spin and test all possible pairs of electron, proton, and neutron spins. However, before our measurement there had not been a search for anomalous neutron-neutron spin coupling.

Practically speaking, tests of anomalous spin-spin couplings have one primary advantage over searches for Lorentz symmetry breaking background fields to the universe: the ability to choose the modulation frequency of the interaction mediating possible new physics. Thus, unlike in Ch. 4, the analysis of the sensitivity level achieved by the ^3He and ^{129}Xe maser is fairly straightforward and agrees well with our white frequency noise floor. However, the limits placed on the new physics are not just determined by the sensitivity of the detector, but also the proximity and size of the source, which adds additional complications and

further optimization.

5.1 Limits on Anomalous Spin-Spin Couplings Between Neutrons

Below we reproduce the paper we published on searches for new spin dependent forces [7]. Note that the results given here have since been surpassed by an experiment performed by the Romalis group [9] by approximately three orders of magnitude for all relevant interactions. The experimental techniques and physics for our experiment are no different than those we have discussed in the previous chapters with one exception: we use the adiabatic fast passage technique from NMR to change the orientation of the ^3He spins in the spin source. However, we made no attempt to optimize this procedure as the first set of parameters we used enabled rotation of the spins with a low enough loss rate for our purposes. Subsequently, a far lower loss rate (three orders of magnitude improvement) was obtained for a similar ^3He spin source in [9].

Limits on Anomalous Spin-Spin Couplings Between Neutrons

Alexander G. Glenday,^{1,2} Claire E. Cramer,¹ David F. Phillips,¹ Ronald L. Walsworth^{1,2}

¹*Harvard-Smithsonian Center for Astrophysics, Cambridge, Massachusetts 02138.*

²*Department of Physics, Harvard University, Cambridge, Massachusetts 02138.*

Abstract

We report experimental limits on new spin-dependent macroscopic forces between neutrons. We measured the nuclear Zeeman frequencies of a ${}^3\text{He} / {}^{129}\text{Xe}$ maser while modulating the nuclear spin polarization of a nearby ${}^3\text{He}$ ensemble in a separate glass cell. We place limits on the coupling strength of neutron spin-spin interactions mediated by light pseudoscalar particles like the axion ($g_p g_p / (4\pi\hbar c)$) at the 3×10^{-7} level for interaction ranges longer than about 40 cm. This limit is about 10^{-5} the size of the magnetic dipole-dipole interaction between neutrons.

Searches for new spin-dependent macroscopic forces explore possible physics beyond the Standard Model, such as Lorentz symmetry violation and the existence of new particles like the axion. Searches for anomalous couplings between spins have typically been interpreted in terms of forces mediated by the axion, which is of interest as a solution to the strong CP problem and a dark matter candidate [2]. In more recent theoretical work, Arkani-Hamed and coworkers have considered the dynamical effects of broken Lorentz symmetry added to the Standard Model, which include new spin-dependent forces [75]. A phenomenological theory developed by Dobrescu and Mocioiu enumerates all possible spin dependent forces that satisfy rotational invariance and standard assumptions of quantum field theory [76]. This theory includes axion-mediated forces as well as the more complex Lorentz symmetry violation considered by Arkani-Hamed and coworkers. In all cases, the strength of the coupling between spins is dependent on the particle species e.g., electron, neutron, proton;

and so a complete experimental survey should cover all particle combinations. There are existing experimental limits on coupling of electron spins to all other species [77, 78, 79], as well as a limit on proton-proton coupling [80]; but there is no published limit on neutron-neutron spin coupling.

To measure new couplings between neutron spins we monitored the nuclear Zeeman frequencies of a $^3\text{He}/^{129}\text{Xe}$ maser, our detector for new spin dependent forces, while modulating the nuclear spin polarization of an ensemble of ^3He atoms in a separate cell, our spin source. Anomalous dipole-dipole couplings between the longitudinally polarized source and maser spins will lead to an additional torque on the precessing maser spins and thus a frequency shift. The two-species $^3\text{He}/^{129}\text{Xe}$ maser has been described previously [81, 82, 83, 5, 6]; here we provide a brief review of its design and operation (see schematic in Fig. 5.1). Collocated ensembles of ^{129}Xe and ^3He atoms at pressures of hundreds of Torr are held in a double-chamber glass cell placed in a homogeneous magnetic field of 6 G. Both species have spin-1/2 nuclei and the same sign nuclear magnetic dipole moment, but no higher-order electric or magnetic nuclear multipole moments. In one chamber of the glass cell, the pump bulb (maintained ≈ 135 °C), the noble gas atoms are pumped into a nuclear Zeeman population inversion by contact interactions with optically-pumped Rb vapor [12]. The noble gas atoms diffuse into the second chamber, the maser bulb (maintained ≈ 45 °C), which is surrounded by an inductive coil connected to a circuit resonant at both the ^3He and ^{129}Xe nuclear Zeeman frequencies (19.6 kHz and 7.1 kHz, respectively). For a sufficiently high flux of population-inverted nuclear magnetization, active maser oscillation of both species can be maintained indefinitely. The maser is protected from external magnetic fields by three layers of magnetic shielding. By comparing one of the noble-gas masers to a stable frequency reference (a hydrogen maser), we can stabilize the magnetic field and then use the other noble gas maser as a sensor for new spin dependent forces. This application relies on the fact that the gyromagnetic ratios of ^3He and ^{129}Xe differ by a factor of ~ 2.75 , whereas the coupling to new spin-dependent forces should be very similar for the two noble gas species since the neutron is the primary contributor to the nuclear spin for both ^3He

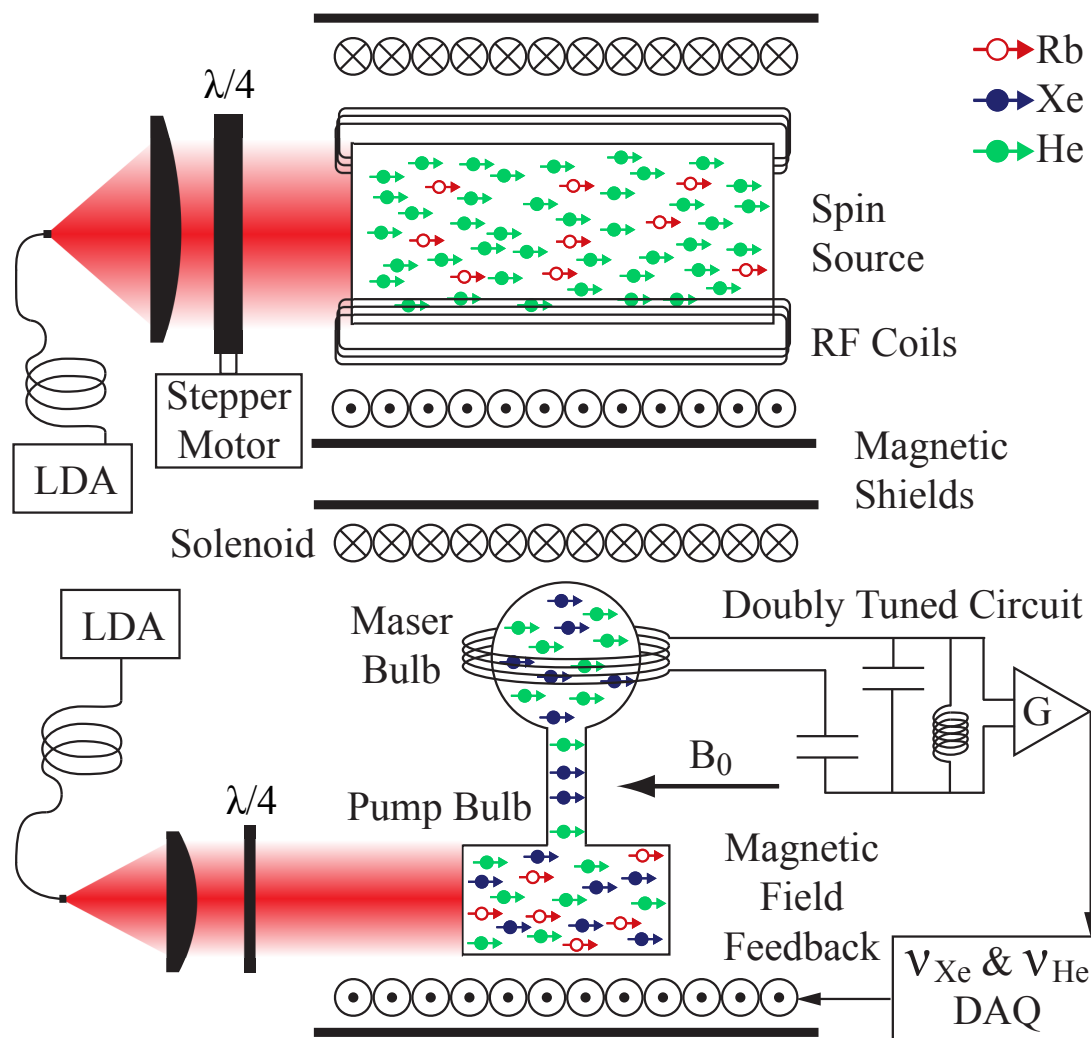


Figure 5.1: Experimental schematic showing the ^3He spin source on top and the ^3He and ^{129}Xe maser on the bottom (not to scale). LDA is a laser diode array and DAQ is the data acquisition system.

and ^{129}Xe (approximately 87% [4] and 75% [3], respectively and with uncertainties less than or equivalent to experimental errors). For all the measurements reported in this paper the magnetic field was locked using the ^{129}Xe maser frequency referenced to a hydrogen maser. Thus the difference between the ^3He maser frequency and the reference is given by,

$$\nu_{He} - \frac{\gamma_{He}}{\gamma_{Xe}}\nu_{Xe} \approx (0.87 - 0.75\frac{\gamma_{He}}{\gamma_{Xe}})\nu_{SF} \approx -1.2\nu_{SF},$$

where ν_{He} and ν_{Xe} are the respective $^3\text{He}/^{129}\text{Xe}$ maser frequencies, γ_{He} and γ_{Xe} are the respective $^3\text{He}/^{129}\text{Xe}$ gyromagnetic ratios, and ν_{SF} is the frequency shift due to an anomalous spin dependent force between neutrons.

Recent upgrades to the $^3\text{He}/^{129}\text{Xe}$ maser have yielded an order of magnitude improvement in frequency stability on timescales of hours, relative to earlier versions of the device [83, 5, 6]. These upgrades include optimization of the noble gas pressures, double bulb cell geometry, and the temperature control and optical pumping systems to maximize maser amplitudes and coherence times; as well as an increase in main magnetic field and hence Zeeman frequency to increase maser power.

For the neutron spin source we used a valved Pyrex glass cell filled with 6.5 amg of ^3He , 0.2 amg of N_2 , and 100 mg of Rb (see schematic in Fig. 5.1). The cell is a cylinder with total volume of 88 cc (12 cm long, 3 cm diameter) and is housed inside an insulated glass oven heated to 160 °C with blown air. The oven is surrounded by a pair of RF coils designed to efficiently invert the ^3He spin polarization via adiabatic fast passage (AFP). The RF coil field homogeneity (few percent across the cell) ensures accurate determination of the ^3He polarization by measuring the amplitude of spin precession induced by resonant NMR pulses. The cell is centered inside a solenoid, which provides a static magnetic field of 1 G and serves as the spins' quantization axis (parallel to the maser's magnetic field). The solenoid has separate end-coils to optimize the magnetic field homogeneity, which is achieved by maximizing the ^3He spin coherence time in the spin source. The high homogeneity of the static magnetic field is necessary to minimize polarization loss due to diffusion through

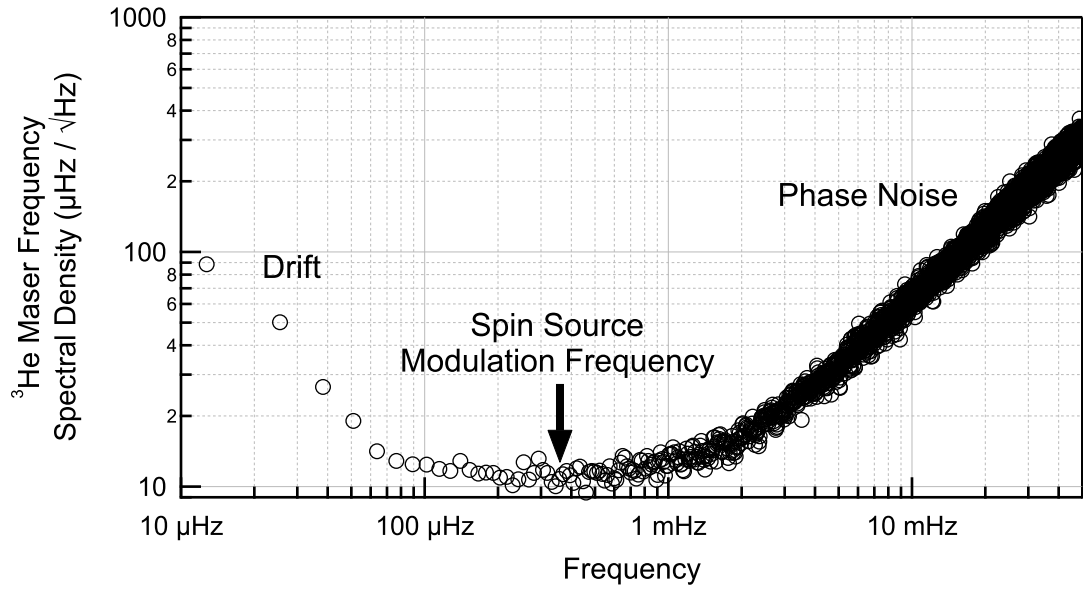


Figure 5.2: Noise spectrum of the ^3He Zeeman maser frequency averaged from three weeks of data. The modulation period of the spin orientation of the spin source was chosen to lie in the white frequency noise dominated part of the spectrum to avoid phase noise at high frequencies and drift at low frequencies.

transverse field gradients. Also, the relatively long ^3He spin coherence time (~ 2 sec) improves polarization measurement accuracy by avoiding dead-time errors between inducing and measuring the spin precession. A cylindrical magnetic shield (38 cm diameter) with endcaps surrounds the spin source. A laser diode array (LDA) shines 25 W of Rb D1 resonant (~ 795 nm), circularly polarized light onto the cell, spin-polarizing the ^3He to $12 \pm 1\%$ by spin-exchange collisions with the optically pumped Rb. Given this level of polarization the spin source contains 1.8×10^{21} polarized ^3He spins located 41 cm from the maser bulb of the $^3\text{He}/^{129}\text{Xe}$ maser (determined relative to the center of the spin source cell and maser bulb).

To modulate the orientation of the ^3He spins in the source, we adiabatically transferred the spins between states by sending a drive signal through the RF coils and scanning this RF signal through the Zeeman resonance on a timescale of ~ 100 msec. The adiabatic transfer was very efficient with only 0.1% fractional loss of total polarization per transfer, as

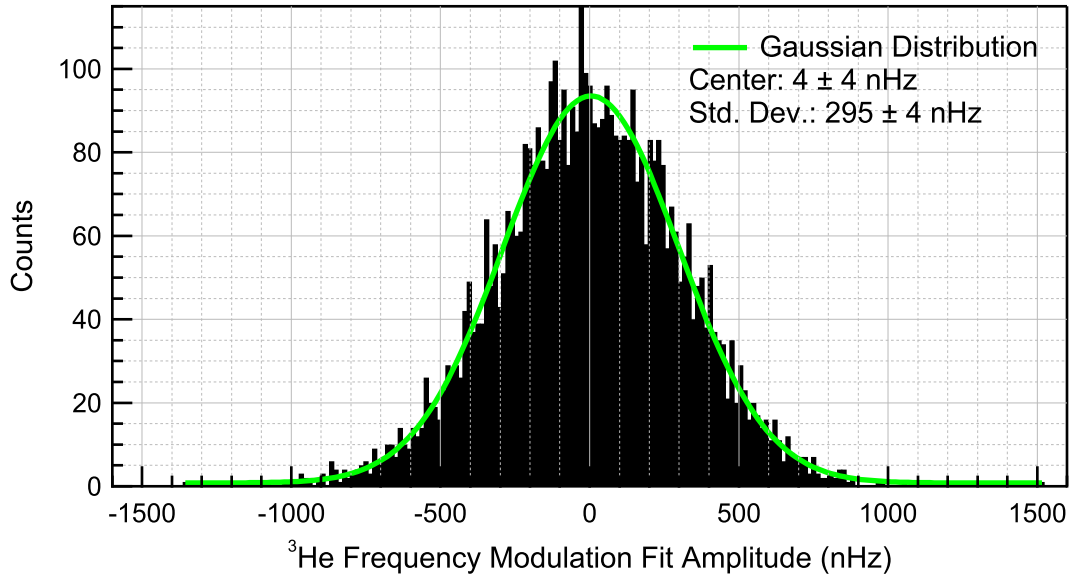


Figure 5.3: Distribution of frequency modulation amplitudes from the fit of the ^3He Zeeman maser frequency to the modulated spin orientation of the spin source. The amplitudes have a Gaussian distribution that agrees well with the noise spectrum shown in Fig. 5.2.

measured by the change in amplitude of induced ^3He spin precession after multiple transfers. In order to maintain a high ^3He polarization level, the angular momentum delivered by the laser must always be in the same direction as the ^3He spins; so we inverted the quarter wave plates using a stepping motor each time we adiabatically reversed the ^3He spin state (Fig. 5.1). The spins and quarter wave plates were typically reversed once every 20 minutes to maximize the $^3\text{He}/^{129}\text{Xe}$ maser sensitivity given white phase noise at short times and long term drifts (see Fig. 5.2) and to avoid room temperature and other system parameter oscillations which have shorter periods.

We collected ^3He maser frequency data for approximately 85 days, resulting in a data set of 3054 modulation periods of the spin source. We analyzed the data in blocks of one spin source modulation period using a least squares fit of the phase of the ^3He maser to the time integrated state of the ensemble ^3He spin in the source (a triangle wave). To eliminate the effects of linear frequency drift, fits were calculated starting every half period giving a total of 6107 fits. We performed fits on the time variation of maser phase

(rather than frequency) to retain a χ^2 distribution of the sum of squares of residuals since the (approximately square wave) spin modulation has significant harmonic components in the white phase noise spectrum of the data (Fig. 5.2). Phase noise was estimated using the modified Allan deviation of the ^3He maser frequency. We rejected fits whose sum of squares of residuals had less than 5% probability given the χ^2 distribution (final results are insensitive to the choice of cutoff), leaving a data set of 4966 fits. Fig. 5.3 shows the distribution of these fit amplitudes converted from phase to frequency. The weighted mean of fit amplitudes that passed the χ^2 test gives a shift of the ^3He Zeeman frequency of 1.9 ± 6.1 nHz (one σ uncertainty). The standard error of this weighted mean was determined using the number of independent modulation periods included in determining the mean (2483). We verified our fitting procedure using a Monte Carlo simulation of the data.

The leading systematic error was the limitation of the magnetic shields and maser co-magnetometry to reject magnetic coupling to the spin source. To test this limitation we performed separate experiments in which we modulated the 1 G quantizing magnetic field of the spin source with the same period that we modulated the spins in the spin source. At the location of the maser bulb this applied magnetic field is 5.5×10^4 larger than the field from the magnetization of the ^3He spins in the spin source. We set a limit of 50 nHz on variation of the ^3He maser frequency induced by the modulated magnetic field; which, after rescaling to the field generated by the spin source, means that this systematic effect is < 1 pHz, far below our statistical sensitivity to anomalous spin-spin couplings.

To interpret the significance for theoretical models of the experiment presented here, we simplify the theoretically proposed new spin-spin interactions to only include parallel spin cases. For example, the potential between two parallel neutron spins mediated by the axion and axion-like pseudoscalar particles is (in SI units):

$$V(r) = \frac{g_p^n g_p^n}{4\pi\hbar c} \frac{\hbar^3}{4m_n^2 c} \left(\frac{1}{\lambda r^2} + \frac{1}{r^3} \right) e^{-r/\lambda}, \quad (5.1)$$

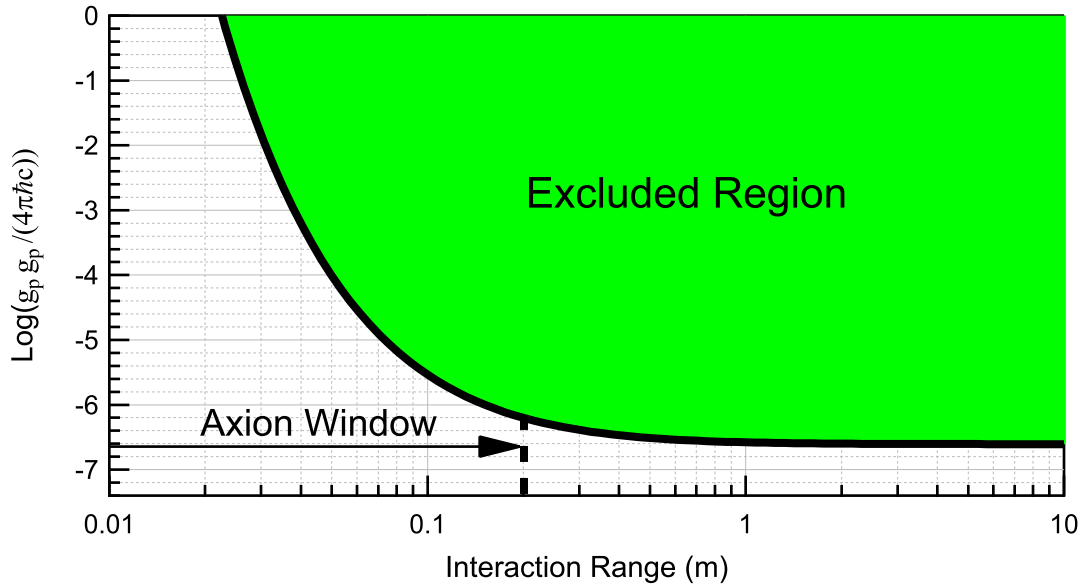


Figure 5.4: One σ excluded region from the present experiment for the dimensionless coupling constant $g_p^n g_p^n / (4\pi\hbar c)$ as a function of interaction range for a neutron-neutron spin interaction mediated by the axion or an axion-like pseudoscalar particle (see Eq. 5.1).

where $g_p^n g_p^n / (4\pi\hbar c)$ is the dimensionless coupling constant, m_n is the neutron mass, r is the separation between spins, and λ is the Compton wavelength of the axion-like particle that determines the range of the interaction [2]. While constraints on the axion interaction from astrophysical observations correspond to $\lambda \sim 20$ cm to $200 \mu\text{m}$ [84], other axion-like pseudoscalars are not constrained in this way [85]. Our measurement, when interpreted in terms of an axion-like mediated force between neutrons and including finite-sample-size effects, leads to a one σ limit of $g_p^n g_p^n / (4\pi\hbar c) < 3 \times 10^{-7}$ for distances longer than about 41 cm, with the full exclusion region shown in Fig. 5.4. The theoretical estimate for the size of $g_p^n g_p^n / (4\pi\hbar c)$ for axions that would solve the strong CP problem is $5 \times 10^{-30} \text{m}^2 / \lambda^2$ which is far below our limit or any that could be set with a similar experiment [86].

Next we consider the broken symmetry proposed by Arkani-Hamed and coworkers, which gives rise to Goldstone bosons whose exchange between fermions leads to a long range $1/r$ spin dependent potential [75]. The potential also depends on where the spins being measured are located relative to the spin source that generates the potential and its motion relative

to the background field of Goldstone bosons. The form of the Goldstone boson mediated potential between two parallel spins is (in SI units, except where noted):

$$V(r) = - \left(\frac{M}{F} \right)^2 \frac{\hbar c}{8\pi} \frac{1}{r} A(\alpha, \gamma, \theta_v), \quad (5.2)$$

$$\alpha = M \frac{rv}{\hbar c^2}, \quad \gamma = M \frac{Rv}{\hbar c^2}, \quad \cos \theta_v = \hat{r} \cdot \hat{v},$$

where M (given in eV) is the spontaneous symmetry breaking scale, F (given in eV) is the mass scale determining the strength of the coupling to Dirac fermions ($\frac{M}{F}$ is the dimensionless coupling), r is the separation between spins, and R is the radius of the spin source. The final term, $A(\alpha, \gamma, \theta_v)$, gives a parabolic shadow in the wake and shockwaves in front of the spin source as it moves at velocity v with respect to the rest frame of the background field, which is taken to be the rest frame of the CMB (see Fig. 5.5). The velocity of the spin source relative to the CMB rest frame is assumed to be given by the dipole moment of the CMB, which has been measured as $1.23 \times 10^{-3} c$ [87]. This gives a vector that sweeps out a cone (inner angle of 166°) in the local lab frame over the course of a sidereal day. As a further simplification to the potential we only consider interactions in the parabolic shadow region of $A(\alpha, \gamma, \theta_v)$, whose boundary with the shockwave region is well approximated by $x = 3.15 - 0.0796y^2$, where $y = \alpha \sin \theta_v$ and $x = \alpha \cos \theta_v$, for $\gamma < 1$. For larger γ the parabola is still an excellent approximation for $\alpha > 5\gamma$ where errors only develop in the offset of the parabola ($\sim 20\%$ for $\gamma = 10$). The value of $A(\alpha, \gamma, \theta_v)$ in the shadow region is approximated as being uniformly 0.7 (the average value of A for most transits across the shadow region) and the shockwave region is set to zero. Errors introduced by these approximations and finite-sample-size effects were all on the same scale, or smaller, than experimental uncertainties.

The sensitivity of our experiment to the potential derived by Arkani-Hamed and coworkers (Eq. 5.2) depends on M , as this determines the width of the parabolic wake generated by the spin source and hence the fraction of the sidereal day for which there is any potential to measure. For example, for values of $M < 1$ meV, at which point there is a non-zero

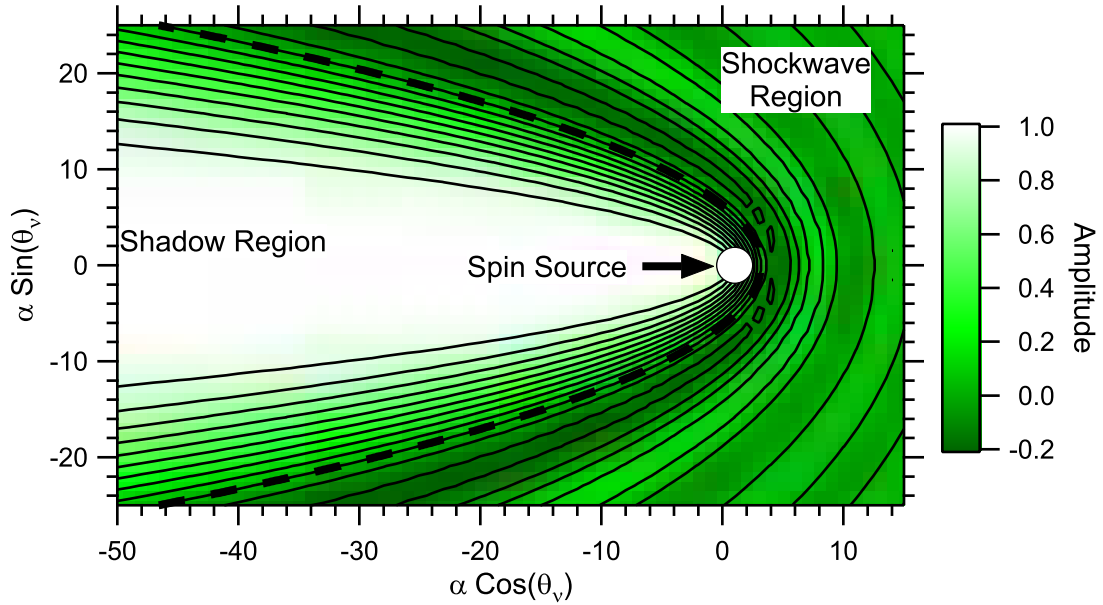


Figure 5.5: Calculation of amplitude $A(\alpha, \gamma, \theta_v)$ for $\gamma = 0$ for the Goldstone boson mediated potential between two parallel spins (see Eq. 5.2). The dashed line is the parabolic approximation for the boundary between the shadow and shockwave regions.

potential between the spins for the whole day, we find a one σ limit of $\frac{M}{F} < 4 \times 10^{-19}$. The exclusion region due to the spin-spin potential is shown in the center of Fig. 5.6, where the fractional averages of the full data set used to calculate each point are all consistent with zero. The left hand side of the figure shows the regime where the effective field theory breaks down and is no longer predictive. The right hand side of the figure includes the bounds previously set by the $^3\text{He}/^{129}\text{Xe}$ maser for a Lorentz violating background field as the Earth, and hence the experiment, rotated over a sidereal day [75, 5]. While there is no theoretical estimate for the size of M or F , the Goldstone bosons that mediate the spin force have particular cosmological significance for two values of M . If $M \sim 1$ meV then the bosons could be dark energy and if $M \sim 1$ eV then the bosons could be a dark matter candidate.

Finally, we consider the phenomenological theory developed by Dobrescu and Mocioiu, which contains nine new spin dependent potentials. Six of these depend on the relative velocity between the spins (zero in our experiment). Of the remaining three potentials, one

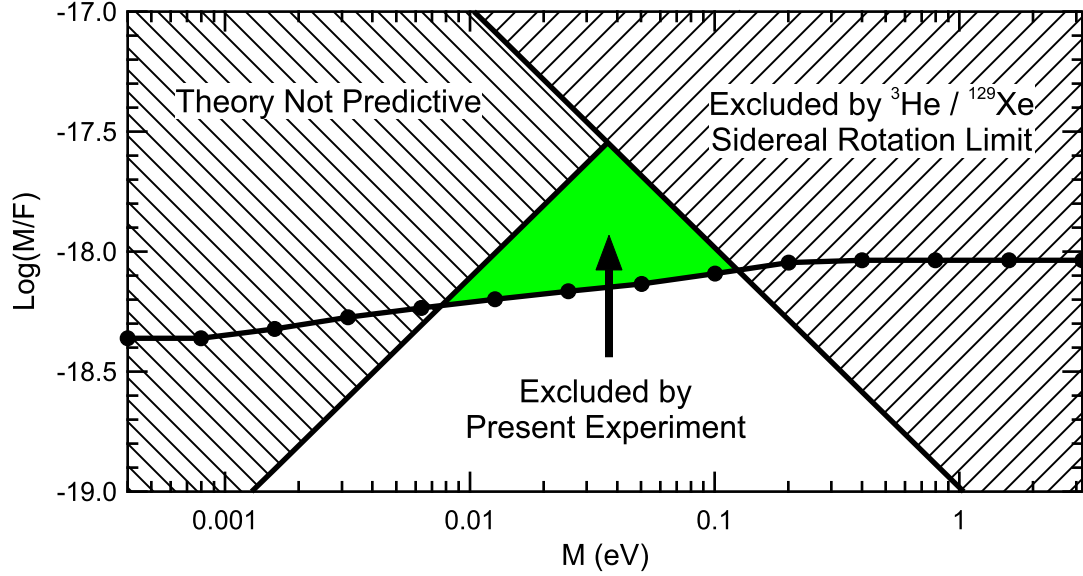


Figure 5.6: One σ excluded region from the present experiment for neutron-neutron spin coupling as described by Eq. 5.2 (see text).

is the same as the axion potential and one requires perpendicular rather than the parallel spin orientation in our experiment. This leaves the following potential between two parallel spins (in SI units)

$$V(r) = -\frac{g_A^n g_A^n}{\hbar c} \frac{\hbar c}{4\pi r} e^{-r/\lambda}, \quad (5.3)$$

where $g_A^n g_A^n / (\hbar c)$ is the dimensionless coupling constant, r is the separation between spins, and λ is the interaction range [76]. From our experimental data we find a one σ bound on this potential of $g_A^n g_A^n / (\hbar c) < 2 \times 10^{-37}$ for distances greater than about 41 cm. There is no theoretical expectation for the size of this coupling; but we note that a limit on analogous electron-electron interactions $g_A^e g_A^e / (\hbar c) < 4 \times 10^{-35}$ has been set [76].

In conclusion, we have used a ${}^3\text{He} / {}^{129}\text{Xe}$ maser and a separate ensemble of spin-polarized ${}^3\text{He}$ to perform an experimental search for new spin dependent forces between neutrons. This experiment sets bounds on several theoretical frameworks for physics beyond the Standard Model that include Lorentz symmetry violation and particles that are candidates for dark matter. Further improvement in these results could come from higher

density spin sources and improved co-magnetometers [88].

We acknowledge useful discussions with Jesse Thaler and Michael Crescimanno. This work was supported by NSF grant PHY-0502279.

Bibliography

- [1] V. A. Kostelecký and C. D. Lane. Constraints on Lorentz violation from clock-comparison experiments. *Physical Review D*, 60(11):116010, 1999.
- [2] J. E. Moody and F. Wilczek. New macroscopic forces. *Physical Review D*, 30(1):130–138, 1984.
- [3] V. A. Dzuba, V. V. Flambaum, and P. G. Silvestrov. Bounds on electric dipole moments and T -violating weak interactions of the nucleons. *Physics Letters B*, 154(2-3):93–95, 1985.
- [4] P. L. Anthony, R. G. Arnold, H. R. Band, H. Borel, P. E. Bosted, V. Breton, G. D. Cates, T. E. Chupp, F. S. Dietrich, J. Dunne, et al. Deep inelastic scattering of polarized electrons by polarized ^3He and the study of the neutron spin structure. *Physical Review D*, 54(11):6620–6650, 1996.
- [5] D. Bear, R. E. Stoner, R. L. Walsworth, V. A. Kostelecký, and C.D. Lane. Limit on Lorentz and CPT violation of the neutron using a two-species noble-gas maser. *Physical Review Letters*, 85(24):5038–5041, 2000.
- [6] F. Cane, D. Bear, D. F. Phillips, M. S. Rosen, C. L. Smallwood, R. E. Stoner, R. L. Walsworth, and V. A. Kostelecký. Bound on Lorentz and CPT violating boost effects for the neutron. *Physical Review Letters*, 93(23):230801, 2004.
- [7] A. G. Glenday, C. E. Cramer, D. F. Phillips, and R. L. Walsworth. Limits on anomalous spin-spin couplings between neutrons. *Physical Review Letters*, 101(26):261801, 2008.
- [8] J. M. Brown, S. J. Smullin, T. W. Kornack, and M. V. Romalis. New limit on Lorentz- and CPT -violating neutron spin interactions. *Physical Review Letters*, 105(15):151604, Oct 2010.
- [9] G. Vasilakis, J. M. Brown, T. W. Kornack, and M. V. Romalis. Limits on new long range nuclear spin-dependent forces set with a $\text{K-}^3\text{He}$ comagnetometer. *Physical Review Letters*, 103(26):261801, 2009.
- [10] C. Gemmel, W. Heil, S. Karpuk, K. Lenz, C. Ludwig, Y. Sobolev, K. Tullney, M. Burghoff, W. Kilian, S. Knappe-Grüneberg, et al. Ultra-sensitive magnetometry based on free precession of nuclear spins. *The European Physical Journal D*, 57(3):303–320, 2010.

- [11] H. G. Robinson and T. Myint. ^3He nuclear Zeeman maser. *Applied Physics Letters*, 5(6):116, 1964.
- [12] T. G. Walker and W. Happer. Spin-exchange optical pumping of noble-gas nuclei. *Reviews of Modern Physics*, 69(2):629–642, 1997.
- [13] S. Appelt, A. B. A. Baranga, C. J. Erickson, M. V. Romalis, A. R. Young, and W. Happer. Theory of spin-exchange optical pumping of ^3He and ^{129}Xe . *Physical Review A*, 58(2):1412–1439, 1998.
- [14] M. V. Romalis, E. Miron, and G. D. Cates. Pressure broadening of Rb D_1 and D_2 lines by ^3He , ^4He , N_2 , and Xe: Line cores and near wings. *Physical Review A*, 56(6):4569–4578, 1997.
- [15] W. Happer, E. Miron, S. Schaefer, D. Schreiber, W. A. Van Wijngaarden, and X. Zeng. Polarization of the nuclear spins of noble-gas atoms by spin exchange with optically pumped alkali-metal atoms. *Physical Review A*, 29(6):3092–3110, 1984.
- [16] X. Zeng, Z. Wu, T. Call, E. Miron, D. Schreiber, and W. Happer. Experimental determination of the rate constants for spin exchange between optically pumped K, Rb, and Cs atoms and ^{129}Xe nuclei in alkali-metal–noble-gas van der Waals molecules. *Physical Review A*, 31(1):260–278, 1985.
- [17] J. Pascale and J. Vandeplanque. Excited molecular terms of the alkali-rare gas atom pairs. *The Journal of Chemical Physics*, 60:2278, 1974.
- [18] G. D. Cates, R. J. Fitzgerald, A. S. Barton, P. Bogorad, M. Gatzke, N. R. Newbury, and B. Saam. Rb- ^{129}Xe spin-exchange rates due to binary and three-body collisions at high Xe pressures. *Physical Review A*, 45(7):4631–4639, 1992.
- [19] N. Ramsey, E. Miron, X. Zeng, and W. Happer. Formation and breakup rates of RbXe van der Waals molecules in He and N_2 gas. *Chemical Physics Letters*, 102(4):340–343, 1983.
- [20] I. A. Nelson and T. G. Walker. Rb-Xe spin relaxation in dilute Xe mixtures. *Physical Review A*, 65(1):12712, 2001.
- [21] T. J. Killian. Thermionic phenomena caused by vapors of rubidium and potassium. *Physical Review*, 27(5):578–587, 1926.
- [22] A. Ben-Amar Baranga, S. Appelt, M. V. Romalis, C. J. Erickson, A. R. Young, G. D. Cates, and W. Happer. Polarization of ^3He by spin exchange with optically pumped Rb and K vapors. *Physical Review Letters*, 80(13):2801–2804, 1998.
- [23] T. E. Chupp, K. P. Coulter, T. B. Smith, R. C. Welsh, and M. A. Rosenberry. Spin exchange pumped ^3He targets: Progress and prospects. *Nuclear Instruments and Methods in Physics Research A*, 402:250–255, 1998.
- [24] M. E. Wagshul and T. E. Chupp. Laser optical pumping of high-density Rb in polarized ^3He targets. *Physical Review A*, 49(5):3854–3869, 1994.

- [25] F. Canè. *Progress Towards an Optimized $^{129}\text{Xe}/^3\text{He}$ Zeeman Maser and a Test of Boost Symmetry*. PhD thesis, Harvard University, 2006.
- [26] W. Shao, G. Wang, and E. W. Hughes. Measurement of spin-exchange rate constants between ^{129}Xe and alkali metals. *Physical Review A*, 72(2):22713, 2005.
- [27] I. A. Nelson. *Physics of Practical Spin-Exchange Optical Pumping*. PhD thesis, University of Wisconsin-Madison, 2001.
- [28] Y. Y. Jau, N. N. Kuzma, and W. Happer. High-field measurement of the ^{129}Xe -Rb spin-exchange rate due to binary collisions. *Physical Review A*, 66(5):52710, 2002.
- [29] Y.Y. Jau, N.N. Kuzma, and W. Happer. Magnetic decoupling of ^{129}Xe -Rb and ^{129}Xe -Cs binary spin exchange. *Physical Review A*, 67(2):22720, 2003.
- [30] B. Chann, E. Babcock, L. W. Anderson, and T. G. Walker. Measurements of ^3He spin-exchange rates. *Physical Review A*, 66(3):32703, 2002.
- [31] M. V. Romalis and G. D. Cates. Accurate ^3He polarimetry using the Rb Zeeman frequency shift due to the Rb- ^3He spin-exchange collisions. *Physical Review A*, 58(4):3004–3011, 1998.
- [32] S. R. Schaefer, G. D. Cates, T. R. Chien, D. Gonatas, W. Happer, and T. G. Walker. Frequency shifts of the magnetic-resonance spectrum of mixtures of nuclear spin-polarized noble gases and vapors of spin-polarized alkali-metal atoms. *Physical Review A*, 39(11):5613–5623, 1989.
- [33] J. Kestin, K. Knierim, E. A. Mason, B. Najafi, S. T. Ro, and M. Waldman. Equilibrium and transport properties of the noble gases and their mixtures at low density. *Journal of Physical and Chemical Reference Data*, 13(1):229–303, 1984.
- [34] J. Bzowski, J. Kestin, E. A. Mason, and F. J. Uribe. Equilibrium and transport properties of gas mixtures at low density: Eleven polyatomic gases and five noble gases. *Journal of Physical and Chemical Reference Data*, 19:1179, 1990.
- [35] M. Pfeffer and O. Lutz. ^{129}Xe gas NMR spectroscopy and imaging with a whole-body imager. *Journal of Magnetic Resonance. Series A*, 108(1):106–109, 1994.
- [36] P. J. Mohr, B. N. Taylor, and D. B. Newell. CODATA recommended values of the fundamental physical constants: 2006. *Reviews of Modern Physics*, 80(2):633–730, 2008.
- [37] R. P. Feynman, F. L. Vernon Jr, and R. W. Hellwarth. Geometrical representation of the Schrödinger equation for solving maser problems. *Journal of Applied Physics*, 28:49, 1957.
- [38] L. D. Landau, E. M. Lifshits, and L. P. Pitaevskii. *Electrodynamics of Continuous Media*, volume v. 8 of *Course of theoretical physics / L.D. Landau & E.M. Lifshitz*. Pergamon, Oxford, 2nd ed., rev. and enl. edition, 1984.

- [39] N. W. Ashcroft and N. D. Mermin. *Solid State Physics*. Holt, Rinehart and Winston, New York, 1976.
- [40] J. H. Wesenberg and K. Mølmer. Field inside a random distribution of parallel dipoles. *Physical Review Letters*, 93(14):143903, 2004.
- [41] J. D. Jackson. *Classical Electrodynamics*. Wiley, New York, 3rd ed edition, 1999.
- [42] P. Elleaume, O. Chubar, and J. Chavanne. Computing 3D magnetic field from insertion devices. In *Proceedings of the PAC97 Conference May 1997*, pages 3509–3511, May 1997.
- [43] David Chaiyarat Bear. *Fundamental Symmetry Tests Using a $^{129}\text{Xe}/^3\text{He}$ Dual Noble Gas Maser*. PhD thesis, Harvard University, 2000.
- [44] J. Bechhoefer. Feedback for physicists: A tutorial essay on control. *Reviews of Modern Physics*, 77(3):783–836, 2005.
- [45] R. L. Gamblin and T. R. Carver. Polarization and relaxation processes in He^3 gas. *Physical Review*, 138:946–960, 1965.
- [46] L. D. Schearer and G. K. Walters. Nuclear spin-lattice relaxation in the presence of magnetic-field gradients. *Physical Review*, 139(5A):A1398–A1402, 1965.
- [47] G. D. Cates, S. R. Schaefer, and W. Happer. Relaxation of spins due to field inhomogeneities in gaseous samples at low magnetic fields and low pressures. *Physical Review A*, 37(8):2877–2885, 1988.
- [48] N. R. Newbury, A. S. Barton, G. D. Cates, W. Happer, and H. Middleton. Gaseous ^3He - ^3He magnetic dipolar spin relaxation. *Physical Review A*, 48(6):4411–4420, 1993.
- [49] I. L. Moudrakovski, S. R. Breeze, B. Simard, C. I. Ratcliffe, J. A. Ripmeester, T. Seideman, J. S. Tse, and G. Santyr. Gas-phase nuclear magnetic relaxation in ^{129}Xe revisited. *The Journal of Chemical Physics*, 114:2173, 2001.
- [50] B. Chann, I. A. Nelson, L. W. Anderson, B. Driehuys, and T. G. Walker. ^{129}Xe -Xe molecular spin relaxation. *Physical Review Letters*, 88(11):113201, 2002.
- [51] J. Schmiedeskamp, W. Heil, E. W. Otten, R. K. Kremer, A. Simon, and J. Zimmer. Paramagnetic relaxation of spin polarized ^3He at bare glass surfaces. *The European Physical Journal D-Atomic, Molecular, Optical and Plasma Physics*, 38(3):427–438, 2006.
- [52] A. Deninger, W. Heil, E. W. Otten, M. Wolf, R. K. Kremer, and A. Simon. Paramagnetic relaxation of spin polarized ^3He at coated glass walls. *The European Physical Journal D-Atomic, Molecular, Optical and Plasma Physics*, 38(3):439–443, 2006.
- [53] J. Schmiedeskamp, H. J. Elmers, W. Heil, E. W. Otten, Y. Sobolev, W. Kilian, H. Rinneberg, T. Sander-Thömmes, F. Seifert, and J. Zimmer. Relaxation of spin polarized ^3He by magnetized ferromagnetic contaminants. *The European Physical Journal D-Atomic, Molecular, Optical and Plasma Physics*, 38(3):445–454, 2006.

- [54] B. Driehuys, G. D. Cates, and W. Happer. Surface relaxation mechanisms of laser-polarized ^{129}Xe . *Physical Review Letters*, 74(24):4943–4946, 1995.
- [55] K. C. Hasson, G. D. Cates, K. Lerman, P. Bogorad, and W. Happer. Spin relaxation due to magnetic-field inhomogeneities: Quartic dependence and diffusion-constant measurements. *Physical Review A*, 41(7):3672–3688, 1990.
- [56] D. D. McGregor. Transverse relaxation of spin-polarized ^3He gas due to a magnetic field gradient. *Physical Review A*, 41(5):2631–2635, 1990.
- [57] N. F. Ramsey. Resonance transitions induced by perturbations at two or more different frequencies. *Physical Review*, 100(4):1191–1194, 1955.
- [58] F. Bloch and A. Siegert. Magnetic resonance for nonrotating fields. *Physical Review*, 57(6):522–527, 1940.
- [59] C. J. Jameson. Understanding NMR chemical shifts. *Annual Review of Physical Chemistry*, 47(1):135–169, 1996.
- [60] P. Raghavan. Table of nuclear moments. *Atomic data and nuclear data tables*, 42(2):189–291, 1989.
- [61] C. J. Jameson, A. K. Jameson, and S. M. Cohen. Temperature and density dependence of ^{129}Xe chemical shift in xenon gas. *Journal of Chemical Physics*, 59:4540–4546, 1973.
- [62] C. J. Jameson, A. K. Jameson, and H. Parker. Second virial coefficient of ^{129}Xe chemical shielding in Xe interacting with CO and N_2 molecules. *Journal of Chemical Physics*, 68:3943–3944, 1978.
- [63] C.J. Jameson, D.N. Sears, and A.C. de Dios. The ^{129}Xe nuclear shielding tensor surfaces for Xe interacting with rare gas atoms. *The Journal of chemical physics*, 118(6):2575–2580, 2003.
- [64] G. R. Davies, T. K. Halstead, R. C. Greenhow, and K. J. Packer. High-resolution NMR of low pressure laser-polarized ^{129}Xe gas. *Chemical Physics Letters*, 230(3):237–242, 1991.
- [65] S. K. Lee and M. V. Romalis. Calculation of magnetic field noise from high-permeability magnetic shields and conducting objects with simple geometry. *Journal of Applied Physics*, 103:084904, 2008.
- [66] T. W. Kornack, S. J. Smullin, S. K. Lee, and M. V. Romalis. A low-noise ferrite magnetic shield. *Applied Physics Letters*, 90:223501, 2007.
- [67] VO Altemose. Helium diffusion through glass. *Journal of Applied Physics*, 32(7):1309–1316, 1961.
- [68] S. J. Seltzer and M. V. Romalis. High-temperature alkali vapor cells with antirelaxation surface coatings. *Journal of Applied Physics*, 106(11):114905, 2009.

- [69] S. J. Seltzer, D. M. Rampulla, S. Rivillon-Amy, Y. J. Chabal, S. L. Bernasek, and M. V. Romalis. Testing the effect of surface coatings on alkali atom polarization lifetimes. *Journal of Applied Physics*, 104(10):103116, 2009.
- [70] F. Roméo and D. I. Hoult. Magnet field profiling: analysis and correcting coil design. *Magnetic Resonance in Medicine*, 1(1):44–65, 1984.
- [71] I. M. Savukov, S. J. Seltzer, and M. V. Romalis. Detection of NMR signals with a radio-frequency atomic magnetometer. *Journal of Magnetic Resonance*, 185(2):214–220, 2007.
- [72] S. Butterworth. Eddy-current losses in cylindrical conductors, with special applications to the alternating current resistances of short coils. *Philosophical Transactions of the Royal Society of London. Series A*, 222:57–100, 1922.
- [73] R. Bluhm, V. A. Kostelecký, C. D. Lane, and N. Russell. Probing Lorentz and *CPT* violation with space-based experiments. *Physical Review D*, 68(12):125008, 2003.
- [74] N. R. Draper and H. Smith. *Applied Regression Analysis*. Wiley series in probability and statistics. John Wiley & Sons, New York, 3rd edition, 1998.
- [75] N. Arkani-Hamed, H. C. Cheng, M. Luty, and J. Thaler. Universal dynamics of spontaneous Lorentz violation and a new spin-dependent inverse-square law force. *Journal of High Energy Physics*, 2005(7):029, July 2005.
- [76] B. A. Dobrescu and I. Mocioiu. Spin-dependent macroscopic forces from new particle exchange. *Journal of High Energy Physics*, 2006(11):005, Nov 2006.
- [77] D. J. Wineland, J. J. Bollinger, D. J. Heinzen, W. M. Itano, and M. G. Raizen. Search for anomalous spin-dependent forces using stored-ion spectroscopy. *Physical Review Letters*, 67(13):1735–1738, Sep 1991.
- [78] T. C. P. Chui and W. T. Ni. Experimental search for an anomalous spin-spin interaction between electrons. *Physical Review Letters*, 71(20):3247–3250, Nov 1993.
- [79] W. T. Ni, T. C. P. Chui, S. S. Pan, and B. Y. Cheng. Search for anomalous spin-spin interactions between electrons using a DC SQUID. *Physica B*, 194:153–154, Feb 1994.
- [80] N. F. Ramsey. Tensor force between 2 protons at long-range. *Physica A*, 96(1-2):285–289, 1979.
- [81] T. E. Chupp, R. J. Hoare, R. L. Walsworth, and B. Wu. Spin-exchange-pumped ^3He and ^{129}Xe Zeeman masers. *Physical Review Letters*, 72(15):2363–2366, Apr 1994.
- [82] R. E. Stoner, M. A. Rosenberry, J. T. Wright, T. E. Chupp, E. R. Oteiza, and R. L. Walsworth. Demonstration of a two species noble gas maser. *Physical Review Letters*, 77(19):3971–3974, 1996.
- [83] D. Bear, T. E. Chupp, K. Cooper, S. DeDeo, M. Rosenberry, R. E. Stoner, and R. L. Walsworth. Improved frequency stability of the dual-noble-gas maser. *Physical Review A*, 57(6):5006–5008, 1998.

-
- [84] S. J. Asztalos, L. J. Rosenberg, K. van Bibber, P. Sikivie, and K. Zioutas. Searches for astrophysical and cosmological axions. *Annual Review of Nuclear and Particle Science*, 56(1):293–326, 2006.
- [85] G. G. Raffelt. Axions - motivation, limits and searches. *Journal of Physics A: Mathematical and Theoretical*, 40(25):6607–6620, Jun 2007.
- [86] A. N. Youdin, D. Krause, K. Jagannathan, L. R. Hunter, and S. K. Lamoreaux. Limits on spin-mass couplings within the axion window. *Physical Review Letters*, 77(11):2170–2173, Sep 1996.
- [87] C. L. Bennett, M. Halpern, G. Hinshaw, N. Jarosik, A. Kogut, M. Limon, S. S. Meyer, L. Page, D. N. Spergel, G. S. Tucker, E. Wollack, E. L. Wright, C. Barnes, M. R. Greason, R. S. Hill, E. Komatsu, M. R. Nolta, N. Odegard, H. V. Peiris, L. Verde, and J. L. Weiland. First-year Wilkinson Microwave Anisotropy Probe (WMAP) observations: preliminary maps and basic results. *The Astrophysical Journal Supplement Series*, 148:1, 2003.
- [88] I. K. Kominis, T. W. Kornack, J. C. Allred, and M. V. Romalis. A subfemtotesla multichannel atomic magnetometer. *Nature*, 422(6932):596–599, 2003.